Search for Topological Superconductivity in Doped Bi_2Se_3

by

Benjamin John Lawson

A dissertation submitted in partial fulfillment
of the requirements for the degree of
Doctor of Philosophy
(Physics)
in the University of Michigan
2017

Doctoral Committee:

Associate Professor Lu Li, Chair
Professor Cagliyan Kurdak
Assistant Professor Xiaogan Liang
Assistant Professor Kai Sun
Assistant Professor Liuyan Zhao

Benjamin John Lawson

bjlawson@umich.edu

ORCID iD: 0000-0003-0767-0886

For Lauren.

Acknowledgments

I would like to thank my advisor Professor Lu Li. Lu has far exceeded my hopes and expectations for a research advisor. I attribute any of my success in graduate school to his excellent mentorship. He has not only taught me much about physics and research, but has also genuinely invested in me as a person. I am very honored to have worked under him.
Much of the research was done under the National Science Foundation Graduate Research Fellowship under Grant No. F031543.
Thanks to Professor Yew San Hor for growing the many interesting materials used in this thesis, and to Professors Kai Sun and Liang Fu for theoretical support.
In addition, this thesis was made possible by many others working in Lu Li's lab. First and foremost, I would like to acknowledge Gang Li for working with me and teaching me everything from experimental techniques to data reduction. Also, my fellow graduate student Tomoya Asaba for being an excellent colleague as well as a close friend. Furthermore, thank you to the other graduate students and postdocs who contributed time and energy working with me on these projects - Fan Yu, Colin Tinsman, Lu Chen, and Ziji Xiang. Lastly, I would like to acknowledge Paul Corbae, the undergraduate who worked with me on the study of Nb-doped Bi_2Se_3. Paul was an excellent student and has a bright future.
Outside of the lab, I would like to thank my friends and family for doing life with me and keeping me sane. In particular, Midhat Farooq for many mid-day ice cream escapes, my dad Ron Lawson for frequently listening to me vent about graduate school frustrations, and lastly to my wife Lauren for holistically supporting me and putting all this work in perspective.

TABLE OF CONTENTS

LIST OF TABLES

LIST OF FIGURES

LIST OF APPENDICES

LIST OF ABBREVIATIONS

2D two dimensional

3D three dimensional

ARPES Angle Resolved Photoemission Spectroscopy

BCS Bardeen Cooper Schrieffer

dHvA de Haas-van Alphen

FFT Fast Fourier transformation

MPMS Magnetic Properties Measurement System

NMR nuclear magnetic resonance

PPMS Physical Properties Measurement System

SdH Shubnikov-de Haas

SQUID Superconducting QUantum Interference Device

STM Scanning Tunneling Microscopy

STS Scanning Tunneling Spectroscopy

TEM transmission electron microscopy

TRI time-reversal invariant

XRD X-ray Diffraction

ABSTRACT

Bi_2Se_3 is a known topological insulator. When doped with certain metals, this compound becomes superconducting. To date, doping Bi_2Se_3 has been one of the leading avenues to search for topological superconductivity. In this dissertation, I present toque mangetometry studies on Cu-doped and Nb-doped Bi_2Se_3, which are candidates to be topological superconductors.

Quantum oscillations are generally studied to resolve the electronic structure of topological insulators. Using torque magnetometry, I observed quantum oscillations (the de Haas-van Alphen effect) in Cu-doped and Nb-doped Bi_2Se_3. The doping of Cu in Bi_2Se_3 increases the carrier density and the effective mass without increasing the scattering rate or decreasing the mean free path. As the magnetic field tilts from the crystalline c axis to the ab plane, the change of the oscillation period follows the prediction of the ellipsoidal Fermi surface. As the doping level changes, the 3D Fermi surface becomes quasicylindrical at high carrier density. Such a transition is potentially a Lifshitz transition of the electronic state in Cu-doped Bi_2Se_3. In addition, the Fermi velocity remains the same in Cu-doped Bi_2Se_3 as that in Bi_2Se_3. These results imply that the insertion of Cu does not change the band structure and that conduction electrons in Cu doped Bi_2Se_3 sit in the linear Dirac-like band.

In the fully superconducting Nb-doped Bi_2Se_3 crystal, two distinct quantum oscillations frequencies are observed, in sharp contrast to Bi_2Se_3 and Cu-doped Bi_2Se_3. The multiple frequencies observed in the quantum oscillations, combined with the electrical transport studies, indicate the multi-orbit nature of the electronic state of Nb-doped Bi_2Se_3. The observation of the multiple orbits in the superconducting Nb-doped Bi_2Se_3 also points to Fermi surface nesting as a possible superconducting mechanism, and reveals that the insertion of Nb radically changes the band structure of Bi_2Se_3.

For topological superconductors, the coupling between the physical properties in the

superconducting state and its underlying crystal symmetry is a crucial test for the topological nature of the superconductivity. The superconducting magnetic response in Nb-doped Bi_2Se_3 couples strongly to the underlying 3-fold crystal symmetry. More importantly, the magnetic response is greatly enhanced along one preferred direction spontaneously breaking the rotational symmetry. This confirms the presence of nematic order in the superconducting ground state of Nb-doped Bi_2Se_3. The observation of nematic order in the superconducting state provides a strong evidence of odd-parity topological superconductivity.

CHAPTER 1

Introduction

1.1 Introduction to Topological Superconductivity

Topological superconductivity sits at the intersection of two exciting fields in condensed matter physics - unconventional superconductivity and topological materials. A superconductor has zero electrical resistance and it completely expels magnetic flux (i.e. the Meissner effect). A conventional superconductor can be described by the Bardeen Cooper Schrieffer (BCS) theory. An unconventional superconductor does not follow the predictions of BCS theory leading to interesting physical consequences such as enhanced critical temperature. Unconventional superconductivity has been an exciting field of research that has captivated the condensed matter community for over 30 years since it was first discovered [25].

Topological materials are a class of materials classified by a bulk topological invariant. The theory originally arose to explain the integer Quantum Hall effect [26] where time-reversal symmetry is broken. However, more recently it has been found that the time-reversal invariant Quantum Spin Hall effect arises because of a topological index, which distinguishes the Quantum Spin Hall phase from a trivial phase [27, 28]. Over the last decade, there has been a flurry of research on new topological phases of matter. The first three dimensional (3D) topological insulating phase was discovered in 2008 in $Bi_{1-x}Sb_x$ [29]. Topological phases usually give rise to symmetry protected edge or surface conduction with spin-momentum locking. Despite a hundred years of band theory successfully describing electronic phases of matter like metals, insulators, and semiconductors, studying the topological aspects of band theory and the role of symmetries and Berry phase has lead to the discoveries of completely new properties of matter in the last 10 years.

At the crossroads of these two fascinating fields, topological superconductivity has been theoretically established but has yet to be experimentally realized. A topological superconductor is an unconventional superconductor with a gap classified by a non-trivial topologi-

cal invariant. Similar to the topological insulator, the superconducting topological invariant can cause the superconducting gap to close due to a symmetry protected surface state. On the other hand, unlike the topological insulator, the surface state on the topological superconductor may support Majorana fermions - a particle that is its own antiparticle.

A normal solid has negatively charged electrons and positively charged holes. Due to the charge difference, these two particles are definitely not their own antiparticle. However, in a superconductor, charge carriers form Cooper pairs, and the particle number is no longer conserved. The Bosonic condensate of Cooper pairs masks the charge properties of carriers making a superconductor a promising platform to realize Majorana particles [30]. However, a problems still exists: an antiparticle is the negative energy counterpart of a particle and thus the particle and antiparticle are different. This is the case of electrons which exist in the conduction band above the Fermi level and holes which exist in the valence band below the Fermi level. For a Majorana particle to be realized, there has to be a zero-energy mode at the Fermi level (i.e. the gap needs to be closed). This is where the cross-section of topological band theory and superconductivity comes to the rescue. The non-trivial topology of a topological superconductor closes the gap giving rise to the possibility of Majorana zero modes on the surface where the gap closes [31].

In the case of the Majorana, the exciting prospect of discovering a new quasiparticle with exotic physical properties is coupled by the coinciding applications should it be discovered. Recently, a framework has been developed for encoding a quantum state that is robust to decoherence on a Majorana in a topological superconductor [31, 32]. This has lead to the exciting prospect of topological quantum computation that is robust against decoherence, the main obstacle of traditional quantum computers. However, whether topological superconductivity is a real piece of nature or simply an interesting mathematical exercise is still a mystery waiting to be discovered.

Bi_2Se_3 is a topological insulator that has attracted special interest since Cu, Sr, or Nb intercalation between quintuple layers of Bi_2Se_3 can induce superconductivity. It is proposed that doped Bi_2Se_3 is a topological superconductor [5], which has a full pairing gap in the bulk and a topologically protected gapless surface state consisting of Majorana fermions.

Specific heat measurement showed that $Cu_xBi_2Se_3$ is a bulk superconductor with a full pairing gap [6]. Furthermore, point-contact spectroscopy studies discovered that $Cu_xBi_2Se_3$ exhibits a surface Andreev bound state [8]. However, the observation of quantum oscillations, which are generally studied to resolve the electronic structure of topological materials, was missing in $Cu_xBi_2Se_3$. For a topological superconductor, as well as the topological insulators such as Bi_2Se_3 and Bi_2Te_3, the observation of quantum oscillations (arising from Landau level quantization) is important since it is a direct measurement of the bulk and

surface states [33, 34, 35]. As a result, before the observation of quantum oscillations, the exact measurement of the effective mass and the scattering rate of this topological superconductor candidate was controversial [4, 6, 36, 37]. Furthermore, the geometry of the Fermi surface has profound consequences on topological superconductivity [5, 38]. Quantum oscillations can be used to map the Fermi surface and thus are an important probe into the nature of topological superconductor candidates.

This work contributes to the search for topological superconductivity by answering some key questions to one of the most promising platforms for topological superconductivity to date - doped Bi_2Se_3. Here, I studied the quantum oscillations of Cu-doped Bi_2Se_3 [39, 40] and Nb-doped Bi_2Se_3 [41] presenting the first report of Landau level quantization in both of those systems. Furthermore, using torque magnetometry rotational symmetry breaking, a feature of a new theory for topological superconductivity [12], was observed in Nb-doped Bi_2Se_3 [42].

The rest of chapter 1 introduces some of the theoretical framework for topological superconductivity and briefly presents other candidates for topological superconductivity. Chapter 2 is a review of the literature to date concerning the search for topological superconductivity in doped Bi_2Se_3, including some of the key questions and debates. Chapter 3 describes the experimental techniques used in this thesis. And chapters 4 and 5 present the key results of this work for $Cu_xBi_2Se_3$ and $Nb_xBi_2Se_3$ respectively.

1.2 Signatures of Topological Superconductivity

1.2.1 Topological Superconductor Criteria

In a paper by Fu and Berg [5], sufficient criteria for the realization of topological superconductivity are derived. Fu and Berg show that a time-reversal invariant (TRI), centrosymmetric superconductor is necessarily a topological superconductor if it meets the following two criteria

1. The superconducting pairing is odd-parity, and
2. There are an odd number of TRI momenta enclosed in the Fermi surface.

Much of the experimental literature (discussed further in chapter 2) concerns the first criteria. Odd-parity superconductivity is rare, even in unconventional superconductors, and has some clear experimental signatures. Many other papers concern the Majorana surface modes expected to arise from non-trivial bulk topology, as shown in the next section. The

experiments in this thesis, which probe the Fermiology of topological superconductor candidates, address the second criteria.

Here, I will walk through the proof made in ref. [5] which shows that criteria 1 and 2 lead to topological superconductivity.

As shown in ref. [43] (and work out in Appendix A), Z_2 topological invariants are calculated from

$$\delta_i = \frac{\sqrt{\det[w(\Gamma_i)]}}{\mathrm{Pf}[w(\Gamma_i)]} = \pm 1, \tag{1.1}$$

δ_i is related to the change in time-reversal polarization (see Appendix A) giving rise to Kramers pairs switching partners [44]. This results in edge states crossing the Fermi energy an odd number of times. In equation 1.1, Pf donates the Pfaffian of a matrix and $w(\mathbf{k})$ is a unitary, antisymmetric matrix that connects time-reversed wavefunctions given by

$$w_{mn}(\mathbf{k}) = \langle u_m(-\mathbf{k})| \, \Theta \, |u_n(\mathbf{k})\rangle \,, \tag{1.2}$$

where $|u_n(\mathbf{k})\rangle$ are eigenstates of the Block Hamiltonian and Θ is the time-reversal operator given by

$$\Theta = e^{i\pi S_y} K. \tag{1.3}$$

S_y is a spin operator and K is the complex conjugate operator. Θ takes $\mathbf{k}$ to $-\mathbf{k}$. A TRI Hamiltonian will be transformed by Θ as

$$\Theta H(\mathbf{k}) \Theta^{-1} = H(-\mathbf{k}) \tag{1.4}$$

$\mathbf{k} = \Gamma_i$ are the TRI momenta given by a superposition of reciprocal lattice primitive vectors, b_i,

$$\Gamma_{i=(n_1 n_2 n_3)} = \frac{1}{2}(n_1 \mathbf{b}_1 + n_2 \mathbf{b}_2 + n_3 \mathbf{b}_3) \tag{1.5}$$

Γ_i satisfy

$$-\Gamma_i = \Gamma_i + \mathbf{G} \tag{1.6}$$

where $\mathbf{G}$ is a reciprocal lattice vector. The solution to the periodic Block Hamiltonian for a topological insulator are Bloch waves, $e^{i\mathbf{k}\cdot\mathbf{r}} |u_n(\mathbf{k})\rangle = |\psi_{n,\mathbf{k}}\rangle$, with the property, $|\psi_{n,\mathbf{k}}\rangle = |\psi_{n,\mathbf{k}+\mathbf{G}}\rangle$, thus at TRI momenta

$$\Theta H(\Gamma_i)\Theta^{-1} = H(\Gamma_i) \tag{1.7}$$

In two dimensions there are 4 TRI momenta in the Brillouin zone and there are 8 in three dimensions - consisting of high symmetry points such as Γ, Z, K, etc.

As shown in appendix A, the topological invariant, ν, is given by the product of δ_i over all the TRI momenta in the Brillouin zone. In two dimensions this is given by [44, 45]:

$$(-1)^{\nu} = \prod_{i=1}^{4} \delta_i, \tag{1.8}$$

and in three dimensions, there are four invariants given by

$$(-1)^{\nu_0} = \prod_{i=1}^{8} \delta_i \tag{1.9}$$

and

$$(-1)^{\nu_{i=1,2,3}} = \prod_{n_i=1;n_{j\neq i}=0,1} \delta_{(i=n_1n_2n_3)}. \tag{1.10}$$

For a 3D TRI insulator, $\nu_0 = 1$ is sufficient criteria for a strong topological insulator; however, with $\nu_0 = 0$ and $\nu_{i\neq 0} = 1$ for any $i \neq 0$, a weak topological insulator phase is realized with topological surface states on some surfaces. In a weak topological insulator, the surface states can be destroyed without violating time-reversal symmetry [44].

For the superconductor Hamiltonian (Bogoliubov-de Gennes Hamiltonian) and the band insulator Hamiltonian (Bloch Hamiltonian), the time-reversal operator, Θ, is the same. Thus, the topological invariant, ν_0 = 1, is sufficient to establish a topological phase in a superconductor as well as an insulator [5].

Consider the superconducting Hamiltonian [38]

$$H = \frac{1}{2}\sum_{\mathbf{k}\alpha\alpha'} (c^{\dagger}_{\mathbf{k}\alpha}, c_{-\mathbf{k}\alpha}) H(\mathbf{k}) \begin{pmatrix} c_{\mathbf{k}\alpha'} \\ c^{\dagger}_{-\mathbf{k}\alpha'} \end{pmatrix}, \tag{1.11}$$

where $H(\mathbf{k})$ is the Bogoliubov-de Gennes Hamiltonian given by

$$H(\mathbf{k}) = \begin{pmatrix} E(\mathbf{k})_{\alpha\alpha'} & \Delta(\mathbf{k})_{\alpha\alpha'} \\ \Delta^{\dagger}(\mathbf{k})_{\alpha\alpha'} & -E^{T}(-\mathbf{k})_{\alpha\alpha'} \end{pmatrix}. \tag{1.12}$$

$c^{\dagger}_{\mathbf{k}\alpha}$ is the creation operator for an electron with momentum, $\mathbf{k}$. The subscript, α, indexes the electron spins and orbital degrees of freedom. Fu and Berg explicitly give the spin

degree of freedom in their Hamiltonian, but not the orbital degree of freedom [5]. $\Delta(\mathbf{k})_{\alpha\alpha'}$ is the superconducting gap function, and $E(\mathbf{k})_{\alpha\alpha'}$ is the matrix giving the normal state electron energy. The Bogoliubov-de Gennes Hamiltonian can also be written as [5]

$$H(\mathbf{k}) = [H_0(\mathbf{k}) - \mu]\tau_z + \Delta(\mathbf{k})\tau_x \tag{1.13}$$

where $E(\mathbf{k})_{\alpha\alpha'}$ is replaced by the difference between kinetic energy, H_0, and the chemical potential, μ. $\tau_{x,z}$ are the Pauli spin matrices in Nambu space (particle-hole space). Nambu space is often used with describing superconductors [47, 48]. The Pauli matrices in this space are identical to the Pauli matrices in spin-space [49]; however in Nambu space, z-spin up represents and occupied state and z-spin down represents an unoccupied state [5, 46].

Criteria 1 requires that the superconducting gap has odd-parity, or $P\Delta(\mathbf{k})P = -\Delta(-\mathbf{k})$. P is the parity operator that takes $r \to -r$ and $\mathbf{k} \to -\mathbf{k}$. Note, since $P = P^{-1}$ and since P is unitary, $P = P^\dagger$. Here I will use P for P^{-1} and $P^\dagger$ as done in ref. [5]. $H_0(\mathbf{k})$ is even under parity, so $PH_0(\mathbf{k})P = H_0(-\mathbf{k})$

Given the odd parity gap function, the Hamiltonian in equation 1.12, or equivalently 1.13, has the following symmetry

$$\Pi H(\mathbf{k})\Pi = H(-\mathbf{k}), \text{where } \Pi = P \otimes \tau_z = \begin{pmatrix} P & 0 \\ 0 & -P \end{pmatrix}, \tag{1.14}$$

which allows the Z_2 topological invariant in equation 1.9 to be solved in similar fashion to the inversion symmetric topological insulator [45]. This is done by rephrasing $\sqrt{\det[w(\Gamma_i)]}$ and $\mathrm{Pf}[w(\Gamma_i)]$ in terms of the eigenvalues of Π at the TRI momenta as shown below.

The eigenstates of the Bogoliubov-de Gennes Hamiltonian at Γ_i can be approximated by the Block eigenstates, $|u_n(\mathbf{k})\rangle$, since Γ_i is generally far from the Fermi surface [5]. Given the symmetry in equation 1.14, $[\Pi, H(\Gamma_i)] = 0$, thus the eigenstates of the Bogoliubov-de Gennes Hamiltonian at Γ_i are also eigenstates of Π:

$$\Pi \left|u_n(\Gamma_i)\right\rangle = \xi_n(\Gamma_i) \left|u_n(\Gamma_i)\right\rangle . \tag{1.15}$$

To start, I'll introduce a new matrix

$$v_{mn}(\mathbf{k}) = \left\langle u_m(\mathbf{k})\right| \Pi\Theta \left|u_n(\mathbf{k})\right\rangle . \tag{1.16}$$

The matrix, $w_{mn}(\mathbf{k})$ from equation 1.2 at $\mathbf{k} = \Gamma_i$ can be restated as

$$w_{mn}(\Gamma_i) = \xi_m(\Gamma_i) v_{mn}(\Gamma_i) \tag{1.17}$$

by noting

$$\begin{aligned} v_{mn}(\Gamma_i) &= \langle u_m(\Gamma_i)| \, \Pi\Theta \, |u_n(\Gamma_i)\rangle \\ &= \xi_m(\Gamma_i) \, \langle u_m(-\Gamma_i)| \, \Theta \, |u_n(\Gamma_i)\rangle \\ &= \xi_m(\Gamma_i) \, \langle u_m(\Gamma_i)| \, \Theta \, |u_n(\Gamma_i)\rangle \\ &= \xi_m(\Gamma_i) w_{mn}(\Gamma_i) \end{aligned}$$

then dividing both sides by $\xi_m(\Gamma_i)$, which can be moved to the numerator because $\xi_m(\Gamma_i) = \pm 1$.

The determinant of $w_{mn}(\Gamma_i)$ from equation 1.17 is given by

$$\det[w(\Gamma_i)] = \det[v(\Gamma_i)] \prod_m \xi_m(\Gamma_i) \tag{1.18}$$

$\det[v(\Gamma_i)] = 1$ by gauge choice. In fact, the more rigorous condition of $\mathrm{Pf}[v(\mathbf{k})] = 1 \; \forall \; \mathbf{k}$ can be shown, thus $\det[v(\Gamma_i)] = \mathrm{Pf}[v(\Gamma_i)]^2 = 1$ [45]. Since $[\Pi, \Theta] = 0$, Kramer's pairs, $|u_{2n}(\Gamma_i)\rangle$ and $|u_{2n+1}(\Gamma_i)\rangle \equiv \Theta \, |u_{2n}(\Gamma_i)\rangle$ also share the same Π eigenvalue. $\prod_m \xi_m(\Gamma_i) = 1$ because $\xi_m(\Gamma_i) = \pm 1$ and thus the product of each Kramer's pair must be 1. In conclusion, $\det[w(\Gamma_i)] = 1$ and therefore

$$\sqrt{\det[w(\Gamma_i)]} = 1. \tag{1.19}$$

Due to Kramer's degeneracy, the product in equation 1.18 can be restated over one of each Kramer's pair

$$\prod_m \xi_m(\Gamma_i) = (\prod_m \xi_{2m}(\Gamma_i))^2 \tag{1.20}$$

From the definition of the Pfaffian, $\mathrm{Pf}[w(\Gamma_i)]^2 = \det[w(\Gamma_i)]$. $\mathrm{Pf}[w(\Gamma_i)]$ can be solved by taking the square root of the right hand side of equation 1.18 after substituting equation 1.20 for the product. This gives

$$\mathrm{Pf}[w(\Gamma_i)] = \sqrt{\det[v(\Gamma_i)]} \prod_m \xi_{2m}(\Gamma_i) = \prod_m \xi_{2m}(\Gamma_i). \tag{1.21}$$

Substituting equations 1.19 and 1.21 into equation 1.1 yields

$$\delta_i = \frac{1}{\prod_m \xi_{2m}(\Gamma_i)} = \prod_m \xi_{2m}(\Gamma_i). \tag{1.22}$$

The second equality follows because $\prod_m \xi_{2m}(\Gamma_i) = \pm 1$. Thus, the topological invariant in equation 1.9 can be restated in terms of the product of the eigenvalues of Π at the TRI momenta

$$(-1)^{\nu_0} = \prod_{i,m} \xi_{2m}(\Gamma_i). \tag{1.23}$$

The eigenstates of the Bogoliubov-de Gennes Hamiltonian at Γ_i were previously approximated by the Block eigenstates. This is equivalent to taking $\Delta(\Gamma_i) \to 0$ since the energy scale of the gap function is generally much smaller than $H_0(\mathbf{k}) - \mu$ when $\mathbf{k} = \Gamma_i$. Thus the eigenstates of the Bogoliubov-de Gennes Hamiltonian in equation 1.13 are $|\phi(\Gamma_i)\rangle \otimes |\tau_z = 1\rangle$ for an occupied band ($\mathrm{sgn}[\mu - \epsilon_m(\Gamma_i)] > 0$) or $|\phi(\Gamma_i)\rangle \otimes |\tau_z = -1\rangle$ for an unoccupied band ($\mathrm{sgn}[\mu - \epsilon_m(\Gamma_i)] < 0$). Where $|\phi(\Gamma_i)\rangle$ are eigenstates of H_0 with energy $\epsilon_m(\Gamma_i)$. This can be also be noted in matrix form using the Hamiltonian from equation 1.12 used in ref. [38].

As the eigenstates of H are also the eigenstates of Π,

$$\xi_m(\Gamma_i) = p_m(\Gamma_i)\tau_m(\Gamma_i) \tag{1.24}$$

where $p_m(\Gamma_i) = \pm 1$ is the eigenvalue of the parity operator and $\tau_m(\Gamma_i) = \pm 1$ is the eigenvalue of the particle-hole operator. The product of these two operators make up Π in equation 1.14. Substituting equation 1.24 into equation 1.23 yields

$$\begin{aligned}(-1)^{\nu_0} &= \prod_{i,m} p_{2m}(\Gamma_i)\tau_{2m}(\Gamma_i) \\ &= \prod_{i,m} p_{2m}(\Gamma_i)\mathrm{sgn}[\mu - \epsilon_{2m}(\Gamma_i)]\end{aligned}$$

$\prod_{i,m} p_{2m}(\Gamma_i) = \prod_i \det[P] = 1$ since there are an even number of TRI momenta in the Brillouin zone and $\det[P]$ is independent of Γ_i. Thus the previous equation simplifies to

$$(-1)^{\nu_0} = \prod_{i,m} \mathrm{sgn}[\mu - \epsilon_{2m}(\Gamma_i)] = \prod_i (-1)^{N(\Gamma_i)} \tag{1.25}$$

where $N(\Gamma_i)$ is the number of unoccupied bands at Γ_i. For a topologically nontrivial superconductor, $\nu_0 = 1$. Again, since there are an even number of TRI momenta in the

Brillouin zone, this can be simply interpreted as criteria 2 from the beginning of the section: A topological superconductor has an odd number of TRI momenta enclosed in the Fermi surface.

It is interesting to note that the topological superconductor keeps time-reversal symmetry [5]. This is not necessarily the case for odd-parity superconductors such as Sr_2RuO_4 where time-reversal symmetry is shown to be broken using the Kerr effect [50]. Time-reversal invariance supports the spacial separated Majorana surface states discussed briefly in the next section [51]. In superconductors like Sr_2RuO_4 with broken time-reversal symmetry, Majorana modes can arise from half-quantum vortices [52].

1.2.2 Majorana Surface State

Topological superconductors are predicted to host non-abelian, Majorana modes on its surface [38, 51, 53, 54, 55]. Due to the non-abelian statistics, methods have been suggested to utilize these modes to build a robust quantum computer that is resistant to decoherence [31, 32]. The potential applications of a topological superconductor which hosts Majorana modes has been a key motivator for this field outside of the interest for fundamental science.

The theory of Majorana modes in a 3D, time-reversal invariant topological superconductor [51] will not be worked out here. However, to introduce the idea of Majorana modes, consider a simple Hamiltonian of a spinless one-dimensional superconductor [51, 56]:

$$H = -\mu \sum_{i=1}^{N} c_i^\dagger c_i - \sum_{i=1}^{N-1} (t c_i^\dagger c_{i+1} - \Delta c_i c_{i+1} + t c_{i+1}^\dagger c_i - \Delta c_{i+1}^\dagger c_i^\dagger) \tag{1.26}$$

where μ is the chemical potential, $c_i^\dagger$ and c_i are the creation and annihilation operators respectively at site i, Δ is the superconducting gap (which we assume for simplicity $\Delta = |\Delta|$), and t is the hopping strength. To show that the eigenstates of this Hamiltonian are Majorana fermions, we split each fermion operator into Majorana operators:

$$c_i = \frac{1}{2}(\gamma_{2i-1} + i\gamma_{2i}) \tag{1.27}$$

$$c_i^\dagger = \frac{1}{2}(\gamma_{2i-1} - i\gamma_{2i}) \tag{1.28}$$

The operators, γ_i, are seen to be Majorana since they are their own Hermitian conjugates as is clear in equations 1.29 and 1.30.

$$\gamma_{2i-1} = c_i + c_i^\dagger \tag{1.29}$$

$$\gamma_{2i} = i(c_i^\dagger - c_i) \tag{1.30}$$

Subsituting equations 1.27 and 1.28 into equation 1.26 while taking advantage of the anti-commutator relations

$$\{\gamma_i, \gamma_{i'}\} = 2\delta_{i,i'} \tag{1.31}$$

yields

$$H = \frac{i\mu}{2}\sum_{i=1}^{N}\gamma_{2i}\gamma_{2i-1} - \frac{i}{2}\sum_{i=1}^{N-1}[(t-\Delta)\gamma_{2i-1}\gamma_{2i+2} + (t+\Delta)\gamma_{2i+1}\gamma_{2i}] \tag{1.32}$$

In the trivial phase, $\mu < 0$ and $\Delta = t = 0$, the Hamiltonian becomes

$$H = \frac{i\mu}{2}\sum_{i=1}^{N}\gamma_{2i}\gamma_{2i-1} \tag{1.33}$$

where each Majorana is coupled to another at each physical site. However, in the topological phase, $\mu = 0$ and $\Delta = t > 0$, the Hamiltonian becomes

$$H = -it\sum_{i=1}^{N-1}\gamma_{2i+1}\gamma_{2i} \tag{1.34}$$

where γ_1 and γ_{2N} are uncoupled resulting in two spatially separated Majorana modes. Here for simplicity the chemical potential is taken to be 0 for the topologically non-trivial phase. It can be further demonstrated that in this 1D system the topological phase holds for any chemical potential in the gap: $|\mu| < 2t$ [56].

1.3 Search for Topological Superconductivity

To date, the search for the Majorana fermion in a topological system involving a superconductor has taken many forms. A prevalent method is to create a heterostructure with a superconductor-topological insulator interface [57]. In particular, there has been promising preliminary results with topological insulator Bi_2Se_3 and superconductor $NbSe_2$ [58] and with a Nb-Bi_2Te_3-Nb junction [59]. Similarly, it has been proposed that a Majorana

could be realized by building a heterostructure with a semiconducting thin film sandwiched between a superconductor and a magnetic insulator [60].

Other than with heterostructures, topological superconductivity hosting Majorana particles have been proposed for nodal superconductors with spin-orbit coupling [61] or magnetic order [62]. Theoretical work on p-wave superconductors show topological order and Majorana modes [63, 64]. Sr_2RuO_4 has been proposed to be spin-triplet and has drawn a lot of attention lately [65]. A whole class of half-Heusler materials, RPtBi and RPdBi (R = La, Y, Lu, Er, Ce, Lu), have been suggested to be candidates of topological superconductivity [66, 67, 68]. Closer to this work, doped semiconductor, $Sn_{1-x}In_xTe$, has also shown promising signs of topologically protected surface Majorana states [69].

Bi-based topological insulators, Bi_2Se_3 and Bi_2Te_3, have taken a central role in the search for topological superconductivity. One method to realize topological superconductivity in these materials has been to induce superconductivity by applying pressure [70, 71]. Another method, which is the topic of this thesis, has been to dope these known topological insulators with metals to induce superconductivity [5]. To date, $Cu_xBi_2Se_3$ has been the most researched topological superconductor candidate.

CHAPTER 2

Search for Topological Superconductivity in Doped Bi_2Se_3

2.1 Cu-doped Bi_2Se_3

Topological insulators make up a novel state of matter consisting of an insulating bulk and symmetry-protected conductive surface states. Since the discovery of the first 3D topological insulator bismuth-antimony [29] and the subsequent bismuth and antimony-based systems [72, 73, 74], a new field emerged sparking broad research interest.

Since the 3D topological insulator can also be a platform for magnetization and superconductivity, there is much interest in the interaction of topological order and phases with broken symmetry [4]. This interest first manifested with the study of proximity effects of spin-triplet superconductors with 3D topological insulators [30, 57], but has also spurred on a search for 3D topological superconductors [5, 53, 75].

Bi_2Se_3 is one of the few 3D topological insulators to date. It has attracted special attention since Cu intercalation between quintuple layers of Bi_2Se_3 can induce superconductivity below 3.8 K [3, 76]. $Cu_xBi_2Se_3$ has been proposed to be a leading candidate for topological superconductivity for this reason [5]. Cu-doped Bi_2Se_3 was the first of a series of doped Bi_2Se_3 materials that has been studied in the search for 3D topological superconductivity.

In this section, I describe the literature on $Cu_xBi_2Se_3$ as it applies to the question of topological superconductivity. The progression of this topic has been very fascinating. Early results made the condensed matter community very optimistic that $Cu_xBi_2Se_3$ would be the first material to realize topological superconductivity [4, 5, 6, 7, 8, 39, 77]. This excitement fizzled out as an increasing number of controversial results emerged [9, 10, 11], but the prediction and following observations of topological nematic superconductivity in $Cu_xBi_2Se_3$ has renewed some of the early promise in this material [12, 13, 14].

2.1.1 Early Results on Cu-doped Bi_2Se_3

The first report of superconducting Cu doped Bi_2Se_3 was by Y.S. Hor in 2010 [3]. This report details the growth conditions needed to obtain high quality superconducting crystals by melting stoichiometric ratios of the reactants. The crystal structure of $Cu_xBi_2Se_3$ taken from this report is shown in fig. 2.1. Hor et. al. successfully characterized the crystal structure and superconducting property of $Cu_xBi_2Se_3$ through X-ray Diffraction (XRD), Scanning Tunneling Microscopy (STM), Superconducting QUantum Interference Device (SQUID) magnetometry, and electric transport. The notable result from this early work is that Bi_2Se_3 could be made superconducting below 3.8 K when Cu (with concentration $0.10 < x < 0.30$) is intercalated between quintuple layers rather than substituting Bi sites in the parent compound. The difference between intercalated Cu dopants and Cu substitutions was observed in an earlier work to have a profound effect on the number of free carriers [78]. It was shown that intercalated Cu acts as a donor, and substituted Cu acts as an acceptor. However, though this was known since the 1970s, the presence of superconductivity and the effect of the Cu inclusion on the superconductivity was not noted until Hor et. al. in 2010.

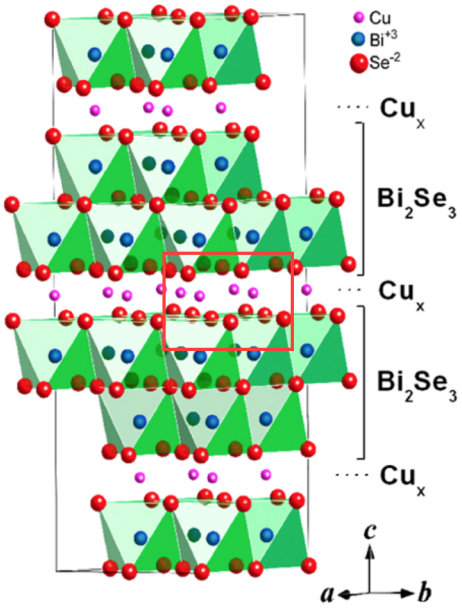

Figure 2.1: Crystal structure of $Cu_xBi_2Se_3$. Taken from ref [3].

A year later, Kriener et. al. developed a new method of intercalating Cu dopants into Bi_2Se_3 using an electrochemical synthesis and annealing technique [36]. Kriener et. al. reports superconductivity in $Cu_xBi_2Se_3$ for Cu concentration between $0.09 < x < 0.64$,

far wider than that achieved by the melt method [3, 36]. Also, they achieved a shielding fraction near 50%, exceeding the previous shielding fraction of 20% [3]. Later improvements increased the shielding fraction of crystals grown with the melt method [79], which, by studying the quenching conditions, eventually achieved a superconducting fraction of 56% [80]. Another growth method combining the melt and electrochemical technique consistently produced samples with a shielding fraction larger than 40% [81]. Large single crystals of $Cu_xBi_2Se_3$ were also grown with a floating zone [80] and high Cu concentration crystals by a novel layered nanoribbon method [82], but good superconducting crystals were not achieved by these means.

Soon after superconductivity was observed in Cu-doped topological insulator Bi_2Se_3, it was proposed to be a prime candidate to realize topological superconductivity by Fu and Berg [5]. In this report, Fu and Berg established that if a fully gapped, centrosymmetric odd-parity superconductor were to have an odd number of TRI momentum enclosed in its Fermi Surface, it would necessarily be a topological superconductor. This result was concurrently arrived at by Sato [38] (see chapter 1 subsection 1.2.1 for a detailed derivation of these criteria). Fu and Berg developed a model hamiltonian for $Cu_xBi_2Se_3$ based on a first principle band structure calculation of Bi_2Se_3 [83] and proposed that $Cu_xBi_2Se_3$ realizes the topological superconductor phase. This prediction sparked a flurry of research on this new superconductor.

Around the same time as Fu and Berg's theoretical prediction of topological superconductivity in $Cu_xBi_2Se_3$ was a Angle Resolved Photoemission Spectroscopy (ARPES) paper by Wray et. al. which revealed that superconducting Cooper pairing occurs in a relativistic, Dirac bulk band in $Cu_xBi_2Se_3$ [4]. Fig. 2.2(f) taken from Wray et. al. reveals that the bulk conduction band is best modeled by a Dirac distribution (blue) over a classical parabolic distribution (gray). The residuals from the Dirac fitting, shown in the inset of fig. 2.2(f), have a kink likely arising from electron-boson interactions. This suggests that Cooper pairing occurs in the Dirac regime where the chemical potential is located. A massive, bulk Dirac band is characteristic of the topological insulator state.

Even more significant in the result by Wray et. al. was that Cooper pairing at the chemical potential occurred in the presence of a non-degenerate surface state. Fig. 2.2(g) contrasts the band structure of a surface state that is degenerate and non-degenerate with the bulk band. Comparing with the ARPES data in panels (a)-(f), $Cu_xBi_2Se_3$ clearly fits with the non-degenerate model. Wray. et. al. suggest that the surface state revealed by ARPES is topological in nature and appears in the presence of bulk superconducting pairing.

Lastly, the photoemission data from Wray et. al. in conjunction with a theoretical model from Fu and Berg suggest that $Cu_xBi_2Se_3$ could have an odd-parity pairing symmetry - a

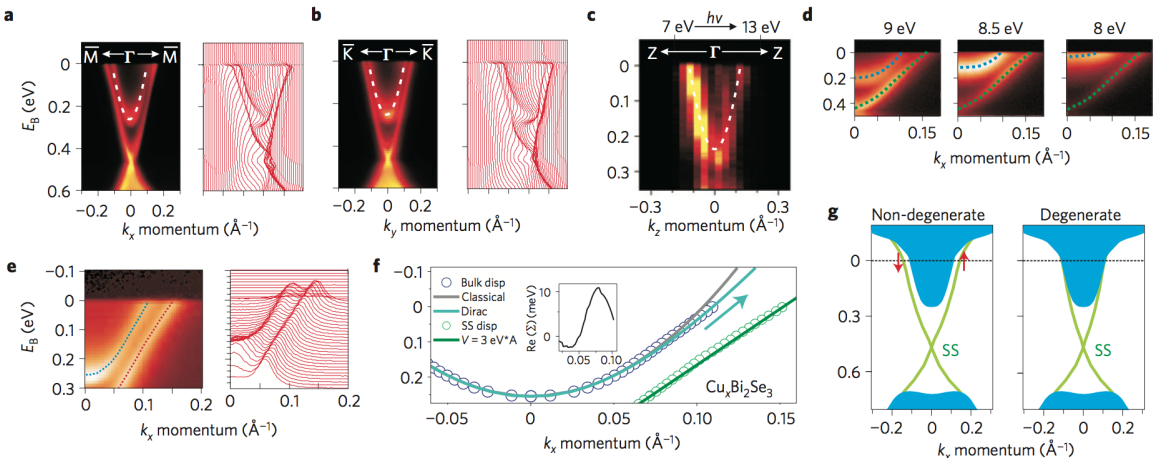

Figure 2.2: ARPES data on $Cu_{0.12}Bi_2Se_3$ taken from ref. [4]. (a)(b)(c) Bulk and Surface conduction bands along the $\Gamma - M$, $\Gamma - K$, and $\Gamma - Z$ directions. (d) Zoomed in view of ARPES data near chemical potential reveal non-degenerate bulk and surface bands. (e)(f) Comparison of Dirac fitting and classical parabolic fitting of ARPES data. Inset shows a kink in the residuals of the Dirac fit, indicative of electron-boson interaction. (g) Non-degenerate bulk and surface bands suggest the presence of topologically nontrivial surface state.

necessary condition for topological superconductivity. The theoretical model from Fu and Berg produced a phase boundary between an odd parity pairing and even parity pairing phase given by

$$\frac{U}{V} = 1 - \frac{2m^2}{\mu^2} \tag{2.1}$$

where U is the intraorbital interaction, V is the interorbital interaction, m is the Dirac rest mass, and μ is the chemical potential [5]. From this phase boundary equation, Fu and Berg developed the phase diagram in fig. 2.3. In this diagram Δ_2 represents the odd-parity topologically nontrivial phase and Δ_1 represents an even-parity topologically trivial phase. The red arrow indicates $m/\mu = 1/3$, which is the value extracted from the ARPES result in Wray et. al. Given the small value of m/μ, as long as V is sufficiently larger than U, the topologically nontrivial odd-parity phase will be realized. The results by Wray et. al. were later elaborated on in a second, more comprehensive publication a year later [37].

The results from Wray et. al. in conjunction with Fu and Berg caused no little stir in the condensed matter community and several more papers came out in the next few years discussing experimental signatures of topological superconductivity in $Cu_xBi_2Se_3$. One of the most pressing questions was whether the superconducting pairing in $Cu_xBi_2Se_3$ had even or odd parity.

A heat capacity study by Kriener et. al. in 2011 was one of the first investigations of

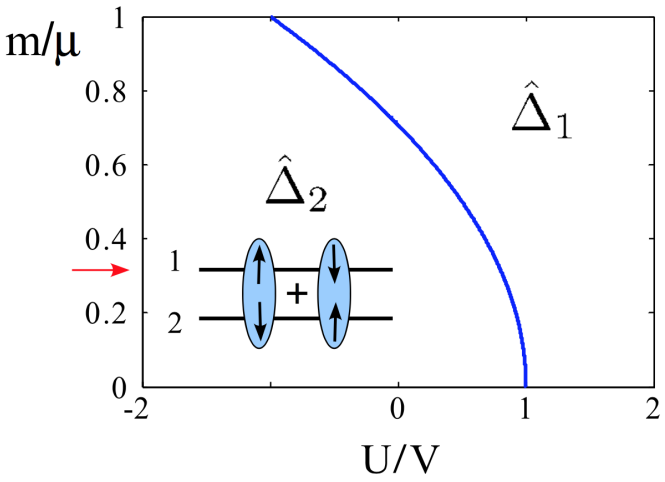

Figure 2.3: Phase diagram taken from ref [5]. Δ_1 and Δ_2 are even and odd parity phases respectively. The red arrow is the experimental value of m/μ from ref. [4].

the superconducting gap of $Cu_xBi_2Se_3$ [6]. Fig. 2.4 shows the temperature dependence of the heat capacity of $Cu_xBi_2Se_3$ from this study. Panel (a) shows c_p/T as a function of temperature in the normal state (applied external field B = 2 T) and in the superconducting state (no external field). From the normal state heat capacity, the phonon contribution was determined and subtracted to get the electronic contribution of the heat capacity in the superconducting state, c_{el}/T, shown in panel (b).

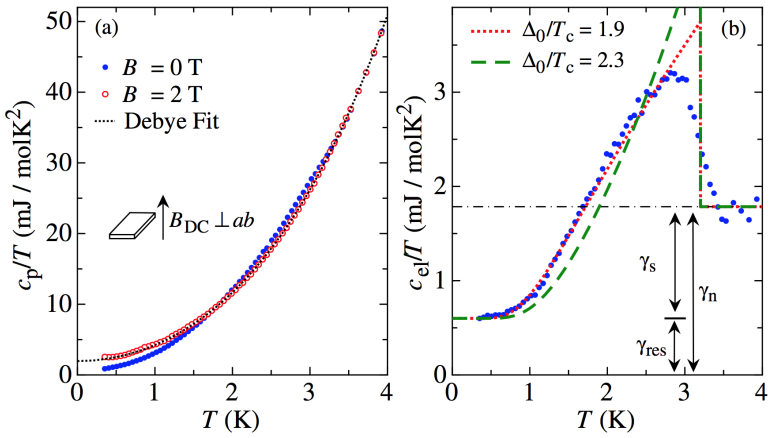

Figure 2.4: Heat capacity of $Cu_xBi_2Se_3$ taken from ref [6]. (a) The heat capacity, c_p/T, as a function of temperature in the superconducting state (blue) and normal state (red). (b) The electronic contribution of the heat capacity, c_{el}/T, after the subtraction of the phonon contribution determined from the normal state.

There are two interesting conclusions from the heat capacity data drawn by Kriener et. al.. First, the exponential decay of c_{el}/T at low temperature is indicative of a fully-gapped,

nodeless superconducting state (see chapter 5 section 5.1 for a discussion of how nodes effect the heat capacity).

Second, they determine that the superconducting gap does not have conventional s-wave symmetry. Using their transport and magnetization data, Kriener et. al. determined the superconducting gap size at 0 K, Δ_0, to be 7.3 K. From this they found $\Delta_0/T_c = 2.3$. Δ_0/T_c is the parameter for the α model used to describe the heat capacity verses temperature for superconductors with strong coupling [84]. As seen in fig. 2.4(b), the calculated Δ_0/T_c does not fit the heat capacity data for $Cu_xBi_2Se_3$. Kriener et. al. concludes that the temperature dependence of the superconducting gap is not well described by BCS theory and thus may not be s-wave. This result, suggesting an unconventional superconducting order parameter, gives rise to the possibility that $Cu_xBi_2Se_3$ could be a odd-parity superconductor.

A magnetization study by Das et. al. also claims that the superconductivity in $Cu_xBi_2Se_3$ is odd-parity, spin triplet [77]. Based on a theoretical study of the effect of vortex currents on the magnetic flux in a superconductor [85], they calculate the non-uniform magnetic field in the superconducting vortices. They find that for a spin-singlet superconductor, the magnetic field induced by vortices is always positive meaning that the interaction between vortices should always be repulsive. However, for a spin-triplet superconductor the vortex magnetic field is negative at a set distance away from the vortex center resulting in an attractive force between vortices.

The measured magnetization data showed a rapid increase of the sample's magnetization just above H_{c1}, which then slows down at higher field. Das et. al. suggests that the rapid increase in the magnetization is due to the low vortex density at H_{c1}. For a spin-triplet superconductor, when the vortices are far apart, the attractive magnetic force between vortices would rapidly increase the vortex density. Once the vortex density is high, the vortices would feel a repulsive force, thus leveling off the increase in magnetization. In this way, Das et. al. argues that the magnetization in $Cu_xBi_2Se_3$ is consistent with the prediction for a spin-triplet superconducting order. It should be noted that some theoretical calculations have been critical of this argument [86].

A study of the upper critical field under pressure by Bay et. al. also suggests spin-triplet superconductivity in $Cu_xBi_2Se_3$ [7]. Fig. 2.5(a) shows the upper critical field in $Cu_xBi_2Se_3$ as a function of temperature for different pressures. Bay et. al. calculates the Pauli paramagnetic limit for the upper critical field [87, 88] given the orbital and spin limiting effects to be $B_{c2}(0) = B_{c2}^{orb}(0)/\sqrt{1+\alpha^2} = 3.3$ T [7, 89] where $B_{c2}^{orb}(0)$ is the orbital limited upper-critical field given by $B_{c2}^{orb}(0) = 0.72 \times T_c|dB_{c2}/dT|_{T_c}$ [7, 89] and α is the Maki parameter given by $\alpha = \sqrt{2}B_{c2}^{orb}(0)/B^P(0)$ [7, 89, 90] with $B^P(0) = 1.86 \times T_c$ the weak coupling Pauli paramagnetic limit at 0 K [7, 91]. The upper critical field seen in fig.

2.5(a) at ambient pressure clearly exceeds the 3.3 T Pauli paramagnetic limit with orbital and spin considerations. In the absence of Pauli limiting on the upper critical field, the presence of spin-triplet superconductivity, which is not subject to the Pauli limit, is likely. This has been seen in other spin-triplet superconductors like URhGe [92], UCoGe [93], and (most likely spin-triplet) Sr_2RuO_4 [94, 95].

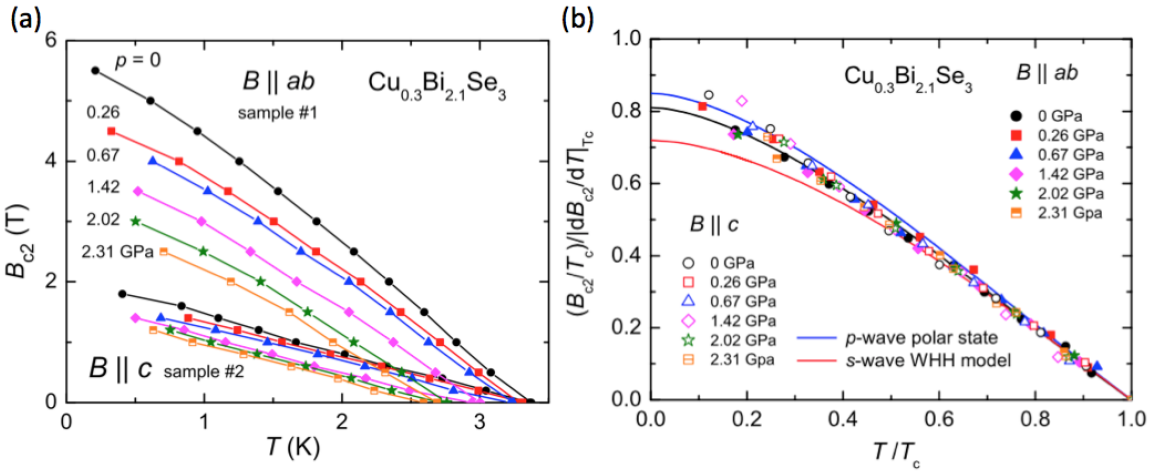

Figure 2.5: Pressure dependence of upper critical field in $Cu_xBi_2Se_3$ taken from ref [7]. (a) Upper critical field as a function of temperature for different pressures. (b) Upper critical field follows the same functional form at every pressure. Data agrees best with a p-wave model with a 5% adjustment of the initial slope (black). The s-wave and p-wave models are shown in red and blue respectively.

Bay et. al. found that at every pressure, the upper critical field followed the same functional behavior as seen in fig. 2.5(b). Furthermore, the functional fitting for a spin-singlet, orbital-limited superconductor [89] (red curve) is not a good fit of the data. However, the functional fit for a p-wave superconductor [96] (blue) is a much better fit to the data, especially after a small adjustment of the initial slope (black).

An important feature of p-wave superconductivity is that it is very sensitive to impurities [7, 93, 94, 97]. As noted by Bay et. al., to meet this condition the mean free path, l, must be larger than the coherence length, ξ [94]. From the upper critical field, in $Cu_xBi_2Se_3$ the coherence length is ξ = 13-14 nm [3, 6, 7]. Bay et. al. estimates the mean free path to be 34 nm and argues that $Cu_xBi_2Se_3$ is in the clean limit because $l > \xi$. Furthermore, using a model for the slope of the temperature dependence of the upper critical field in the clean limit [98], Bay et. al. calculates l = 90 nm and ξ = 9 nm further reinforcing the possibility of spin-triplet superconductivity.

The mean free path was later determined from quantum oscillations to range between 14 nm and 30 nm depending on the sample [40]. Bay et. al. suggests that superconductivity

in $Cu_xBi_2Se_3$ is in the clean limit [7], but the high dingle temperature reported by quantum oscillations [39, 40, 99] challenges this view. This remains as a challenge for triplet superconductivity in $Cu_xBi_2Se_3$.

Though the issue of impurity scattering has cast doubts on possible p-wave superconductivity in $Cu_xBi_2Se_3$, a theoretical work by Michaeli and Fu argues that chiral symmetry and spin-orbit effects can counteract the pair breaking due to impurity scattering [100]. In conjunction with an experimental work following the theory [101], it is possible that $Cu_xBi_2Se_3$ could host a disorder-resistant odd-parity superconducting phase. Later theoretical works also showed that topological superconductivity can be robust against disorder [102, 103, 104].

The combined results by Kriener et. al. [6], Das et. al. [77], and Bay et. al. [7] all pointed to odd-parity pairing in $Cu_xBi_2Se_3$, a necessary condition to realize 3D topological superconductivity. In the meantime, the smoking gun for topological superconductivity, Majorana zero-modes, was reported to be seen by point-contact spectroscopy by Sasaki et. al. [8] and later confirmed in other works [105, 106, 107].

Majorana excitations on the surface of a topological superconductor should result in a finite density of states in the middle of the superconducting gap. This density of states will lead to a conductance peak at zero bias in tunneling or Andreev reflection measurements. Fig. 2.6 shows the point-contact spectroscopy data for $Cu_xBi_2Se_3$ by Sasaki et. al. [8]. As seen in panels (a) and (b), a zero bias conductance peak exists in the center of the gap. Sasaki et. al. argues that this feature is evidence of Majorana zero-modes on the surface of $Cu_xBi_2Se_3$. From the magnetic field dependence of the zero bias conductance peak (fig. 2.6(c)), Sasaki et. al. rules out spurious effects such as heating that could give rise to a non-intrinsic zero bias conductance peak. Two theoretical works following this observation interpret the zero bias conductance peak in Sasaki et. al. as evidence of surface Majorana modes in a 3D topological superconductor [55, 108].

The strong suggestion that $Cu_xBi_2Se_3$ is a spin-triplet superconductor [6, 7, 77] and the apparent observation of Majorana zero-modes on its surface [8] created extreme enthusiasm in the topological materials community. Quantum oscillations, which are used to probe the electronic state of topological materials [33, 34, 35], were missing up to this point. Detailed knowledge of the Fermiology in $Cu_xBi_2Se_3$ is particularly necessary since the criteria for topological superconductivity developed by Fu and Berg requires that there are an odd number of TRI momenta enclosed in the Fermi surface [5]. Lawson et. al. solved this problem by measuring quantum oscillations in the magnetization of $Cu_xBi_2Se_3$ using torque magnetometry [39].

Lawson et. al. measured a single ellipsoidal Fermi surface centered on the Γ point

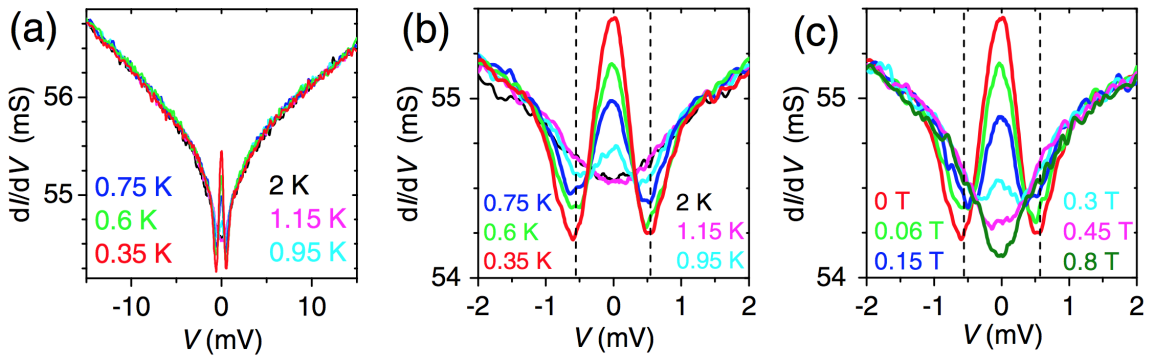

Figure 2.6: Zero Bias Conductance Peak in $Cu_xBi_2Se_3$ taken from ref [8]. (a) Temperature dependence of point-contact spectrum (dI/dV versus bias voltage). Peak in the center of the gap is evidence of Majorana surface state. (b) Point-contact spectrum in narrow energy range. (c) Field dependence of point-contact spectrum at T = 0.35 K.

as in the parent compound [39]. This Fermi surface contains only one TRI momentum, thus meets the criteria for topological superconductivity set by Fu and Berg [5]. For more details on the result by Lawson et. al. see chapter chapter 4.

2.1.2 Evidence Against Topological Superconductivity in Cu-doped Bi_2Se_3

In early 2013, Levy et. al. came out with a STM study on $Cu_xBi_2Se_3$ [9]. As shown in fig. 2.7, they observed a full superconducting gap. In particular, the data in fig. 2.7(b) is well fit by an s-wave superconducting model (blue). In contrast to suggestions of p-wave superconductivity as described in the previous section [6, 7, 77], the simplest explanation of the tunneling spectrum in $Cu_xBi_2Se_3$ is conventional s-wave superconductivity. Levy et. al. notes that an exotic pairing could account for the full gap seen in the tunneling spectrum, but it is most likely s-wave.

Mostly notably, the in-gap state observed by point-contact spectroscopy [8, 105, 106, 107] is completely missing in the tunneling spectrum [9]. Though they see an apparent zero bias peak in fig. 2.7(c), this occurred when the tip crashed into the sample resulting in a zero bias peak due to Josephson tunneling rather than surface Majorana modes. Clearly in the two samples shown in fig. 2.7(b) and (d), there are no states in the gap.

The lack of in-gap states in STM was a major case against topological superconductivity in $Cu_xBi_2Se_3$. The conflict between the point-contact results [8, 105, 106, 107] and the tunneling results [9] is an intriguing mystery. This mystery was addressed in an Andreev reflection spectroscopy study by Peng et. al. [10].

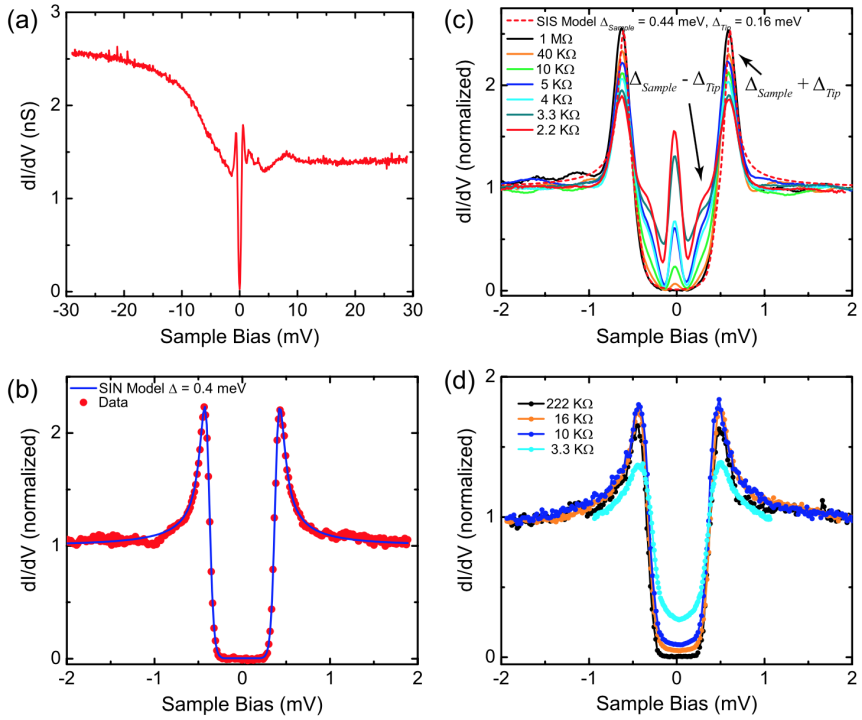

Figure 2.7: STM on $Cu_xBi_2Se_3$ taken from ref [9]. (a) Tunneling spectrum including background. (b) Tunneling spectrum showing full superconducting gap with no in-gap states. Blue line is a fit for an s-wave superconductor. (c) Tunneling spectrum after the STM tip crashed into the sample surface. In-gap peak is due to Josephson tunneling. (d) Tunneling spectrum of a second sample with different junction impedances confirming no in-gap states.

Peng et. al. argues that the zero bias conductance peak observed in $Cu_xBi_2Se_3$ is not due to surface Majorana zero modes [10]. In this study, they performed point contact Andreev reflection spectroscopy [109] in two configurations - one with a finite barrier strength at the metal-superconductor junction and one with a barrier strength in the transparent limit. Fig 2.8(a) and (b) show the Andreev reflection spectrum with a finite barrier strength at different temperatures and external magnetic fields respectively. The two lobes in the data correctly give a superconducting gap of Δ = 0.35 meV in good agreement with the gap from the tunneling spectrum [9]. Notably, the zero-bias conductance peak that is usually seen in point-contact experiments [8, 105, 106, 107] is missing.

Fig 2.8(c) and (d) show the Andreev reflection spectrum with a barrier strength in the transparent limit. Similar to the other point-contact experiments [8, 105, 106, 107], this data shows a peak at zero bias. Peng et. al. argues that in the transparent barrier limit, the metal-superconductor junction is dominated by inelastic scattering that changes the energy of the carriers. They estimate that the threshold for ballistic transport $R_N = 4\rho/3\pi l$ [110]

to be $\sim$13 Ω, where R_N is the junction resistance, ρ is the bulk resistivity of the material being studied, and l is the mean free path of electrons in the junction. Given that the finite barrier strength junctions have $R_N > 100\ \Omega$ and the junctions in the transparent limit have $R_N < 10\ \Omega$, Peng et. al. shows that the transparent barrier junctions are not in the ballistic regime, whereas the finite barrier junctions are.

Furthermore, Peng et. al. points out that the spectrum from the transparent barrier strength experiment did not correctly give the gap energy except for when the barrier strength was at the threshold for ballistic transport [10]. Fig. 2.8(c) and (d) only show the data from when the junction resistance is at the ballistic threshold, but more data sets for different barrier strengths can be found in ref. [10].

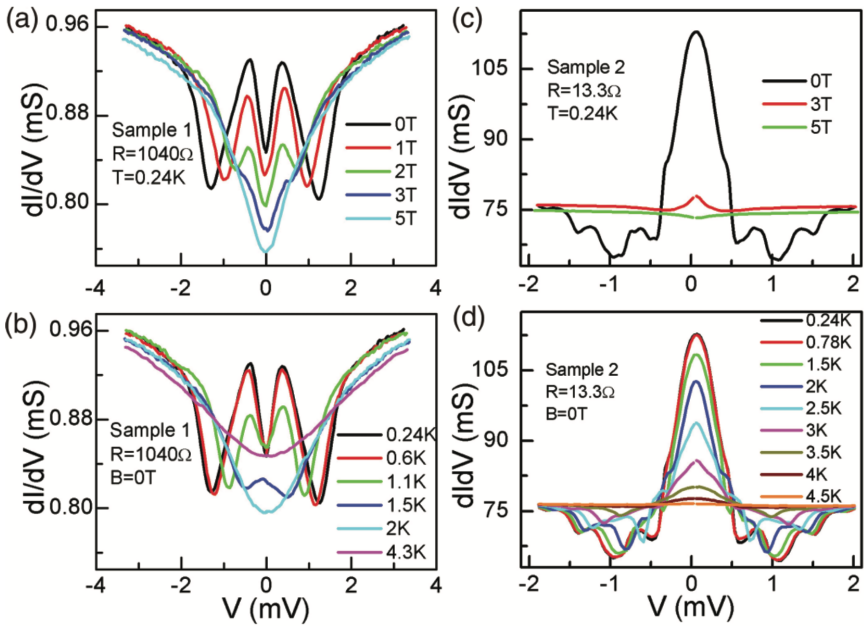

Figure 2.8: Andreev reflection on $Cu_xBi_2Se_3$ taken from ref [10]. (a) Andreev spectrum with finite barrier strength at different magnetic fields and (b) at different temperatures. (c) Andreev spectrum with a barrier strength in the transparent-limit at different magnetic fields and (d) at different temperatures.

Peng et. al. argues that the zero bias conductance peak is unlikely to be due to Majorana surface states since it can be tuned out by varying the barrier strength in the point-contact measurement. Instead, Peng et. al. claims that the zero bias conductance peak is more consistently explained by a conductance enhancement from the Andreev reflection due to the bulk superconducting gap. The origin of the zero bias conductance peak remains a matter of much debate [111, 112, 113].

In addition to the controversy about the supposed in-gap states, the pairing symmetry in $Cu_xBi_2Se_3$ has also been under scrutiny. Despite previous reports of odd-parity super-

conductivity [6, 7, 77], the tunneling spectrum suggests that $Cu_xBi_2Se_3$ is a conventional s-wave superconductor [9]. In addition, the high level of disorder in $Cu_xBi_2Se_3$ casts doubts on the presence of a delicate p-wave superconducting order [39, 40, 99] unless a disorder-tolerant odd-parity superconducting state exists [100, 101].

As stated before, the theoretical criteria for topological superconductivity require (1) odd-parity pairing and (2) an odd number of TRI momenta enclosed in the Fermi surface [5]. In addition to the pairing symmetry being called into question, criteria (2), which was confirmed to be met by the de Haas-van Alphen (dHvA) effect [39], has been shown to be contingent on the doping level [11, 40].

Lahoud et. al. performed an ARPES and Shubnikov-de Haas (SdH) study on $Cu_xBi_2Se_3$ [11]. They found that the ellipsoidal Fermi surface in $Cu_xBi_2Se_3$ becomes increasingly elongated as a function of carrier concentration. Eventually the Fermi surface touches the Brillouin zone boundary and becomes quasi-cylindrical. Fig. 2.9(a)(b)(c) shows the Fermi surface calculated from SdH oscillations at different carrier concentrations. Fig. 2.9(e)(f)(g) shows the size of the Fermi surface with respect to the Brillouin zone. As seen in panel (g), the Fermi surface crosses the Brillouin zone boundary at high carrier concentration. The ARPES data in Lahoud et. al. confirms that, for $Cu_xBi_2Se_3$ samples with high carrier concentrations, the bottom of the bulk conduction band is visible for momenta covering the whole $\Gamma - Z$ range indicating an open Fermi surface. The evolution of the Fermi surface with carrier concentration was later confirmed by dHvA effect in Lawson et. al. [40].

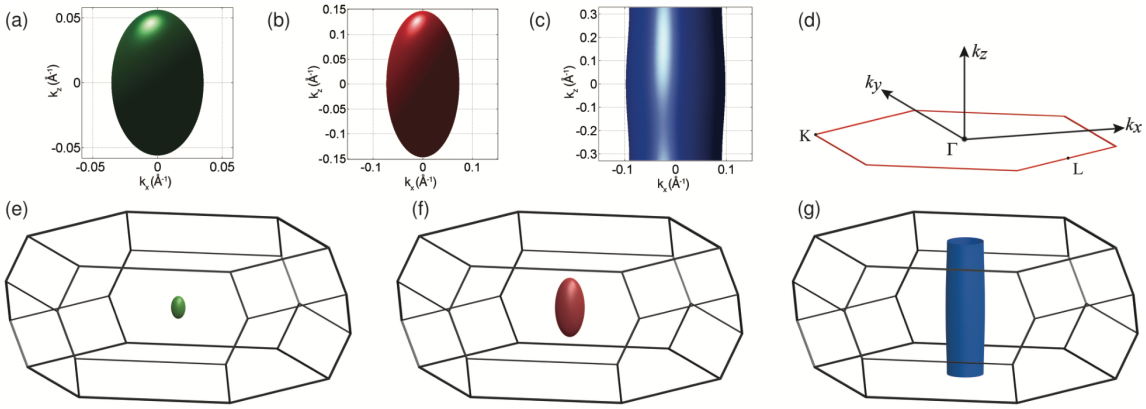

Figure 2.9: Evolution of the Fermi surface in $Cu_xBi_2Se_3$ taken from ref [11]. (a)(b)(c) Fermi surface of $Cu_xBi_2Se_3$ with increasing carrier concentration calculated from SdH oscillations. (d) Momentum axes of the Brillouin zone. (e)(f)(g) Fermi surfaces from (a)-(c) plotted to scale in the Brillouin zone.

This result has significant implications for topological superconductivity in $Cu_xBi_2Se_3$.

The Fermi surface depicted in fig. 2.9(e)(f) only contains the Γ point. However, the Fermi surface in fig. 2.9(g) contains both the Γ point and the Z points. Thus, the Fermi surface contains an even number of TRI momenta in the Brillouin zone. The high carrier concentration $Cu_xBi_2Se_3$ crystal therefore does not meet criteria (2) from the theoretical work by Fu and Berg [5].

It has been suggested that the open cylindrical Fermi surface could indicate two dimensional (2D) topological superconductivity in $Cu_xBi_2Se_3$ [11, 12, 114]. In this case, the topological boundary states would only exist on the edge surfaces and not on the surface perpendicular to the crystal c-axis. This could possibly explain why in-gap states are missing in the tunneling spectrum [9], but seen in point-contact spectroscopy where there could be tunneling into surfaces other than (001) [8, 105, 106, 107].

The question of topological superconductivity in $Cu_xBi_2Se_3$ remains controversial. There have been many other studies for, against, and agnostic about topological superconductivity in $Cu_xBi_2Se_3$ including theoretical works [115, 116, 117, 118, 119, 120, 121, 122, 123, 124, 125, 126], ARPES [127, 128, 129, 130], STM [131, 132], optical [99, 133, 134], transmission electron microscopy (TEM) [135], thermal hall [136], and transport [99, 130, 137].

2.1.3 Renewed Interest in Cu-doped Bi_2Se_3 and Nematic Superconductivity

Until 2015, the debate around $Cu_xBi_2Se_3$ has been centered around whether it realized a A_{1u} (Δ_2) representation of the D_{3d} point group, which was predicted by Fu and Berg to realize the topological superconducting phase [5]. Of the four possible pairing symmetries, only the A_{1u} representation is odd-parity and has a full superconducting gap, both of which are required for topological superconductivity. However, a new theory by Fu [12] argued that the E_u representation can also be fully gapped. The presence of a hexagonal warping term in the Hamiltonian [138] can spontaneously break the rotational symmetry, lifting the nodes in the superconducting gap, and give rise to a new "nematic superconductor" phase that is topological in nature.

To understand this new phase, it is first necessary to understand the possible order parameters for $Cu_xBi_2Se_3$. Fu and Berg give the following 4 possible pairing functions for $Cu_xBi_2Se_3$ [5]:

$$
\begin{aligned}
&\Delta_1 : c_{1\uparrow}c_{1\downarrow} + c_{2\uparrow}c_{2\downarrow} \text{ and } c_{1\uparrow}c_{1\downarrow} - c_{2\uparrow}c_{2\downarrow} \\
&\Delta_2 : c_{1\uparrow}c_{2\downarrow} + c_{1\downarrow}c_{2\uparrow} \\
&\Delta_3 : c_{1\uparrow}c_{1\downarrow} - c_{2\uparrow}c_{2\downarrow} \\
&\Delta_4 : (c_{1\uparrow}c_{2\uparrow}, c_{1\downarrow}c_{2\downarrow})
\end{aligned}
\tag{2.2}
$$

Δ_1 and Δ_3 are spin-singlet. Whereas, Δ_2 and Δ_4 are spin-triplet. Fu and Berg point out that only the Δ_2 pairing function is spin-triplet and fully gapped as is required for topological superconductivity [5].

In a later paper proposing nematic superconductivity in $Cu_xBi_2Se_3$, Fu takes a closer look at the Δ_4 pairing function [12]. To determine the presence of nodes, Fu calculates the superconducting gap from the Hamiltonian derived using $\mathbf{k} \cdot \mathbf{p}$ theory [83] which to first order is

$$
H_0 = \sum_{\mathbf{k}} c^\dagger_{\mathbf{k}}[v(k_x s_y - k_y s_x)\sigma_z + v_z k_z \sigma_y + m\sigma_x - \mu]c_{\mathbf{k}}, \tag{2.3}
$$

where $c^\dagger = (c^\dagger_{1\uparrow}, c^\dagger_{1\downarrow}, c^\dagger_{2\uparrow}, c^\dagger_{2\downarrow})$ is the creation operator for two orbitals, v is the strength of the spin-orbit interaction, s is the spin operator, σ is the orbital operator, m is the rest mass, and μ is the chemical potential [5, 12]. For E_u pairing, electrons form spin-triplet pairs with zero total spin in an in-plane direction given by $\mathbf{n} = (n_x, n_y)$, which is determined to be the "nematic vector". The pair potential for Δ_4 is

$$
V_{\mathbf{n}} = n_x V_x + n_y V_y \tag{2.4}
$$

where

$$
\begin{aligned}
V_x &= i\Delta_0(c^\dagger_{1\uparrow}c^\dagger_{2\uparrow} - c^\dagger_{1\downarrow}c^\dagger_{2\downarrow}) \\
V_y &= \Delta_0(c^\dagger_{1\uparrow}c^\dagger_{2\uparrow} + c^\dagger_{1\downarrow}c^\dagger_{2\downarrow})
\end{aligned}
\tag{2.5}
$$

By diagonalizing the Hamiltonian, $H_{sc} = H_0 + V_{\mathbf{n}}$, the superconducting gap is found to be

$$
\delta_{\mathbf{n}}(\mathbf{k}) = \Delta\sqrt{\tilde{k}_z^2 + (\tilde{\mathbf{k}} \cdot \mathbf{n})^2} \tag{2.6}
$$

where

$$\begin{aligned}\Delta &= \Delta_0\sqrt{1-m^2/\mu^2} \\ \tilde{\mathbf{k}} &= (vk_x, vk_y, v_zk_z)/\sqrt{\mu^2-m^2}\end{aligned} \tag{2.7}$$

It can be seen that when $\pm\mathbf{k}_0 = \pm k_F\hat{\mathbf{z}}\times\mathbf{n}$, $\tilde{\mathbf{k}}$ is completely in plane and orthogonal to $\mathbf{n}$, thus the gap, $\delta_{\mathbf{n}}(\mathbf{k})$ from eq. 2.6, goes to zero. This indicates two point nodes in plane for the E_u pairing function Δ_4.

Fu notes that though H_0 is rotationally invariant, $Cu_xBi_2Se_3$ has a threefold crystalline symmetry [12]. To account for the crystalline anisotropy, Fu adds a hexagonal warping term to the Hamiltonian that accounts for the spin-orbit interaction related to the crystalline anisotropy. This term was previously used to explain the hexagonal Fermi surface in Bi_2Te_3 as resolved by ARPES [138, 139]. Thus the corrected Hamiltonian becomes

$$H = H_0 + \lambda\sum_{\mathbf{k}}(k_+^3 + k_-^3)c_{\mathbf{k}}^\dagger\sigma_z s_z c_{\mathbf{k}} \tag{2.8}$$

where λ is the parameter characterizing the strength of the hexagonal warping and $k_\pm \equiv k_x \pm ik_y$. With the introduction of crystalline anisotropy, it is necessary to define the coordinate axes with respect to the crystal lattice. The x-axis is defined along the normal of the mirror plane as seen in fig. 2.10(a).

By diagonalizing the new Hamiltonian $H_{sc} = H + V_{\mathbf{n}}$, the gap in the presence of the hexagonal warming term becomes

$$\delta_{\mathbf{n}}(\mathbf{k}) = \Delta\sqrt{1-[\tilde{\mathbf{k}}\cdot(\hat{\mathbf{z}}\times\mathbf{n})]^2} \tag{2.9}$$

$\tilde{\mathbf{k}}$, defined in eq. 2.7, has values given by the Fermi surface

$$\mu = \sqrt{m^2 + v^2(k_x^2+k_y^2) + \lambda^2(k_+^3+k_-^3)^2 + v_z^2k_z^2}. \tag{2.10}$$

For $k_z = 0$, this can be simplified to

$$\mu^2 - m^2 = v^2(k_x^2+k_y^2) + \lambda^2(2k_x^3 - 6k_xk_y^2)^2. \tag{2.11}$$

The Fermi surface at $k_z = 0$ is shown in fig. 2.10(b). The gap given by eq. 2.9 goes to zero when $|\tilde{\mathbf{k}}\cdot(\hat{\mathbf{z}}\times\mathbf{n})| = |\mathbf{n}\cdot(\tilde{\mathbf{k}}\times\hat{\mathbf{z}})| = 1$.

Using eq. 2.7, $|(\tilde{\mathbf{k}}\times\hat{\mathbf{z}})| = \sqrt{\frac{v^2}{\mu^2-m^2}(k_x^2+k_y^2)}$ which equals to one when $k_x^2+k_y^2 = \frac{\mu^2-m^2}{v^2}$. As seen in eq. 2.11, for $\mathbf{k}$ on the Fermi surface, this condition can be met only when $\lambda = 0$ or when $2k_x^3 - 6k_xk_y^2 = 0$ which happens at $\mathbf{k} = k_F\hat{\mathbf{y}}$, $\pm k_F(\frac{\sqrt{3}}{2}\hat{\mathbf{x}} + \frac{1}{2}\hat{\mathbf{y}})$, and

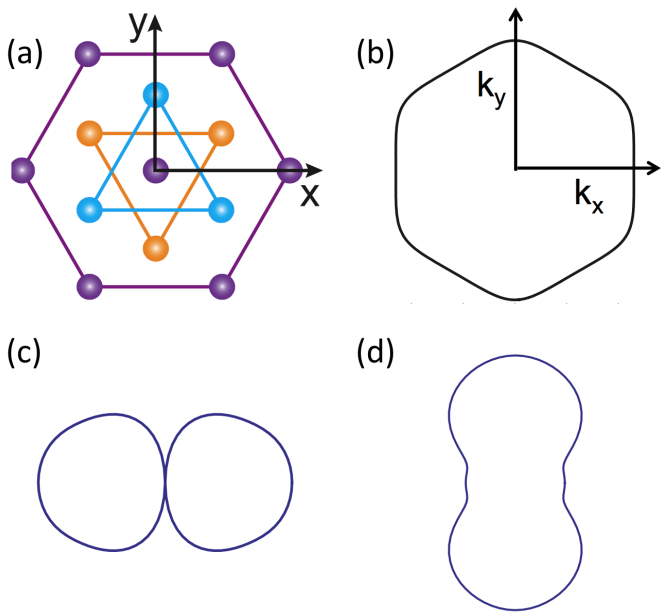

Figure 2.10: Taken from ref [12]. (a) Crystal structure of $Cu_xBi_2Se_3$ viewed down the c-axis. (b) Fermi surface with hexagonal warping from eq. 2.10 with $k_z = 0$. (c) Superconducting gap for Δ_{4x} with $\mathbf{n} \parallel \hat{\mathbf{x}}$, which has point nodes at $\mathbf{k} \perp \mathbf{n}$. (d) Superconducting gap for Δ_{4y} with $\mathbf{n} \parallel \hat{\mathbf{y}}$, which is fully gapped.

$\pm k_F(\frac{\sqrt{3}}{2}\hat{\mathbf{x}} - \frac{1}{2}\hat{\mathbf{y}})$. In other words, for $\mathbf{k}$ on the Fermi surface in eq. 2.10, $|(\tilde{\mathbf{k}} \times \hat{\mathbf{z}})| = 1$ only for $\mathbf{k} = k_F\hat{\mathbf{y}}$ and $\mathbf{k}$ on the other five corners of the Fermi surface shown in fig. 2.10(b).

Thus in the presence of hexagonal warping ($\lambda \neq 0$) the zero gap condition, $|\mathbf{n}\cdot(\tilde{\mathbf{k}}\times\hat{\mathbf{z}})| = 1$, occurs only when $\mathbf{n}$ lies along $\hat{\mathbf{x}}$ or one of the 6 directions orthogonal to the mirror planes (i.e. the directions orthogonal to $\hat{\mathbf{z}}$ and $\tilde{\mathbf{k}}$ for which $|(\tilde{\mathbf{k}} \times \hat{\mathbf{z}})| = 1$). For $\mathbf{n}$ in all other directions, the nodes are lifted leaving a full gap. Thus for E_u pairing there are two different order parameters. The first named Δ_{4x} (illustrated in Fig. 2.10(c)) occurs when the nematic vector points in the $\hat{\mathbf{x}}$ direction, which results in point nodes. For $\mathbf{n}$ in any other direction except those orthogonal to the mirror planes, there is a second order parameter named Δ_{4y} (illustrated in Fig. 2.10(d) with $\mathbf{n} \parallel \hat{\mathbf{y}}$), which is fully gapped. With the lifting of the point nodes, Δ_{4y} is fully gapped and spin-triplet, thus can realize a topological superconducting order. Table 2.1 summarizes the different possible gap structures for $Cu_xBi_2Se_3$, and fig. 2.11 shows a graphic of the same gap structures.

This new phase has been dubbed "nematic superconductor" due to the nematic order in the superconducting gap resulting from the nematic vector, $\mathbf{n}$ [12]. This new superconducting phase is experimentally characterized by a broken in-plane rotational symmetry, which has now been observed for $Cu_xBi_2Se_3$ [14, 13].

Matano et. al. first observed the in-plane rotational symmetry breaking in $Cu_xBi_2Se_3$

Table 2.1: Possible order parameters for $Cu_xBi_2Se_3$. Adapted from ref. [1] and [2].

order parameter	D_{3d} representation	spin pairing	topology	gap
Δ_1	A_{1g}	singlet	-	full
Δ_2	A_{1u}	triplet	$\mathbb{Z}$	full
Δ_3	A_{2u}	singlet	$\mathbb{Z}_2$	point nodes at the poles
Δ_{4x}	E_u	triplet	$\mathbb{Z}_2$	point nodes on equator
Δ_{4y}	E_u	triplet	$\mathbb{Z}$	full

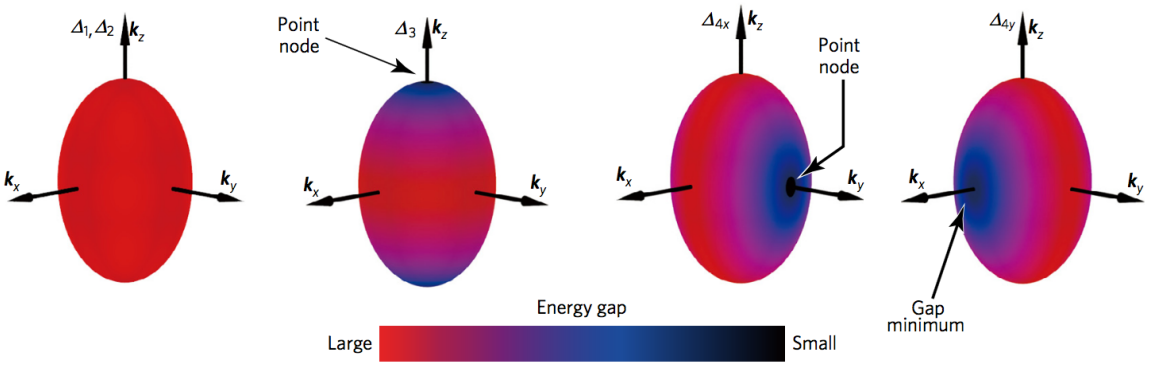

Figure 2.11: Graphics of the gap structures in table 2.1 taken from ref [13]. The oval is the Fermi surface and the color indicates the gap amplitude.

with nuclear magnetic resonance (NMR) [14]. Fig. 2.12 shows the in-plane angular dependence of the of the Knight shift reduction in the superconducting state of $Cu_xBi_2Se_3$. There is a sharp drop in the Knight shift at $\theta = 30°$ and -120°. These two dips are separated by 180°. This is indicative of a nematic order that clearly breaks the hexagonal crystal symmetry.

It is noteworthy that in the normal state, the in-plane Knight shift is isotropic, thus fig. 2.12 reveals broken rotational symmetry only in the superconducting state as predicted by Fu [12]. Matano et. al. argues that the spontaneous rotational symmetry breaking in the superconducting state implies that $Cu_xBi_2Se_3$ is E_u and spin-triplet. This study however is not able to differentiate between a Δ_{4x} and Δ_{4y} order parameter. Nagai shows theoretically that the location of the point nodes can be determined by angle-resolved thermal transport or heat capacity [140].

Yonezawa et. al. solved this problem by measuring the in-plane angular dependence of the heat capacity [13]. By measuring a gap minimum normal to the mirror plane, Yonezawa et. al. concludes that $Cu_xBi_2Se_3$ has the Δ_{4y} order parameter and is a fully gapped, odd parity topological superconductor.

Fig. 2.13 shows evidence for nematic superconductivity in $Cu_xBi_2Se_3$. Fig. 2.13(a) shows the heat capacity divided by temperature, $C(\phi)/T$, for $Cu_xBi_2Se_3$ as a function of

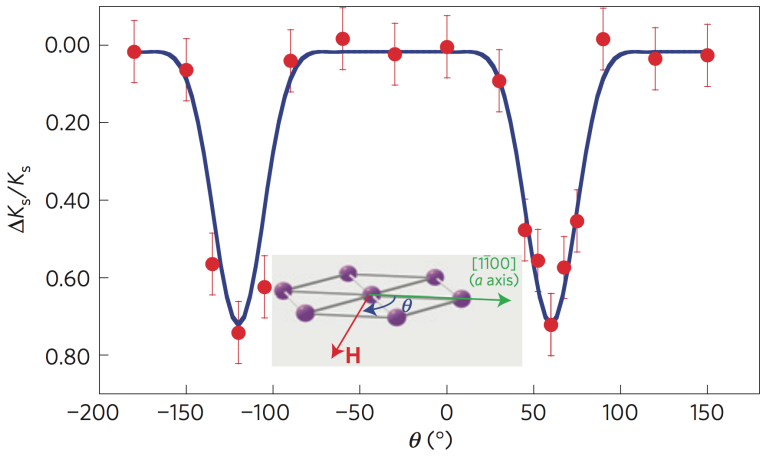

Figure 2.12: Angular dependence of the reduction in the Knight shift taken from ref. [14]. $\Delta K_s = K(3K) - K(1.4K)$ and $K_s = K(3K) - K_{Bi_2Se_3}$. The insert shows the in-plane crystal structure and defines θ as the azimuthal angle measured from the normal to the mirror plane.

the angle, ϕ, between the in-plane external magnetic field and $\hat{\mathbf{x}}$ (the crystal axis orthogonal to the mirror plane). Above H_{c2} in the normal state, $C(\phi)/T$ is completely independent of the azimuthal angle. However, in the superconducting state, there is a clear two-fold oscillation in $C(\phi)/T$. As in the NMR study, this two-fold oscillation, occurring only in the superconducting state, breaks the in-plane hexagonal crystal symmetry. Fig. 2.13(b) displays this same data in a polar plot where the nematic direction is more apparent. The magnitude of $C(\theta, \phi)/T$ is shown in a contour plot in fig. 2.13(c), where θ is the polar angle. The minimum at θ = 90° for all ϕ confirms that the apparent nematic order in fig. 2.13(a) is not due to magnetic field misalignment.

In addition to symmetry breaking in the heat capacity, Yonewaza et. al. observes similar in-plane anisotropy in the upper critical field, H_{c2}. The magnetic field dependence of C/T for different angles is shown fig. 2.13(e). The upper critical field was determined to be the field where the heat capacity deviates from the linear field dependence of the normal state. Fig. 2.13(d) shows upper critical field as a function of the azimuthal angle. Like the heat capacity in fig. 2.13(a), there is a clear two-fold oscillation. A theoretical study on superconductors with a trigonal lattice, like $Cu_xBi_2Se_3$, indicates that broken rotational symmetry of H_{c2} indicates a two-component pairing symmetry such as Δ_{4x} or Δ_{4y} [141].

Yonezawa et. al. argues that the two-fold behavior that breaks the in-plane crystal symmetry arises from a nematic superconducting order parameter, Δ_{4x} or Δ_{4y}. To determine which order parameter, Yonezawa et. al. determines the location of the gap minimum (for Δ_{4y}) or point nodes (for Δ_{4x}). The temperature and field dependence of C/T is sensitive

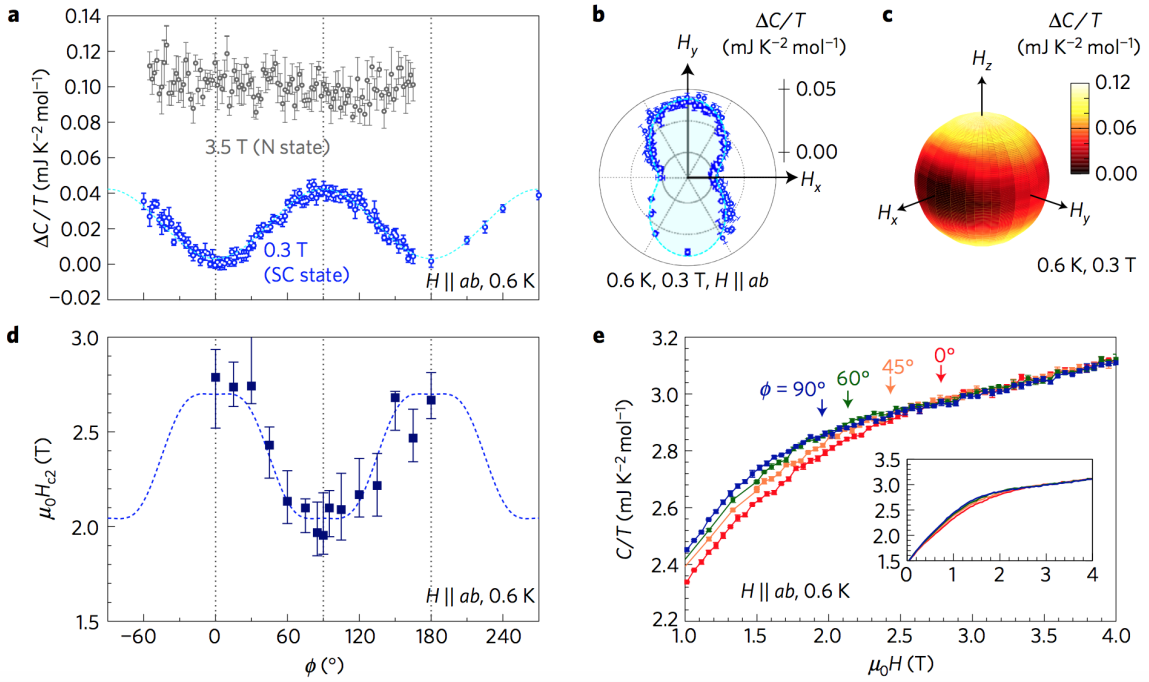

Figure 2.13: Evidence for nematic superconductivity in $Cu_xBi_2Se_3$ taken from ref. [13]. (a) Dependence of heat capacity on azimuthal angle, ϕ. $\Delta C(\phi)/T = C(\phi)/T - C(\mathbf{H} \parallel \hat{\mathbf{x}})/T$. Gray points are in the normal state, and blue points are in the superconducting state. (b) Polar plot of panel (a). (c) Contour plot of heat capacity amplitude. (d) Dependence of upper critical field on azimuthal angle. (e) Field dependence of heat capacity at different angles.

to the location of the gap minimum due to quasiparticle excitations at the gap minimum that are dependent on field and angle [142, 143, 144]. Yonezawa et. al. discovered a sign change in the oscillatory C/T at intermediate temperatures and magnetic field in the superconducting state. By comparing to a theoretical model of a spherical Fermi surface with a gap minimum, Yonezawa et. al. conclude that the gap minimum occurs along the k_x direction. This is consistent with the Δ_{4y} state illustrated in fig. 2.11. Consequently, Yonezawa et. al. claims that $Cu_xBi_2Se_3$ is a fully-gapped, odd-parity superconductor as required for topological superconductivity.

In summary, the nature of the superconducting state in $Cu_xBi_2Se_3$ is still controversial. Early results suggested that it hosts a nodeless, odd-parity A_{1u} state [4, 5, 6, 7] and surface Majorana modes [8] - strong evidence for topological superconductivity. A later STM study called both the pairing symmetry and the existence of surface states into question [9]. An increasing number of results from photoemission to point-contact spectroscopy brought additional scrutiny to claims of topological superconductivity in $Cu_xBi_2Se_3$ [10, 11]. However, various experimental and theoretical studies attempted to reconcile these experiments

and held to the claim of topological superconductivity in $Cu_xBi_2Se_3$ [111] or in the case of a cylindrical Fermi surface, 2D topological superconductivity [11, 12, 114]. Recently, new evidence points to a nematic E_u state in $Cu_xBi_2Se_3$ [12, 13, 14]. However, at the time of this dissertation, there has yet to be a strong consensus in the condensed matter community about these questions.

2.2 Sr-doped Bi_2Se_3

$Cu_xBi_2Se_3$ has been by far the most studied topological superconductor candidate among the doped Bi_2Se_3 compounds. However, $Sr_xBi_2Se_3$ and more recently $Nb_xBi_2Se_3$ have also emerged as promising candidates for topological superconductivity. Though this thesis only presents new contributions made in the pursuit of topological superconductivity with the Cu-doped and Nb-doped systems, the literature on Sr-doped Bi_2Se_3 is of great consequence to the search for topological superconductivity in doped Bi_2Se_3 and will be discussed here.

In many ways, the story about $Sr_xBi_2Se_3$ has been very similar to that of $Cu_xBi_2Se_3$. There were early papers noting that superconductivity can be induced in a topological insulator, Bi_2Se_3, with metallic dopants (this case Sr rather than Cu) [15, 145]. This created some initial interest in the prospect of dopant induced topological superconductivity. Later, ARPES found evidence of a surface state [16, 146], but the tunneling spectrum failed to resolve in-gap states [16, 17]. Lastly, like in $Cu_xBi_2Se_3$, in-plane rotational symmetry breaking suggested evidence of topological nematic superconductivity in $Sr_xBi_2Se_3$ [19, 147, 148]. Now I will discuss these results in a little more detail, with emphasis on the similarities with and differences from the Cu-doped alternative.

The first report of superconductivity in Sr-doped Bi_2Se_3 was in 2015 by Lui et. al. showing T_c = 2.57 K [15]. A few features immediately make $Sr_xBi_2Se_3$ favorably stand out over $Cu_xBi_2Se_3$. First, while $Cu_xBi_2Se_3$ only achieved a maximum superconducting fraction of 56% [80] and more often far lower [3], $Sr_xBi_2Se_3$ has a superconducting fraction of over 90% [15]. Second, $Sr_xBi_2Se_3$ is robust to air. Lui et. al. showed that the superconducting volume fraction in $Sr_xBi_2Se_3$ was unchanged after 4 hours exposure to air. It is commonly known that superconductivity in $Cu_xBi_2Se_3$ is easily damaged over time and especially after exposure to air. This makes $Sr_xBi_2Se_3$ easier to work with and more promising for potential future applications.

Lui et. al. measured quantum oscillations in the magnetoresistance of $Sr_xBi_2Se_3$ (the SdH effect). Fig. 2.14 (a) and (c) show the SdH oscillations in the resistance and hall channels respectively. Lui et. al. indexes the Landau levels and plots them against $1/B$

in fig. 2.14 (b) and (d). The fitting for the Landau level indices gives an intercept, γ, in infinite field limit ($1/B$ = 0). γ = -1/2 is indicative of a π Berry phase revealing the presence of Dirac electrons. This method has been used to identify non-trivial topology in graphene [34, 149] and topological Kondo insulator, SmB_6 [150]. As shown in fig. 2.14, in the infinite field limit, the Landau level plot gives an intercept near γ = -1/2. This is evidence of Dirac electrons and possibly non-trivial topology in $Sr_xBi_2Se_3$.

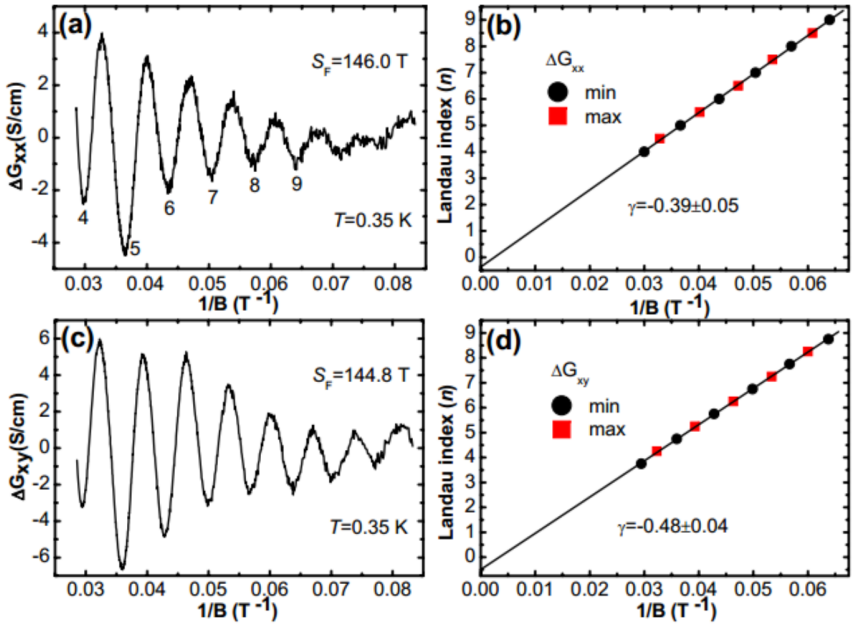

Figure 2.14: SdH oscillations in $Sr_xBi_2Se_3$ taken from ref [15]. (a) Quantum oscillations in magnetoresistance. (b) Landau level index plot of oscillations in magnetoresistance. (c) Quantum oscillations in the Hall signal. (d) Landau level index plot of oscillations in the Hall signal. High field intercepts of γ = -0.39 for magnetoresistance and γ = -0.48 for Hall are near the half-integer Berry phase.

A report by Shruti et. al. provides a conglomeration of transport, Hall, magnetization, XRD, and thermopower data on $Sr_xBi_2Se_3$ [145]. They measure numerous properties such as the effective mass, carrier density, coherence length, upper and lower critical field, etc. Their most notable results are that $Sr_xBi_2Se_3$ is superconducting with Sr levels between $0.1 < x < 0.2$, with optimal doping at $x = 0.1$. Though other reports shows superconductivity with samples with Sr concentration $x < 0.1$ [15, 16]. Shruti et. al. also find that the carrier concentration ($n = 1.85 \times 10^{19} cm^{-3}$, an order of magnitude smaller than in $Cu_xBi_2Se_3$ [3]) is very low for a superconductor given the T_c and suggest that this could indicate an unconventional superconducting order. Furthermore, they find that the superconductivity occurs in the clean limit with an estimated mean free path (assuming a spherical Fermi surface) of 49.4 nm, which is greater than their calculated coherence length, ξ, of

15.3 nm. Despite this, unlike in $Cu_xBi_2Se_3$, they show that the upper critical field is Pauli limited in $Sr_xBi_2Se_3$. This article also briefly discusses the in and out of plane anisotropy of $Sr_xBi_2Se_3$, but the authors later produced another article discussing this particular feature in greater detail, as well as the details of their growth parameters [151].

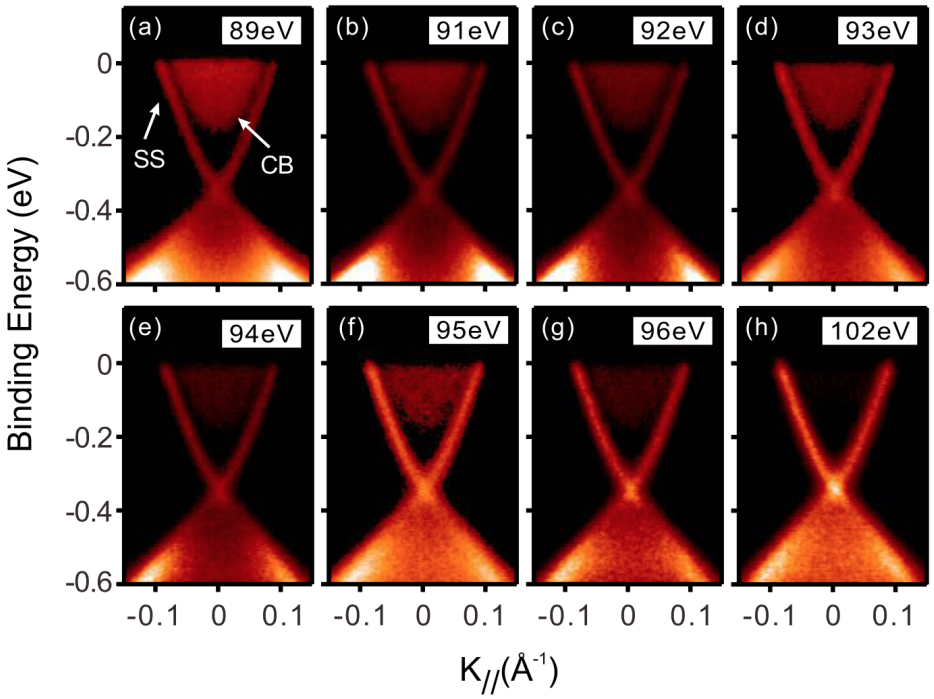

Figure 2.15: ARPES data for $Sr_xBi_2Se_3$ for different incident photon energies taken from ref [16]. In panel (a) the surface state (SS) and conduction band (CB) are labeled.

ARPES studies by Han et. al. [16] and Neupane et. al. [146] both show the coexistence of a Dirac surface state with the bulk conduction band just as in $Cu_xBi_2Se_3$ [4]. Fig. 2.15 shows the ARPES data for $Sr_xBi_2Se_3$ for different incident photon energies. As seen in panel (a), the surface state (labeled SS) is seen along with the bulk conduction band (labeled CB). The Dirac point is also easily recognizable and is comparable to that of $Cu_xBi_2Se_3$ (see fig. 2.2) [4].

From the ARPES data, Han et. al. calculates m/μ, the ratio of the Dirac rest mass and the chemical potential, to be 0.44 [16]. This ratio is a parameter in the phase boundary between the topologically non-trivial, Δ_2, and topologically trivial, Δ_1, phases shown in fig. 2.3 [5]. For $Cu_xBi_2Se_3$, Wray et. al. makes a similar argument that the low value of m/μ (1/3 in the case of $Cu_xBi_2Se_3$) is suggestive of an odd-parity, topologically non-trivial phase [4]. However, it is hard to say whether this phase diagram between the Δ_1 and Δ_2 phases is relevant since there is increasing evidence that the Δ_4 phase (see table 2.1) is more likely than the Δ_2 phase for topological superconductivity in doped Bi_2Se_3.

Just as in $Cu_xBi_2Se_3$, STM measurements on $Sr_xBi_2Se_3$ do not show any in-gap states arising from surface Majorana excitations. [16, 17]. Fig. 2.16 shows the tunneling spectrum of $Sr_xBi_2Se_3$ taken from STM. Also as in $Cu_xBi_2Se_3$ [9], the tunneling spectrum is well fit by an s-wave model.

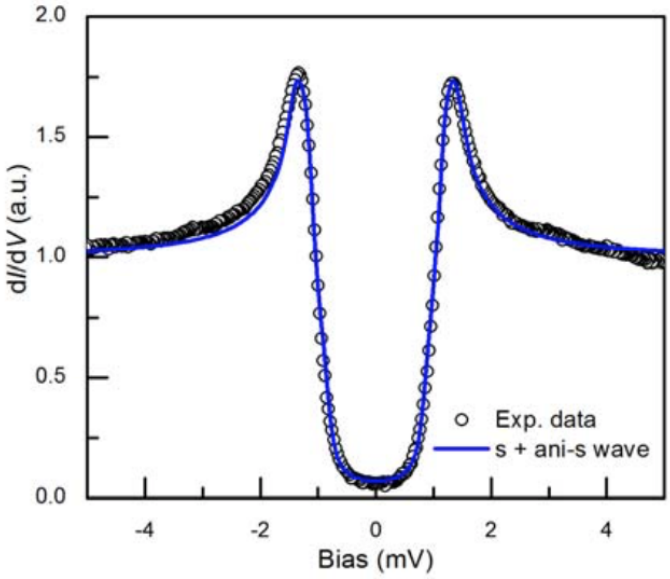

Figure 2.16: STM data for $Sr_xBi_2Se_3$ taken from ref [17]. There are no in-gap states, and the tunneling spectrum is well fit by an s-wave model.

From the fitting of the data in fig. 2.16, Du et. al. concludes that there are two bands that contribute to Cooper pairing in $Sr_xBi_2Se_3$ [17]. Due to the coexistence of a surface Dirac band and bulk conduction band from ARPES [16, 146], Du et. al. argues that Dirac electrons from the surface are driven into Cooper pairs. Furthermore, Du et. al. reports the Scanning Tunneling Spectroscopy (STS) spectrum in magnetic field. They were able to resolve the Landau levels due to surface excitations. They find that the magnitude of the STS signal fluctuations due to Landau quantization within the gap shrinks with magnetic field. Since STS is sensitive to surface excitations, they argue that the amplitude of these fluctuations is related to the population of surface Dirac electrons, and the reduction of the fluctuation amplitude in the gap with increasing magnetic field is due to the breaking of Cooper pairs from the surface state. This unique argument has not been proposed in $Cu_xBi_2Se_3$. Du et. al. claim that the behavior of Cooper pairs made of Dirac surface electrons could form a 2D topological superconductor.

Pressure studies of $Sr_xBi_2Se_3$ by Zhou et. al. [18] show interesting features in contrast to $Cu_xBi_2Se_3$ [7]. Fig. 2.17 shows the resistance of $Sr_xBi_2Se_3$ as a function of temperature for different pressures up to 80 GPa. The first notable difference is that superconductivity

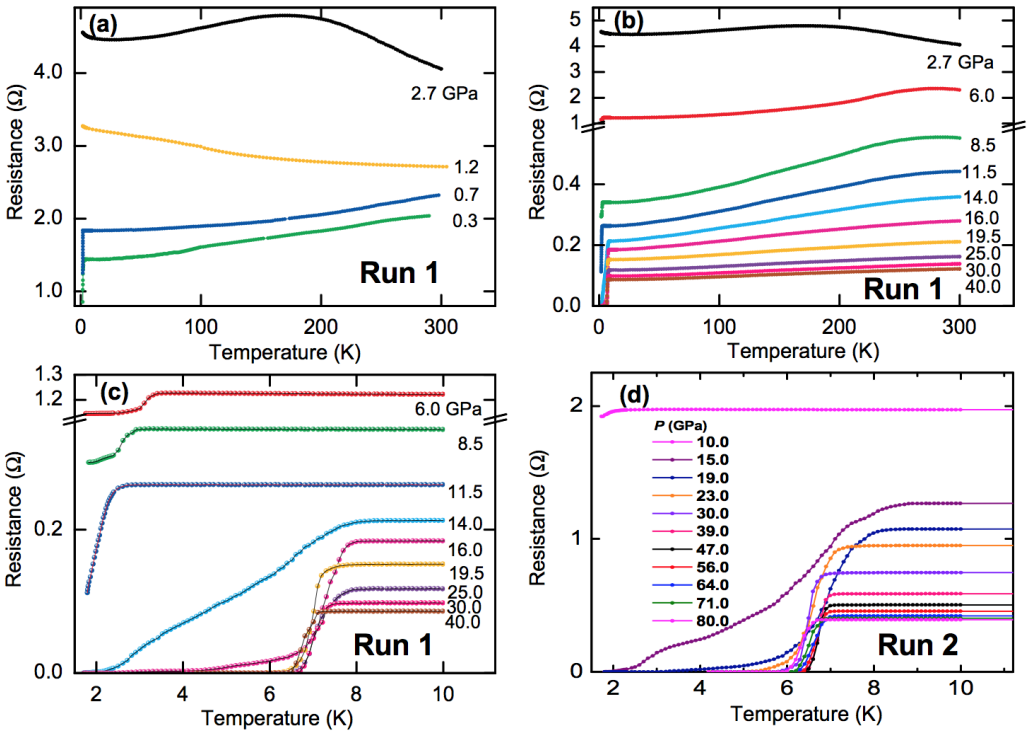

Figure 2.17: Temperature dependence of resistance at different pressures up to 80 GPa in $Sr_xBi_2Se_3$ taken from ref [18]. (a) Low pressure region. (b) High pressure region. (c) Data from (b) in narrow temperature range. (d) Extension of data to higher pressures up to 80 GPa.

is killed much faster in $Sr_xBi_2Se_3$ ($\sim$1.1 GPa [18]) compared to $Cu_xBi_2Se_3$ (6.3 GPa [7]). Another pressure study shows a superconducting transition above 1.1 GPa by measuring the temperature dependence of resistance down to 300 mK rather than the minimum temperature in Zhou et. al. of 2 K [147]. They estimate that the critical pressure is $\sim$3.5 GPa. Either way, the critical pressure in $Sr_xBi_2Se_3$ is much lower than in $Cu_xBi_2Se_3$, which is likely due to the lower carrier concentration.

A second, more interesting difference is that superconductivity reemerges at pressure over 6 GPa as seen in fig. 2.17(b) and (c). This feature has not been reported in $Cu_xBi_2Se_3$. In fig. 2.17(c), it can be seen that the transition temperature in the reemergent superconductive phase increases to 8.3 K over 14 GPa and persists up to the highest measured pressure of 80 GPa. This enhanced superconductivity under pressure has also been observed in iron chalcogenide superconductors such as $Tl_{0.6}Rb_{0.4}Fe_{1.67}Se_2$, $K_{0.8}Fe_{1.7}Se_2$, and $K_{0.8}Fe_{1.78}Se_2$ [152]. Zhou et. al. argues from XRD data that the emergence of superconductivity arises from a pressure-induced structural phase transition. A similar structural phase transition and emergent superconductivity has been observed in undoped Bi_2Se_3 [153, 70], though the behavior of T_c as a function of pressure is different from

$Sr_xBi_2Se_3$.

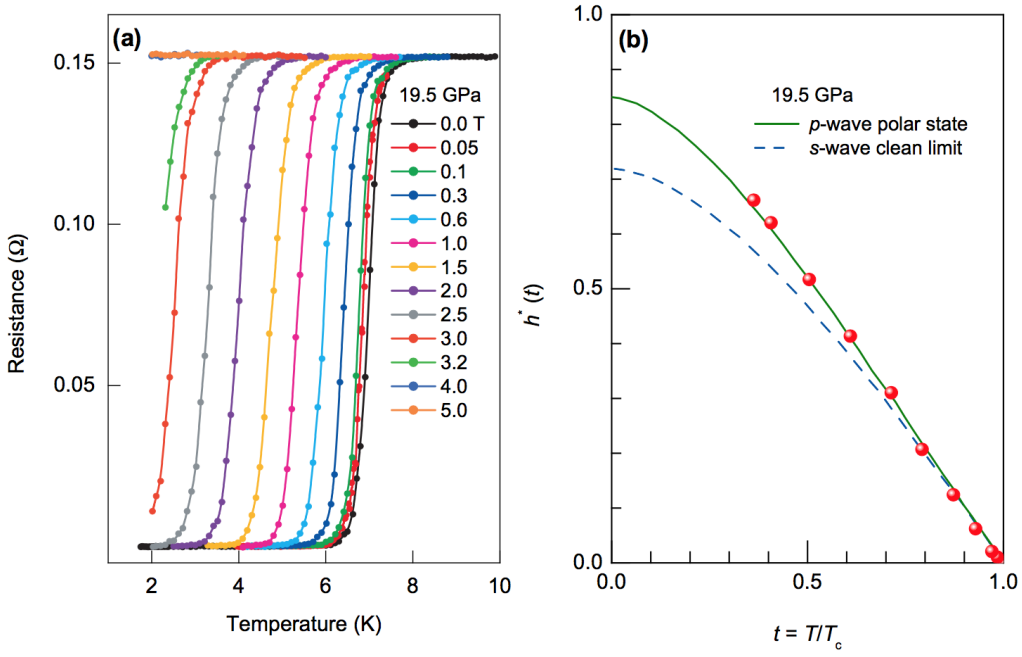

Figure 2.18: (a) Temperature dependence of resistance for $Sr_xBi_2Se_3$ in the reemergent phase (19.5 GPa) in different magnetic fields taken from ref. [18]. (b) Fitting of $h^* = (B_{c2}/T_c)/|dB_{c2}/dT|_{T_c}$ vs T/T_c for an s-wave and p-wave model. Data suggests unconventional superconductivity in $Sr_xBi_2Se_3$.

Similar to Bay et. al., Zhou et. al. plots the relationship of $h^* = (B_{c2}/T_c)/|dB_{c2}/dT|_{T_c}$ against T/T_c for the reemergent superconducting phase. They then fit it with an s-wave and a p-wave model (fig. 2.18). The corresponding plot for $Cu_xBi_2Se_3$ is shown in fig. 2.5. As seen in fig. 2.18(b), the data follows the p-wave model suggesting unconventional superconductivity in the reemergent phase of $Sr_xBi_2Se_3$. The same plot for the low pressure superconducting phase can be found in ref. [147], which also shows good agreement with the p-wave model. Pressure-induced superconductivity with a T_c enhancement is very interesting in its own right, but the implications of unconventional superconductivity make this result relevant to potential topological superconductivity in $Sr_xBi_2Se_3$.

However, a recent contradictory report by Manikandan et. al. [154] suggest that $Sr_xBi_2Se_3$ is a conventional superconductor. Like Zhou et. al., they perform electrical transport under pressure. But in contrast, they do not see the reemergence of superconductivity up to 8 GPa arguing that the result in Zhou et. al. is simply due to the structural transition of Bi_2Se_3 and is unrelated to Sr dopants. However, it is unclear why they do not also see the reemergence of superconductivity due to structural transition or why the behavior of T_c as a function of pressure is different between $Sr_xBi_2Se_3$ [18] and Bi_2Se_3 [70].

Manikandan et. al. further argue that the suppression of T_c as a function of pressure in $Sr_xBi_2Se_3$ is consistent with the model for conventional superconductors. The debate about the interpretation of the pressure dependent superconductivity in $Sr_xBi_2Se_3$ is very new at the time of this dissertation and is thus unresolved.

Another point of disagreement in the $Sr_xBi_2Se_3$ community concerns the location of the Sr dopants. In $Cu_xBi_2Se_3$, the consensus is that superconductivity occurs when Cu-dopants are intercalated in the van der Waals gap between quintuple Bi_2Se_3 layers. It has been clearly seen that when the Cu dopants substitute Bi sites, they act as an acceptor rather than a donor and there is no superconductivity [3, 78].

In agreement with $Cu_xBi_2Se_3$, Liu et. al. [15] and Shanti et. al. [145] argue that the Sr dopants intercalate in the van der Waals gap in superconducting $Sr_xBi_2Se_3$. Liu et. al. measures the expansion of the c-axis lattice parameter by XRD and argue that it is evidence of Sr sitting in the van der Waals gap [15]. Shanti et. al. perform XRD and TEM on $Sr_xBi_2Se_3$. In agreement with Liu et. al. they claim that Sr dopants sit in the van der Waals gap due to the size of the van der Waals gap [145].

Data from STM studies are a bit more contradictory. Han et. al. does not observe any Sr atoms by STM in the van der Waals gap where $Sr_xBi_2Se_3$ cleaves [16]. They find that the cleaved surface is much cleaner than $Cu_xBi_2Se_3$ and appears much like undoped Bi_2Se_3. Due to the absence of Sr atoms on the cleaved surface, they argue that most of the Sr atoms are intercalated within the quintuple layer rather than between quintuple layers. In contrast to this result, Du et. al. measures clumps of Sr atoms in the van der Waals gap by STM, and they find that the Sr clusters can be moved around by the STM tip [17]. Furthermore, Du et. al. finds regions where there is Sr substitution; however, there is not a superconducting gap in these regions as seen by STS.

Rotational symmetry breaking in $Sr_xBi_2Se_3$. As discussed in section 2.1.3, evidence of odd-parity, E_u superconducting pairing in $Cu_xBi_2Se_3$ was discovered with the observation of basal plane rotational symmetry breaking in the knight shift [14] and heat capacity [13]. Similarly, in-plane rotational symmetry breaking has been observed in the resistivity and upper critical field, H_{c2}, in $Sr_xBi_2Se_3$ [19].

Fig. 2.19 shows the magnetoresistance of $Sr_xBi_2Se_3$ as a function of angle, θ, in a polar plot for different temperatures between 2 K and 3 K. θ is defined to be the angle between the mirror plane axis (called a^* in Pan et. al. [19] and $\hat{y}$ in fig. 2.10) and an in-plane external magnetic field of 0.4 T. A diagram defining a and a^* is in the inset of fig. 2.20(b).

In the superconducting state of $Sr_xBi_2Se_3$, there is a clear two-fold anisotropy. For example, in the data at 2.2 K (in pink), the $Sr_{0.1}Bi_2Se_3$ crystal is superconducting with the magnetic field pointed normal to the mirror plane ($\theta = 90°$), but it is in the normal state with

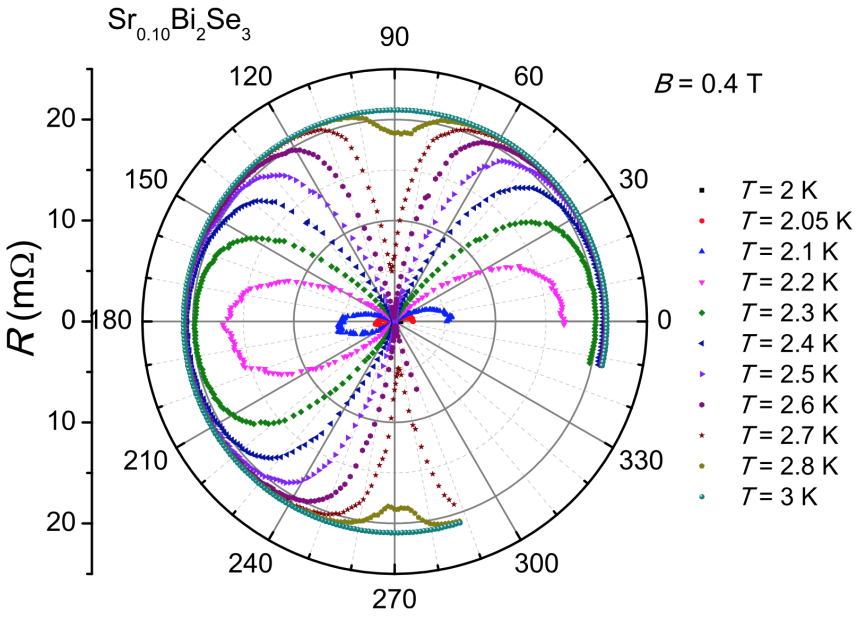

Figure 2.19: Polar plot of the basal plane magnetoresistance for different temperatures in $Sr_{0.1}Bi_2Se_3$ taken from ref. [19]. Strong in-plane anisotropy can be clearly seen below T_c, but vanishes above T_c.

field in the mirror plane (θ = 0°). At higher temperature above T_c, the in-plane anisotropy of $Sr_xBi_2Se_3$ vanishes.

Fig. 2.20, shows the in-plane anisotropy of H_{c2} as a function of θ for $Sr_{0.1}Bi_2Se_3$ (a) and $Sr_{0.15}Bi_2Se_3$ (b). As can be seen, H_{c2} is enhanced normal to the mirror plane (labeled a in fig. 2.20 and $\hat{x}$ in fig. 2.10) thus breaking the rotational symmetry. Using the Ginzburg-Landau relations $B^a_{c2} = \Phi_0/(2\pi\xi_{a^*}\xi_c)$, $B^{a^*}_{c2} = \Phi_0/(2\pi\xi_a\xi_c)$, and $B^c_{c2} = \Phi_0/(2\pi\xi_{a^*}\xi_a)$, Pan et. al. calculates the coherence lengths in various crystal directions to be ξ_a = 19.6 nm, ξ_{a^*} = 7.6 nm, and ξ_c = 5.4 nm. Naively, since the coherence length is inversely proportional to the gap size by $\xi_0 = \frac{\hbar v_F}{\pi\Delta(0)}$, the superconducting gap in-plane should have a minimum in the a direction. This is consistent with the Δ_{4y} order parameter from table 2.1, which was proposed by Fu to be a candidate order parameter for topological superconductivity (discussed in detail in section 2.1.3) [12]. However, a detailed theoretical study of the relationship between the superconducting gap and the coherence length for a non-BCS superconductor with basal plane anisotropy is needed.

A later paper from the same group shows that the rational symmetry breaking of the upper critical field in $Sr_xBi_2Se_3$ persists and is enhanced under pressure up to 2.2 GPa [147]. A more recent report by Du et. al. shows that the nematic axis is sample dependent, sometimes falling on the mirror plane and sometimes normal to the mirror plane [148]. This result is intriguing since a nodeless, potentially-topological Δ_{4y} order parameter is realized

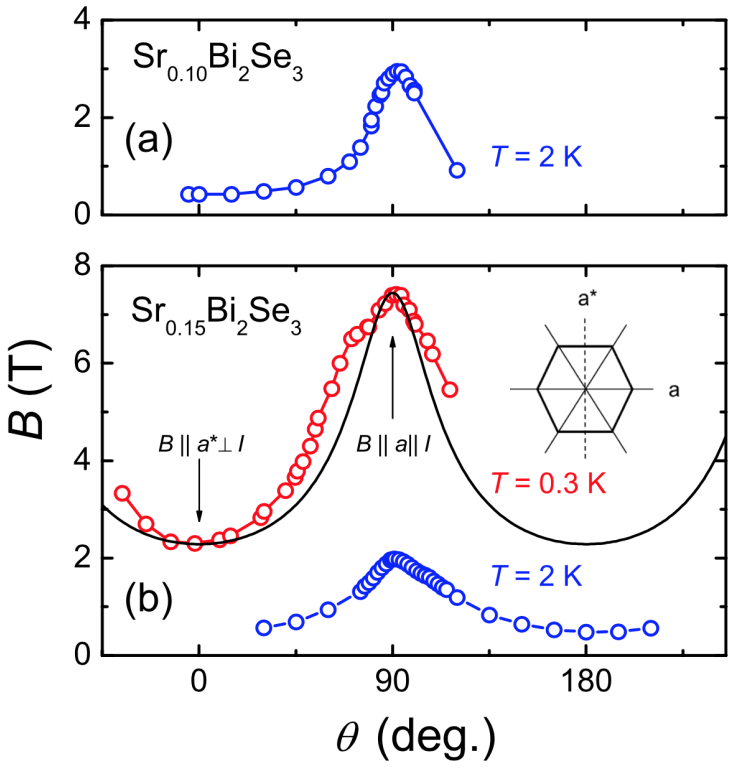

Figure 2.20: Basal plane anisotropy of upper critical field in $Sr_{0.1}Bi_2Se_3$ (a) and $Sr_{0.15}Bi_2Se_3$ (b) taken from ref. [19]. Inset of panel (b) shows the definition of a and a^* axes.

when the nematic director falls on the mirror plane. However, when the nematic director falls normal to the mirror plane, the order parameter is Δ_{4x} and the superconducting gap develops point nodes on the equator as seen in fig. 2.11.

Du et. al. fails to comment on the sharp contrast between the Δ_{4x} and Δ_{4y} order parameters that seem to be realized in different $Sr_xBi_2Se_3$ samples. In particular, they don't comment on what could be the difference between the samples to realize these different superconducting phases.

If their result is true, this has potentially large impacts on the search for topological superconductivity. Since the Δ_{4x} order parameter does not realize topological superconductivity and Δ_{4y} is a candidate order parameter for topological superconductivity, studying the difference between these two samples by other means could be quite illuminating. For example, if point-contact spectroscopy measured in-gap states as was reported in $Cu_xBi_2Se_3$ [8] for the Δ_{4y} sample and not the Δ_{4x} sample, this would prove to be strong evidence of Majorana surface states in the Δ_{4y} $Sr_xBi_2Se_3$ and provide strong experimental confirmation of Fu's theory [12].

One shortcoming of the observation of rotational symmetry breaking in $Sr_xBi_2Se_3$ as

opposed to $Cu_xBi_2Se_3$ is that it was done by electrical transport. In transport studies, a current must be applied which inherently breaks the rotational symmetry. Pan et. al. argues that their observed in-plane anisotropy is not due to the current direction by performing the experiment with the current both along the a axis and c axis. Du et. al. tries to avoid this problem by using a Corbino geometry that is described in other works [155]. However, these methods are not as robust as the purely thermodynamic measurements used with $Cu_xBi_2Se_3$ that don't introduce any external symmetry breaking [13, 14].

2.3 Nb-doped Bi_2Se_3

From all the doped Bi_2Se_3 compounds, $Nb_xBi_2Se_3$ is the newest and least investigated. At the time of this dissertation, there are only three peer-reviewed articles on $Nb_xBi_2Se_3$ [21, 41, 42], two of which are from the University of Michigan [41, 42] and will be discussed in chapter 5. However, there are various papers on *arXiv* [20, 156, 157], and $Nb_xBi_2Se_3$, though very young, is shaping up to be an interesting system that potentially hosts topological superconductivity [20, 21, 42, 156, 157], nematic superconductivity [42, 156, 157], coexistence of superconductivity and ferromagnetism [20], chiral superconductivity [156, 157], and/or topological Weyl superconductivity [156, 157].

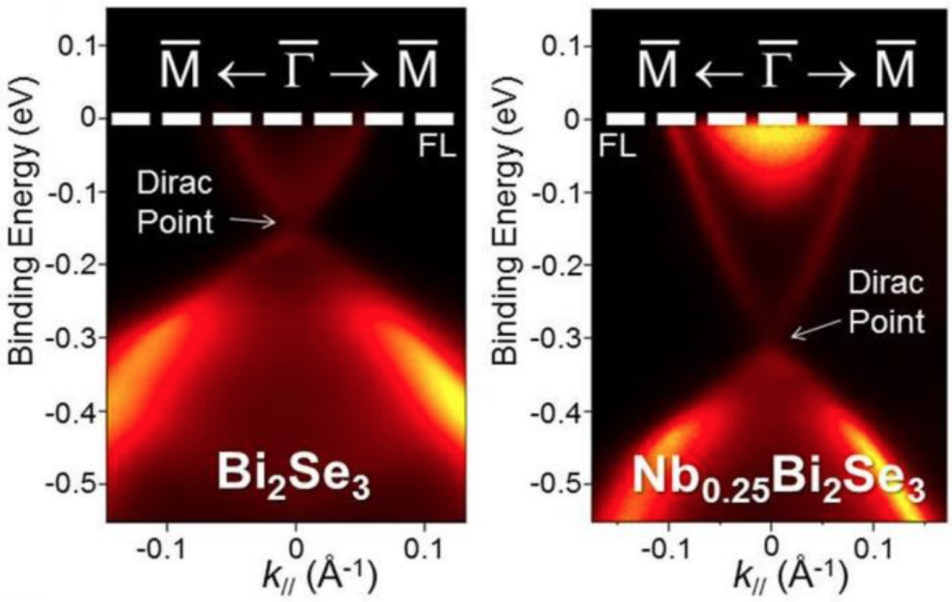

Figure 2.21: Comparison of ARPES data between $Nb_xBi_2Se_3$ and undoped Bi_2Se_3 both showing a Dirac point taken from ref. [20].

Superconductivity in $Nb_xBi_2Se_3$ was first observed by Qiu et. al. with T_c = 3.6 K [20]. Like in Bi_2Se_3, $Cu_xBi_2Se_3$ and $Sr_xBi_2Se_3$, ARPES revealed a Dirac band in the gap. Fig.

2.21 shows the ARPES comparison between $Nb_xBi_2Se_3$ and undoped Bi_2Se_3. For comparison, see fig. 2.2 for $Cu_xBi_2Se_3$ and fig. 2.15 for $Sr_xBi_2Se_3$.

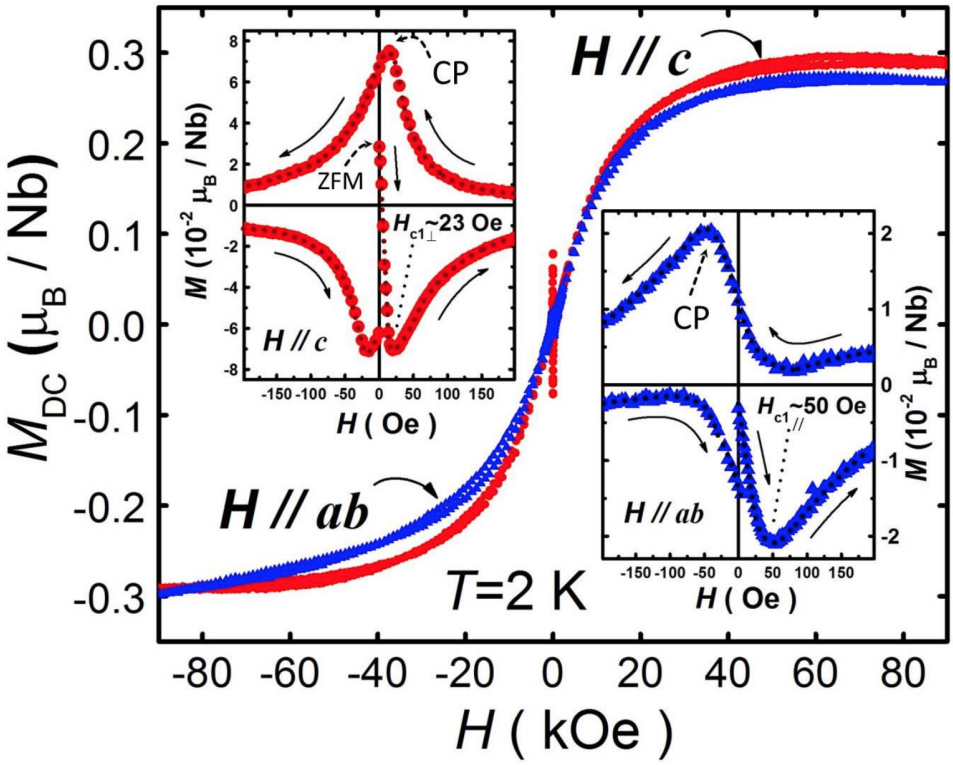

Figure 2.22: Magnetization of $Nb_xBi_2Se_3$ taken from ref. [20]. Insets show the low-field hysteresis behavior typical of type-II superconductors for H in the ab plane (upper left) and H in the c plane (bottom right). A zero-field magnetic moment is seen inside the superconducting hysteresis loop.

The most striking feature observed by Qiu et. al. is in the magnetization data. They report broken time reversal symmetry in $Nb_xBi_2Se_3$ with the observation of a zero-field magnetic moment within the superconducting state and abnormal hysteresis behavior. The magnetization data for $Nb_xBi_2Se_3$ is show in fig. 2.22. The insets show the low field magnetic hysteresis typical of type-II superconductors. Oddly, the magnetization curves start from a non-zero magnetic moment in the superconducting state (labeled ZFM in fig. 2.22). Qiu et. al. argue that this is evidence of the coexistence of ferromagnetism and superconductivity in $Nb_xBi_2Se_3$ previously only seen in Uranium based superconductors [158, 159, 160]. In addition, Qiu et. al. note an unusual behavior of the central peak in the hysteresis loop (labeled CP in fig. 2.22). They argue that the position of the central peak is explained by contributing effects of superconducting vortex current and the Nb magnetic moments similar to layered superconductor/ferromagnetic films [161].

This experimental observation of unusual magnetic order in the superconducting state

has motivated new theories suggesting the possibility of Weyl physics in $Nb_xBi_2Se_3$ that is very distinct from its Cu-doped and Sr-doped counterparts [156, 157]. These unusual features and subsequent theories are in their very early stages and haven't had the opportunity to face the scrutiny of the community. None of these works have been published in peer reviewed journals due to how recently they've appeared on the scene, and there has not been any further experimental works confirming or denying these results.

One argument put forth from Qiu et. al. is that Nb dopants do more that simply move the chemical potential as is the case in Cu-doped Bi_2Se_3 [20]. This indeed has been confirmed by quantum oscillations, which, through the observation of multiple Fermi surfaces, have clearly shown that $Nb_xBi_2Se_3$ has different Fermiology from other doped Bi_2Se_3 compounds [41]. This quantum oscillation study is one of the key works of this thesis and will be discussed in detail in chapter 5.

As in $Cu_xBi_2Se_3$ and $Sr_xBi_2Se_3$, basal plane rotational symmetry breaking has also been observed in $Nb_xBi_2Se_3$ [42]. This time it has been observed in the superconducting hysteresis loop as measured by torque magnetometry. This result as well is discussed in chapter 5.

Lastly, a penetration depth study by Smylie et. al. observed nodes in the superconducting gap of $Nb_xBi_2Se_3$ [21]. Fig. 2.23 shows the penetration depth (translated into nm on right axis) vs T/T_c for $Nb_xBi_2Se_3$. The data is fit by a quadratic curve, which is indicative of point nodes in the superconducting gap. Smylie et. al. also plots exponential fits with dashed lines according to a model for BCS full gapped superconductors. The data clearly deviates from these fits suggesting a nodal gap.

A gap with point nodes in $Nb_xBi_2Se_3$ is very interesting in light of the history of the search for topological superconductivity in doped Bi_2Se_3. As has been discussed in this chapter, it has been thought that a topological superconductor requires a nodeless gap - hence special attention has been given to the Δ_2 and Δ_{4y} order parameters from table 2.1. From the penetration depth study [21] and the observation of basal plane rotational symmetry breaking [42], Smylie et. al. argues that $Nb_xBi_2Se_3$ has the Δ_{4x} order parameter with point nodes on the equator. Early theoretical works would have thus eliminated $Nb_xBi_2Se_3$ as a candidate for topological superconductivity [5, 12]. However, there has more recently been some discussion of nodal topological superconductivity in non-centrosymmetric and Weyl superconductors [162], and as stated above, $Nb_xBi_2Se_3$ has been considered as a platform for Weyl physics [156, 157]. In addition, other theoretical works have not precluded nodal superconductors from the topological superconductor discussion [104, 126, 140]. A theoretical work by Sato also briefly discusses the condition under which a nodal superconductor could be topological [38]. In light of the observation of nodes in $Nb_xBi_2Se_3$ and

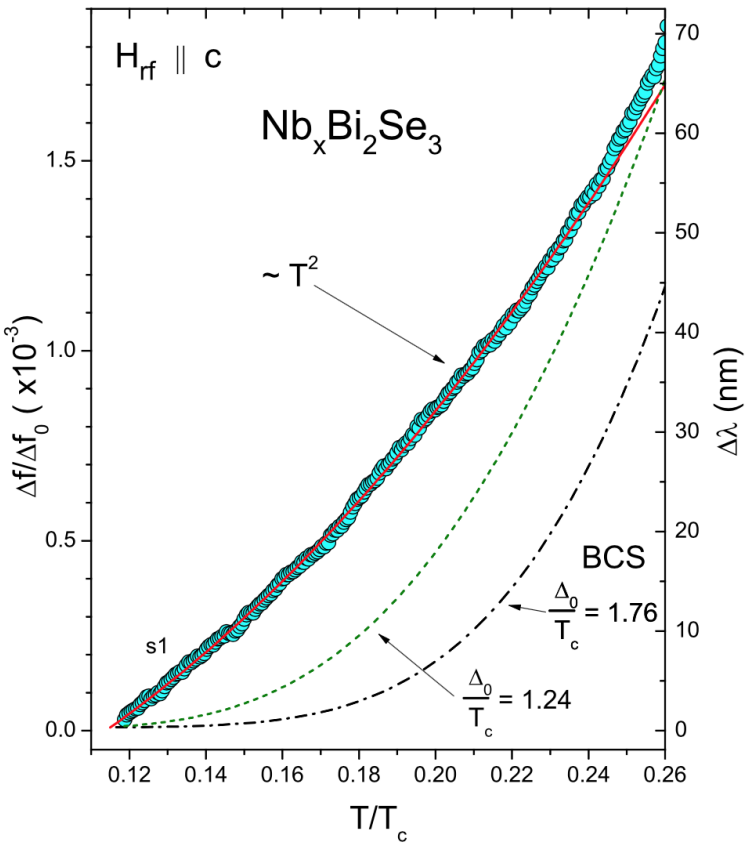

Figure 2.23: Penetration depth in $Nb_xBi_2Se_3$ vs T/T_c taken from ref. [21]. The quadratic fit is characteristic of point nodes. Fully-gapped, exponential models are show for comparison.

these theoretical developments, a more detailed theoretical analysis on the role of nodes in topological superconductors would be an asset to the field.

2.4 Summary

In summary, there have been three material candidates for topological superconductivity in the Bi_2Se_3 family - $Cu_xBi_2Se_3$, $Sr_xBi_2Se_3$, and $Nb_xBi_2Se_3$. The search for topological superconductivity in these compounds began in 2010 and has yet to reach consensus in the condensed matter community. There has been an increase in controversial evidence for and against topological superconductivity in $Cu_xBi_2Se_3$; however, signatures of new physics with implications for topological order in all three compounds has reinvigorated life into this excited field. For example, basal plane rotational symmetry breaking in all three doped Bi_2Se_3 compounds has been the subject of much discussion in the community [13, 19, 42]. Potential coexistence of magnetic order and superconductivity in $Nb_xBi_2Se_3$ has been a

platform for several exotic new theories [156, 157]. For $Sr_xBi_2Se_3$ and $Nb_xBi_2Se_3$, there is still a lot more to be done to solidify their position in this search. This dissertation is written in midst of the development of this fascinating field. Knowledge of the Fermiology, electronic and magnetic properties of doped Bi_2Se_3 is essential for clarifying the physics in these exotic materials. Torque magnetometry, the primary tool in this work, is sensitive to these properties. The results from my studies have been some of the staple results in field [39, 41, 42], including the first published work on $Nb_xBi_2Se_3$ [41].

CHAPTER 3

Experiments

3.1 Torque Magnetometry

3.1.1 Experimental Setup

The primary technique used in this study is torque magnetometry. Torque magnetometry is a very versatile tool that is sensitive to magnetic properties. In particular, capacitive torque magnetometry, which is described here, can be performed at ultra-low temperatures down to 10 mK and high magnetic field up to 45 T. This makes it an ideal technique for studying materials at low temperatures and high magnetic fields.

Generally, quantum oscillation experiments are used to reveal the electronic structure of topological materials and topological material candidates. These experiments reveal many important material properties such as the effective mass, mean free path, Fermi velocity, etc. They also can be used to map the Fermi surface. In the search for topological superconductivity, the shape of the Fermi surface of a topological superconductor candidate is crucial in order to identify whether it contains an odd number of TRI momentum - one of the sufficient criteria for topological superconductivity described in section 1.2.1.

High magnetic fields are needed to resolve quantum oscillations. Also quantum oscillations are strongly suppressed by temperature. Torque magnetometry, which can operate under these harsh conditions, is an ideal technique to search for quantum oscillations. Furthermore, the magnetic properties probed by torque magnetometry depend on the density of states at the Fermi level - the origin of quantum oscillations as described in section 3.1.2.

Beyond quantum oscillations, torque magnetometry is sensitive to phase transitions, magnetic anomalies, and symmetry breaking. Sections 5.4 and 5.5 discuss some of these observations by torque magnetometry in $Nb_xBi_2Se_3$.

The principle of torque magnetometry is based on elementary electrodynamics. When an external magnetic field is applied to a material, the induced magnetic moment in the sample causes a torque given by

$$\tau = \mu_0 \mathbf{m} \times \mathbf{H} \tag{3.1}$$

where μ_0 is the vacuum permeability, $\mathbf{m}$ is the sample magnetic moment, and $\mathbf{H}$ is an applied external magnetic field. Without losing any generality the coordinate system can be defined such that the cross product simplifies to

$$\begin{aligned} \tau &= \mu_0 V \mathbf{M} \times \mathbf{H} \\ &= \mu_0 V (M_z H_x - M_x H_z) \hat{y} \end{aligned} \tag{3.2}$$

where V is the volume of the sample and $\mathbf{M}$ is the sample magnetization.

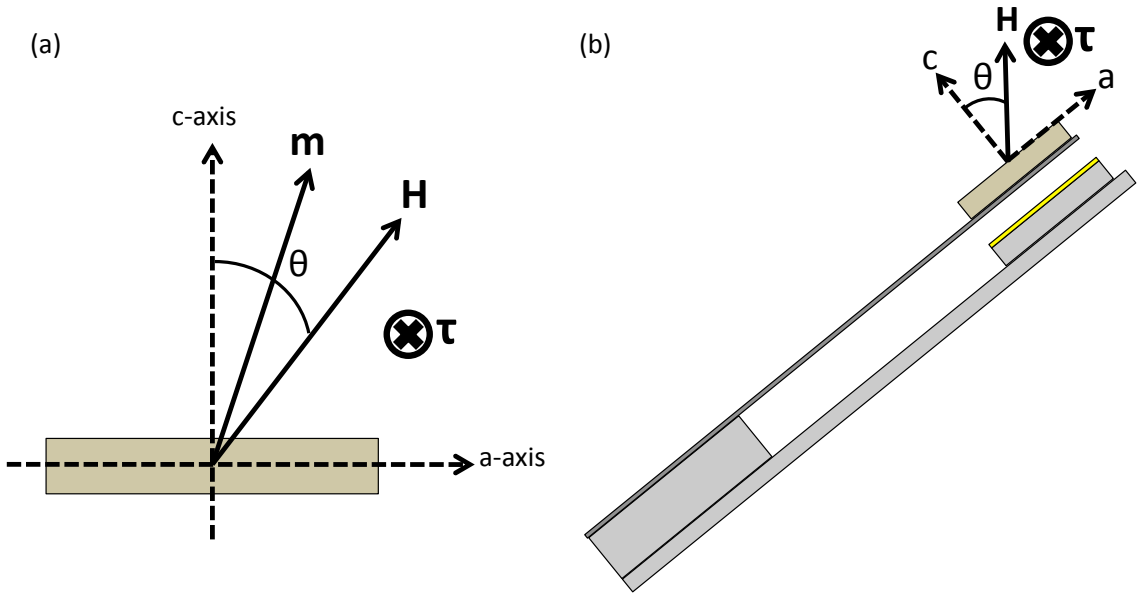

Figure 3.1: (a) Schematic of the magnetic torque of a sample with magnetic moment, $\mathbf{m}$ and external field $\mathbf{H}$. The angle θ is defined as the angle between the external magnetic field and the crystal c-axis. (b) Magnetic torque on a sample mounted on a thin metallic cantilever.

Fig. 3.1(a) is a schematic of the magnetic moment of the sample and the applied magnetic field. When the sample is glued to the end of a cantilever as shown if fig. 3.1(b), $\mathbf{H}$ lies in the a-c plane and the torque is isolated to in or out of the page. For samples with basal plane rotational symmetry breaking such as doped Bi_2Se_3, the sample can be mounted on its side such that the applied magnetic field is always in the a-b plane rather than the a-c plane as in section 5.5.

Given the configuration in fig. 3.1(b) it is convenient to define the z-axis to be along the

crystalline c-axis, and to define the the x-axis to be along the crystalline a-axis. This definition would change depending on the crystalline direction that points along the cantilever arm.

Using $\mathbf{M} = \chi\mathbf{H}$ where χ is the magnetic susceptibility and the coordinate system described above, equation 3.1 simplifies further to

$$\begin{aligned} \tau &= \mu_0 V(\chi_z H_z H_x - \chi_x H_x H_z)\hat{y} \\ &= \mu_0 V \Delta\chi H^2 \sin\theta\cos\theta\hat{y} \end{aligned} \tag{3.3}$$

Thus the magnetic torque on the sample is proportional to the magnetic susceptibility anisotropy of the sample, the square of the external magnetic field, and factors related to the angle, θ, between the external magnetic field and the crystal c-axis. The angle, θ, can be changed by rotating the cantilever in field as shown in fig. 3.1(b). Typically, the whole cantilever setup is mounted on a rotation stage via thermal joint compound or N-grease in order to measure the angular dependence of the magnetic torque on the sample. The angle is determined by a Hall sensor attached to the rotation stage, which has a strong angular dependence. It is further confirmed by tracking the angular dependence of C_0, the zero-field capacitance of the cantilever, which will change as a function of the angle as the weight of the sample applies a torque on the cantilever. This is discussed in more detail below.

The samples are glued to the tip of a thin-film cantilever using GE varnish. The torque is then measured by tracking the capacitance between the thin metallic cantilever and a gold film underneath as shown in fig. 3.2(b). The capacitance is tracked with a digital Andeen-Hagerling AH2700A 50 Hz - 20 kHz Ultra-Precision Capacitance Bridge. Gold leads connected to the metallic cantilever and gold film connect to co-ax cables leading to the digital capacitance bridge. Co-ax cables are necessary to provide good shielding to prevent excess noise and stray capacitance.

The torque magnetometers shown in fig. 3.2 are handmade. The substrate and spacer are made of quartz or sapphire. The gold film is evaporated on thin sapphire. The size of the gap between the metallic cantilever and gold film is determined by the relative width of the spacer and gold film. The spacers are typically 500 μm and the sapphire on which the gold film is evaporated is 250 μm. This gives a gap of 250 μm. However, this can be adjusted depending on the needs of the experiment.

A small gap leads to a larger zero-field capacitance, C_0. For a larger C_0 the change in capacitance is easier to measure. The capacitance for the cantilever shown in fig. 3.2 is given by

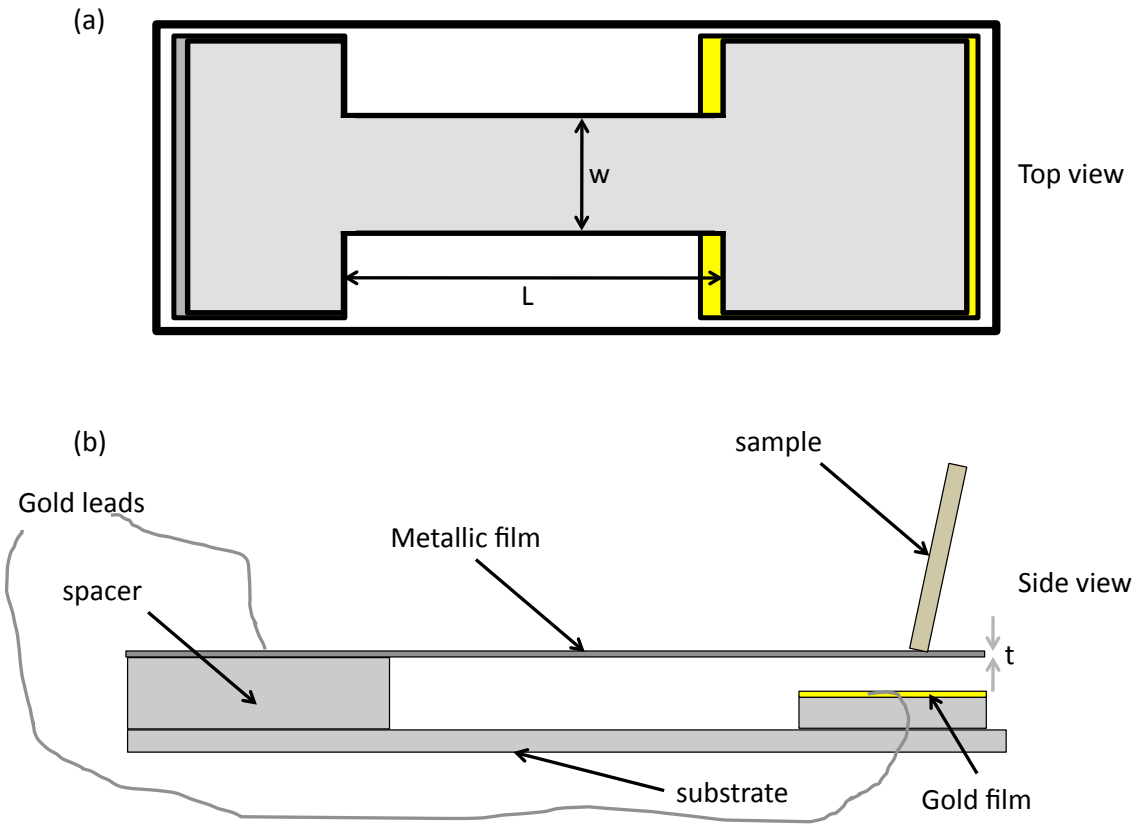

Figure 3.2: (a) Top view of handmade torque magnetometer. w and L are the width and the length of the cantilever arm respectively. (b) Side view of torque magnetometer with various components labeled. t is the thickness of the thin metallic cantilever. The torque is tracked by measuring the capacitance of the metallic cantilever and gold film. Gold leads from these two components lead to the digital capacitance bridge.

$$C_0 = \epsilon_0 \frac{A}{d} \tag{3.4}$$

where A is the area of the cantilever head and d is the gap between the metallic cantilever and gold film. When a torque is applied to the cantilever, the deflection can be seen in the change in the capacitance caused by a shrinking or growing gap. This is given by

$$C = \epsilon_0 \frac{A}{(d + \Delta d)} \tag{3.5}$$

where Δd is the change in the gap size caused by the magnetic torque on the cantilever. For a small Δd, this is approximately

$$\begin{aligned} C &= \epsilon_0 \frac{A}{d}(1 + \frac{\Delta d}{d}) \\ &= C_0(1 + \frac{\Delta d}{d}) \end{aligned} \tag{3.6}$$

Using Hooke's law, the torque is given by $\tau \propto \Delta\phi$. Where $\Delta\phi$ is the angular displacement of the cantilever, which is approximately equal to $\Delta d/L$. $\Delta C = C_0 \frac{\Delta d}{d} \sim C_0 \frac{L}{d} \Delta\phi$. Thus, for a small deflection of the cantilever, the magnetic torque is proportional to the change in capacitance.

$$\tau \propto \Delta C \tag{3.7}$$

If Δd is a large fraction of the gap, d, equation 3.6 is not valid. In this case, Δd can be expressed exactly as

$$\begin{aligned} \Delta\frac{1}{C} &= \frac{1}{C} - \frac{1}{C_0} \\ &= \frac{(d + \Delta d)}{\epsilon_0 A} - \frac{d}{\epsilon_0 A} \\ &= \frac{\Delta d}{\epsilon_0 A} \end{aligned} \tag{3.8}$$

Thus $\Delta d \propto \Delta\frac{1}{C}$. Since $\Delta d \propto \tau$, $\tau \propto \Delta\frac{1}{C}$. The absolute value of the torque is rarely of interest, and the physical information from quantum oscillations can be extracted directly from the change in capacitance. In most circumstances (especially in this study), the small angle approximation in equation 3.6 is sufficient. If the percent change of the gap size is even larger (larger than 20% - 30%), Hooke's law breaks down and the torque is no longer proportional to the angular deflection of the cantilever. In this case, a stiffer cantilever is needed as described below.

The digital capacitance bridge can measure a capacitance down to 10^{-6} pF. However, the noise floor is typically on the order of 10^{-4} pF to 10^{-5} pF. Using equation 3.6 given a typical $C_0 \sim 0.3$ pF - 1 pF, a 0.1% - 0.01% change in the gap can be detected. A smaller signal can be detected by increasing C_0 via shrinking the gap. However for a cantilever with too small a gap, the magnetic torque can cause the metallic film to touch the gold film, which will short the capacitor. So a small gap is advantageous for samples with a small signal and a larger gap is needed for samples with a large signal. It should also be noted that the weight of the sample can cause the cantilever to short if the gap is too small. So the

cantilever must be custom made to fit the need of the sample weight and signal strength.

The thin metallic film is cut brass or beryllium copper. Occasionally, a softer cantilever can be made from Kapton with a thin film of aluminum evaporated on the bottom for higher sensitivity. The sensitivity of the cantilever is determined by its spring constant, which is given by

$$k = \frac{Ewt^3}{4L^3} \tag{3.9}$$

where E is the Young's modulus of the metallic cantilever, w is the width of the cantilever arm, t is the thickness of the cantilever arm, and L is the length of the cantilever arm [163]. These geometric parameters of the cantilever are labeled in fig. 3.2. By varying E, w, t, and L, the cantilever can be made more sensitive to pick up small signals or more stiff to handle larger, heavier samples. A stiffer cantilever is also often used in high field measurements up to 45 T to prevent the cantilever from shorting.

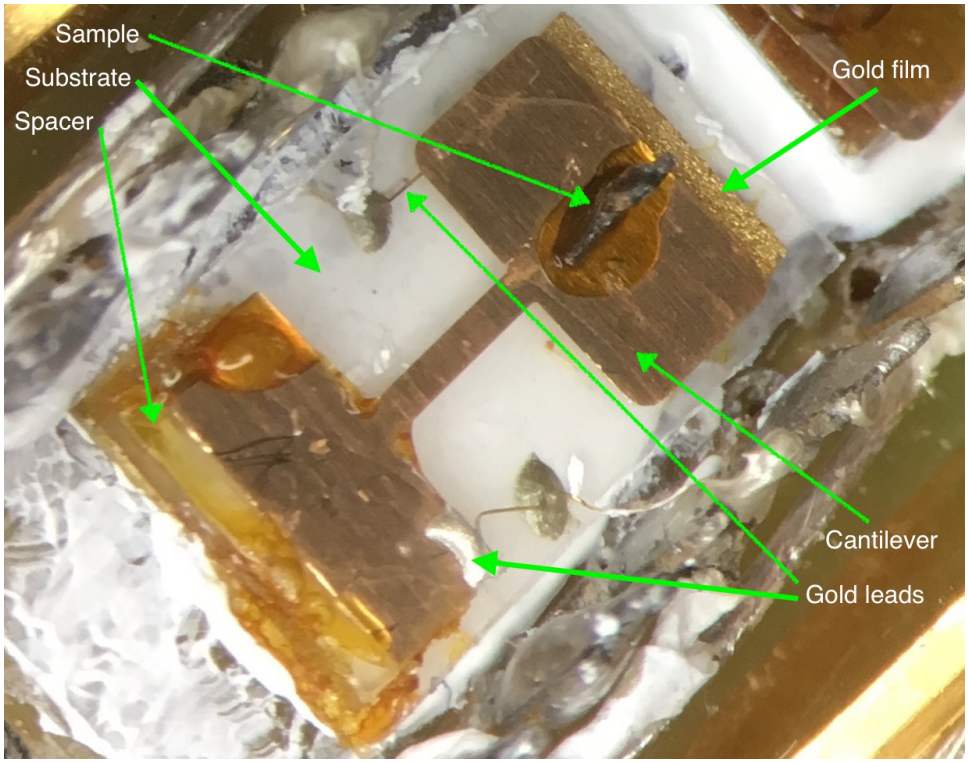

Figure 3.3: Photograph of handmade torque magnetometer under magnification. The sample mounted is $Nb_xBi_2Se_3$.

The typical cantilever thickness is either 25 μm, 75 μm, or 125 μm. For brass and beryllium copper which have a higher Young's modulus, 25 μm is most commonly used. For Kapton which has a much lower Young's modulus, 75 μm is standard. The length of

the cantilever arm is typically kept to ~ 3 mm, and the width, which is most often used to fine tune the cantilever's spring constant, is usually less than 1 mm. A photograph under magnification of one of these handmade cantilevers with $Nb_xBi_2Se_3$ mounted on it is shown in fig. 3.3.

3.1.2 The de Haas-van Alphen Effect

Though other experiments will be reported in brief, the focus of this thesis is the de Haas-van Alphen effect (dHvA) in doped Bi_2Se_3. Torque magnetometry as described in the previous section is sensitive to quantum oscillations in the magnetization of materials. Here I describe the dHvA effect and the information that can be extracted from it.

Quantum oscillations are used to resolve Fermi surface geometry and to discover electronic properties of topological materials. Oscillations in magnetization are called the dHvA effect and oscillations in magneto-transport are called the Shubnikov-de Haas effect (SdH). Both result from the quantization of the orbitals of charge carriers into Landau levels resulting in the oscillation of the density of states at the chemical potential.

An applied magnetic field will quantize the motion of electrons or other charge carriers in the plane normal to the applied field. These quantized orbitals are called Landau levels. For a free electron, solving the Schrödinger equation in a uniform magnetic field gives the following energy levels

$$E_\nu(k_H) = (\nu + \frac{1}{2})\hbar\omega_c + \frac{\hbar^2 k_H^2}{2m_0} \tag{3.10}$$

where ν is the quantized orbital of the electron, ω_c is the cyclotron frequency for a free electron, m_0 is the free electron mass, and k_H is the component of the electron momentum parallel to the external field, H. For a free electron, the orbitals quantized by ν are the Landau levels.

In general, for an electron or charge carrier in a solid, this quantization condition isn't as easily calculated. However, by utilizing the correspondence principle, the energy difference between two Landau levels should be $\hbar\omega_c$, where ω_c is the classical cyclotron frequency given by

$$\omega_c = \frac{eB}{m^*} \tag{3.11}$$

where m^* is the cyclotron effective mass, which can be derived from the semiclassical orbit of a carrier in a uniform magnetic field [22, 164] to be

$$m^*(E, k_z) = \frac{\hbar^2}{2\pi} \frac{\partial A(E, k_z)}{\partial E}. \tag{3.12}$$

In this equation, $A(E, k_z)$ is the k-space area inclosed by an orbital of energy E. For a free electron, $m^* = m_e$ and for a metal with an isotropic effective mass, m^* is the effective mass of the carriers. Though the following arguments are based on these equations derived from the correspondence principle, which should only be valid for large quantum numbers, it is found to be a good approximation in general [165].

The density of states from the Landau levels is a delta function at each Landau level since all other energies are forbidden. However, the carrier momentum parallel to the external magnetic field is not quantized. This contributes a one-dimensional density of states, which is proportional to $E^{-1/2}$, at each Landau level. Therefore, the density of states for a metal in an external magnetic field looks like figure 3.4 where the energy of the ν^{th} Landau level is given by $E_\nu = \hbar\omega_c(\nu + \frac{1}{2})$ as is the case for a free-electron.

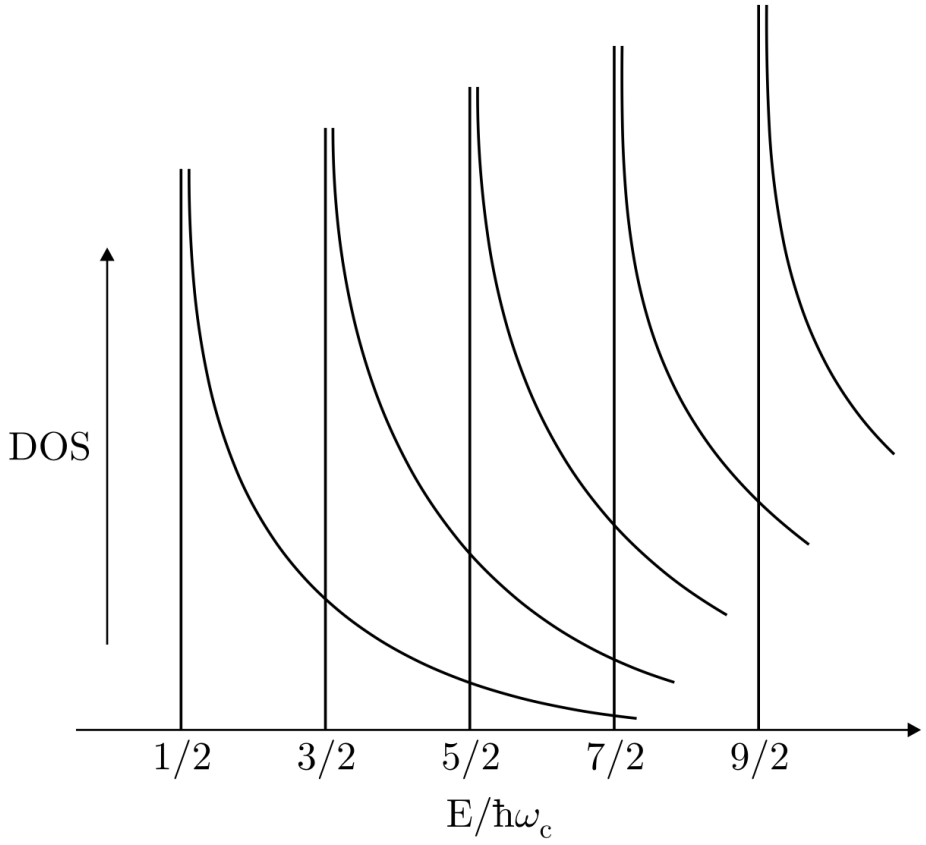

Figure 3.4: Density of states of a 3D metal in an applied magnetic field take from ref. [22]. The x-axis gives the energy of each Landau level where the energy of the ν^{th} Landau level is given by $E_\nu = \hbar\omega_c(\nu + \frac{1}{2})$.

Since $\omega_c \sim B$, the energy distance between the Landau levels increases as the magnetic field increases. Consequently, the peaks in the density of states (occurring at the Landau levels) will sweep across the chemical potential, μ, as the magnetic field increases. Thus the density of states at the chemical potential will oscillate as the chemical potential corresponds with the peaks and troughs in the density of states. At low temperatures, the chemical potential is roughly equal to the Fermi energy. Many physical phenomena depend on the density of states at the Fermi energy, so this oscillatory behavior can be measured in these physical properties such as resistance (SdH effect) or magnetization (dHvA effect).

Plotting the available energies in k-space will produce Landau tubes. Fig. 3.5 shows how an external field quantizes k-space into tubes of allowed states. Fig. 3.5(a) shows Landau tubes for a spherical Fermi surface and Fig. 3.5(b) for an ellipsoidal Fermi surface with H pointing in an arbitrary direction. In both panels, the dashed line shows the Fermi surface. Only states within this line are occupied at zero temperature.

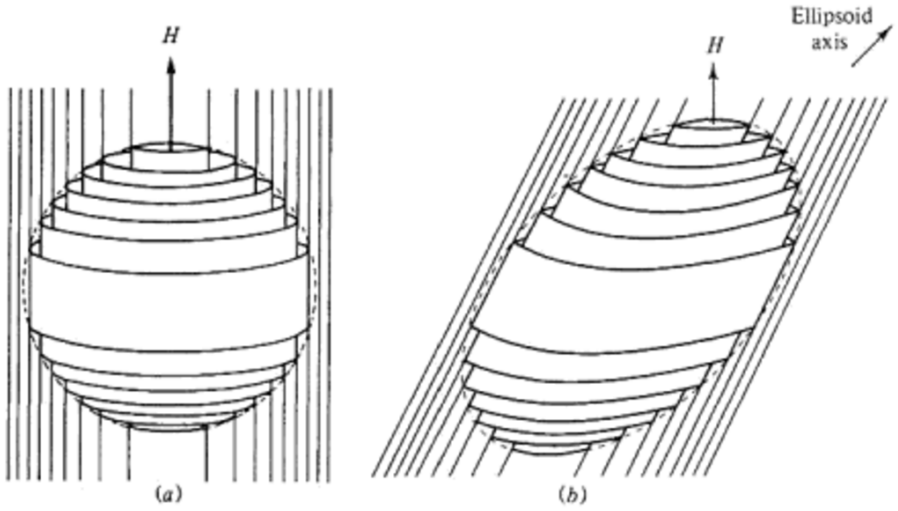

Figure 3.5: Landau tubes in k-space take from ref. [23] with (a) a spherical Fermi surface and (b) and ellipsoidal Fermi surface. The direction of the external field, H, is indicated.

Fig. 3.6 shows a Landau tube as it crosses a surface of constant energy, E. As the field, B, increases, the tube expands outward. The number of orbits between the constant energy surfaces E and $E+dE$ is maximized when an extremal cross-section of the constant energy surface, E, corresponds to the cross-section of the Landau tube perpendicular to B.

Thus, for the constant energy surface at $E = E_F$ ($\mu = E_F$ at zero temperature), the density of states at the Fermi level is maximized when the Landau tube crosses an extremal cross-section of the Fermi surface. To determine when this happens, first we must find the area of the cross-section of the Landau tube perpendicular to the magnetic field. This

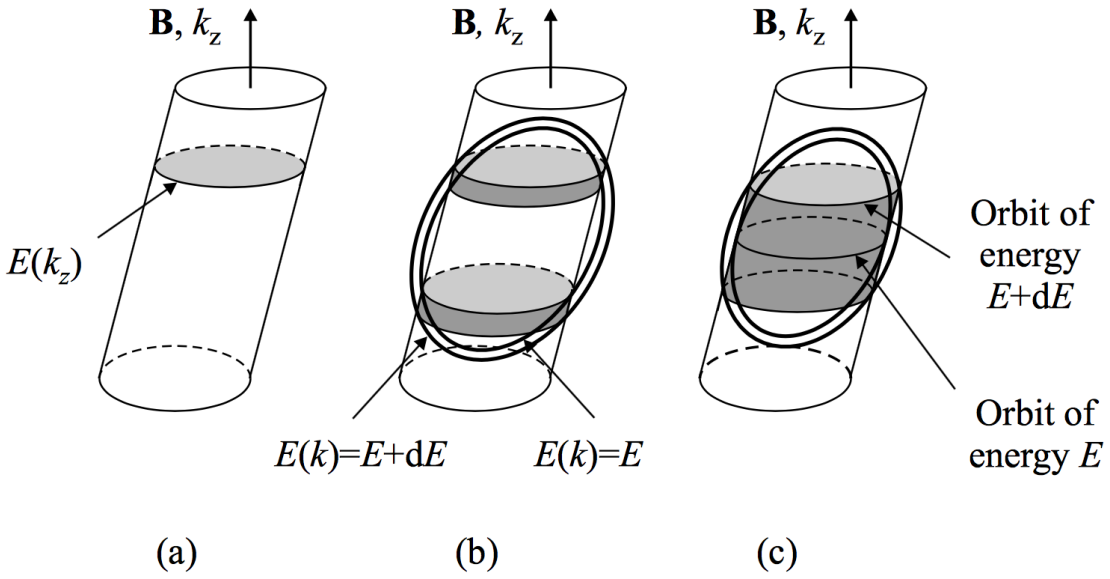

Figure 3.6: Landau tube crossing an constant energy surface in k-space, taken from ref. [22]. (a) Landau tube with magnetic field pointed in the z-direction. (b) Orbits (i.e. states) on the Landau tube lying between E and $E + dE$. (c) When the Landau tube's cross-section is equal to an extremal cross-section of the constant energy surface, E, the number of states between E and $E + dE$ is maximized.

quantity can be determined with the following argument. As stated above, the energy between two successive energy levels is given by

$$E(\nu + 1) - E(\nu) = \Delta E = \hbar\omega_c = \frac{\hbar eB}{m^*}. \tag{3.13}$$

Substituting m^* from equation 3.12 and rearranging gives

$$\Delta E \frac{\partial A(E, k_z)}{\partial E} = \frac{2\pi eB}{\hbar}. \tag{3.14}$$

Near E_F, the energy difference between adjacent levels is much smaller than E_F. Thus

$$\frac{\partial A(E, k_z)}{\partial E} \sim \frac{A(E(\nu + 1), k_z) - A(E(\nu), k_z)}{E(\nu + 1) - E(\nu)} = \frac{\Delta A(E, k_z)}{\Delta E}. \tag{3.15}$$

Substituting 3.15 into 3.14 gives the difference in the k-space cross-sectional area of two successive Landau levels:

$$\Delta A = \frac{2\pi eB}{\hbar}. \tag{3.16}$$

Thus, the k-space cross-sectional area of the ν^{th} Landau tube is $\nu\Delta A$ plus some con-

stant, which can be expressed as

$$A = (\nu + \lambda)\Delta A = (\nu + \lambda)\frac{2\pi eB}{\hbar} \tag{3.17}$$

where λ is a constant. As argued above, the density of states at the Fermi level is maximized when this k-space area is equal to an extrema of the Fermi surface. Thus, the density of states at the Fermi level will oscillate with a period of

$$\Delta(\frac{1}{B}) = \frac{2\pi e}{\hbar A_{ext}} \tag{3.18}$$

where A_{ext} is an extremal Fermi surface cross-section. Thus it is clear that quantum oscillations are periodic in inverse magnetic field. This is more often expressed by the Onsager relation

$$F_s = \frac{\hbar}{2\pi e}A_{ext} \tag{3.19}$$

where F_s is the frequency of the quantum oscillation measured in units of Telsa. By measuring this frequency as a function of angle, the Fermi surface of a metal can be constructed. There are many resources with further details on the origins of quantum oscillations in metals, this brief discussion is based on arguments from ref. [22, 23, 164].

So far, I've focuses on how the Fermiology of a material can be extracted from the quantum oscillation frequency. However, the quantum oscillation amplitude also reveals a lot of useful properties of a metal such as the effective mass, Fermi velocity, and mean free path.

In metals, the first harmonic of the oscillating magnetic torque is well described by the Lifshitz-Kosevich formula [23]. The amplitude of the quantum oscillation is proportional to the thermal damping factor R_T and the Dingle damping factor R_D, as follows,

$$R_T = \frac{\alpha T m^*}{B\sinh(\alpha T m^*/B)}, \tag{3.20}$$

$$R_D = \exp(\alpha T m^*/B), \tag{3.21}$$

where m^* is the effective mass, $T_D = \hbar/2\pi k_B\tau_s$ is the Dingle temperature, τ_s is the scattering time, and $\alpha = 2\pi^2 k_B m_e/e\hbar \sim 14.69$ T/K.

From eq. 3.20, it is seen that by fitting the temperature dependence of the quantum oscillation amplitude, the effective mass of the carriers can be extracted. The amplitude damping occurs from the broadening of the Fermi-Dirac distribution edge by k_BT. Due to this thermal broadening, at finite T, the density of states moves across a more gradual

transition at the chemical potential. If $\hbar\omega_c$ is smaller than k_BT, successive peaks in the density of states will pass through the transition around the chemical potential together and quantum oscillations can't be resolved. This is why quantum oscillation experiments must be done at low temperatures. The temperature required to observe quantum oscillations depends on the effective mass in eq. 3.20 - heavier masses require lower temperatures due to larger amplitude damping.

The Dingle damping factor, eq. 3.21, is due to scattering in the metal. Therefore, the Dingle temperature, T_D, is a measure of the disorder in the system. Given the effective mass extracted by the thermal damping factor, the scattering time can be extracted by fitting the field dependence of the quantum oscillation amplitude to eq. 3.20.

Dingle damping occurs because scattering causes the Landau levels to broaden. Thus the density of states from the orbital motion of the carriers is no longer a delta function, but are broadened by $\sim \hbar/\tau_s$ [22]. If the broadening is too great, successive Landau levels will smear into each other and a higher magnetic field (thus a higher $\hbar\omega_c$) is needed to resolve the Landau levels. As is the case with the thermal damping, the broadening of the density of states peaks due to disorder will dampen the amplitude of the quantum oscillations at low B.

The Fermi velocity, v_F, can be determined by

$$v_F = \frac{\hbar k_F}{m^* m_e} \tag{3.22}$$

where m^* is determined from the thermal damping of the quantum oscillations and k_F is determined from the Fermi surface cross-section - for example, for a spherical Fermi surface, $k_F = (A_{ext}/\pi)^{1/2}$ where A_{ext} is calculated from eq. 3.19. The Fermi velocity is the slope of the band structure at the chemical potential. Lastly, the mean free path is given by

$$l = v_F \tau_s. \tag{3.23}$$

3.2 Cryostats and Magnets

As discussed in the previous section, the broadening of the Landau levels due to disorder and the smearing of the Fermi level due to thermal excitation dampen the amplitude of quantum oscillations. Thus low temperatures and high magnetic fields are needed to resolve Landau level quantization and quantum oscillations. In this section, I will briefly discuss the experimental apparatuses used to achieve low temperatures and high magnetic fields.

The data in this dissertation was largely acquired at the National High Magnetic Field Laboratory in Tallahassee, FL. But some measurements were performed at the University of Michigan in our Janis Variable Temperature cryostat with a 12 T magnet.

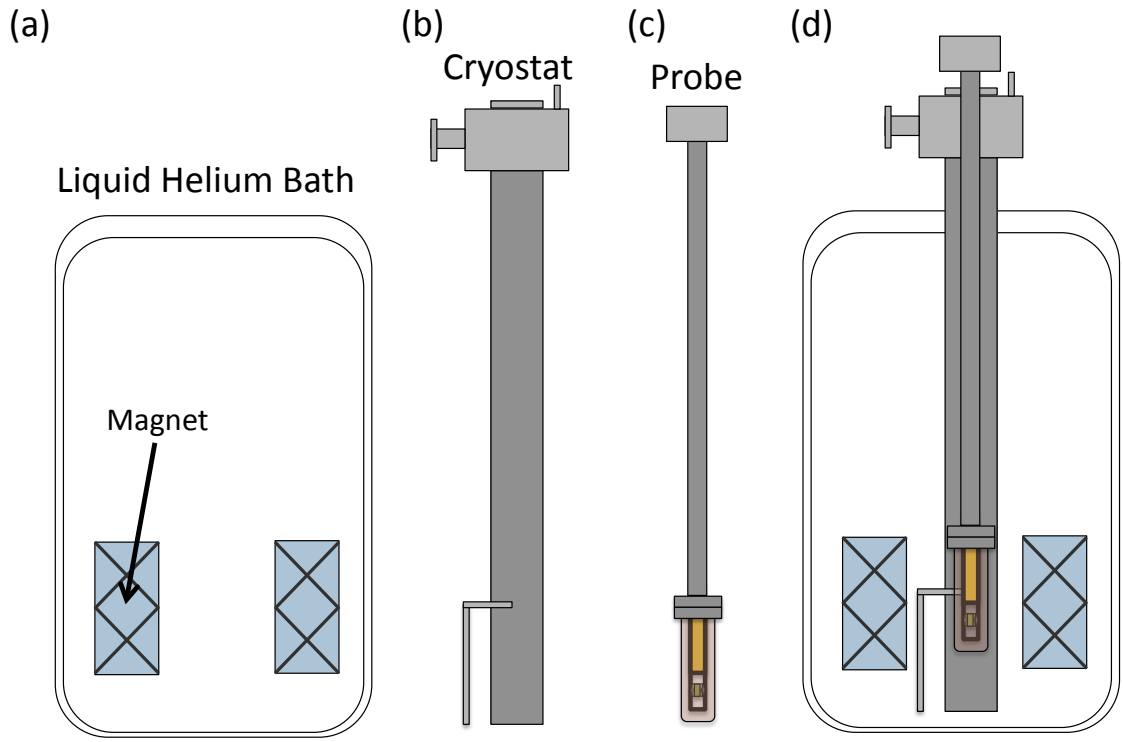

Figure 3.7: The three parts of the cryostat/magnet apparatus. (a) The helium bath and magnet. For superconducting magnets, the magnet is submerged in the liquid helium-4 bath, whereas resistive magnets are not submerged in liquid. (b) The cryostat gets placed inside the magnet bore and is submerged in the helium bath. There are three kinds of cryostats used in this work - helium-4, helium-3, and dilution refrigerator. (c) The sample is mounted on the probe, which is placed within the cryostat. (d) Schematic of the assembled apparatus.

The basic principle behind the cooling and magnet apparatus is fairly simple and comes in three parts. Fig. 3.7 shows these three parts. First is the magnet shown in panel (a). There are three kinds of magnets used in this study - superconducting magnet, resistive magnet, and hybrid magnet. These magnets will be discussed in greater detail in section 3.2.2. Only the superconducting magnet is submerged in liquid helium as shown in fig. 3.7(a). However, a liquid helium bath is still utilized in every apparatus in this study.

The second part of the apparatus is the cryostat shown in fig. 3.7(b). The cryostat allows the sample temperature to be regulated, and for low temperatures to be achieved. There are three kinds of cryostats used in this study: a helium-4 cryostat (base temperature

1.5 K), helium-3 cryostat (base temperature of 300 mK), and dilution refrigerator (base temperature of 10 mK). A detailed discussion of the cryostats, their operation and working principles, is given in section 3.2.1.

The third part of the apparatus is the probe shown in fig. 3.7(c). The sample is mounted on the probe, which has a rotation stage. Though different probes are used in this study, they all have the same basic characteristics - a rotation stage, coax cables, twisted pairs, and feedthroughs. There are some important differences between probes used in different cryostats, which will be discussed in section 3.2.3. Fig. 3.7(d) shows a cross-section of the assembled magnet-cryostat apparatus.

3.2.1 Cryogenics

Here I will discuss the three cryogenic apparatuses used in this study. Each of these have their own advantages and setbacks. This is meant to serve as an overview of how these systems work and how they are operated in general terms.

The first cryostat is the Variable Temperature Insert for a Janis cryogenic system, which is a helium-4 cryostat. Though similar cryostats can be used at the facilities at the National High Magnetic Field Lab, the only helium-4 cryostats used in this study were the in-house Janis cryogenic system with a 12 T superconducting magnet at the University of Michigan and the cryostats in the Quantum Design Physical Properties Measurement System (PPMS) and Magnetic Properties Measurement System (MPMS). These systems were mostly used for screening samples and taking preliminary data.

The principle behind the helium-4 cryostat is fairly simple in comparison to the other types of cryostats. Fig. 3.8 shows the main elements of a helium-4 cryostat. This apparatus is placed into a liquid helium bath as shown in fig. 3.7(d). Liquid helium-4 at atmospheric pressure is 4.2 K. By submerging the cryostat into the liquid helium bath, it is cooled to this temperature.

The space within the helium-4 cryostat is kept under vacuum. The vacuum flange shown in fig. 3.8 is connected to a standard roughing pump. Near the bottom of the cryostat, a pickup line can pull liquid helium out of the bath and deposit it in the low pressure environment within the cryostat. The flow of the helium can be controlled by a needle valve at the top of the cryostat. Liquid helium under low pressure within the cryostat can bring the temperature down to 1.4 K - 1.7 K depending on the conditions and thermal isolation.

The operation of the needle value is a delicate matter. If the flow is too high, the sample space will be flooded with liquid helium and the low pressure required to reach

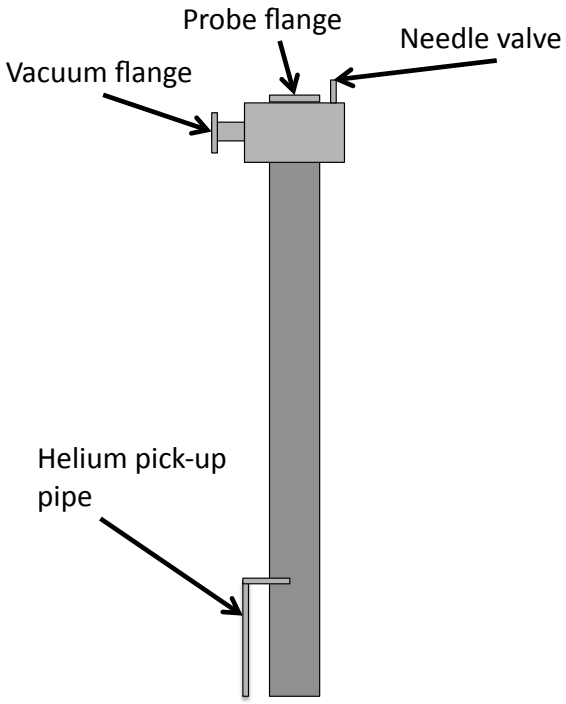

Figure 3.8: General schematic of a helium-4 cryostat.

base temperature will not be able to be maintained. On the other hand, if the needle valve is not open enough, the helium in the cryostat will get pumped out and there won't be enough cooling power to maintain base temperature. In the Janis system at the University of Michigan, the needle valve must be kept open wider (0.5 - 0.75 turns) while the cryostat is cooling down and the heat load is high, but closed to about a quarter turn to achieve base temperature.

This cryostat can be regulated even above room temperature by applying heat through a resistor within the cryostat. This is why it is called a Variable Temperature Insert. The temperature is measured by Cernox thermometers near the bottom of the cryostat and in the probe. Temperature is controlled via PID using a LakeShore 340 temperature controller.

On the top of the cryostat is the probe flange. The sample and measurement apparatus (i.e. torque magnetometer) is mounted to a probe and loaded through this flange. The top of the probe is sealed to this flange via a standard rubber o-ring.

The procedure for loading a probe depends on the specifics of the cryostat. The cryostats used at the National High Magnetic Field Lab use a load-lock technique to load the probe. Since only helium-3 cryostats and dilution refrigeration was used at the National High Magnetic Field Lab, discussion of this technique will be saved for those cryostats.

For the Variable Temperature Insert at the University of Michigan, the probe loading

procedure is straightforward. Before opening the probe flange, a pressurized helium cylinder (with a pressure regulator) is attached to the vacuum flange. A positive pressure is applied to the cryostat before the probe flange is opened. After, the probe flange is opened and the probe is lowered into the cryostat. The positive pressure prevents air from contaminating the cryostat during loading of the probe. Once the probe is loaded, it is sealed to the probe flange. Once the cryostat is sealed, the cryostat is purged and flooded with helium gas several times to clear out any contaminates that may have entered during the loading of the probe.

The second type of cryostat is a helium-3 cryostat. This utilizes an isotope of helium, helium-3, rather than the naturally occurring helium-4. Helium-3 is rather expensive, so great care is taken to prevent any loss of helium-3 to the air or the contamination of the helium-3 by the air. The main advantage of the helium-3 cryostat is that the base temperature is 0.3 K. This is the simplest method to do experimental physics below 1 K.

Fig. 3.9 shows a schematic of a helium-3 cryostat. The three main elements of the helium-3 cryostat are labeled: the sorb, 1 K pot, and helium-3 pot.

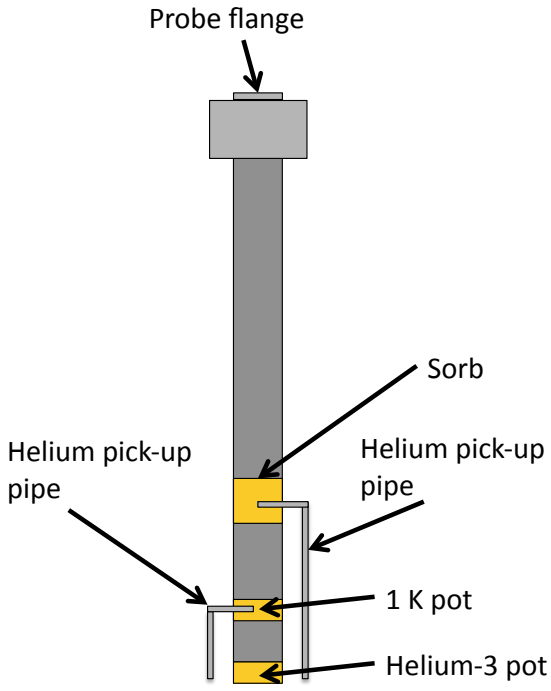

Figure 3.9: General schematic of a Helium-3 Cryostat.

The sorb contains charcoal, which is used to absorb the helium-3 gas. The temperature of the charcoal is controlled by a resistive heater and a helium pick-up line. As in the helium-4 cryostat, the helium pick-up line is directly submerged in a liquid helium-4 bath.

Unlike the Variable Temperature Cryostat, this pick-up line does not deposit liquid helium-4 into the main chamber of the cryostat. Rather, it is kept in an isolated chamber that is thermally linked to the charcoal to prevent mixing of the helium-3 and helium-4 isotopes.

Below the sorb is the 1 K pot. This element of the helium-3 cryostat functions much like the helium-4 cryostat. As before, this chamber is kept under low pressure by continually pumping via a roughing pump not shown in fig. 3.9. A pick-up pipe to the liquid helium-4 bath deposits liquid helium-4 into the 1 K pot. A needle valve on top of the cryostat is used to control the flow of the helium-4 to keep the 1 K pot near base temperature. The 1 K pot serves to cool a region of the main cryostat chamber below the boiling point of helium-3 (3.2 K), so that helium-3 can condense. The condensed liquid helium-3 then falls down to the helium-3 pot where a pool of liquid helium-3 accumulates.

To condense liquid helium-3, first the temperature of the sorb is raised to 45 K. This releases all the gaseous helium-3 trapped in the charcoal. As the chamber fills with gaseous helium-3, some starts to condense on the 1 K pot and drips down to the helium-3 pot until a pool of liquid helium-3 accumulates in the helium-3 pot. Spending more time condensing the helium-3 will increase the holding time of the base temperature with eventual diminishing returns. The holding time that can be achieved before recondensing depends on the particular design of the cryostat and the heat load applied by the experiment. For the helium-3 cryostats at the National High Magnetic Field Lab, one hour of condensing will allow base temperature to be held for a couple days unless a significant heat load is applied by the experiment.

After condensation, the sorb heater is turned off and the sorb is cooled back to 4.2 K by the thermal link to the liquid helium-4. As the sorb is cooled, gaseous helium-3 gets reabsorbed by the charcoal. This reduces the pressure on the pool of liquid helium-3 in the helium-3 pot. As the pressure is reduced by the charcoal pump, the temperature of the helium-3 pot falls. By this method, a base temperature of 0.3 K can be obtained.

The sorb is used to regulate the temperature between 0.3 K and $\sim$2 K. By applying heat to the sorb, warm gaseous helium-3 is released and warms up the helium-3 pot. There is a one-to-one correspondence between the sorb temperature and the helium-3 pot temperature in this temperature range after condensation of the liquid helium-3. To regulate the temperature above 2 K, a resistive heater on the helium-3 pot and PID can be used just like in the helium-4 cryostat. Going above 2 K will boil any liquid helium-3 in the helium-3 pot and a recondensation is needed to recover base temperature. Unlike the helium-4 cryostat, the helium-3 cryostat cannot be stabilized above about 40 K - 70 K depending on the cryostat. So for high temperature measurement, the helium-4 cyostat is required.

Loading a probe into a chamber with gaseous helium-3 is tricky because any exposure

to air could cause contamination to the helium-3 or a very expensive loss of helium-3 gas to the air. For this reason, many commercial helium-3 cryostats have the helium-3 in a closed system that is never opened during operation. These systems, rather than mounting the experiment on a probe, have the experiment mounted on a copper cold finger that is thermally linked to the helium-3 pot. This is called a "dry system" because the sample and experiment sit in vacuum and is cooled by the thermal link to the helium-3 pot.

Dry systems are generally bad for torque magnetometry since the sample sits on the end of a thin cantilever. The small cross-section of the cantilever makes it difficult to cool down the sample in a dry cryostat. Though it is not impossible to perform torque magnetometry in a dry system, it takes a long time for the sample to thermalize, and unless there is an independent thermometer on the sample, the exact temperature of the sample is suspect. This is even a bigger problem in dilution refrigerators. Dry systems are ideal for transport measurements where the sample can be directly thermalized by contact with the cold finger. In thermal transport measurements, a dry system is required because if the sample was sitting in cold gas, it would be impossible to establish a thermal gradient across the sample.

The helium-3 cryostats at the National High Magnetic Field Lab are wet systems - meaning that the experiment is put directly in cold helium-3 gas or submerged in liquid helium-3. This is perfect for torque magnetometry since the whole experiment including the sample can be quickly thermalized. However, great care needs to be taken while loading the probe into a wet helium-3 cryostat to prevent loss or contamination of helium-3.

To prevent exposure of helium-3 to air, a lock-lock chamber is used to load a probe into a wet helium-3 cryostat. An expanded view of the probe flange from fig. 3.9 is shown in fig. 3.10 where the o-ring seal is the top of the helium-3 cryostat.

With the gate valve in fig. 3.10 closed, the load-lock chamber and probe can be mounted and attached at the o-ring seal. Then, the sliding seal valve and the load-lock valve are opened evacuating the load-lock chamber. Once the load-lock chamber is fully evacuated, the load-lock valve is closed and the gate valve is opened. At this point the probe can be lowered into the helium-3 cryostat. The sliding seal is kept under vacuum during loading to prevent any contamination to the helium-3 while the probe is lowered. The sample stage indicated in fig. 3.10 is at the bottom of the probe.

The gate valve separates the helium-3 chamber from the loading and unloading mechanism. For this reason, it is paramount that the load-lock chamber is fully evacuated before opening the gate valve to prevent contamination of the helium-3. Furthermore, the load-lock valve must be closed before opening the gate valve or else helium-3 will be pumped out of the cryostat into the air.

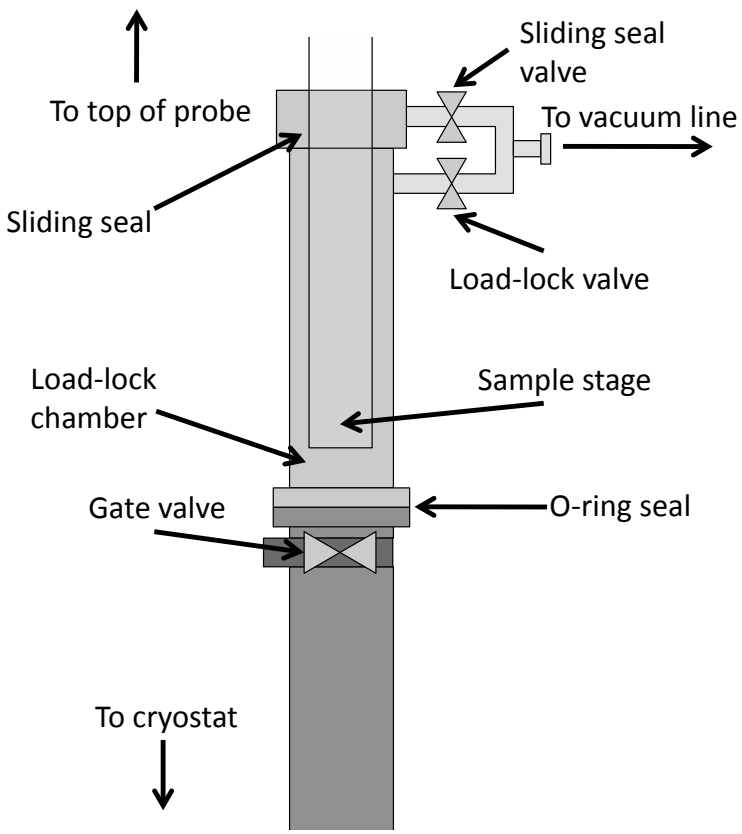

Figure 3.10: Schematic of the load-lock mechanism for loading a probe into a wet helium-3 cryostat or dilution refrigerator.

During loading and unloading, the sorb temperature is raised to 20 K to allow exchange gas to cool down the probe. During unloading after the probe has been fully raised back into the load-lock chamber, the sorb must fall below 5 K before closing the gate valve to ensure all the helium-3 has returned to the sorb. Failure to do this would result in a loss of helium-3 trapped in the load-lock chamber after it is detached from the cryostat.

The dilution refrigerator is the most complex of the three apparatuses. However, it is the only continuous method to reach temperatures below the helium-3 cryostat, and can maintain temperatures down to 10 mK. Fig. 3.11 is a block diagram of the main elements of the dilution refrigerator.

In the dilution refrigerator, helium-3 is recycled in a closed loop. After being pre-cooled to liquid helium-4 temperature (4.2 K), it passes into the helium-3 cooling line. The helium-3 cooling line is thermally linked at various stages. The first, the 1 K pot, is essentially a helium-4 refrigerator described above for the helium-3 cryostat and the Variable Temperature Insert. Here the helium-3 is cooled to 1 K and begins to condense.

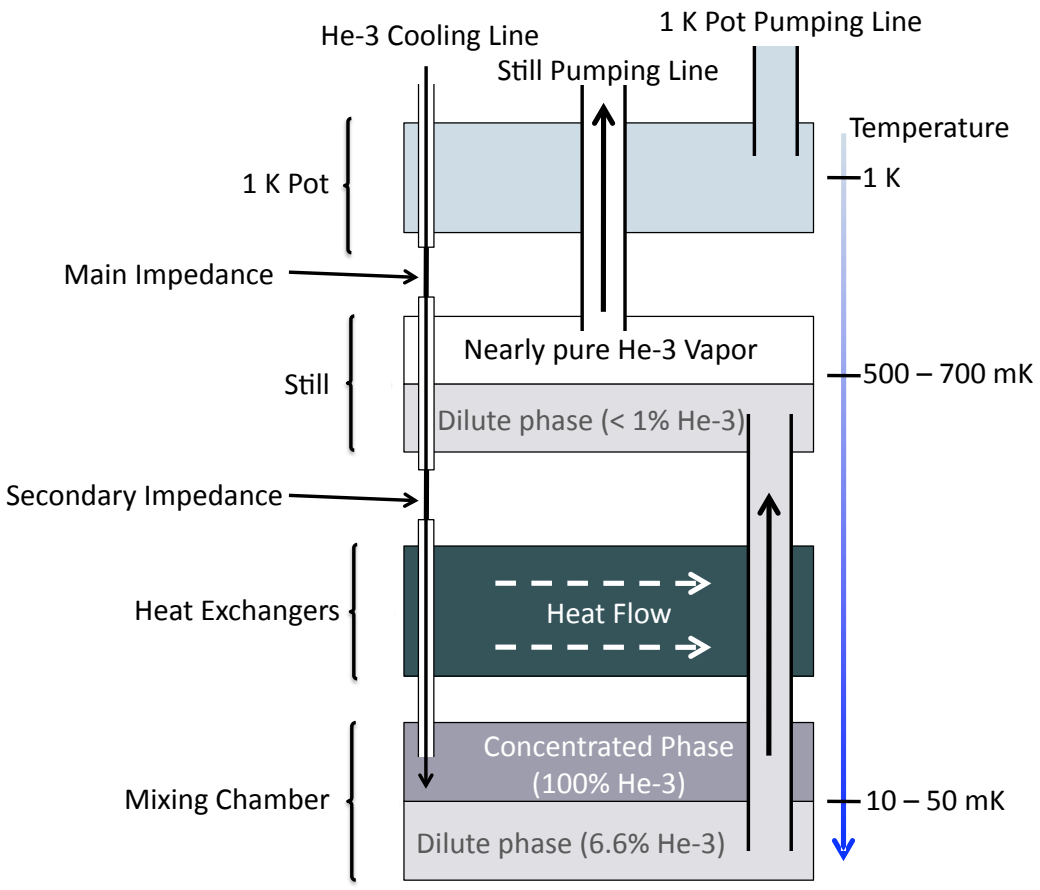

Figure 3.11: Block diagram of the dilution refrigerator. Helium-3 is initially cooled through the helium-3 cooling line. It finally enters the mixing chamber where the dilution of the helium-3 into superfluid helium-4 provides the cooling power of the refrigerator. The helium 3 is then separated from the helium-4 in the still where it is recycled back into the helium-3 cooling line.

Next it is forced through the main impedance, a region in the cooling line that resists the flow of helium-3 thus raising the pressure above the vapor pressure for helium-3 at 1 K guaranteeing that all the helium-3 is liquified.

After the main impedance, the helium-3 is further cooled to 500 mK - 700 mK from a thermal link to the still, which will be described later in the helium-3 cycle. Next it passes through the secondary impedance. This keeps the pressure high enough to prevent the helium-3 from revaporizing. The helium is then further cooled in a series of heat exchangers that thermally link the incoming helium-3 with the outgoing helium-3/helium-4 mixture later in the cycle.

At the bottom and coldest section of the dilusion refrigerator, the helium-3 enters the mixing chamber. In the mixing chamber, there are two helium phases separated by a phase

boundary. The lighter, concentrated phase is pure helium-3. Underneath is the heavier dilute phase consisting of superfluid helium-4 with a 6.6% helium-3 concentration mixed in.

Fig. 3.12 is a phase diagram of helium-3/helium-4 mixture. Below 100 mK, the 100% helium-3 rich phase and the 6.6% helium-3, 93.4% superfluid helium-4 mixed phase are separated by a phase gap, which produces the sharp phase boundary in the mixing chamber.

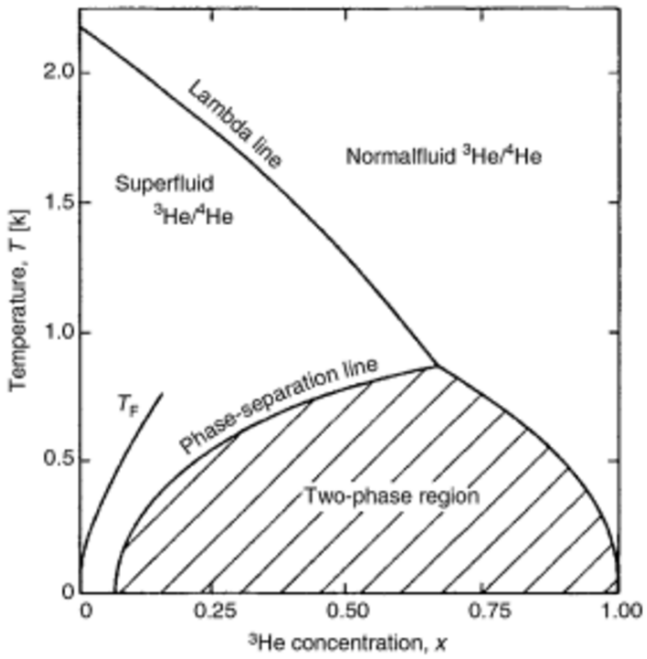

Figure 3.12: Phase diagram of helium-3/helium-4 mixture taken from ref. [24].

The enthalpy of mixing as the helium-3 dilutes into the dilute phase region of the mixing chamber provides the cooling power of the dilution refrigerator. This method can produce a base temperature of $\sim$10 mK depending on the heat load and thermal isolation of the mixing chamber.

The dilute phase is then pumped through the heat exchangers to precool the helium-3 in the cooling line. It is then deposited into the still. In the still, the helium-3 is removed from the dilute phase since the vapor pressure of helium-3 is lower than helium-4 at 700 mK. The gaseous helium-3 is then pumped out of the still and recycled back to through the helium-3 cycle.

The base temperature of a dilusion refrigerator is very sensitive to the thermal isolation. Heat shielding and vacuum layers are often used to prevent any excess heat load from reaching the mixing chamber. References [24, 166] provide more detail about the principles behind dilusion refrigeration. In the wet dilusion refrigerators at the National High

Magnetic Field Lab, the probe is deposited directly into the mixing chamber utilizing the load lock technique described for a helium-3 cryostat. However, most commercial dilution refrigerators are dry systems where the sample is cooled on a cold finger that is thermally linked to the mixing chamber.

Cernox thermometers are useful from 0.1 K up to room temperature, but are most sensitive above 1 K. However, they cannot be used to measure temperature at dilution refrigerator temperatures. Therefore, RuOx thermometers are used which are sensitive down to 10 mK. Since RuOx thermometers aren't very accurate above 1 K, the mixing chamber and probe usually have both a RuOx and Cernox thermometer, so that the temperature can be tracked while the system is cooling down. In addition, Cernox and sometimes RuOx thermometers also track the temperature on the 1 K pot and still. The probe and still both have resistive heaters with a PID to regulate temperature. All the thermometry is controlled by Lakeshore temperature controllers. Models 336, 340, and 350 can be used.

3.2.2 Magnets

There are three classes of magnets used in this thesis - superconducting magnets, resistive magnets, and a hybrid magnet. The superconducting magnets are all very similar in principle. They are made by winding superconducting Nb_3Sn or NbTi coils into a solenoid. The superconducting magnet is placed directly into the helium-4 bath so that it can be cooled below its critical temperature. A power supply is then used to place a voltage across the superconducting coil producing a magnetic field.

The maximum magnetic field obtainable by a superconducting magnet is limited in theory by the upper critical field of the superconducting material where the coil ceases to superconduct. However, practically it is limited by the critical current density of the superconducting wire. Currently, no superconducting magnet can support a magnetic field above about 27 T due to the limiting factor of the critical current. But the National High Magnetic Field Lab is in process of building a 32 T superconducting magnet.

One advantage of superconducting magnets is that they can be run in persistent mode where the supercurrent continually flows through the magnet without any applied voltage. This allows for a high magnetic field to continually be applied without expensive power consumption. In normal operation, a small segment of the superconducting magnet is heated above T_c to allow a voltage to be applied. The persistence heater provides the heat necessary to raise part of the magnet above T_c. Typically the persistence heater stays on during the whole operation of the magnet. However, to put the magnet in persistent mode, the persistence heater is turned off allowing for a continual flow of supercurrent. With the

heater off, the power supply can also be turned off without changing the magnetic field.

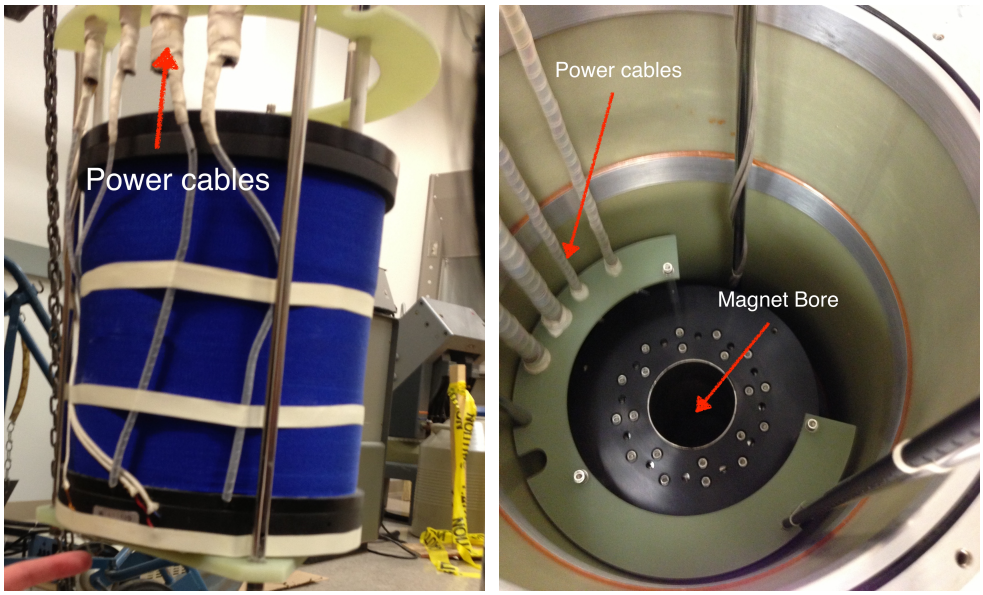

Figure 3.13: Picture of the 12 T superconducting magnet in the Janis cryostat. (Left) Side view of superconducting magnet. Cables to the power supply are marked. (Right) Top view of superconducting magnet as it is lowered into the empty helium bath. The magnet bore which fits the Variable Temperature Insert and probe is labeled.

The magnetic field in a superconducting magnet must be ramped slowly. At the National High Magnetic Field Lab, the maximum sweep rate is 0.3 T/min. At the University of Michigan it is even slower. A fast sweep rate can cause joule heating to occur in the magnet. If the heating is too great, a small piece of the magnet becomes resistive and much more heat creates a cascading effect pushing the whole magnet into the normal state. This is called a quench and it can result in damage to magnet as well as a rapid boiling of the liquid helium bath.

Five superconducting magnets were used in this study. For heat capacity and transport measurements, a quantum design PPMS with a 14 T superconducting magnet was used. To measure the superconducting volume fraction, a SQUID magnetometer in a quantum design MPMS with a 5 T superconducting magnet was employed. For torque magnetometry and transport measurements, a 12 T magnet with a Janis Variable Temperature Insert was used as well as the millikelvin lab at the National High Magnetic Field Lab which has two 18 T superconducting magnets. The first, SCM1, has a wet dilution refrigerator and the second, SCM2, has a helium-3 cryostat.

Fig. 3.13 shows a picture of the 12 T superconducting magnet from the Janis system. There are four power cables. Two are for the power supply of the main solenoid, and two are for the magnet gradient that was not used in this study. The right panel shows the

magnet from above as it is lowered into the empty helium bath. The magnet bore fits the Variable Temperature Insert and probe. The max field occurs in the center of the bore.

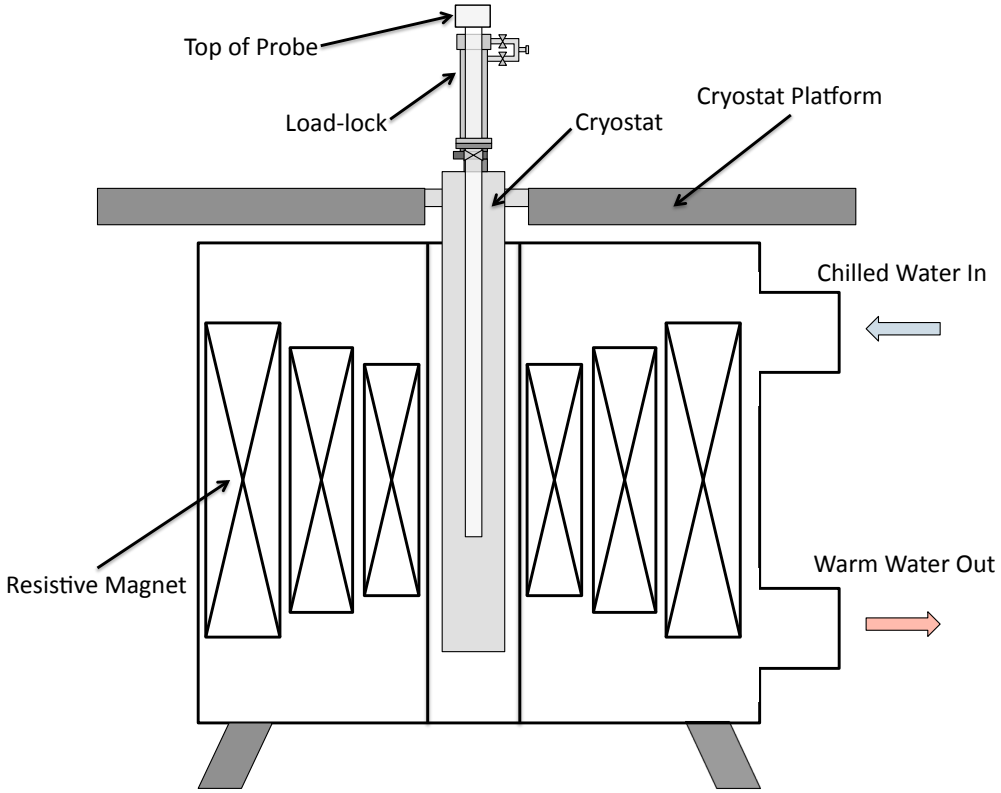

Figure 3.14: Schematic of a resistive magnet from the National High Magnetic Field Lab with probe fully loaded.

To achieve higher magnetic fields, a resistive magnet is needed. The National High Magnetic Field Lab has numerous resistive magnets consisting of stacks of metal sheets. A large current is run through the sheets producing a magnetic field as high as 35 T. In this study, two resistive magnets were used - the 31 T magnet in cell 9 and the 35 T magnet is cell 12 of the National High Magnetic Field Lab. Fig. 3.14 shows a schematic of a resistive magnet from cell 9 or 12 with a probe fully loaded. Note that the bottom of the probe sits at the field center. The load-lock from fig. 3.10 sits on top of the cryostat.

To prevent the magnet from melting due to resistive heating, chilled water is constantly run through holes in the metal sheets at 15,000 liters/min. The water is de-ionized and must maintain a high level purity because conductive impurities can cause neighboring metal sheets of the magnet to short. The path of the cooling water is indicated in fig. 3.14.

Other than a higher peak field, the magnetic field sweep rate is much faster than in a

superconducting magnet - up to 7 T/min. However, it is expensive to sweep the resistive magnets slowly, which would provide more data per Tesla, because of the enormous power consumed by the magnet. In practice, the magnet sweep rate is typically kept between 2-3 T/min.

The strong electric currents and flow of the cooling water creates substantial mechanical noise in resistive magnets. To combat this effect, the cryostat is mechanically isolated from the magnet by hanging it from a concrete platform above the magnet that is mechanically isolated from the magnet itself. This is depicted in fig. 3.14.

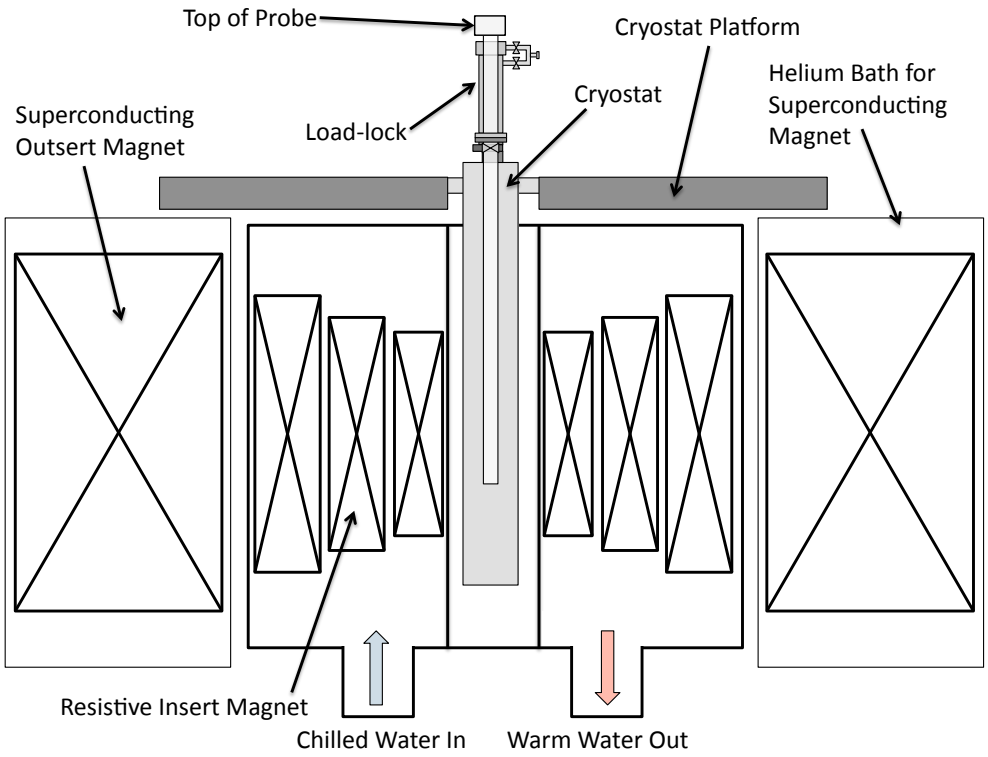

Figure 3.15: Schematic of the hybrid magnet at the National High Magnetic Field Lab with probe fully loaded.

Lastly, the 45 T hybrid magnet at the National High Magnetic Field lab was used. This is the largest DC magnet in the world. Its high field is achieved by putting a 33.5 T resistive magnet inside a large bore 11.5 T superconducting magnet. In normal operation, the superconducting outsert is ramped up to full field and placed in persistent mode. The magnetic field is then swept via the resistive insert from a combined field of 11.5 T (insert off) to 45 T (insert at full field). Consequently, a fully field trace from 0 T to 45 T can

only be taken at the beginning of the day during the outsert up ramp and the end of the day during the outsert ramp down.

Fig. 3.15 shows a schematic of the hybrid magnet with a probe fully loaded. As with the normal resistive magnet, the cryostat hangs from a platform to create mechanical isolation from the magnet. The superconducting outsert magnet is submerged in a liquid helium bath to keep it in the superconducting state. Unlike other superconducting magnets, the helium bath is pumped liquid helium kept at 1.8 K. Unlike the solely resistive magnet, the path of the chilled water goes through the bottom of the resistive insert magnet rather than the top/bottom on the side.

Figure 3.16: Photograph taken from the hybrid platform at the National High Magnetic Field Lab before the probe is loaded into the hybrid magnet. The sample stage at the bottom of the probe sits just above the gate valve. When the probe is loaded, the top of the probe will rest at the top of the load-lock chamber and the sample stage will be in the field center.

Fig. 3.16 is a picture taken from the top of the hybrid platform (labeled cryostat platform in fig. 3.15) before the probe is inserted. The top of the probe, load-lock chamber, gate valve (see fig. 3.10), and the top of the cryostat are labeled. The hybrid magnet is underneath the ground in this picture. When the probe is fully loaded, the top of the probe will be at the top of the load-lock as indicated in the schematic in fig. 3.15. In the picture, the sample stage at the end of the probe sits right above the gate valve. After the probe is inserted into the hybrid magnet, the sample stage will be at the field center.

3.2.3 Probes

All the cryostats used in this study are top loading cryostats. This means that the experimental apparatus is loaded into the cryostat via a probe from the top of the cryostat. The size of the probe depends on the bore size of the magnet. The superconducting magnets used in this study tend to have a larger bore and the sample stage is consequently bigger allowing for more samples to be measured at once.

The experiment (such as a torque magnetometer) is mounted on a socket that is then attached to the sample stage on the probe. Two kinds of sockets are used for different probes. Larger probes, such as the ones that fit into the larger superconducting magnet bores, have 16 pin sockets. The sockets plug in to a female socket receptacle. The pins of the socket are then electrically connected to twisted pairs or coax cables that run up the probe.

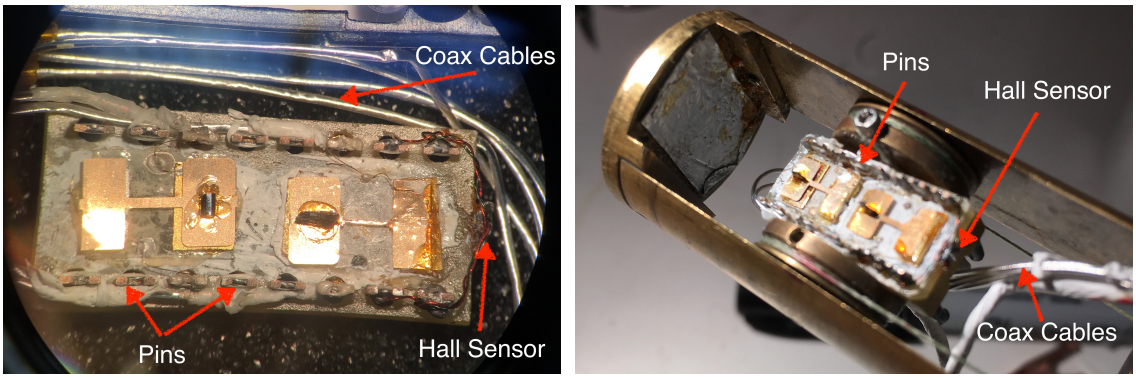

Figure 3.17: Picture of 16 pin socket used in many of the superconducting magnets. Left panel shows a socket with two torque magnetometers before it is mounted on a probe. Right panel shows a socket mounted on the probe used in SCM1.

Fig. 3.17 shows a picture of a 16 pin socket with two torque magnetometers mounted. The left image is the socket under magnification before it is mounted on the probe. The right picture is the socket after mounted on the probe used in SCM1 at the National High

Magnetic Field Lab. The 16 pins line the sides of the socket. Coax cable extensions are soldered onto four of the pins and gold leads connect the cantilevers to these pins. The Hall sensor, which is used to determine the position of the socket with respect to the external field is labeled. The Hall sensor is electrically connected to four pins corresponding to two sets of twisted pairs at one end of the socket. SCM2 has a larger bore and can accommodate two of these 16 pin sockets - large enough to measure two torque magnetometers and four transport experiments at once as shown in fig. 3.18.

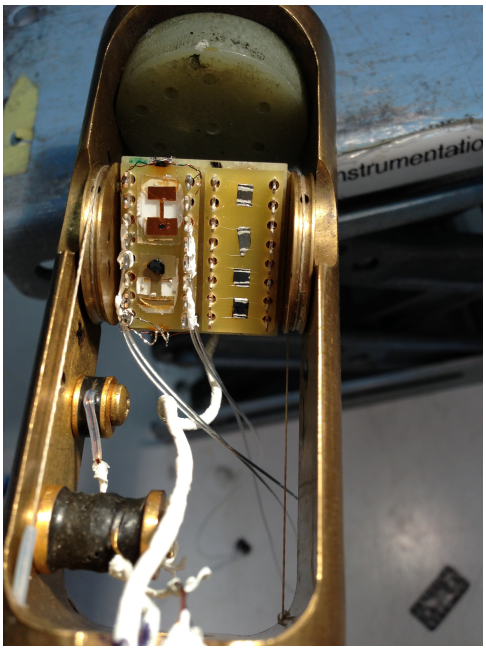

Figure 3.18: Sample stage for the probe used in SCM2 at the National High Magnetic Field Lab. The left socket has two cantilevers for torque magnetometry and the right socket has four transport measurements.

Smaller probes, like the one used for the hybrid magnet, use a round socket that fits into a hole at the end of the probe. The socket remains in place mechanically because it fits tightly into the hole. There are no pins to make electrical contacts, so extension wires run from the socket further up the probe to make contact with coax cables or twisted pairs.

Fig. 3.19 shows a picture of a socket used for a resistive magnet probe with a torque magnetometer attached. The left picture is the socket before being mounted on the probe. Coax cables for the cantilever and twisted pairs for the Hall sensor are labeled. The right panel shows the socket after being mounted on the probe. The socket fits tightly into the hole in the probe. GE varnish is added for extra security. A thin piece of teflon is tied around to prevent wires from protruding. The twisted pairs and coax cables connect with the probe wires further up the probe.

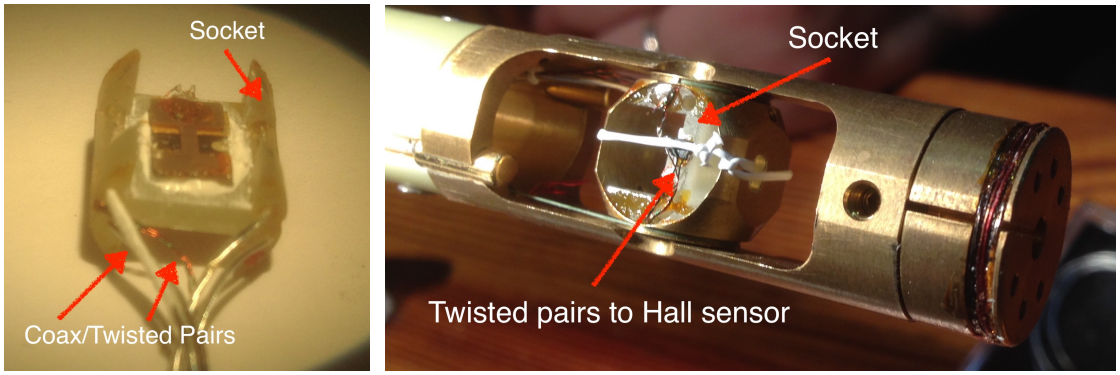

Figure 3.19: Picture of a socket used in resistive magnets. Left panel shows a socket with a torque magnetometer before it is mounted on a probe. Right panel shows a socket mounted on the probe used in the hybrid magnet.

Many physical phenomena depend on the angle between the crystal axis of the sample and the external magnetic field. For example, to map the Fermi surface from quantum oscillations, an angular dependence is needed. For this reason, it is important to be able to change the angle of the sample with respect to the magnetic field in situ. To change the angle of the sample, the probes used in this study all have a rotation stage where the sample socket is attached. In this way, the sample stage can rotate and the crystal axis of the sample changes with respect to the fixed magnetic field.

The mechanism for the sample rotation is the same in all the probes used. There is a rotation stage that receives the socket as described above. The rotation stage shown in the right panel of fig. 3.20 sits on a bearing. On the left side of the stage, there is a string that connects to a fixed spring. The tension in the spring provides a leftward torque on the rotation stage. On the right side of the rotation stage, a string is attached that extends all the way to the top of the probe. The tension in the string provides a rightward torque on the rotation stage. By giving slack to the string, the spring will contract rotating the rotation stage counterclockwise as viewed from the right. By pulling on the string, the spring will stretch and the rotation stage will rotate clockwise.

On the top of the probe, there is a rotation mechanism shown in the left panel of fig. 3.20. The string connecting to the rotation stage connects to this mechanism. The rotation mechanism has a turn dial that will pull the string or give slack to the string. This will cause the sample stage to rotate. Tension on the string will cause the sample stage to turn towards the probe bottom and slack on the string will cause the sample stage to rotate towards the probe head. The rotator position can be approximated by the value on the turn dial, which can change the length of the string with precision down to 0.001". The angular change of the rotation stage by a change in the string length of Δs depends on the radius of the

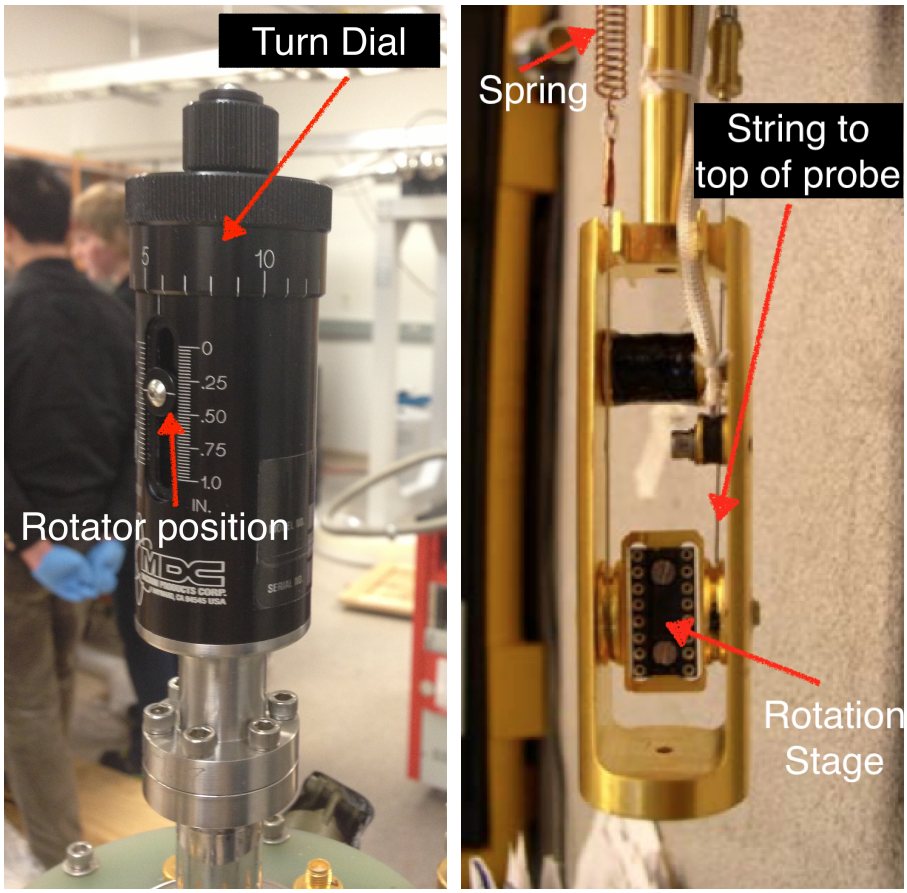

Figure 3.20: Mechanism for rotating sample in magnetic field. Left panel shows a picture of the rotator on the top of the probe. Right panel shows the rotation stage where the experiment is mounted.

rotation stage, R, by $R\theta = \Delta s$.

The exact position of the rotation stage cannot be reliably determined by the position of the rotation dial on the top of the probe. This mechanism always has some backlash when changing the rotation direction. Also, occasionally the rotation stage will get stuck due to the cables used in the experiment. The coax extensions can pull on the rotation stage if too short or push on the rotation stage if they run into the sides of the cryostat after the probe is loaded. Therefore, a Hall sensor is typically employed which has a strong angular dependence with the applied magnetic field to confirm the position of the rotation stage with respect to the external field.

The probes are fitted with twisted pairs of phosphor-bronze wires connected to feedthroughs at the top of the probe. Twisted pairs are used to minimize noise picked up by the changing magnetic flux through the wire loops. Phosphor-bronze rather than copper is used because of the comparatively low thermal conductivity. The heat load from the top of the probe

through copper wires is enough to raise the temperature of the cryostat. These twisted pairs are used to supply current and measure voltage for transport measurements, to measure the Hall sensor, and to track the resistance of resistive thermometers. The probes also have thin coax cables for measuring capacitance.

3.3 Other Characterization Methods

3.3.1 Electrical Transport

Electrical transport measurements, such as resistivity and Hall effect, are standard techniques in experimental condensed matter physics. Resistivity measurements are sensitive to phase transitions such as the superconducting transition and they can be used to measure quantum oscillations - the SdH effect. The Hall effect can reveal whether the carriers in the sample are electrons or holes as well as give a measure of the carrier density. Thus electrical transport is an important probe into the properties of novel condensed matter systems.

A standard 4-wire resistivity measurement was performed on the doped Bi_2Se_3 samples. Gold wires are attached to the sample using a conductive paste as illustrated in fig. 3.21. Most often, silver paste is used to make contacts, but silver epoxy is sometimes also used for more robust contacts. Contacts can be directly soldered to the sample to achieve a lower contact resistance; however, this technique was not used in this study. An AC current is applied on the outer terminals from a Keithley 6220 current source. The voltage is measured on the inner terminals with a Stanford Research SR830 lock-in amplifier. The current source and lock-in amplifier are connected with a trigger link.

The resistivity of the sample is given by

$$\rho = \frac{VA}{Il} \tag{3.24}$$

Where V is the voltage measured across the sample, I is the current in the sample, A is the cross-sectional area of the sample perpendicular to the current, and l is the distance between the voltage leads. To extract the resistivity of the sample, the geometric factors need to be carefully measured. Typically, these factors are measured using a reticle in a high-magnification microscope. Often the sample shape is irregular rather than a nice bar shown if fig. 3.21(b). When this is the case, the geometric factors are estimated by taking a average of the geometric factors of the sample.

In the case of an AC measurement like the lock-in method, V_{RMS} and I_{RMS} are used to determine the resistivity. The advantage of using a lock-in amplifier is that it only measures the voltage at the excitation frequency. This isolates the signal of interest from much of the

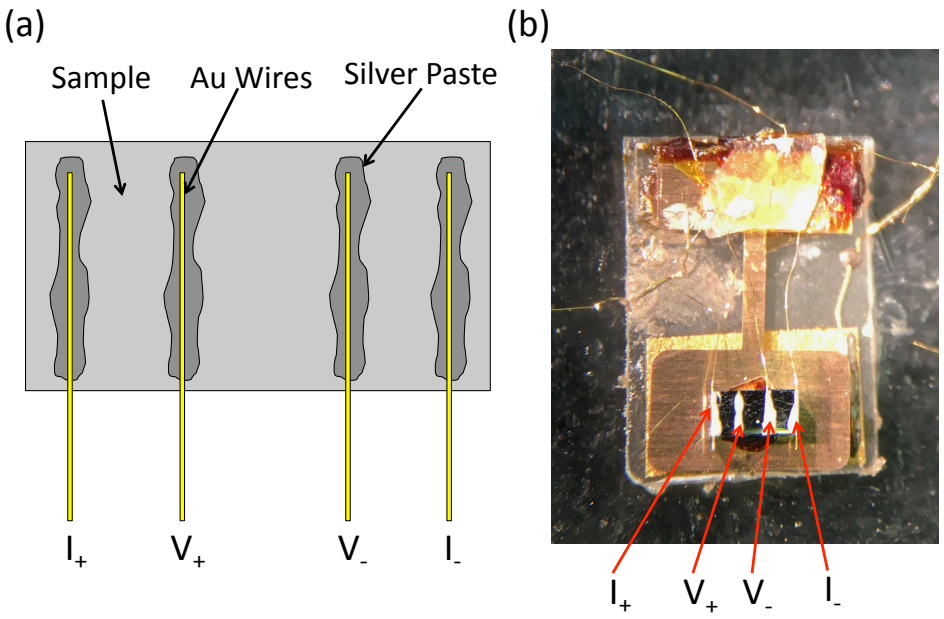

Figure 3.21: (a) Schematic of 4-wire resistivity measurement. A current is applied via the outer leads and the resulting voltage is measured on the inner leads. Contacts between gold wires and the sample are made with silver paste. (b) Resistivity and torque magnetometry can be measured in tandem by attaching current and voltage leads to a sample mounted on a cantilever.

other noise.

Though the AC lock-in method was most commonly used to measure transport in this study, other techniques were also used. The Electrical Transport Option of a Quantum Design PPMS was occasionally used to measure resistivity. This utilizes the same configuration as fig. 3.21; however, the current source and voltmeter are integrated into the PPMS.

The other method less often used is a DC resistance technique using the Delta Mode option of the Keithley 6220 or 6221. In this method, the Keithley current source provides a square wave that switches the current direction rather than using a sinusoidal waveform. Thus in short time intervals, there is a DC current in the sample. The voltage is then measured by a Keithley 2182A nano-voltmeter. The difference in the voltage for the top and bottom of the square wave divided by 2 provides a measure of the voltage response to the applied current. Averaging over several cycles can remove thermal or electrical noise from the measurement with similar effect as the lock-in technique.

As depicted in fig. 3.21(b), resistivity and torque magnetometry can be measured in tandem by attaching current and voltage leads to a sample mounted on a cantilever. In addition to taking advantage of the limited magnet time available at the National High

Magnetic Field Lab, by attaching wires to the sample, there is further insurance that if the sample becomes detached from the cantilever, it won't fall into the cryostat.

To measure the Hall effect, the contacts are arranged as shown in fig. 3.22. Though four voltage leads are not required to measure the Hall effect, having four voltage leads serves a couple purposes. First, by tracking both the longitudinal voltage, ΔV_{12} or ΔV_{34}, in tandem with the transverse voltage, ΔV_{13} or ΔV_{24}, both the Hall resistance and the traditional magnetoresistance can be measured. In addition, the small contacts used to measure the Hall effect are very fragile. If one breaks during loading and cooling of the probe, the measurement can commence with the other three available leads.

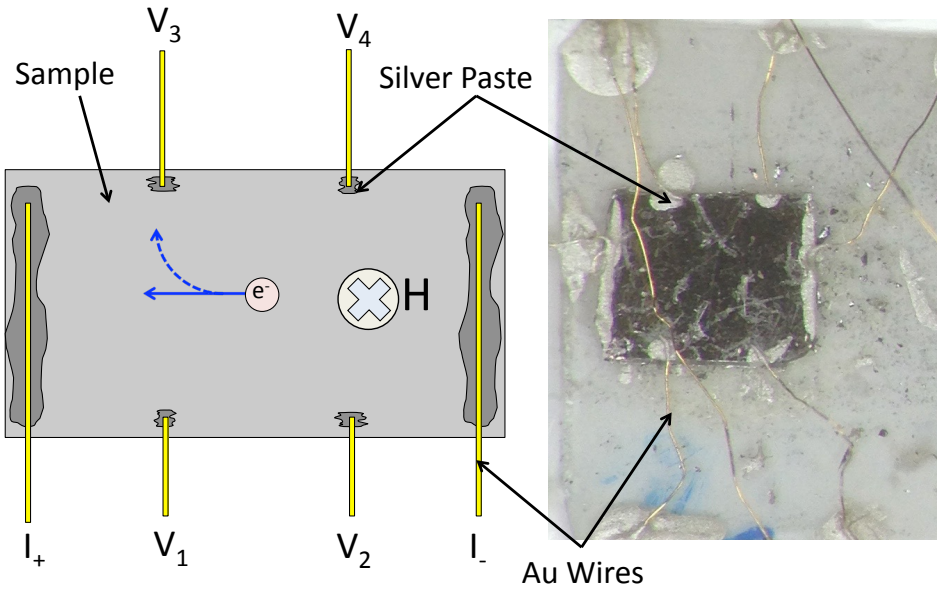

Figure 3.22: Placement of leads to measure both magnetoresistance and the Hall effect. The motion of a negative charge carrier in the presence of a magnetic field, **H**, is indicated. The photograph shows a sample under magnification with the same contact configuration as the schematic.

Generally, the voltage leads that are being measured should be connected to the same twisted pair. So when measuring the Hall effect, V_1 and V_3 should be together on the same twisted pair. If Hall effect and magnetoresistance are being measured together, one of the voltage measurements will be connected to different twisted pairs introducing extra noise. For example, if V_1 and V_3 share a twisted pair and V_2 and V_4 share a twisted pair as is ideal for measuring the Hall effect, then the voltage giving the magnetoresistance, ΔV_{12}, will be measured from different twisted pairs.

The principle behind the Hall effect is very simple. When charge carriers are put in an applied magnetic field, H, they experience the Lorentz force,

$$\mathbf{F} = q(\mathbf{E} + \mu_0 \mathbf{v} \times \mathbf{H}) \tag{3.25}$$

where q is the charge of the carrier, $\mathbf{E}$ is the electric field, μ_0 is the vacuum permeability, $\mathbf{v}$ is the velocity of the carriers, and $\mathbf{H}$ is the external magnetic field.

In the presence of the magnetic field, charge carriers are forced to the sides of the sample by the Lorentz force until the resultant transverse electric field balances out the magnetic force. For an external field into the page as shown in fig. 3.22, negative charge carriers, like electrons, will be forced to the top of the sample resulting in a positive ΔV_{13}. If the sample is dominated by positive charge carriers, such as holes, the positive charge carriers will be forced to the top of the sample resulting in a negative ΔV_{13}. Note that the conventional current goes from I_+ to I_-, and q$\mathbf{v}$ points in the direction of the conventional current regardless of the sign of the charge carrier since both q and $\mathbf{v}$ change sign according the sign of the charge carrier. Thus the sign of the transverse voltage reveals the sign of the charge carriers.

The Hall coefficient is given by

$$R_H = \frac{E_H}{j\mu_0 H_\perp} \tag{3.26}$$

where E_H is the transverse electric field created by the build up of charge carriers at the sides of the sample, j is the current density, and $H_\perp$ is the component of the magnetic field perpendicular to the large crystal face. The current density can be given by the sign of the charge carrier, $q = \pm e$, the carrier density, n, and the velocity of the carriers, $\mathbf{v}$, as $\mathbf{j} = qn\mathbf{v}$. The Lorentz force becomes zero when $\mathbf{E}_H = -\mathbf{v} \times \mu_0 \mathbf{H}$ (i.e. when the magnitude of E_H is given by $|\mathbf{v}|\mu_0 H_\perp$). Substituting the steady state condition and the magnitude of the current density into eq. 3.26 yields

$$R_H = \frac{1}{qn}. \tag{3.27}$$

Thus, the carrier density, n, can be extracted from the Hall coefficient. By substituting $E_H = V_H/d$ and $j = I/A$ into eq. 3.26, the Hall coefficient can be written in terms of the measured parameters:

$$R_H = \frac{V_H A}{I d \mu_0 H_\perp} = \frac{V_H t}{I \mu_0 H_\perp} \tag{3.28}$$

where V_H is the measured Hall voltage (such as ΔV_{13} in fig. 3.22), A is the cross-sectional area of the sample perpendicular to the current, I is the applied current, and d is the distance between voltage contacts in Hall configuration. Since the cross-sectional

area is given by the thickness of the sample, t, times the width of the sample, which is approximately equal to d, the second equality follows. Thus R_H is proportional to the slope of the V_H vs $H_\perp$ curve. So for samples with large carrier concentrations, the slope of V_H vs $H_\perp$ is shallow and for samples with small carrier concentrations, the slope of V_H vs $H_\perp$ is steep.

From eq. 3.28, it can be seen that the Hall voltage should be linear with magnetic field. The V_H vs $H_\perp$ curve is antisymmetrized to extract the Hall signal from any magnetoresistance being picked up by misalignment of the voltage leads. For samples with carriers from multiple bands, the Hall voltage won't be linear with magnetic field, thus a non-linear V_H vs $H_\perp$ curve indicates a complicated electronic structure.

Since the Hall effect depends on the angle between the current and the applied magnetic field, the Hall effect can be used to extract the angle between the applied magnetic field and the rotation stage of the probe. This is the principle behind the Hall sensor described in the previous section.

3.3.2 Heat Capacity

Heat capacity is a useful tool to determine the properties of superconductors including their gap structure. Since superconducting gap structure has implications on topological superconductivity as discussed in chapter 2, heat capacity is a useful tool for probing topological superconductor candidates. Section 5.1 discusses in greater detail the interpretation of the heat capacity in Nb-doped Bi_2Se_3. Here I will briefly discuss how heat capacity is measured.

Heat capacity was measured using a Quantum Design PPMS. The PPMS measures heat capacity at constant pressure given by

$$C_p = \frac{\partial Q}{\partial T}|_p. \tag{3.29}$$

In basic terms, a known quantity of heat, Q, is applied to the sample and the response of the temperature, T, is tracked. The experimental apparatus is shown in fig. 3.23. Fig. 3.23(a) shows the apparatus from the side. A platform is suspended by wires from the puck frame, which is in thermal equilibrium with the cryostat. The cryostat is considered an infinite thermal bath. The PPMS in this study has both a helium-3 and helium-4 option, so heat capacity can be measured down to 300 mK. There are four wires holding the platform. As can be seen from the top view in panel (b), two wires are connected to a heater and two to a thermometer. The heater provides a known heat load to the platform and the thermometer tracks the temperature. The whole setup is kept in vacuum so that the most

significant source of thermal conduction is through the support wires.

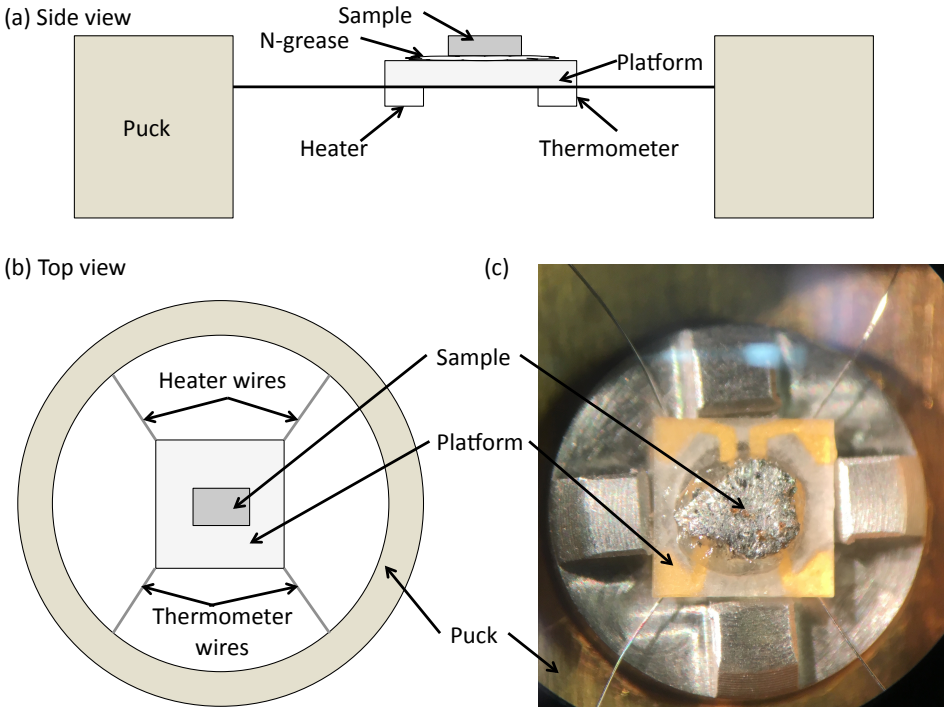

Figure 3.23: (a) Side view of heat capacity apparatus. The sample is attached to a platform using N-grease. The platform is suspended by support wires from the puck which acts as a thermal bath. (b) Top view of the heat capacity apparatus. Two of the four support wires provides current to a heater which supplies a known power load. The other two wires are connected to a thermometer which tracks the temperature. (c) Photograph of Nb-doped Bi_2Se_3 mounted on the heat capacity platform. A silver stage holds the platform in place during mounting to prevent damage to the support wires.

The sample is mounted on the platform via N-grease. Before mounting the sample, the heat capacity of the platform and grease are measured alone. Then when the heat capacity is measured with the sample included, the heat capacity of the grease and platform is subtracted away. If a temperature and magnetic field dependence of the heat capacity of the sample are going to be measured, the temperature and field dependence of the grease must be measured in the same range.

When mounting the sample or applying grease, a custom puck holder is used to prevent damage to the four support wires. As seen in the picture in fig. 3.23(c), a silver stage holds the platform in place to prevent stress on the wires. Below the platform, a small roughing pump provides a low pressure to fix the platform in place.

When heat is applied to the platform, the flow of heat can be used to determine the temperature response of the platform/sample by

$$\frac{dQ}{dt} = C_p \frac{dT}{dt} = -K_w[T(t) - T_0] + P(t) \tag{3.30}$$

where C_p is the heat capacity of the system consisting of the sample, platform and N-grease, K_w is the thermal conductance of the support wires, T_0 is the temperature of the puck (temperature of the cryostat), and $P(t)$ is the power as a function of time provided by the heater, which is a step function given by $P(t) = P_0$ when the heater is on and $P(t) = 0$ when the heater is off.

Solving 3.30 with the conditions that $T(0) = T_0$ and $T(t)$ is continuous at time, t_0, when the heater is turned off yields

$$T(t) = \begin{cases} T_0 + \frac{P_0}{K_w}(1 - e^{-t/\tau}) & t \leq t_0 \\ T_0 + \frac{P_0}{K_w}(1 - e^{-t_0/\tau})e^{-(t-t_0)/\tau} & t \geq t_0 \end{cases} \tag{3.31}$$

This solution contains a time constant $\tau = C_p/K_w$, which can be extracted by fitting the temperature data as a function of time. From the time constant, the heat capacity is determined. The heat capacity of the sample is arrived after subtracting the heat capacity of the platform and N-grease previously measured.

The PPMS also uses a more complicated model considering the heat flow between the sample and platform in case the thermal link between the two is poor. Several heat capacity measurements are done at each temperature and field and an average is taken. The PPMS uses the model that gives the smallest variation between measurements taken at the same temperature and field.

3.3.3 SQUID Magnetometry

The magnetic moment of a sample contains a lot of useful information. Most basically, with magnetic field dependence, it can show whether a material is diamagnetic or paramagnetic. For superconductors in particular, measuring the magnetic susceptibility as a function of temperature can give the superconducting volume fraction - an important indicator of the percent of the superconductor that is in the superconducting state. This is one indicator of the quality of a superconductor. As discussed in chapter 2, finding a $Cu_xBi_2Se_3$ crystal with a large superconducting fraction is difficult. Therefore, measuring the superconducting volume fraction is an important way to screen samples for further studies. Furthermore, it is an important quantity to report to verify the quality of samples reported on.

In this study a Quantum Design MPMS was used to screen and measure the magnetic moment of doped Bi_2Se_3 crystals. The MPMS utilizes a SQUID magnetometer to determine the magnetic moment of the sample. Fig. 3.24 shows a schematic of the SQUID

magnetometer. It is comprised of a single superconducting coil. As shown in the figure starting at the bottom, it has a single counterclockwise loop followed by two clockwise loops in the center and ends with a counterclockwise loop. The balance of the right-handed and left-handed loops in the coil should cancel out any emf coming from non-local change in magnetic flux.

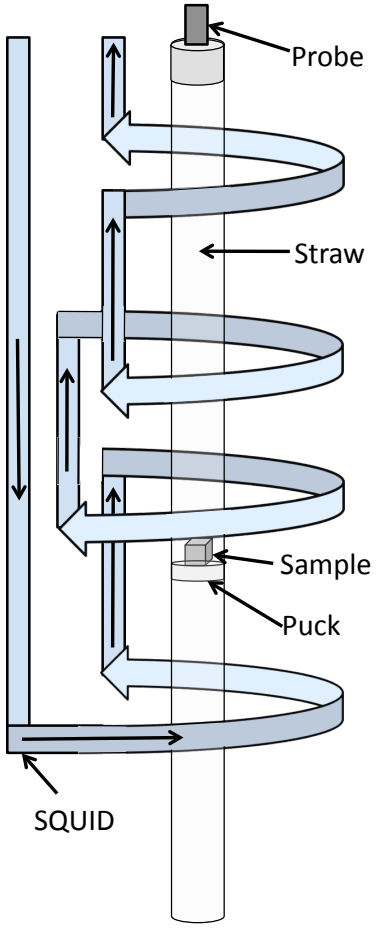

Figure 3.24: Model of SQUID magnetometer. The magnetometer is made from a single coil of superconducting wire. The loops are a balance of left-handed loops and right-handed loops to remove the pick up of changing non-local magnetic fields. The sample is mounted on a puck placed within a straw. The straw is attached to a rigid probe which is moved up and down inside the SQUID. The local change in the magnetic flux through a coil due to the motion of the sample induces a current in the SQUID from which the magnetization of the sample can be extracted.

During measurement, the sample is moved up and down through the magnetic coil. The changing magnetic flux coming from the dipole moment of the moving sample induces a voltage in the superconducting coil. Since the coil is superconducting, the resulting current doesn't decay with time. The sign and magnitude of induced voltage in the coil depends on

the magnetic moment of the sample and the handedness of the local coil where the sample is passing through. As the sample moves through the coil, the voltage in the superconducting coil as a function of the sample position can be used to extract the magnetic moment of the sample.

To move the sample through the coil, the sample is mounted to a small plastic puck with N-grease. The puck is then fit into a drinking straw as shown in fig. 3.24. The puck is machined to fit tightly in the straw, but sometimes a small about of N-grease is used to keep undersized pucks from sliding around. The bottom of the straw is covered with a small piece of Kapton tape to prevent loss of the sample into the MPMS if the puck gets displaced. The straw is then stuck to the end of a rigid probe and lowered into the MPMS. Before lowering the probe, the straw and sample are closed in a small version of a load-lock. The load-lock is flooded with helium and purged several times to prevent contamination to the cryostat. Several holes are placed in the straw above and below the sample puck to prevent the sample puck from dislodging when the pressure changes during the flood/purge.

After the probe is lowered, the sample can be moved up and down from a stepper motor that raises and lowers the probe. Before commencing the measurement, a series of short measurements are taken to center the sample in the middle of the SQUID. There is a peak in the voltage profile when the sample passes through the central turns in the coil. If this peak is not in the center of the probe's motion, then the sample will not pass through the entire SQUID. The MPMS has a method for automatically or manually recentering the sample in the SQUID. There is a limited range for which the probe position can be readjusted, so the sample must be initially mounted at a given distance from the top of the straw according to the specifications of the MPMS.

The MPMS used in this study is fitted with a helium-4 cryostat that can measure the temperature dependence of the magnetization down to 1.8 K. It also has a 5 T superconducting magnet for measuring the field dependence. Before each measurement, the field and temperature are stabilized at the desired value. Even though the coils are designed to not pick up changing magnetic flux from non-local magnetic sources - like the magnet - the coils can never be perfectly balanced. To counter this effect, the MPMS heats a portion of the SQUID while the magnetic field is changing. In addition, occasionally a technique called "rocking the field" is applied where the magnetic field is swept up and down eventually settling on zero. This serves to remove any trapped supercurrent in the SQUID.

Sometimes, the presence of trapped magnetic flux cannot be fully removed from the magnetometer. When measuring the magnetic susceptibility to determine the superconducting volume fraction, a small field (such as 5 Oe) is applied and a temperature depen-

dence is taken. When the field is very small, the trapped flux in the SQUID can act as another external magnetic field that is a significant fraction of the applied field. To eliminate this effect, the measurement is repeated with the magnetic field in the opposite direction (-5 Oe). This can be used to determine the true value of the magnetic susceptibility. For example, the measured value of the magnetization at base temperature with field, H_{app}, in the positive z-direction, M_+, and with the field in the negative z-direction, M_-, is given by

$$\begin{aligned} M_+ &= \chi(H_{app} + H_0) \\ M_- &= \chi(-H_{app} + H_0) \end{aligned} \tag{3.32}$$

where χ is the magnetic susceptibility of the sample and H_0 is the field from trapped flux in the SQUID. The effect of trapped flux can be eliminated and the magnetic susceptibility can be found to be

$$\chi = \frac{M_+ - M_-}{2H_{app}}. \tag{3.33}$$

The volume magnetic susceptibility can be found from the dimensions of the sample and the magnetic susceptibility. This is an measurement of the superconducting volume fraction of the sample.

CHAPTER 4

de Haas-van Alphen Effect in Cu-doped Bi_2Se_3

$Cu_xBi_2Se_3$ has drawn much attention as the leading candidate to be the first topological superconductor and the realization of coveted Majorana particles in a condensed matter system. However, there has been increasing controversy about the nature of its superconducting phase. This study, based on my publication [39, 40], sheds light on ambiguity in the normal-state electronic state by providing a complete look at the quantum oscillations in magnetization in $Cu_xBi_2Se_3$ at high magnetic fields up to 31 T. This study focuses on the angular dependence of the quantum oscillation pattern for samples with different carrier concentrations. As the magnetic field tilts from the crystalline c axis to the ab plane, the change of the oscillation period follows the prediction of the ellipsoidal Fermi surface. As the doping level changes, the 3D Fermi surface becomes quasi-cylindrical at high carrier density. Such a transition is potentially a Lifshitz transition of the electronic state in $Cu_xBi_2Se_3$.

A comparison is made between the superconducting $Cu_xBi_2Se_3$ and its parent compound, the topological insulator Bi_2Se_3. The doping of Cu in Bi_2Se_3 increases the carrier density and the effective mass without increasing the scattering rate or decreasing the mean free path. In addition, the Fermi velocity remains the same in $Cu_{0.25}Bi_2Se_3$ as that in Bi_2Se_3. These results imply that the insertion of Cu does not change the band structure and that conduction electrons in $Cu_xBi_2Se_3$ sit in a linear Dirac-like band.

Topological superconductors are a novel phase of matter that has been theoretically predicted but has yet to be experimentally verified. Among topological materials, topological superconductors are especially interesting because they are a platform to realize Majorana particles, an elusive particle that is its own antiparticle. Furthermore, topological superconductors have been proposed as a platform for topological quantum computation [30, 57, 167]. The robustness of the topological surface states makes this avenue an attractive alternative to traditional methods for realizing quantum computation [56].

As discussed in chapter 1 section 1.2.1, sufficient criteria for topological superconductivity are a full superconducting gap in the bulk with odd-parity pairing, and a Fermi

surface enclosing an odd number of time-reversal-invariant momenta in the Brillouin zone; i.e., the Fermi surface must contain an odd number of high-symmetry points such as Γ, Z, X, etc. It also has a topologically protected gapless surface state with Majorana fermions [57]. $Cu_xBi_2Se_3$ has been proposed as a leading candidate for topological superconductivity [5] and has sparked a lot of interest. Experiments have shown that by intercalating Cu between Se layers in the known topological insulator Bi_2Se_3 the compound becomes superconducting at 3.8 K [3].

$Cu_xBi_2Se_3$ has been confirmed to be a bulk superconductor with a full pairing gap by specific-heat measurement [6]. There are some reports of surface Andreev bound states through the observation of a zero bias conductance peak [8], but other reports suggest that the zero bias conductance peak can be removed with gating [10]. The zero bias conductance peak was also not observed in other works using scanning tunneling spectroscopy [9]. ARPES measurements have argued against the topological superconducting mechanism in $Cu_xBi_2Se_3$ by reporting an even number of time-reversal-invariant momenta in the Brillouin zone [11]. Both ARPES and quantum oscillation experiments show a Dirac dispersion in $Cu_xBi_2Se_3$ - a characteristic feature of topological systems [4, 39]. The continued interest in $Cu_xBi_2Se_3$ and the increasing controversy over its exotic phase calls for this thorough look at quantum oscillations in magnetization.

Single crystals of $Cu_xBi_2Se_3$ were grown by Yew San Hor at the Missouri Institute of Science and Technology. Stoichiometric mixtures of high-purity elements Bi (99.999%), Cu (99.99%), and Se (99.999%) were melted in a sealed evacuated quartz tube then slowly cooled from 850°C down to 620°C at which point the crystal was quenched in cold water. The nominal doping level was determined by the mole ratio of the reactants used in the crystal growth. However, the samples were categorized by their measured carrier concentration since the Cu concentration could not be directly measured. The samples used in the study were cut out from larger boules. They are generally black with a typical size of about 5 mm x 2 mm x 0.5 mm.

Six samples are reported on in this study. The original paper only reported on a single sample with a nominal doping of 0.25. That crystal is labeled $Cu_{0.25}Bi_2Se_3$ [39]. Five other crystals were measured in the second paper comparing samples different carrier concentrations [40]. These samples are labeled sample 1-5, where sample 4 was broken into two pieces - sample 4a and sample 4b. A single crystal Bi_2Se_3 was also measured.

4.1 Superconductivity in Cu-doped Bi_2Se_3

To determine the superconducting properties of the $Cu_xBi_2Se_3$ crystals, the resistivity was measured to verify a zero-resistance superconducting transition. Also, the volume magnetic susceptibility was measured in a Quantum Design MPMS.

The resistance, R, of the $Cu_{0.25}Bi_2Se_3$ sample from the first study was measured with the four-wire method. R as a function of T is shown in fig. 4.1(a). As T decreases, a superconducting phase transition is observed. R starts to fall at 3.3 K, then rapidly decreases through T = 3 K, and becomes zero below T = 1.2 K.

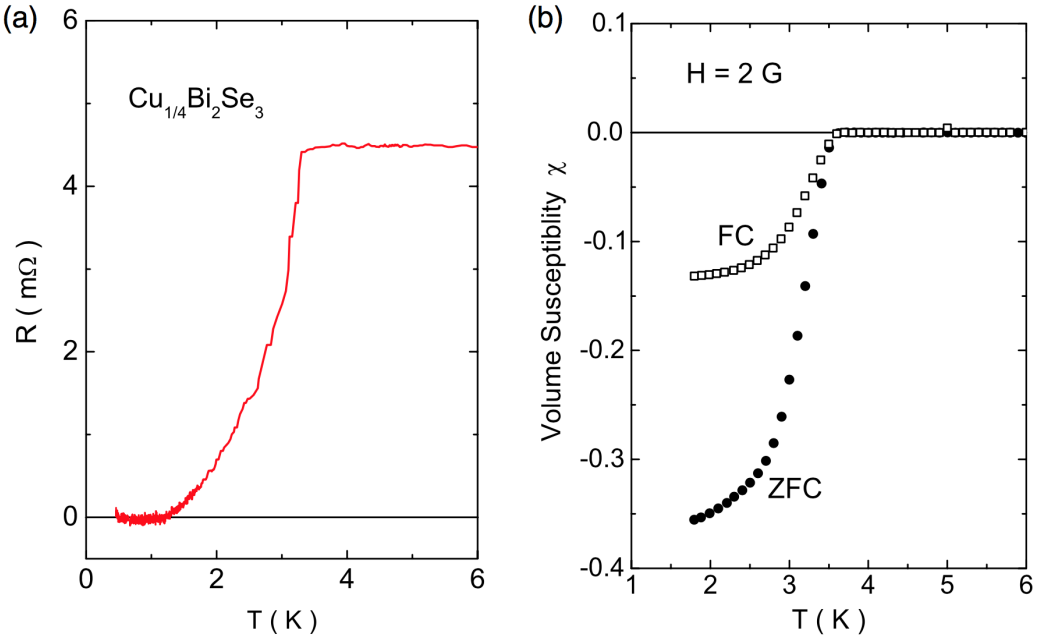

Figure 4.1: (a) The temperature dependence of sample resistance R. Zero resistance is observed below 1.2 K. (b) Volume magnetic susceptibility, χ, with external magnetic field H = 2 G in the crystal ab plane. χ is measured under both the zero-field-cooled (ZFC) and the field-cooled (FC) conditions. From the ZFC curve, the nominal superconducting fraction is found to be around 35%.

Figure 4.1(b) shows the volume magnetic susceptibility $\chi = M/\mu_0 H$ in the temperature range $1.8 \leq T \leq 6$ K. First the sample is cooled to 1.8 K without any external magnetic field. An external magnetic field H = 2 G was applied and χ was measured while warming up. This is the zero-field-cooled (ZFC) run shown in fig. 4.1(b). Afterwards, the sample was cooled again under the 2 G magnetic field, while measuring χ. This is the field-cooled (FC) sweep.

In both runs, rapid decrease of χ was observed at T = 3.5 K. At the lowest temperature, T = 1.8 K, χ reaches a minimum of -0.35 in the zero-field-cooled run. This suggests a

35% superconducting volume. This is not the highest superconducting volume observed in $Cu_xBi_2Se_3$ [80]; however, it is typical for $Cu_xBi_2Se_3$ and is comparable to other reports [6]. This relatively large superconducting fraction suggests that this $Cu_{0.25}Bi_2Se_3$ sample is indeed high quality single phased crystal. Moreover, the observation of zero resistance implies that a large scale phase separation does not occur.

Fig. 4.2 shows the volume magnetic susceptibility of three of the other $Cu_xBi_2Se_3$ samples. Sample 4 shows a superconducting transition with a 16% superconducting volume. Samples 3 and 5 don't show a superconducting transition. The magnetic susceptibility was measured two weeks after the high-field torque experiments. $Cu_xBi_2Se_3$ generally is susceptible to degradation over time and exposure to air. There is even a possibility that the samples could lose Cu over time and exposure. Therefore, the non-superconducting samples may or may not have been superconducting when their quantum oscillations were measured.

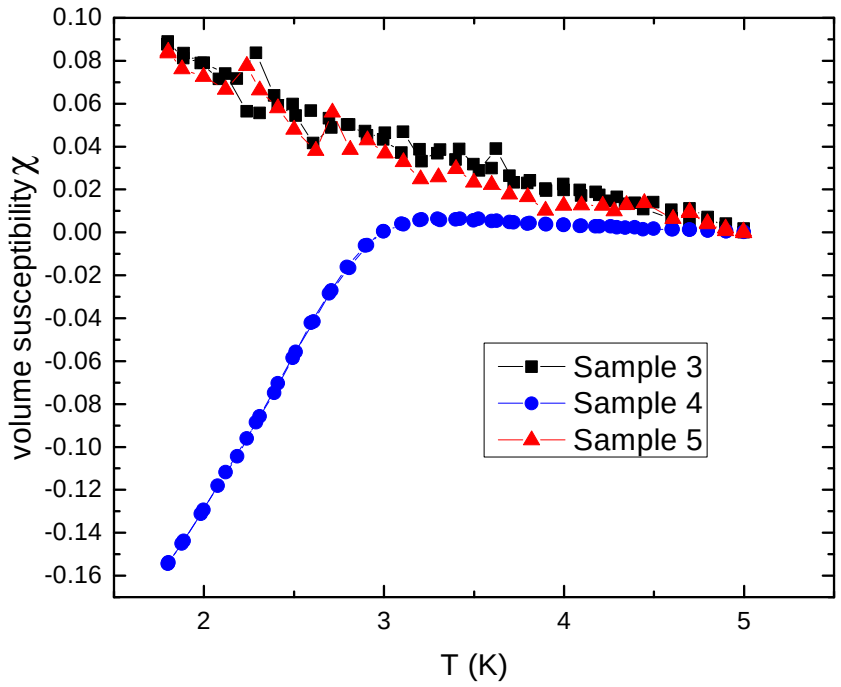

Figure 4.2: Volume susceptibility measurements of 3 different samples. Sample 4 shows a superconducting transition at 3 K and a 16% superconducting volume. Samples 3 and 5 do not show any superconducting property most likely due to sample quality degradation over time.

From the Dingle temperature (see section 4.3.2), sample 4 turns out to have the highest

level of disorder of any of the $Cu_xBi_2Se_3$ samples measured. However, it shows a superconducting transition whereas sample 5, which has twice the mean free path as sample 4, does not. On the other hand, the $Cu_{0.25}Bi_2Se_3$ sample from the original paper is superconducting but has the same mean free path as sample 5 [39, 40]. Therefore, it is not the case that superconductivity only occurs in the extreme case of highly disordered samples. Rather, the degradation from the two weeks between measuring the magnetic torque (from which the mean free path is determined) and measuring the magnetic susceptibility makes it impossible to draw conclusive comparisons between sample quality and superconductivity in this study.

To further elucidate the relation between sample quality and superconductivity, as well as search for basal plane rotational symmetry breaking (which wasn't predicted until after the publication of the second dHvA study on $Cu_{0.25}Bi_2Se_3$ [40]), more high quality crystals were screened. All of the samples from the earlier study had lost their superconducting properties.

Fig. 4.3 shows the magnetic susceptibility taken when screening samples from a new batch - designated sample 6 and 7. Sample 7 only had a 7% superconducting volume fraction and sample 6 had less than a 1% superconducting volume fraction.

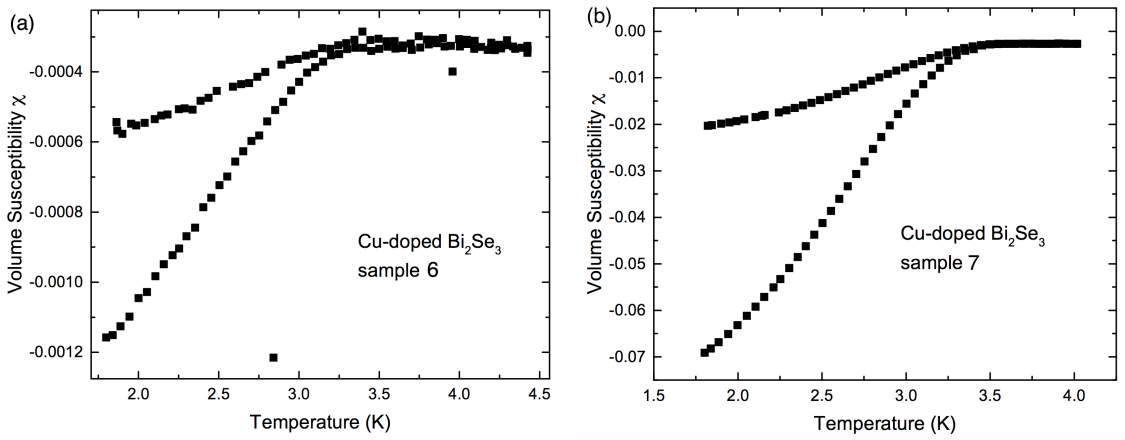

Figure 4.3: Volume susceptibility measurements while screening a new batch of $Cu_xBi_2Se_3$ crystals. Neither of the new crystals showed larger than a 10% superconducting volume.

This illustrates a common problem while working with $Cu_xBi_2Se_3$. First, it is difficult to find high quality superconducting crystals. Second, when good crystals are found, they must be measured quickly and great care is needed during storage to prevent loss of their superconducting quality.

4.2 Angular Dependance of Quantum Oscillations

Quantum oscillations are used to resolve Fermi surface geometry and to discover the electronic properties of topological materials. Oscillations in magnetization, the dHvA effect, arise from the quantization of the Fermi surface into Landau levels. To measure quantum oscillations in magnetization, M, I employed a highly sensitive torque magnetometry method described in chapter 3 section 3.1.

The samples are glued to the head of a thin-film cantilever. To provide a balance between strength for heavier samples and sensitivity, both brass cantilevers and Kapton cantilevers with a metalized surface were used. The brass cantilevers are thinner, 0.001", but have a higher Youngs modulus, whereas the Kapton thin films are 0.003" thick but have a lower Youngs modulus. The magnetic torque was tracked by measuring the capacitance between the metal surface of the cantilever and a thin gold film underneath. An example of oscillations in the torque is shown in fig. 4.4 with a schematic of the experimental setup in the bottom left.

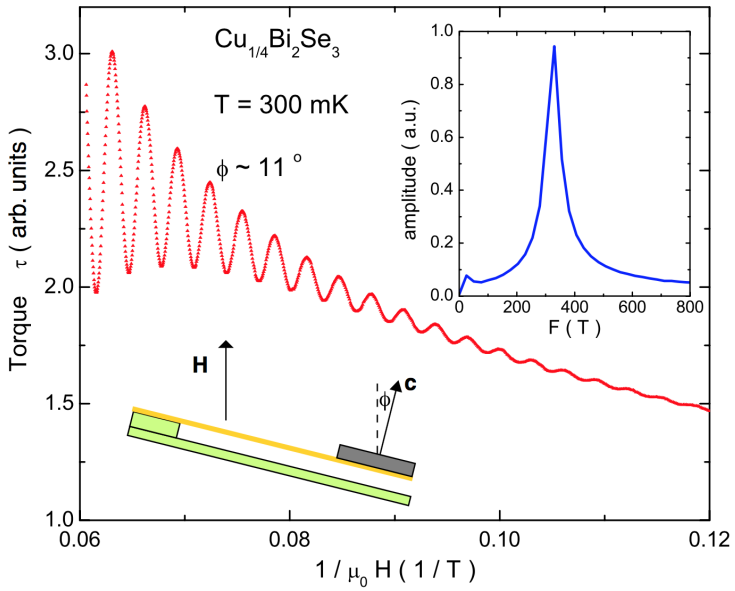

Figure 4.4: Quantum oscillations in $Cu_{0.25}Bi_2Se_3$ observed by torque magnetometry. Magnetic torque τ is plotted as a function of $1/\mu_0$H. The lower left panel shows the sketch of the torque magnetometer, where the magnetic field is applied to the sample with a tilt angle ϕ relative to the crystalline c axis. The fast Fourier transform (FFT) plot of the torque signal is shown in the upper right panel. The FFT is taken after subtracting the polynomial background in the raw torque signal.

As discussed in chapter 3 section 3.1.2, the magnetic oscillations are periodic in $1/\mu_0 H$, so fig. 4.4 shows the torque on the cantilever as a function of $1/\mu_0$H to highlight the peri-

odicity of the oscillations. This particular curve was taken at the National High Magnetic Field Laboratory in the superconducting magnet in SCM2. This facility is fitted with a helium-3 cryostat with a base temperature of 300 mK. This curve is taken at base temperature with the magnetic field at ϕ = 11° from the crystal c-axis.

In the upper right panel of fig. 4.4, the Fast Fourier transformation (FFT) of the oscillatory torque is displayed. There is a single peak in the FFT corresponding to F_S, the frequency of the quantum oscillation, of 325 T. All $Cu_xBi_2Se_3$ crystals show a single peak in the FFT at all angles. This is indicative of a single Fermi surface. As derived in section 3.1.2, the frequency of the quantum oscillation is proportional to extrema in the Fermi surface cross-section by the Onsager relation,

$$F_s = \frac{\hbar}{2\pi e} A_{ext}. \tag{4.1}$$

Before extracting the oscillation frequency some processing must be performed on the raw data. Fig. 4.5 shows some raw data taken on undoped Bi_2Se_3. It is curious that quantum oscillations should be seen in an insulator since they arise from Fermi surface quantization, which should only exist in metals. Indeed in topological insulators, quantum oscillations can arise from the topological surface state [150]; however, the oscillations seen in Bi_2Se_3 arise from the bulk as is clear from the angular dependence. In fact, Bi_2Se_3 turns out to be a poor insulator, and defects can pin the the Fermi level to the bottom of the conduction band leading to bulk conductivity [168]. This is unideal for studying the topological surface states of Bi_2Se_3, but is useful for drawing comparisons between the electronic structures of undoped and doped Bi_2Se_3.

Fig. 4.5 is raw, unprocessed torque data as a function of the applied external magnetic field. Note that the y-axis is capacitance measured in picoFarads (pF). This is what is measured directly from the Andeen-Hagerling AH2700A 50 Hz - 20 kHz Ultra-Precision Capacitance Bridge. As derived in section 3.1, the torque on the cantilever is proportional to the change in capacitance of the magnetometer. Furthermore, it was shown that the torque should go as

$$\tau = \mu_0 V \Delta\chi H^2 \sin\phi \cos\phi \tag{4.2}$$

where V is the volume of the sample, $\Delta\chi$ is the magnetic susceptibility anisotropy, H is the external magnetic field, and ϕ is the angle between the external magnetic field and the crystal c-axis. The oscillations in torque are due to oscillations in the magnetic susceptibility anisotropy. The paramagnetic background goes as H^2 as seen in equation 4.2. Fig. 4.5 has a quadratic fit of the data. The residuals of this fit represent the oscillatory

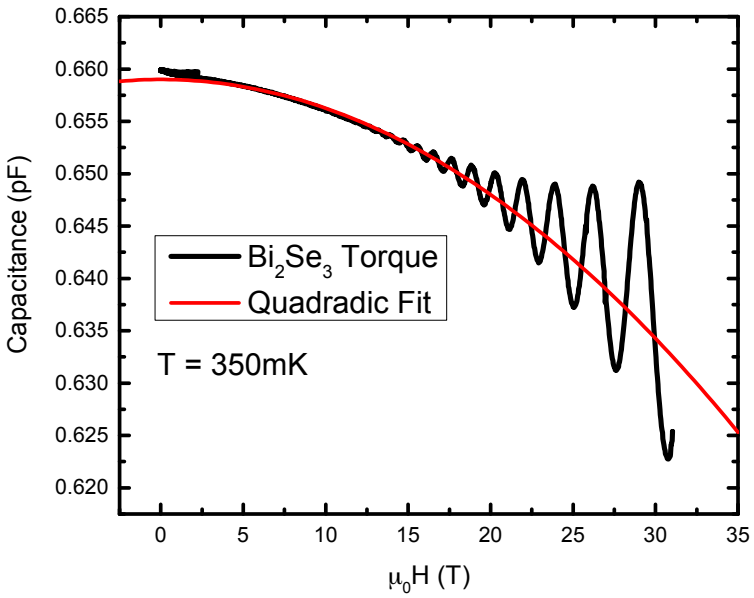

Figure 4.5: Raw torque data on undoped Bi_2Se_3. The torque is proportional to the change in capacitance. The red line is a fit to the polynomial background, which is subtracted to get the oscillatory torque signal.

torque, τ_{osc}.

After extracting the oscillatory torque, the data is interpolated so that the data points are evenly spaced in magnetic field. Then the data is smoothed either by adjacent averaging or by applying a Savitzky-Golay filter. The later locally fits the region around each data point with a linear regression and then replaces the data with a new data point less effected by noise in the data. Lastly, the data is interpolated in inverse magnetic field so that an FFT can be performed.

Fig. 4.6 shows the oscillatory torque, τ_{osc}, after the background is subtracted for sample 4 plotted against inverse magnetic field. This curve was measured in a 31 T resistive magnet at the National High Magnetic field Lab down to 300 mK. As before, the FFT shows a single oscillation frequency.

To highlight the effect of Cu doping on Bi_2Se_3, fig. 4.7 shows the oscillation frequency F_s as a function of tilt angle for $Cu_{0.25}Bi_2Se_3$ (panel a) and Bi_2Se_3 (panel b). The solid red lines are fits based on a model of an ellipsoidal Fermi surface given by

$$F(\phi) = F_0(\cos^2[\phi] + (\frac{k_F^x}{k_F^z})^2 \sin^2[\phi])^{-\frac{1}{2}} \tag{4.3}$$

where $F(\phi)$ is the frequency of the quantum oscillations at a particular ϕ, F_0 is the quantum oscillation frequency at ϕ = 0°, and k_F^x/k_F^z is the ratio of the Fermi momentum

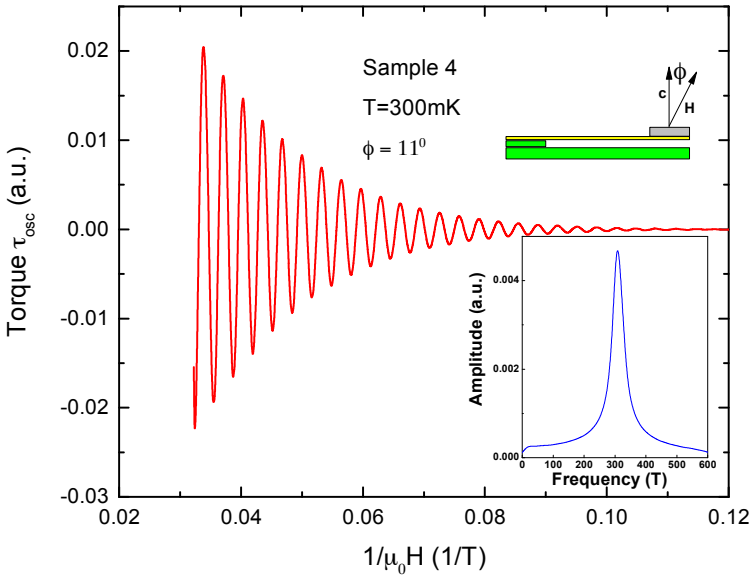

Figure 4.6: Oscillations in the torque data of sample 4 with the polynomial background subtracted. The inset in the upper right-hand corner is a schematic of the experimental setup. The lower inset is a fast Fourier transformation (FFT) of the oscillatory torque after subtracting the polynomial background. The single peak in the FFT spectrum reveals a single Fermi pocket.

in the k_x direction and k_z direction - a measure of the eccentricity of the Fermi surface. A model of the ellipsoidal Fermi surface is shown in the lower right inset of fig. 4.7(a). The extremal cross-section perpendicular to H is proportional to F_s at that angle.

First of all, F_s for $Cu_{0.25}Bi_2Se_3$ is much larger than that of the undoped sample, suggesting the Cu doping indeed adds carriers into the electronic state. For both samples the oscillation from the bulk state shows only one oscillation frequency, implying a single ellipsoidal Fermi pocket in both samples.

The angular dependence of the quantum oscillation frequency provides the size of the Fermi pocket. From the Onsager relation (equation 4.1), the frequency of the quantum oscillation is proportional to the cross-sectional area of extrema in the Fermi surface. For an ellipsoidal Fermi surface, this is given by

$$A = \pi k_F^x k_F(\phi), \tag{4.4}$$

with $k_F(\phi)$ and k_F^x, the semimajor and seminor axes, respectively, of the elliptical cross-section of the Fermi surface. Thus F_0 from equation 4.3 yields $k_F^x = k_F^y$ and the eccentricity gives k_F^z. For a closed, ellipsoidal Fermi pocket, the bulk carrier concentration, n, is given by

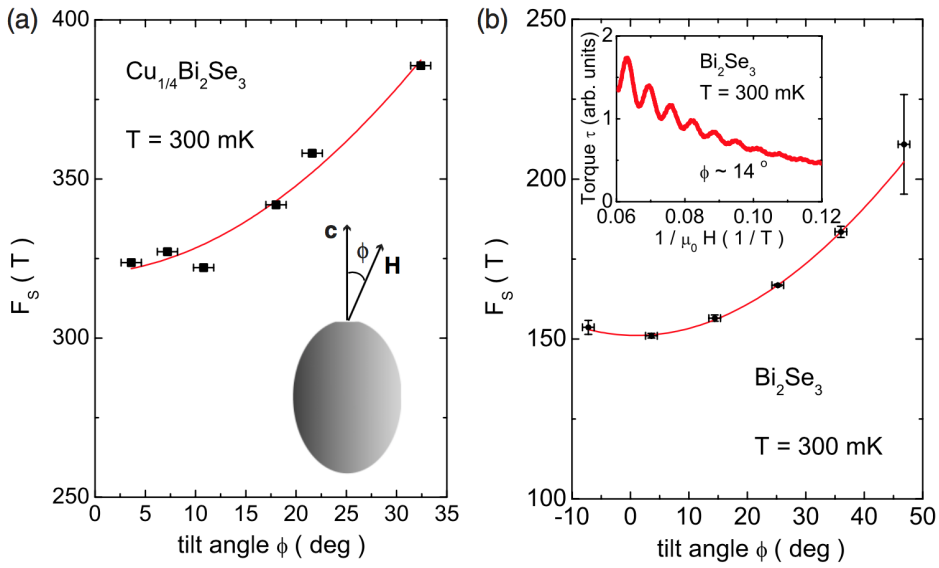

Figure 4.7: Angular dependence of the oscillation frequency F_s is compared between (a) $Cu_{0.25}Bi_2Se_3$ and (b) Bi_2Se_3. Solid lines are the fits based on a single ellipsoidal Fermi surface. A model of the ellipsoidal Fermi surface is shown in the lower right of panel (a). The extremal cross-section perpendicular to H is proportional to F_s at that angle. An example of the oscillating magnetic torque is shown in the inset of (b) for Bi_2Se_3.

$$n = \frac{1}{3\pi^2} k_F^x k_F^y k_F^z. \tag{4.5}$$

The F_s vs ϕ curve of $Cu_{0.25}Bi_2Se_3$ is consistent with an ellipsoidal Fermi surface with cross section $A_{xz} \sim 4.02$ nm^{-2}. Based on the data in fig. 4.7(a), $k_F^x = k_F^y = 0.97$ nm^{-1} and $k_F^z = 1.3$ nm^{-1}. Thus, the bulk carrier density n is 4.3×10^{19} cm^{-3}. This carrier density is similar to that derived from the Hall effect [169] and ARPES [4].

For the undoped Bi_2Se_3 sample, the fit gives $k_F^x = k_F^y = 0.69$ nm^{-1} and $k_F^z = 1.2$ nm^{-1}. The bulk carrier density n is calculated to be 1.8×10^{19} cm^{-3}. This number is larger than those generally seen in results based on quantum oscillations [170], which suggests that there are quite a number of carriers caused by defects. Table 4.1 summarizes the quantum oscillation data for Cu doped and undoped Bi_2Se_3.

Table 4.1: Comparison of quantum oscillation data for Cu doped and undoped Bi_2Se_3.

	$n(10^{19}cm^{-3})$	$F_0(T)$	$k_F^x(nm^{-1})$	k_F^z/k_F^x
$Cu_{0.25}Bi_2Se_3$	4.3	325	0.97	1.3
Bi_2Se_3	1.8	150	0.69	1.6

The data taken to produce fig. 4.7 was taken in the 18 T superconducting magnet in SCM2 at the National High Magnetic Field Lab. As seen in the panel (a), data is only taken

up to 35°. Above this angle, quantum oscillations weren't resolved due to insufficient magnetic field. With such a small angle range, the shape of the Fermi surface is somewhat questionable. Therefore, more samples were measured in a resistive magnet up to 31 T.

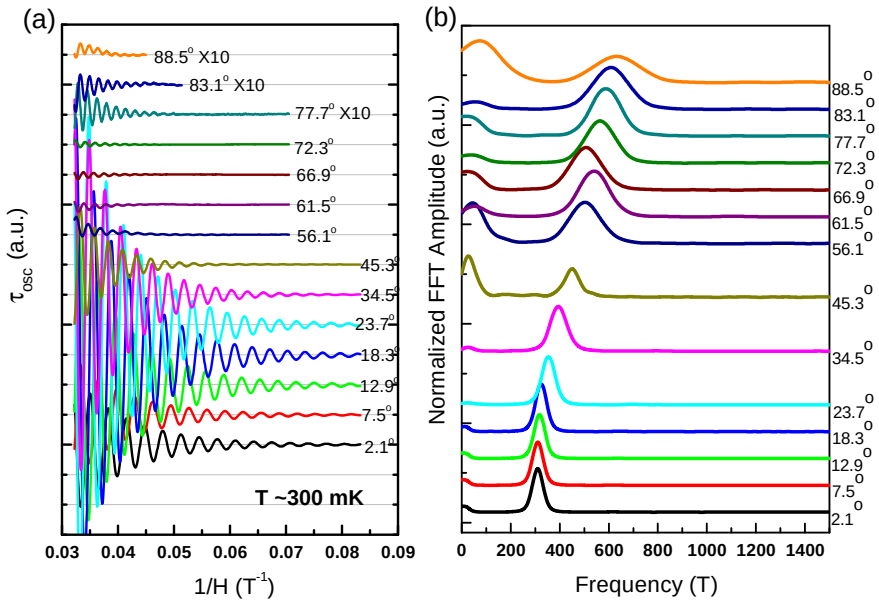

Figure 4.8: (a) Quantum oscillations in torque of sample 4 at different angles after background subtraction. Oscillations are visible in the raw signal up to 90°. At high tilt angle, the oscillation signal is multiplied by a factor of 10 for clarity. (b) The FFT spectra of oscillations in panel (a) show a single Fermi pocket with clear angular dependence. The FFT amplitude is normalized by the height of the peak in the range of 200-600 T. For the high tilt angles, the divergence of FFT amplitude in the dc end arises from an incomplete background subtraction.

Fig. 4.8 shows the torque signal from sample 4 from the 31 T resistive magnet at different angles. This is done in a helium-3 cryostat at 300 mK. As compared with the data taken in the superconducting magnet, the high field and low temperature increase the sensitivity of the measurement to be able to resolve more quantum oscillations.

In fig. 4.8(a), oscillations are clearly seen up to 90° in the raw data. This indicates that the Fermi surface has a cross-section perpendicular to the field when the field is pointing in plane. In other words, the Fermi surface is a closed ellipsoid. Note that the amplitude of the oscillations above 77° in fig. 4.8(a) are multiplied by a factor of 10 to make them visible. Figure 4.8(b) shows the FFT of the raw signal from panel (a). Clear angular dependence can be tracked up to 90°, where H is parallel to the plane.

Fig. 4.9 shows the angular dependence up to 90° of the quantum oscillation frequencies

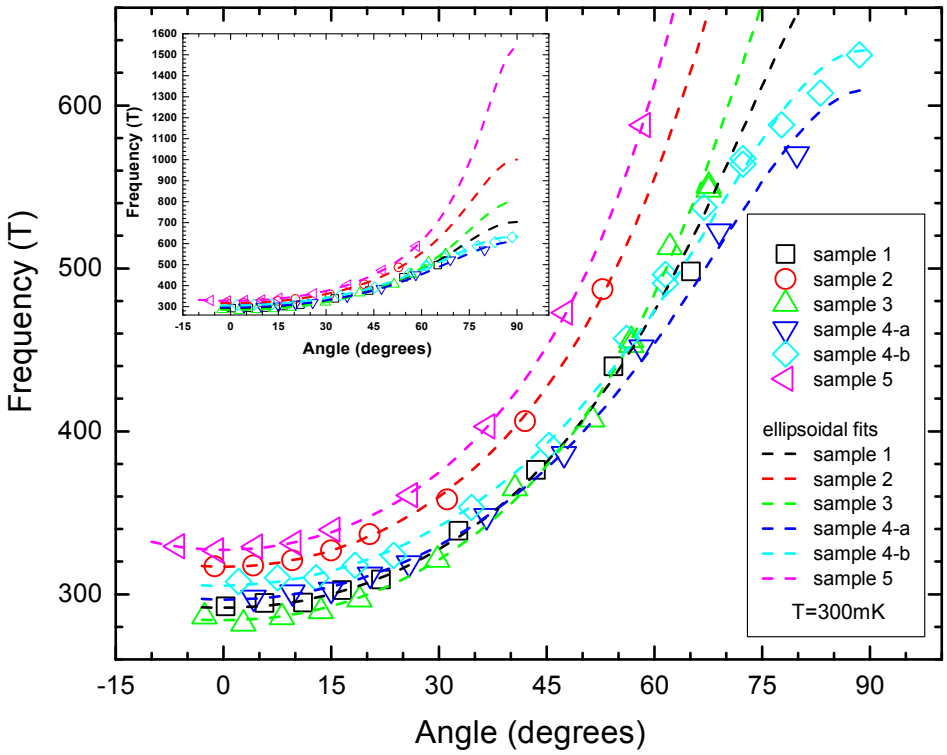

Figure 4.9: Angular dependence of the oscillation frequency of the various $Cu_xBi_2Se_3$ samples. Dashed lines are ellipsoidal fits for the Fermi surfaces. The inset expands the y axis of the data plot to a higher frequency range to show the extrapolation of the ellipsoidal fits.

for various samples measured in the 31 T magnet. As before, 0° is field along the c-axis and 90° is field in the basal plane. The inset in the upper left corner is the same data in a wider frequency range to see the extrapolation of the fits. For Sample 4a, $k_F^x = k_F^y = 0.95$ nm^{-1} and $k_F^z/k_F^x = 2.06$.

Most of the samples are fit well by a closed, ellipsoidal Fermi Surface; however, for the highest carrier concentration sample (sample 5), a closed Fermi Surface fitting yields $k_F^z = 4.69$ nm^{-1}, which is longer than the Brillouin Zone height of ∼3.28 nm^{-1} [171]. Thus, it is clear that the Fermi Surface crosses the Brillouin Zone boundary and becomes open at high carrier concentration as was reported in SdH [11].

For sample 5, which has an open Fermi surface, the bulk carrier concentration was calculated by integrating the ellipsoidal fit up to the Brillouin zone boundary to find the volume of the Fermi surface. The validity of this model relies on the assumption that the deviation from the ellipsoidal fit around the Brillouin Zone boundary due to bending is small. In this case the carrier concentration is given by

$$n = \frac{1}{2\pi^2} k_F^x k_F^y (k_{BZ} - \frac{k_{BZ}^3}{(k_F^z)^2}) \tag{4.6}$$

where k_{BZ} is the $\Gamma - Z$ distance.

For various $Cu_xBi_2Se_3$ samples, the value of k_F^z/k_F^x goes from 2.06 to 3.10 as the carrier concentration increases from 5.9×10^{19} cm^{-3} to 10.1×10^{19} cm^{-3} revealing that the Fermi surface gets increasingly elongated in the z direction as carriers are added. Then the Fermi surface opens up and becomes quasi-cylindrical at high carrier concentration consistent with quantum oscillation measurements in magnetoresistance [11].

The evolution of the Fermi surface from a closed ellipsoid to an open cylinder has implications for topological superconductivity in $Cu_xBi_2Se_3$. As discussed in chapter 1 section 1.2.1, the sufficient criteria for topological superconductivity developed by Fu and Berg include a Fermi surface that contains an odd number of TRI momenta in the Brillouin zone [5]. The closed ellipsoid seen in the lower carrier concentration samples only contain the Γ point. However, sample 5, which touches the Brillouin Zone boundary contains both the Γ and the Z point - thus including an even number of high symmetry points.

As mentioned in chapter 2, an open cylindrical Fermi surface could still be a platform to realize 2D topological superconductivity, which only has topological boundary states on the edge surfaces rather than all exposed surfaces [11, 12, 114]. On the other hand, whereas this result clearly excludes $Cu_xBi_2Se_3$ from 3D topological superconductivity in the heavily doped regime (at least according to the current theory), it does not exclude the samples of lower doping levels.

To confirm the carrier densities measured by quantum oscillations, the Hall effect was also studied in all the $Cu_xBi_2Se_3$ samples. Figure 4.10(a) shows the antisymmeterized Hall effect data of all the $Cu_xBi_2Se_3$ samples taken at T = 1.5 K in the Janis Variable Temperature Insert at the University of Michigan.

Two key features are found in the Hall effect data. First, the Hall signal ρ_{xy} is linear with H, confirming the single-band nature of the electronic state. Second, the carrier density determined by the Hall effect closely agrees with the carrier density determined from the dHvA effect.

Table 4.2 summarizes the data for various $Cu_xBi_2Se_3$ samples in order of increasing carrier concentration as determined by the dHvA effect. The in-plane Fermi surface cross-section doesn't change much between samples, but the eccentricity increases. The comparison between the hall carrier density, n_H, and the dHvA carrier density, n_M, is also summarized in table 4.2.

In addition to extracting the carrier density from the Hall effect in low field, 3 out of the

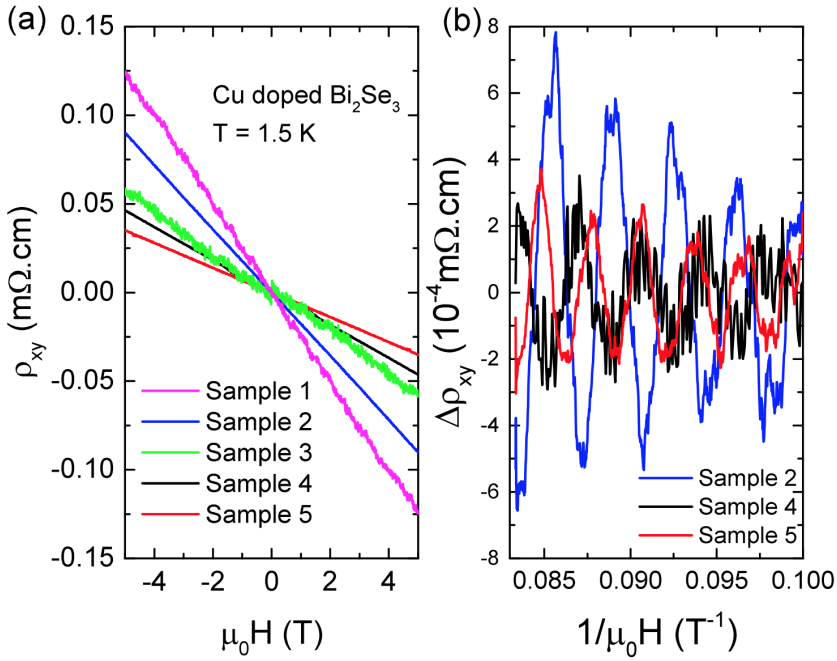

Figure 4.10: Hall effect on Cu-doped Bi_2Se_3. Each sample is cleaved from the same batch as the samples used in the torque measurement. (a) The Hall signal ρ_{xy} is plotted against field H up to 5 T at T =1.5 K. The Hall signal curves have been antisymmetrized to eliminate the magnetoresistance pickup. The slopes of the ρ_{xy}-H curves are used to determine the Hall carrier density shown in Table 4.2. (b) Measurements of ρ_{xy} in H up to 12 T show quantum oscillations in three samples. In this panel, a polynomial background is subtracted to show the oscillatory part of ρ_{xy}. The oscillation frequency is found to be the same as the measured frequency in the dHvA effect.

5 samples show quantum oscillations in the Hall signal in higher magnetic field up to 12 T (the SdH effect). The SdH oscillations after background subtraction, $\Delta\rho_{xy}$, are shown in fig. 4.10(b) plotted against inverse magnetic field. In this measurement, the magnetic field is pointed along the c-axis. The frequency of the oscillations in the Hall effect, F_{0H}, agree with those measured by torque magnetometry. Though the comparatively low field, 12 T, provides less precision in determining the frequency as compared to the torque experiment which was performed up to 31 T. The comparison of the frequency of quantum oscillations in magnetization, F_0, and in magnetoresistance, F_{0H}, with the magnetic field in plane are shown in table 4.2. F_0 was determined from the ellipsoidal fit of angular dependence of the quantum oscillation frequencies, whereas F_{0H} is directly determined by the oscillations in the Hall channel.

The nominal Cu doping, x, in the $Cu_xBi_2Se_3$ crystals as determined by the mole ratio of the reactants during the crystal growth is also listed in table 4.2. As the nominal doping increases, the Hall carrier density increases accordingly. This may suggest that the nom-

Table 4.2: Summary of results in order of increasing carrier concentration. *The value of k_F^z/k_F^x for sample 5 is ill-defined since k_F^z is taller than the Brillouin Zone. This is the value extracted from the ellipsoidal fit.

	x	$n_M(10^{19}cm^{-3})$	$n_H(10^{19}cm^{-3})$	$F_0(T)$	$F_{0H}(T)$	$k_F^x(nm^{-1})$	k_F^z/k_F^x
$4a$	0.25	5.93	6.6	297	300	0.95	2.06
$4b$	0.25	6.31	no data	306	no data	0.96	2.09
1	0.02	6.78	2.51	292	no data	0.94	2.41
3	0.20	7.65	5.16	284	no data	0.93	2.83
2	0.15	10.05	3.46	317	300	0.98	3.16
5	0.30	13.91	8.87	327	360	1.00	(4.69)*

inal doping level is relatively accurate, though it was never confirmed by measurements sensitive to the stoichiometry.

4.3 Temperature Dependance of Quantum Oscillations

4.3.1 Thermal Damping of Quantum Oscillation Amplitude

The effective mass can be extracted from the temperature dependence of the oscillation amplitudes. The amplitude of the dHvA oscillation is damped by the thermal damping factor [23],

$$R_T = \frac{\alpha T m^*}{B \sinh(\alpha T m^*/B)} \tag{4.7}$$

where the effective mass $m = m^* m_e$. m_e is the bare electron mass, $B = \mu_0 H$ is the magnetic flux density, and $\alpha = 2\pi^2 k_B m_e/e\hbar$ ~14.69 T/K.

Fig. 4.11(a) displays the oscillatory amplitude $d\tau$ versus $1/\mu_0 H$ at selected T between 300 mK and 30 K. The curves are offset for clarity. Fig. 4.11 is a temperature dependence with H near the c-axis. ϕ = 4° for panels (a) and (b). Later, the angular dependence of the effective mass will be discussed.

With the external magnetic field fixed, the temperature dependence of normalized $d\tau$ is determined by the effective mass $m^* m_e$ according to eq. 4.7. Fig. 4.11(b) shows $d\tau$ versus T at H = 16.07 T. The oscillating amplitude $d\tau$ is normalized by $d\tau_0$, the amplitude of the quantum oscillation at the lowest temperature, T = 300 mK. Fitting the data with the thermal damping R_T formula in equation 4.7, yields the effective mass $m = 0.194\ m_e$.

To see the effect of Cu dopants on the topological insulator Bi_2Se_3, the same analysis was performed in undoped Bi_2Se_3 as shown in Fig. 4.11(c). Here the field value at which the amplitude analysis is performed is H = 16.5 T. The fit from equation 4.7 yields an

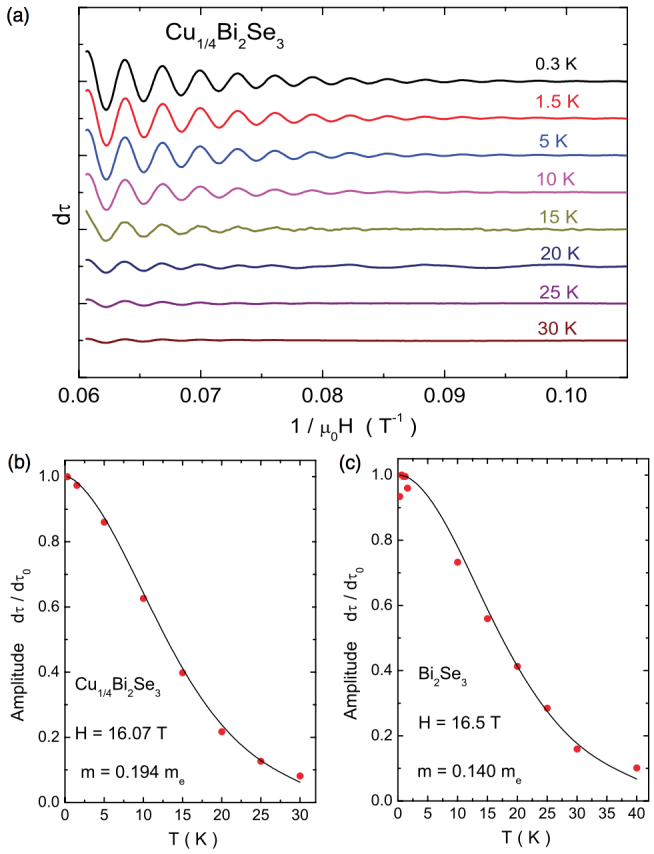

Figure 4.11: Temperature dependence of oscillatory magnetic torque. (a) Magnetic torque after subtracting a polynomial background $d\tau$ is plotted as a function of $1/\mu_0 H$ at selected T between 0.3 and 30 K. The magnetic field, H, is at an angle $\phi = 4°$ from the crystal c-axis. Curves at different T are offset for clarity. (b) In $Cu_{0.25}Bi_2Se_3$, temperature dependence of an oscillating amplitude $d\tau$ yields the effective mass $m = 0.194\ m_e$. (c) In updoped Bi_2Se_3, the T dependence of $d\tau$ at $H = 16.5$ T yields $m = 0.140\ m_e$.

effective mass of $m = 0.140\ m_e$ for undoped Bi_2Se_3. This is in good agreement with other reports [170].

Comparing the thermal damping of quantum oscillations between Cu-doped and undoped Bi_2Se_3 shows that the effective mass increases slightly in the topological superconductor candidate $Cu_{0.25}Bi_2Se_3$. However, this result does not agree with the large mass enhancement suggested by heat capacity measurements [6].

To determine the angular anisotropy of the effective mass, a temperature dependence was taken for sample 4b at two different angles. Fig. 4.12 shows the temperature dependence of the oscillatory torque at two different angles. Fig. 4.12(a) has oscillatory torque curves taken with the magnetic field at a tilt angle of $\phi = 10°$ from the crystal c-axis. The oscillatory torque curves for select temperatures from 0.3 to 25 K are stacked to emphasize

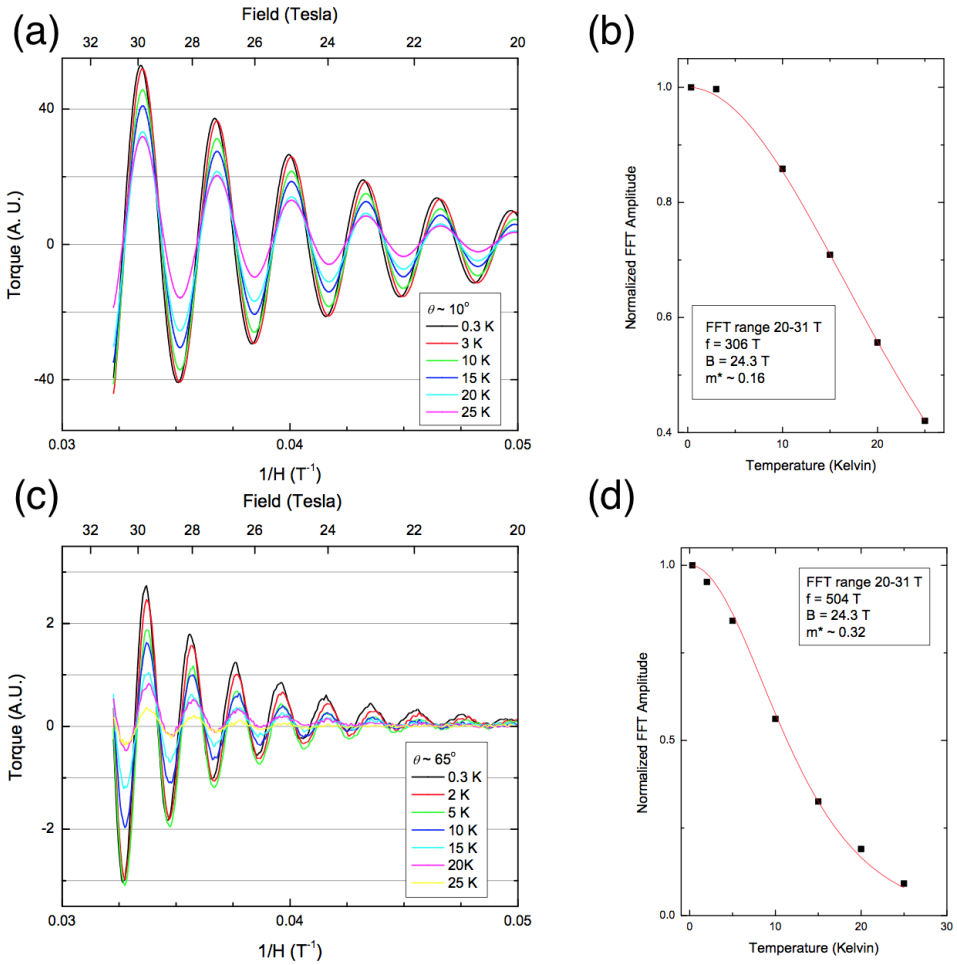

Figure 4.12: Temperature dependence from 0.3 to 25 K of the quantum oscillation amplitude in sample 4b. Oscillatory torque was measured with the magnetic field at a tilt angle of $\phi = 10°$ (panel a) and $\phi = 65°$ (panel c) from the crystal c-axis. Panels (b) and (d) are the normalized amplitude of the FFT on the data in panel (a) and (c) respectively plotted as a function of temperature. The fits gives an effective mass of 0.16 m_e (b) and 0.32 m_e (d).

the damping in the oscillation amplitude.

Differently from before, the normalized amplitude of the FFT peak corresponding to the oscillation frequency is plotted as a function of temperature in fig. 4.12(b). This serves to average the effect of thermal damping over all the oscillation peaks, rather than isolating a single peak whose amplitude is susceptible to errors from the background subtraction. The FFT used to build fig. 4.12(b) is taken in the field range from 20 - 31 T. The frequency of the oscillation at $\phi = 10°$ is 306 T. Equation 4.7 takes a field value as an input. This field value is given to be 24.3 T, which is one over the average of the inverse magnetic fields of the FFT range. The effective mass derived from the fit to the thermal damping factor is 0.16 m_e.

Fig. 4.12(c)(d) show the same analysis with the magnetic field tilted ϕ = 65° from the crystal c-axis. The effective mass increases from 0.16 m_e to 0.32 m_e as the angle increases from 10° to 65°. A temperature dependence on sample 3 was also measured at ϕ = 57° yielding an effective mass of 0.29 m_e. Effective mass anisotropy was seen in early studies of infrared reflection on Cu-doped Bi_2Se_3 measuring $m_{\parallel}/m_{\perp}$ to be 4.35 [169].

The temperature dependence of the oscillations seen in the Hall measurement (see fig. 4.10) was also measured. The effective masses for the various samples extracted by SdH is in good agreement with those extracted from dHvA. Table 4.3 gives the effective mass from dHvA, m_M, and from SdH, m_H, with the field pointed along the c-axis. No temperature dependence was taken for sample 3 with magnetic field along the c-axis. The last two rows of table 4.3 gives the comparison of doped and undoped Bi_2Se_3.

The Fermi velocity, v_F, was determined from the Fermi momentum, k_F^x, and the effective mass by

$$v_F = \frac{\hbar k_F^x}{m^* m_e}. \tag{4.8}$$

Based on the effective mass values and k_F^x, the Fermi velocity is found to be 5.8 $\times$ 10^5 m/s for $Cu_{0.25}Bi_2Se_3$, and 5.7 $\times$ 10^5 m/s for undoped Bi_2Se_3.

The Fermi velocity is the slope of the energy momentum dispersion at the chemical potential. Adding Cu dopants to Bi_2Se_3 adds carriers to the bulk band, and thus increases the chemical potential. As the chemical potential increases, k_F^x will increase. For a quadratic dispersion, the slope of the E-k curve, v_F, increases as the chemical potential (and k_F^x) gets larger. In contrast, for a linear dispersion, v_F should remain unchanged since the slope of a linear band is constant. From undoped Bi_2Se_3 to $Cu_{0.25}Bi_2Se_3$, k_F^x increases by more than 40% from 0.69 nm^{-1} to 0.97 nm^{-1}, yet the value of v_F remains unchanged indicating that carriers sit in a linear, Dirac band.

However, even for a quadratic band the change in the slope of the E-k curve could be small if the chemical potential is sufficiently high on the band. Regardless, the Dirac-like band is consistent with the band structure calculation and ARPES measurements [4, 83]. Furthermore, Se vacancies cause the chemical potential to pin near the bottom of the conduction band at the Γ point in undoped Bi_2Se_3. Nonetheless, the possibility that the chemical potential is high up on a quadratic band cannot be completely ruled out. It should also be noted that the measured Fermi velocity v_F is slightly larger than the averaged v_F measured by ARPES [37].

Table 4.3 gives the Fermi velocities, v_F, and Fermi momentums, k_F^x, for the various samples measured in this study. Sample 3 is omitted from table 4.3 since its temperature

Table 4.3: Effective masses extracted from quantum oscillations in magnetization, m_M, and in the Hall effect, m_H. No temperature dependence was performed on sample 3 with field along the c-axis. The last two rows gives a comparison of doped and undoped Bi_2Se_3. The last column gives the Fermi velocities, v_F, for the various $Cu_xBi_2Se_3$ samples.

	$n_M(10^{19}cm^{-3})$	$F_0(T)$	$\frac{m_M}{m_e}$	$\frac{m_H}{m_e}$	$k_F^x(nm^{-1})$	$v_F(10^5m/s)$
1	6.78	292	0.17	no data	0.94	6.4
2	10.05	317	0.19	0.18	0.98	6.0
4	5.93	297	0.16	0.15	0.95	6.9
5	13.91	327	0.17	0.16	1.00	6.8
$Cu_{0.25}Bi_2Se_3$	4.3	325	0.19	no data	0.97	5.8
Bi_2Se_3	1.8	150	0.14	no data	0.69	5.7

dependence was only measured with the magnetic field tilted away from the crystal c-axis and v_F cannot be determined without the in-plane effective mass. v_F is unchanged between the original $Cu_{0.25}Bi_2Se_3$ and Bi_2Se_3 samples; however, it is higher and more varied in the new samples from the second study. In these samples, v_F varies in a random fashion and not proportionally to k_F^x. Therefore, the variation is indicative of the error in the measurement.

4.3.2 Dingle Damping of Quantum Oscillation Amplitude

Further analysis of the quantum oscillation amplitude damping yields the mean free path and scattering times of the samples.

The amplitude of the quantum oscillations are also damped by the Dingle damping factor,

$$R_D = \exp(-\alpha T_D m/B), \tag{4.9}$$

where the Dingle temperature, T_D, is given by

$$T_D = \hbar/2\pi k_B \tau_S, \tag{4.10}$$

$\alpha = 2\pi^2 k_B m_e/e\hbar \sim 14.69$ T/K, and τ_S is the scattering time. Since T_D is proportional to the scattering rate, $1/\tau_S$, it is a measure of disorder.

Fig. 4.13 is a Dingle plot for $Cu_{0.25}Bi_2Se_3$ (panel a) and undoped Bi_2Se_3 (panel b) with magnetic field along the crystal c-axis and at temperature, T = 300 mK. This plot is made from the base temperature curve of the temperature dependence shown in fig. 4.11. The oscillatory torque, $d\tau$, is normalized by the thermal damping factor, R_T, at 300 mK so that the oscillation amplitude will only be proportional to R_D. Then the logarithm is taken so that the amplitude of the quantum oscillations will be linearly proportional to $1/\mu_0 H$.

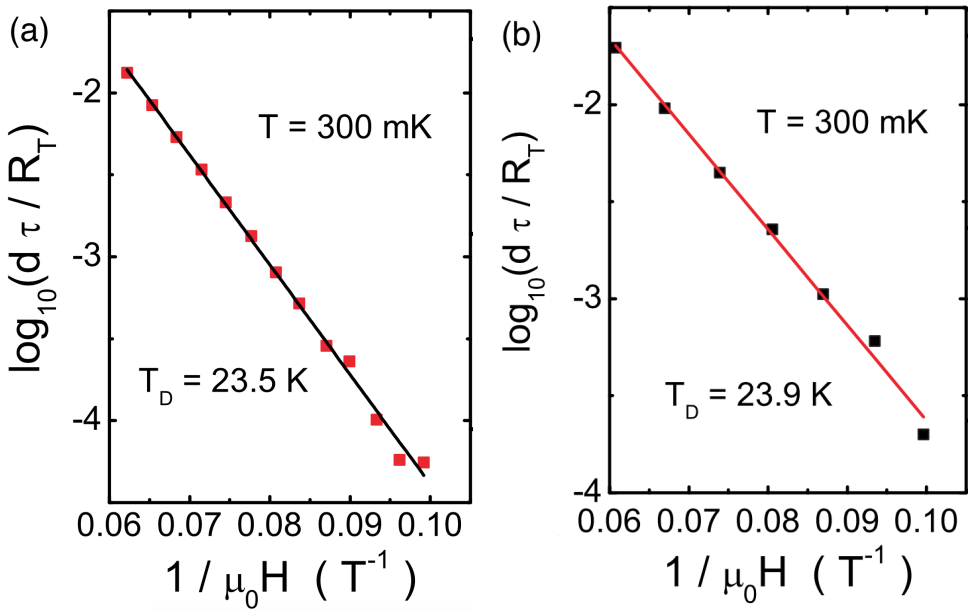

Figure 4.13: Dingle plot of $Cu_{0.25}Bi_2Se_3$ (a) and undoped Bi_2Se_3 (b). Fitting with the Dingle damping factor yields a Dingle temperature of 23.5 K for $Cu_{0.25}Bi_2Se_3$ and 23.9 K for Bi_2Se_3.

The Dingle plot shows the peaks in $\log(d\tau/R_T)$ plotted against $1/\mu_0 H$ with a linear fit. According to equation 4.9, the slope of the linear fit is given by $-\alpha T_D m$, from which the Dingle temperature is extracted to be 23.5 K for $Cu_{0.25}Bi_2Se_3$ and 23.9 K for undoped Bi_2Se_3.

From the Dingle temperature, the scattering time is found to be 5.2×10^{-14} s for $Cu_{0.25}Bi_2Se_3$ and 5.1×10^{-14} s for undoped Bi_2Se_3. The mean free path which is given by

$$l = v_F \tau_S \tag{4.11}$$

is 30 nm for $Cu_{0.25}Bi_2Se_3$ and 29 nm for Bi_2Se_3. Table 4.4 summarizes the Dingle analysis for the various samples. Samples 4b and 3 are not listed because their temperature dependences were taken with the magnetic field tilted far from the crystal c-axis.

In other literature, the Dingle temperature of Bi_2Se_3 varies from 4 K in clean samples [172] to 9.5 K in disordered samples [170]. The higher Dingle temperature in this study suggests that this Bi_2Se_3 sample is very disordered.

With the exception of sample 4, the scattering times and mean free paths are relatively constant with added carriers varying by 25% in a random fashion. The average scattering time, excluding the outlier, is 5.1×10^{-14} s and the average mean free path is 31 nm. The variance in these parameters is due to sample quality. Sample 4 appears to be especially disordered.

Table 4.4: Summary of results from the Dingle analysis. Samples 4b and 3 are not listed here since the temperature dependence for those two samples were taken with the magnetic field tilted far from the crystal c-axis.

	$T_D(K)$	$\tau_s(10^{-14}sec)$	$l(nm)$
1	20.7	5.9	38
2	25.8	4.7	28
$4a$	57.1	2.1	15
5	27.7	4.4	30
$Cu_{0.25}Bi_2Se_3$	23.5	5.2	30
Bi_2Se_3	23.9	5.1	29

Assuming the BCS gap, $\Delta = 1.764 k_B T_c$ the Pippard length can be calculated to be

$$\xi_P = \frac{\hbar v_F}{\pi \Delta} = 230nm, \tag{4.12}$$

which is an order of magnitude larger than the mean free path. Thus the coherence length is determined by the mean free path. Indeed, the coherence length as determined by the upper critical field is 13.9 nm [6], which is on the order of the mean free path determined from quantum oscillations. The dominance of impurity scattering in the superconducting coherence length indicates that superconductivity occurs in the dirty limit.

This analysis considers the ratio of the mean free path and the Pippard length. Assuming the BCS gap, the ratio of T_D to T_c is proportional to the ratio of ξ_P to l by a factor close to one. Thus, the ratio of T_D to T_c also gives a sense of whether a superconductor is in the clean or dirty limit. For $Cu_xBi_2Se_3$, $T_D \sim$ 21 - 57 K and T_c = 3.5 K, which also suggests that superconductivity occurs in the dirty limit.

The disorder measured in $Cu_xBi_2Se_3$ provides a bleak picture for the presence of topological superconductivity in $Cu_xBi_2Se_3$, which requires a p-wave superconducting order. A common feature of p-wave superconductivity is that it is easily destroyed by impurities [7, 93, 94, 97]. However, theoretical works suggest the possibility of disorder-resistant p-wave superconductivity in $Cu_xBi_2Se_3$ [100, 102, 103, 104]. This question is nonetheless troubling and has come up in the debate about topological superconductivity in $Cu_xBi_2Se_3$ as described in chapter 2.

4.4 Discussion

Quantum oscillations are observed in the magnetization of $Cu_xBi_2Se_3$. Based on the quantum oscillation angular dependence, only one Fermi pocket exists in $Cu_xBi_2Se_3$. The doping of Cu to the topological insulator Bi_2Se_3 increases the carrier density and the effective

mass without changing the mean free path or the Fermi velocity, v_F. As v_F determines the slope of the energy dispersion at the chemical potential, the unchanged v_F implies that the added carriers by Cu doping go into the same conductive band as undoped Bi_2Se_3. k_F^x increases by more than 40% in $Cu_xBi_2Se_3$ over Bi_2Se_3, which should lead to an increase in v_F for a quadratic band. The observed unchanged v_F suggests a linear, Dirac band. This is consistent with the expectations for topological superconductivity.

Samples at different doping levels were studied with higher magnetic fields up to 31 T to resolve quantum oscillations up to 90°. The ellipsoidal Fermi pocket was observed to be increasingly elongated as carriers were added, going from being a closed ellipsoid at low carrier concentration to being quasi-cylindrical at high carrier concentration.

The nature of the transition of the Fermi surface topology is an interesting question. At higher concentration, the elongated 3D ellipsoidal Fermi surface touches the Fermi surface in the neighboring Brillouin zone, mandating the transition from the 3D Fermi surface to a quasi-2D cylindrical-like one. Such a dramatic change of the Fermi surface topology suggests a Lifshitz transition [173] or potentially a topological Lifshitz transition [174] as the Cu brings in extra carriers and changes the chemical potential.

Two experimental consequences are essential to confirm the dimensionality change and probe the nature of the transition. First, since every extrema in the Fermi surface cross-section should give rise to quantum oscillations, the highly doped $Cu_xBi_2Se_3$ crystal with the quasi-2D Fermi surface should have two quantum oscillation frequencies, a large one from the belly and a small one from the neck at or near the Brillouin Zone boundary. The large frequency is what was observed in this dHvA study and was confirmed by SdH measurements [11]. In contrast, the small neck frequency was not observed either in dHvA nor SdH [11, 39, 40].

Since this small oscillation frequency arises from a Fermi surface cross-section near the Brillouin Zone boundary, the umklapp scattering will be greatly enhanced. The stronger umklapp scattering can greatly reduce the mean free path [175, 176]. Therefore, quantum oscillation measurements at dilution refrigerator temperatures and even higher fields are needed to resolve the second oscillation frequency and to confirm the 3D to quasi-2D transition.

The second consequence of the dimensionality change in the electronic state is the enhancement of thermopower near the 3D to quasi-2D transition. A topology change in the electronic state usually leads to a large thermopower, a typical signature of the Lifshitz transition [177, 178]. Further thermoelectric measurements are essential to confirm this transition. If the dimensionality change indeed occurs and enhances the thermopower greatly, the Cu doping might lead to another interesting application of topological materials

in thermoelectrics.

Lastly, close to the dimensionality transition, a strong enough magnetic field may lead to magnetic breakdown [179]. The current observations do not reveal the signature of magnetic breakdown, but future studies with fine tuning of the Cu concentration may reveal the interesting phenomenon of magnetic breakdown.

CHAPTER 5

Torque Magnetometry on Nb-doped Bi_2Se_3

There has been much interest in superconductivity induced by copper or strontium dopants in Bi_2Se_3, and extensive studies on those materials reveal their single-band nature [11, 15, 39, 40]. However, questions remain as to whether these materials demonstrate topological superconductivity. The recent discovery of superconducting niobium-doped Bi_2Se_3 makes it an exciting new candidate for the realization of topological superconductivity.

A recent study reveals the coexistence of superconductivity and magnetic ordering in Nb-doped Bi_2Se_3 as well as surface Dirac dispersion [20]. Heat capacity measurements reveal that it has a nodeless superconducting gap consistent with odd-parity p-wave superconductivity [42]. However, penetration depth measures point nodes possibly suggesting an exotic chiral phase [21, 156].

In this early stage, many questions remain about this new topological superconductor candidate. Generally, quantum oscillation experiments are used to reveal the electronic structure of topological materials and topological material candidates. This work, based on my publication [41], was the first, and only to date, report on quantum oscillations in Nb-doped Bi_2Se_3. In Nb-doped Bi_2Se_3, a fully superconducting volume is observed in conjunction with at least two quantum oscillation frequencies. This observation points to a multiband electronic state in Nb-doped Bi_2Se_3 that is distinct from the single-band state seen in the parent compound or Cu-doped and Sr-doped Bi_2Se_3 [11, 15, 39, 40]. Furthermore, my coauthored publication shows rotational symmetry breaking which is indicative of an odd-parity nematic superconducting order [42]. This very interesting combination creates much promise for new physics in this material.

5.1 Superconductivity in Nb-doped Bi_2Se_3

We measured several samples of Nb-doped Bi_2Se_3. Two of these samples from different growth batches, designated samples A and E, are of high enough quality to show a large

superconducting volume. Figure 5.1(a) shows the temperature dependence of the resistivity for samples A and E. Zero resistance is observed below 3.5 K as shown by the inset of Fig. 5.1(a). Figure 5.1(b) shows the volume susceptibility of the two samples measured in a Quantum Design MPMS with an applied magnetic field of 5 Oe. Sample E shows 60% superconducting volume and sample A shows a more than 90% superconducting volume, much higher than that of Cu-doped Bi_2Se_3 [6, 36, 39] and similar to certain dopings in Sr-doped Bi_2Se_3 [15].

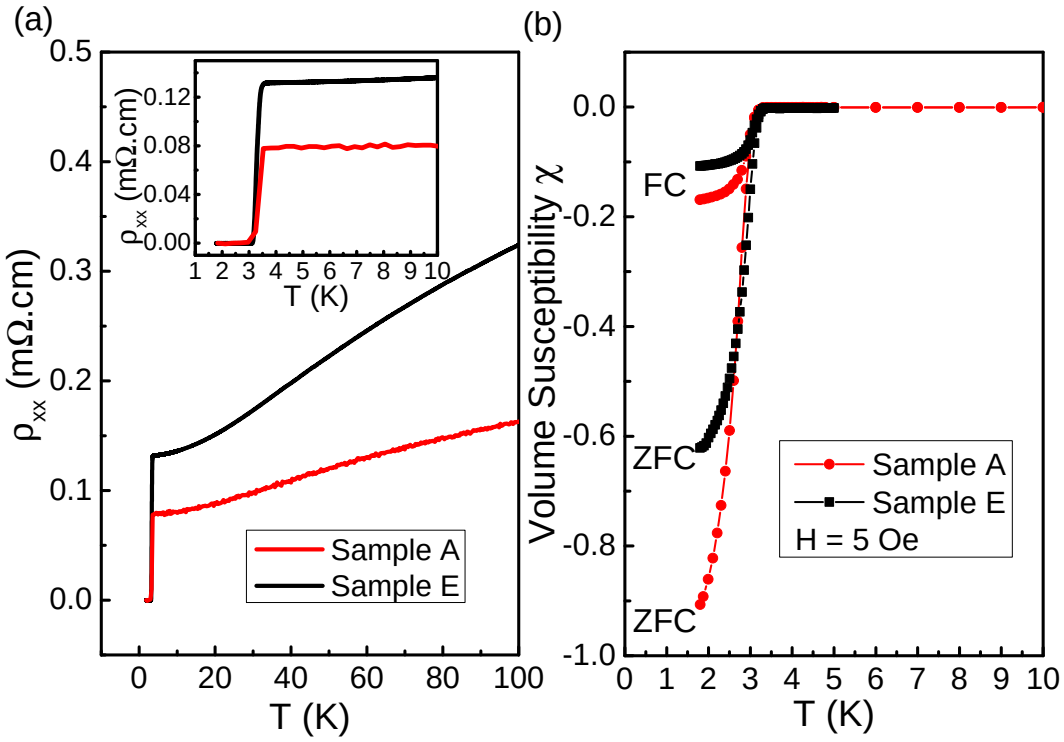

Figure 5.1: Superconducting signal of two Nb-doped Bi_2Se_3 crystals. (a) Resistivity of samples A and E as a function of temperature T . The inset highlights the superconducting transition at 3.5 K. (b) Volume magnetic susceptibility of Nb-doped Bi_2Se_3 crystals, measured in zero-field-cooling (ZFC) and field-cooling (FC) conditions. For sample A, the Meissner effect in the ZFC condition reaches close to -1, indicating a nearly 100% superconducting volume.

The higher superconducting volume fraction makes Nb-doped Bi_2Se_3 a much more convenient material to study than Cu-doped Bi_2Se_3. In addition, there is less concern about experimental results coming from mixed phases.

In addition to resistivity and magnetic susceptibility, heat capacity is a powerful tool to study the properties of superconductors. Fig. 5.2 shows the heat capacity of Nb-doped

Bi_2Se_3 sample A measured in a Quantum Design PPMS. The experimental details of this measurement are described in chapter 3 section 3.3.2.

The heat capacity C was measured at selected T between 0.4 K and 20 K in the helium-3 option of our PPMS. Fig. 5.2(A) shows C/T both in the superconducting state at $\mu_0 H$ = 0 T as well as in the normal state at $\mu_0 H$ = 0.75 T. Above 4 K, the heat capacity C at 0 T is the same as that at 0.75 T, within measurement errors. Therefore, the 0.75 T heat capacity curve can be reliably taken as the normal state heat capacity C_n. From this the phonon contribution was determined following the same practice that was done with Cu-doped Bi_2Se_3 (see Fig. 2.4) [6]:

$$C_n = C_{el}^n(H > H_c) + C_{ph} = \gamma_n T + aT^3 + bT^5 \tag{5.1}$$

where the electronic heat capacity $C_{el}^n(H > H_c) = \gamma_n T$ is the normal state electronic contribution to the heat capacity. By fitting the normal state heat capacity with equation 5.1, the phonon heat capacity, which is unchanged in the superconducting state, can be extracted.

The superconducting state electronic heat capacity C_{el} can be inferred by subtracting the phonon heat capacity, C_{ph}, from the total superconducting state heat capacity, $C(H = 0)$. The resulting superconducting state electronic heat capacity C_{el} at 0 T is plotted as C_{el}/T vs. T in Fig. 5.2(B). The heat capacity at 0 T shows an exponential decay as T drops to base temperature, which is indicative of fully gapped bulk superconductivity.

The exponential decay, rather than a power-law dependence, observed in C_{el} - T is indicative of a nodeless superconducting gap. It has been fairly recognize that in heat capacity measurements, a high order power-law can be hard to distinguish from an exponential decay at low temperatures [8]. For line nodes, C_{el}/T should fall linearly with T, and for point nodes, C_{el}/T should go as T^2 [144, 180]. Line nodes, as have been seen in other unconventional superconductors [181, 182, 183], are not consistent with the data in Fig. 5.2. Therefore, this data is not necessarily in contradiction with the point nodes seen in penetration depth [21]. However, since both this study and the penetration depth study are only performed down to helium-3 temperatures, there remains questions about the nodal structure of the gap. Heat capacity and penetration depth down to 20 mK would provide more robust evidence for a nodal or nodeless gap.

The C_{el}/T trace approaches a finite value γ_{res} near base temperature. This suggests a partial non-superconducting volume in the crystal of about $\frac{\gamma_{res}}{\gamma_n} \sim$<20%. This value is larger than the Meissner effect value of $\sim$10% in sample A. The difference may be from the demagnetization factor due to sample geometry in the SQUID measurement. On the other hand, it is possible that if there are point nodes in the gap, the nodal gap structure

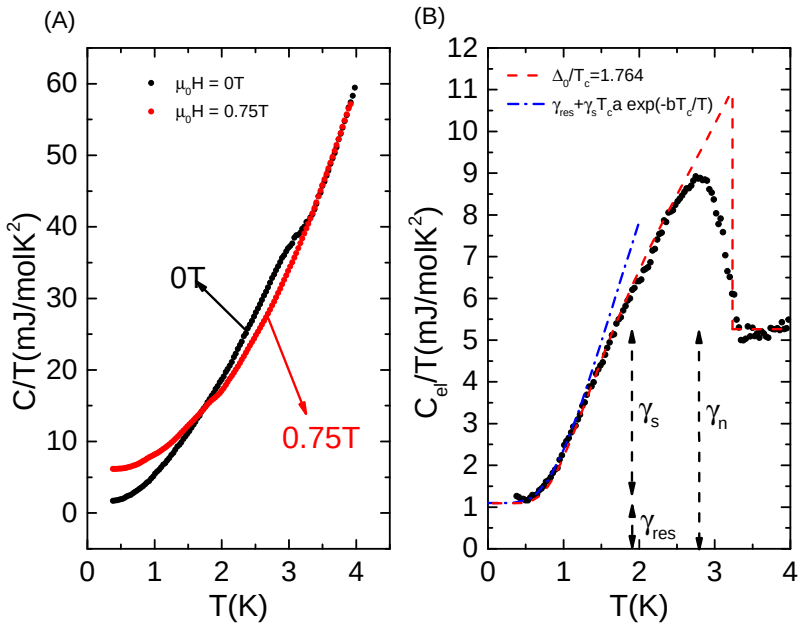

Figure 5.2: Fully gapped bulk superconductivity revealed by the heat capacity of Nb-doped Bi_2Se_3 sample A. (A) Sample heat capacity C is displayed as the ratio of C and temperature T plotted against T. The zero field curve is compared with the $\mu_0 H$ = 0.75 T curve. The 0.75 T curve is used to determine the phonon contribution C_{ph}. (B) The electronic part of heat capacity C_{el} is shown as C_{el}/T vs. T. A clear kink is observed at the superconducting transition temperature T_c. Near T $\sim$ 0, the curve approaches a finite value in C_{el}/T and gives a measurement of the non-superconducting volume fraction of around 20%. As T increases from the base temperature, C_{el}/T follows the exponential curve (dashed pink line), as expected from a fully gapped superconductor. Numerical calculation of C_{el} in BCS superconductors are shown with the only parameter $\alpha \equiv \frac{k_B T_c}{\Delta}$, where Δ is the superconducting gap. For the overall trace, α = 1.76 trace gives the best fit of the heat capacity trace below T_c.

may lead to residual density of states contributing to γ_{res}.

Despite the high superconducting volume fraction, not every $Nb_xBi_2Se_3$ sample shows superconductivity. Fig. 5.3 compares the resistivity (panel a) and volume magnetic susceptibility (panel b) of superconducting sample A with a non-superconducting sample D. Sample D does not show zero-resistance or diamagnetism down to 1.5 K. It is unknown whether this sample will show a superconducting transition in resistance or susceptibility at lower temperature. At 20 mK, a very small superconducting hysteresis loop in the magnetic torque was observed in sample D; however, the amplitude was an order of magnitude smaller than in sample A. Thus sample D does have a small superconducting fraction at zero temperature, though the majority of the sample does not superconduct.

It is not clear what the exact chemical difference is between the superconducting and the

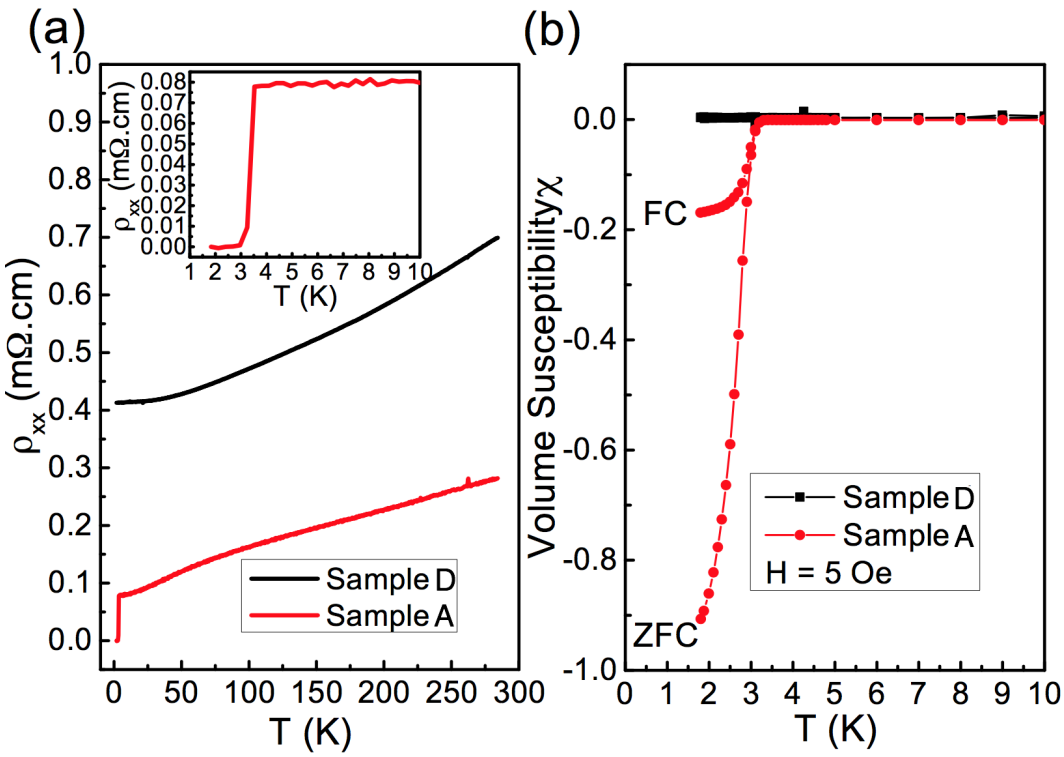

Figure 5.3: The comparison of the electrical resistance (a) and volume magnetic susceptibility (b) of a superconducting (sample A) and non-superconducting (sample D) Nb-doped Bi_2Se_3 crystals.

non-superconducting $Nb_xBi_2Se_3$. Early work on $Nb_xBi_2Se_3$ shows that only the samples with Nb intercalation are superconducting [20]. It is also known that for the superconducting Sr-doped and Cu-doped Bi_2Se_3, the dopant prefers to intercalate between Bi_2Se_3 layers [15, 36].

5.2 Angular Dependance of Quantum Oscillations

Torque magnetometry was used to measure the magnetic properties of Nb-doped Bi_2Se_3. Single crystal samples of Nb-doped Bi_2Se_3, with a nominal stoichiometric Nb concentration of 0.25 for sample A and 0.28 for sample E, were glued to the tip of a beryllium copper thin-film cantilever using GE varnish. Because the Nb concentration was determined from the starting concentration of the reactants, the exact Nb concentration is unknown in these crystals. The torque on the cantilever was then measured by tracking the capacitance between the metallic cantilever and a gold film placed underneath as described in chapter 3.

Due to low field anomalies discussed in section 5.4, the background subtraction of several Nb-doped Bi_2Se_3 torque curves were more complicated than Cu-doped Bi_2Se_3 described in chapter 4. First, the derivative of the raw torque is taken. This does not effect the quantum oscillations, whose derivative are also sinusoidal. Afterwards, the background signal is removed by applying a polynomial fitting in the magnetic field range above the low field anomalies. The residuals of the polynomial fit are just the oscillatory torque signal, τ_{osc}.

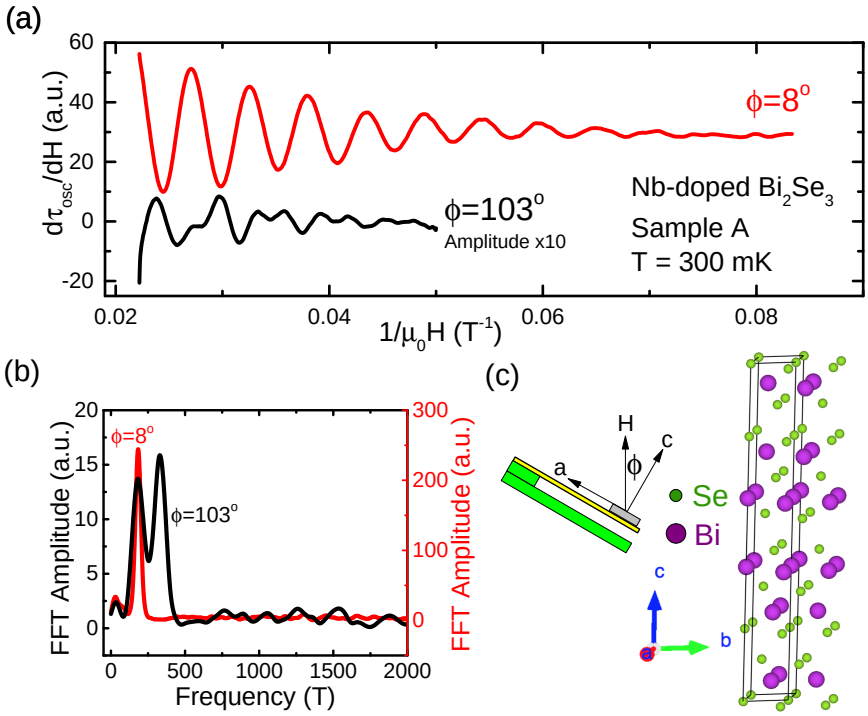

Figure 5.4: (a) Derivative of oscillatory magnetic torque of Nb-doped Bi_2Se_3. Torque from sample A is plotted against inverse magnetic field $1/\mu_0 H$. A polynomial background has been subtracted from the torque $\tau - H$ curves to obtain the oscillatory torque τ_{osc}. The top red curve is taken at a tilt angle of the magnetic field around 8° and shows one oscillation frequency. The lower black curve taken at the magnetic field tilt angle of 103° shows two oscillation frequencies. The amplitude of the second curve is multiplied by a factor of 10 and the two curves have been shifted apart for clarity. (b) The fast Fourier transformation (FFT) of the two $\tau_{osc} - 1/\mu_0 H$ traces. (c) A sketch of the torque magnetometry setup shown together with the crystal structure of Bi_2Se_3 to demonstrate the magnetic field rotation plane.

Examples of $d\tau_{osc}/dH$ plotted against $1/\mu_0 H$ for sample A at two different angles are shown in Fig. 5.4(a). The angle ϕ is defined as the angle between the external magnetic field, H, and the crystal c-axis as shown in the schematic of the torque experiment in fig. 5.4(c). The crystal axes are labeled in the crystal structure diagram in the same panel. Nb

dopants sit intercalated between quintuple Bi_2Se_3 layers.

With the external magnetic field pointing along the c-axis ($\phi = 8°$), a single quantum oscillation frequency is observed similar to Bi_2Se_3, Cu-doped Bi_2Se_3 [39], and Sr-doped Bi_2Se_3 [15]. This can be seen clearly in the FFT of τ_{osc} in fig. 5.4(b). However, at $\phi = 103°$, the two distinct quantum oscillation frequencies are observed, in sharp contrast to Bi_2Se_3, Cu-doped Bi_2Se_3 [39], and Sr-doped Bi_2Se_3 [15]. In fig. 5.4(a), the amplitude of $\tau_{osc}(\phi = 103°)$ is multiplied by a factor of 10 for clarity. The amplitudes of the FFT are plotted on different scales for $\phi = 8°$ (right axis) and $\phi = 103°$ (left axis).

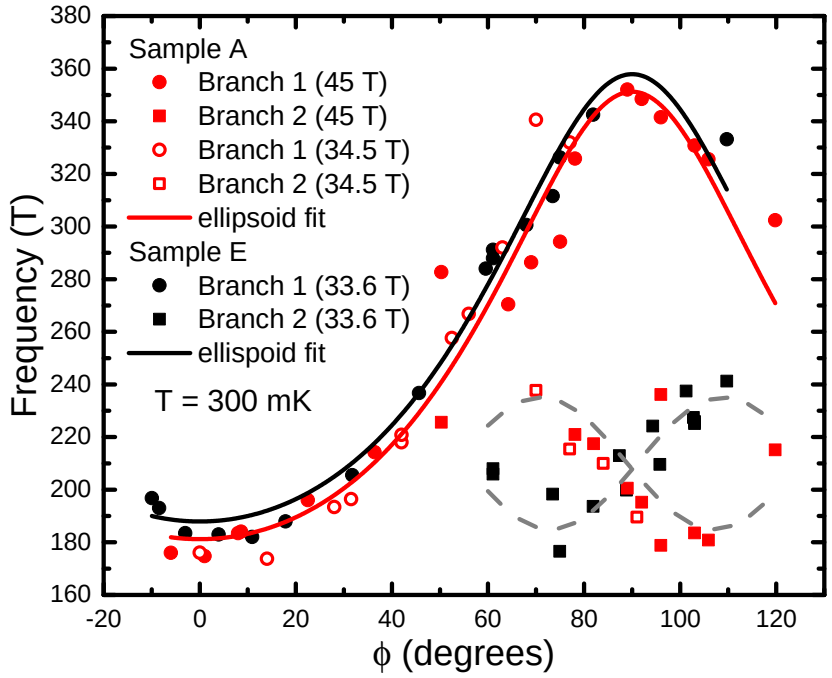

Figure 5.5: Comparison of the angular dependence of the oscillation frequencies of Nb-doped Bi_2Se_3 in sample A (red) and sample E (black) taken at T = 300 mK. The solid lines are fits for ellipsoidal Fermi surfaces. The dashed lines are guides for the eye for the second Fermi pocket. The maximum magnetic field used in each run is labeled in the legend.

Figure 5.5 shows the angular dependence of the dHvA frequencies. Since the dHvA frequency is proportional to the Fermi surface cross section, the angular dependence gives the approximate size and shape of the Fermi surface. These data were taken in three different magnets with different peak magnetic fields. The peak magnetic field is indicated in parentheses in the legend of Fig. 5.5.

In the 33.6 T and 34.5 T magnets, the magnetic field is being rotated from along the

c-axis towards the a-axis. For the 45 T magnet, the magnetic field is being rotated from the c-axis towards the in-plane axis 30° from the a-axis. The angular dependence of the dHvA frequencies does not show any dependence on which in-plane axis the magnetic field rotates into.

There are two branches of quantum oscillation frequencies revealing multiple Fermi surfaces in Nb-doped Bi_2Se_3. The solid lines in Fig. 5.5 are ellipsoidal Fermi surface fits of the first branch of dHvA frequencies. The fitting function is the same as was applied to $Cu_xBi_2Se_3$ (equation 4.3 from chapter 4). The ellipsoidal Fermi surface is located in the center of the Brillouin zone around the Γ point just as it is in the parent compound [39, 170]. Based on the fits and the Onsager relation (equation 3.19 in chapter 3), both samples have an in-plane Fermi momentum of $k_x = k_y \approx 0.75$ nm^{-1} and an out-of-plane Fermi momentum of $k_z \approx 1.43$ nm^{-1} (the details of how this is extracted are discussed in chapter 4 section 4.2). The parameters from the ellipsoidal Fermi surface are summarized in Table 5.1.

The second branch of dHvA frequencies appears at around 60°. This indicates that the superconducting Nb-doped Bi_2Se_3 has an additional smaller Fermi pocket or family of Fermi pockets besides the ellipsoidal pocket seen in the parent compound [39, 170].

The lower branch should be symmetric around 90° because of the crystal symmetry. In the 45 T sweep, there is evidence of splitting in the lower branch of dHvA frequencies indicating the symmetric Fermi pocket. It should be noted, however, that this torque magnetometry study is unable to clearly resolve a splitting of these branches in the 34 T sweeps due to the limited range of the quantum oscillation pattern. As a result, these torque measurements resolve only the dominating feature of the lower branch for each sample, which seems to be asymmetric and varies between samples in the 34 T runs. The sample dependence suggests that the sample quality and even the possible domain structure may affect the apparent features in the FFT spectra. To confirm this frequency splitting, further quantum oscillation studies are required in the higher fields or at lower temperatures in a dilution refrigerator.

The angular dependence of the lower branch of frequencies indicates that the corresponding Fermi surface is tilted with respect to the c-axis. It is probably located away from the Γ point and has symmetric pockets elsewhere in the Brillouin zone. The exact shape of these low-frequency Fermi pockets is unknown. A grey dashed line is drawn on Fig. 5.5 as an eye guide.

The larger Fermi pocket, though slightly fatter and longer, is similar to the bulk Fermi surface in undoped Bi_2Se_3 [39, 170]. However, the second pocket is completely different from anything seen in the parent compound or the other superconducting doped Bi_2Se_3 compounds, such as Cu-doped Bi_2Se_3 [11, 39, 40].

In addition to measuring quantum oscillations in magnetization, quantum oscillations in magnetoresistance were measured in a Quantum Design PPMS using the four probe technique described in chapter 3. The SdH oscillations are shown in fig. 5.6.

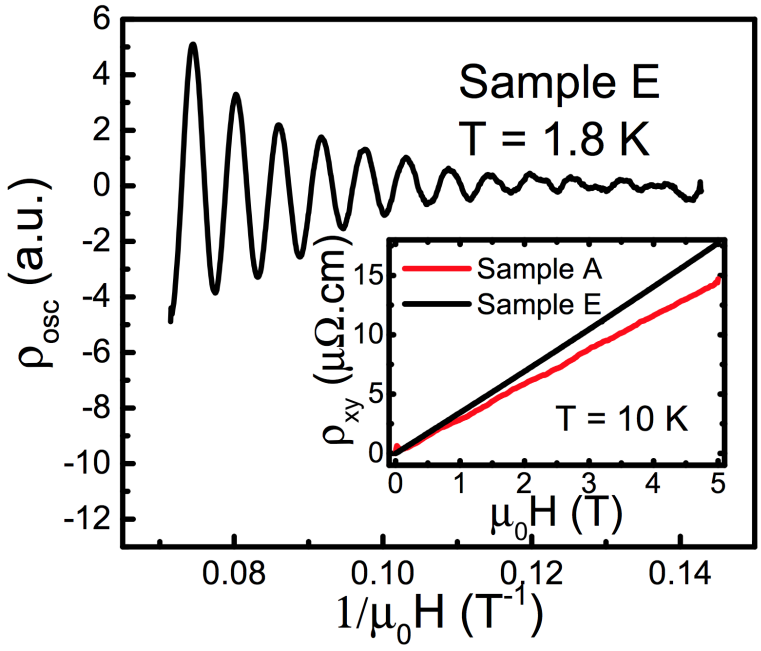

Figure 5.6: Shubnikov-de Haas oscillations in sample E with field along the sample crystalline c axis. The inset shows the Hall signal from the two samples.

To determine the carrier concentration, the Hall effect in both Nb-doped Bi_2Se_3 samples was studied. The Hall data are shown in the inset of fig. 5.6. The carrier density as determined from the Hall effect is n = 2.4 $\times$ 10^{20} cm^{-3} for sample A and n = 1.8 $\times$ 10^{20} cm^{-3} for sample E. The carrier densities are the same order of magnitude of the $Cu_xBi_2Se_3$ sample with the highest carrier concentration. This is the case even though the quantum oscillation frequency in $Nb_xBi_2Se_3$ is half as large as $Cu_xBi_2Se_3$ - indicating a much smaller Fermi surface [40]. Consequently, the second family of Fermi surfaces must contribute many carriers to $Nb_xBi_2Se_3$.

As with $Cu_xBi_2Se_3$, the carrier density can be calculated from the dHvA data using equation 4.5 from chapter 4. However, this will only determine the contribution to the carrier concentration coming from the ellipsoidal Fermi surface. The contribution from the second branch of Fermi pockets cannot be accurately determined since their shape and number are not clear from the data. Nonetheless, the comparison of the ellipsoidal Fermi surface contribution to the carrier density with the carrier density measured by the Hall effect will give a quantitative approximation of the carriers contributed from the second family of Fermi surfaces.

The carrier density coming from the ellipsoidal Fermi surface is calculated to be n=2.6×10^{19} cm^{-3} for sample A and n = 2.8×10^{19} cm^{-3} for sample E. The Hall carrier density is an order of magnitude larger than the carrier density given by the ellipsoidal Fermi surfaces. This indicates that the low frequency branch of quantum oscillations in fig. 5.5 correspond to many symmetric Fermi surfaces in the Brillouin zone. The carrier concentration data from the Hall effect and quantum oscillations are summarized in Table 5.1.

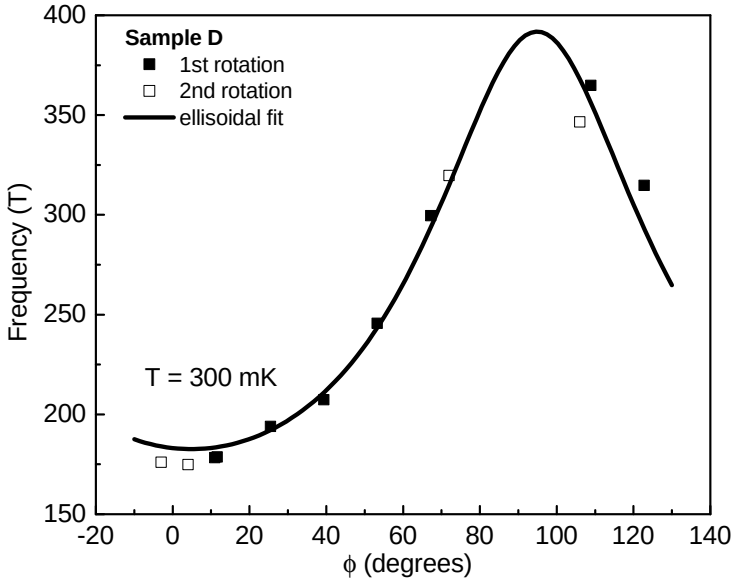

Figure 5.7: Angular dependence of the oscillation frequency in the non-superconducting $Nb_xBi_2Se_3$ sample D. Unlike samples A and E, there is only a single quantum oscillation frequency arising from the ellipsoidal Fermi surface for all angles.

Finally, the quantum oscillations of the non-superconducting sample D were measured. Fig. 5.7 shows the angular dependence of the quantum oscillation frequency for $Nb_xBi_2Se_3$ sample D. Filled squares and empty squares represent data taken different days during the same cool down.

Similarly to samples A, E, and $Cu_xBi_2Se_3$, the quantum oscillation frequencies follow the angular dependence of an ellipsoidal Fermi surface as shown by the fitting function. However, unlike the other $Nb_xBi_2Se_3$ samples, there is no evidence of a second branch of quantum oscillation frequencies in the non-superconducting sample D. Sample D was measured on a stiffer cantilever with a thicker beam width, thus it was less sensitive than the cantilevers used for samples A and E. Indeed, no quantum oscillations were observed, even for the ellipsoidal pocket, in the angular range where most of the second branch oscillations occured ($\sim 70^\circ$ - 110°). However, for samples A and E, the low frequency branch persists down to 60° and up to 120°. Furthermore, the carrier concentration extracted from

the ellipsoidal fit for sample D (n=3.0$\times 10^{19}$ cm^{-3}) is in good agreement with the carrier concentration extracted from the Hall effect for the same sample (n=2.8$\times 10^{19}$ cm^{-3}). Thus all the carriers in the non-superconducting sample D arise from the ellipsoidal Fermi surface. This suggests that the second family of Fermi surfaces are only present in the superconducting $Nb_xBi_2Se_3$ and could be related to the superconducting mechanism.

The observed quantum oscillation signals show a sharp contrast between the fully superconducting Nb-doped Bi_2Se_3 and its non-superconducting counterpart. However, there is still much similarity in their magnetic response, which will be expounded upon in section 5.4.

Table 5.1: Parameters extracted from Torque Magnetometry and Transport in Nb-doped Bi_2Se_3. n_M is the contribution to the carrier density extracted from the quantum oscillations arising from the ellipsoidal Fermi surface. χ(T$\rightarrow$0) is the volume susceptibility measured with a SQUID magnetometer.

	χ(T$\rightarrow$0)	$n_M(10^{19}cm^{-3})$	$n_H(10^{19}cm^{-3})$	$F_0(T)$	$k_F^x(nm^{-1})$	k_F^z/k_F^x
Sample A	-0.9	2.6	24	181	0.74	1.9
Sample E	-0.6	2.8	18	188	0.76	1.9
Sample D	0	3.0	2.8	183	0.75	2.1

5.3 Amplitude Damping of Quantum Oscillations

Examples of the temperature dependence of the FFT amplitude on τ_{osc} are plotted as a function of temperature in Fig. 5.8. This is done in the same fashion as in section 4.3.1 of chapter 4 and is described in detail there. Included is a fit of these data to equation 4.7 from chapter 3 which yields effective masses of the large and small pockets in Nb-doped Bi_2Se_3 samples. The results are listed in Table 5.2.

For sample E, the temperature dependence on the ellipsoidal pocket at ϕ = 0° was performed on the SdH oscillations shown in Fig. 5.6. The frequency of oscillations and effective mass extracted from SdH are in good agreement with dHvA.

The damping of the dHvA oscillations with respect to the field gives a measure of the electron scattering in the crystal. This is called Dingle damping and is described in chapter 4 section 4.3.2. The insets in Fig. 5.8 show the log of the amplitudes of the peaks from the plot of τ_{osc} - 1/$\mu_0 H$ after dividing out the thermal damping factor. The fit using equation 4.9 from chapter 3 yields the Dingle temperature T_D from which the scattering time and mean free path can be extracted. The results of the Dingle analysis are summarized in Table 5.2.

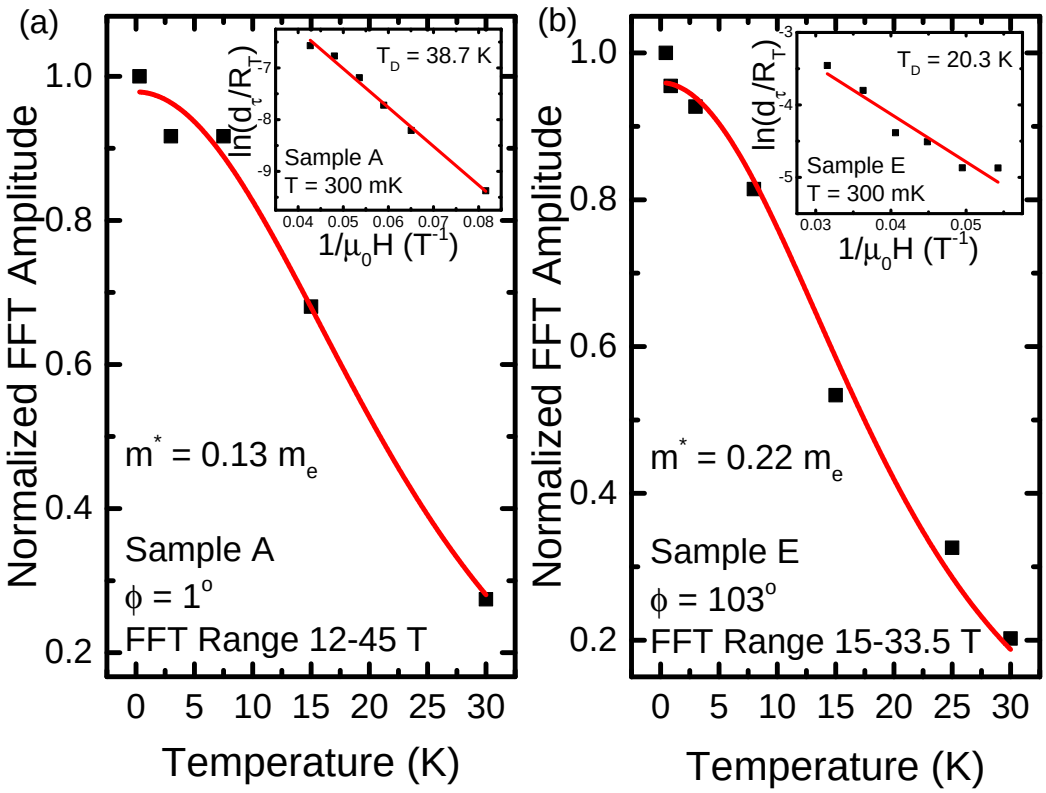

Figure 5.8: Temperature dependence of the oscillation amplitude of (a) sample A at $\phi = 1°$ and (b) ample E at $\phi = 103°$. The insets are the Dingle fits of the oscillation amplitude, with the vertical axis the ratio of the log of the oscillation amplitude and the thermal damping factor.

Furthermore, the scattering time of the lower branch is the same order of magnitude as the higher branch. Therefore, disorder and Dingle phase smearing would unlikely prevent observing the lower branch if the higher branch is observed. If the lower branch is missed, it is due to an intrinsic difference of the electronic state. Therefore, the missing branch of quantum oscillations in sample D is likely intrinsic. The results from the amplitude damping analysis in sample D are also given in Table 5.2.

Lastly, the mean free paths in these crystals are on the order of 20 - 60 nm, which is about two orders of magnitude longer than the crystal lattice. The mean free path of sample A and D are very similar, despite the fact that sample A has the highest superconducting volume and sample D is non-superconducting. The cleanest sample is sample E with l = 60 nm. So it does not appear that the superconducting fraction is related to the variation in the cleanliness of the samples.

Table 5.2: Information extracted from torque magnetometry and transport in Nb-doped Bi_2Se_3. The effective mass and scattering time of the ellipsoidal pocket in sample E was determined from Shubnikov-de Haas oscillations. m_{EP} is the effective mass of the ellipsoidal pocket taken with field along the crystal c-axis. m_{LB} and τ_{sLB} are taken from the low branch quantum oscillations in samples A and E. The temperature dependence for the low branch frequencies was done at ϕ = 72° and 103° for samples A and E respectively. Sample D doesn't show any quantum oscillations from the low branch.

	m_{EP}	v_F (10^5 m/s)	τ_s (10^{-14}s)	l (nm)	m_{LB}	τ_{sLB} (10^{-14}s)
Sample A	0.13 m_e	6.5	3.1	20	0.26 m_e	2.2
Sample E	0.12 m_e	7.3	8.2	60	0.22 m_e	6.0
Sample D	0.12 m_e	7.4	2.2	16	n/a	n/a

5.4 Magnetic Order

So far the sharp contrast in the quantum oscillation patterns of the superconducting and non-superconducting Nb-doped Bi_2Se_3 has been demonstrated. However, there is still similarities in their magnetic response. Fig. 5.9 shows the magnetic torque of the non-superconducting crystal (Sample D) and superconducting crystal (Sample A) of Nb-doped Bi_2Se_3. Both samples display distinct peaks near $\mu_0 H$ = 9 T. The peaks in the τ - H curves suggest that the field-driven magnetic transitions in Nb-doped Bi_2Se_3 do not depend on superconductivity, nor the electronic state revealed by the high field quantum oscillations.

It is unclear from the torque curve what is the exact nature of the magnetic order. However, the first study on Nb-doped Bi_2Se_3 reported an unusual magnetic order and the coexistence of superconductivity and ferromagnetism [20]. The bump feature in Fig. 5.9 cannot confirm that feature; however, such a magnetic transition has never been seen in either Cu-doped Bi_2Se_3 or undoped Bi_2Se_3.

5.5 Rotational Symmetry Breaking

As discussed in chapter 2, basal plane rotational symmetry breaking has been predicted to be a sign of odd-parity topological superconductivity. Such a feature has been observed in Cu-doped Bi_2Se_3 [13, 14] and Sr-doped Bi_2Se_3 [19]. This study, which utilizes a completely new technique, was the first observation of nematic superconductivity in Nb-doped Bi_2Se_3 [42].

Though this result is a central aspect of my dissertation research and I made significant contributions, this project was lead by my colleague Tomoya Asaba who deserves most of the credit. In this section, I will briefly discuss the key results. For greater detail, see ref. [42] and its supplemental materials.

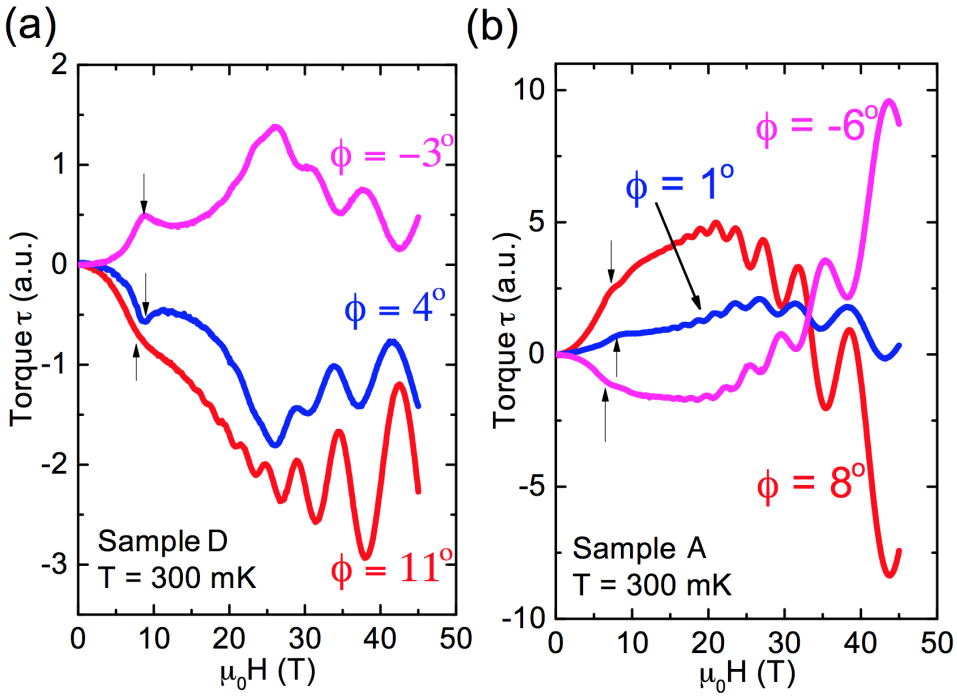

Figure 5.9: (Panel a) The τ - H curves of sample D - the non-superconducting crystal of Nb-doped Bi_2Se_3. The magnetic field H is close to the c-axis of the crystal, and the sample temperature is at 300 mK. (Panel b) The τ - H curves of sample A - a superconducting crystal of Nb-doped Bi_2Se_3 under the same conditions. Black arrows indicate a bump in the torque curve indicative of a magnetic transition.

To measure basal plane rotational symmetry, the torque is measured by mounting the sample on the cantilever standing on its edge. This serves to keep the external magnetic field in the sample's ab plane. A schematic of this set up is shown in Fig. 5.10(a). In addition, a photograph of the experimental setup is given in Fig. 3.3 and Fig. 3.17 from chapter 3. Then, as the cantilever is rotated, an azimuthal angular dependence of the sample's superconducting properties can be studied.

Fig. 5.10(b) shows the crystal structure of Nb-doped Bi_2Se_3 looking down the crystal c-axis. The crystal is made of layered hexagons. The azimuthal angle ϕ is the angle between the external magnetic field and the x-axis, which is defined to be along the cantilever arm. XRD was performed on sample A (which was used in this study) to determine the crystal axes. ϕ = 0°, 60°, and 120° correspond to the in-plane mirror lines of the crystal (marked by dashed lines in Fig. 5.10(b)). The blue arrows in Fig. 5.10(b) are the in-plane crystal axes (30° away from the mirror lines).

In a type-II superconductor, the magnetization as a function of magnetic field shows hysteresis while in the mixed state. An explanation of this phenomena based on the Bean

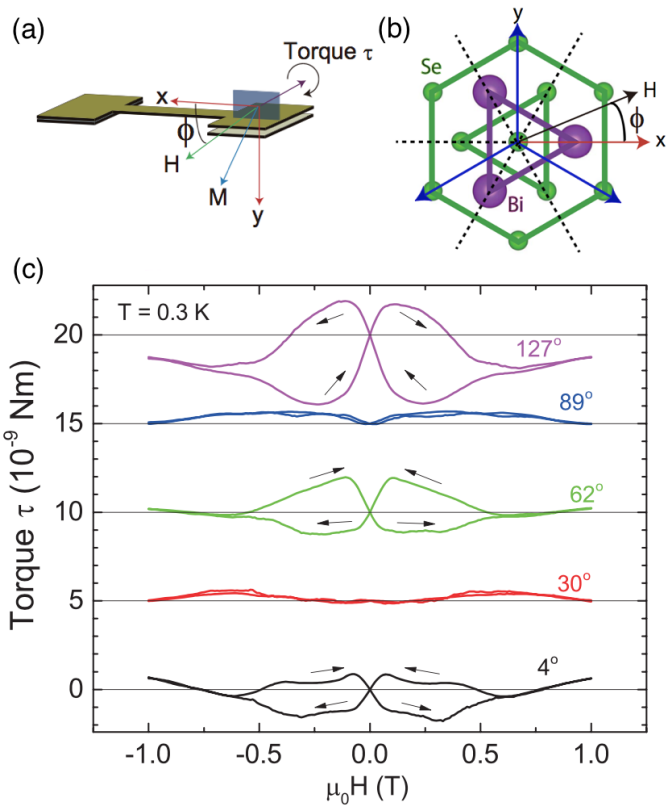

Figure 5.10: Experimental setup, basal plane crystal symmetry, and select torque curves for basal plane study of $Nb_xBi_2Se_3$. (a) Schematic of the torque magnetometry setup with field isolated to the ab plane. The azimuthal angle ϕ is defined as the angle between the external magnetic field and the cantilever arm (x axis). (b) Crystal structure of $Nb_xBi_2Se_3$ viewed down the crystalline c axis. The dashed lines are the mirror planes of the crystal, and the blue arrows are the crystal axes. (c) Selected torque curves at 0.3 K at different ϕ. The magnitude of the hysteresis loop is maximum near ϕ = 120° and is almost zero at 30° and 90°.

model is given in appendix B. Studying the angular dependence of the magnitude of the hysteresis (which is related to the critical current density - a property of the superconducting state) provides a way to probe the basal plane symmetry in the superconducting state.

Figure 5.10(c) shows several magnetic torque curves with evident superconducting hysteresis. Black arrows indicated the direction of the field sweep. The torque, τ, is plotted against the external magnetic field at temperate T = 0.3 K. Unlike quantum oscillations, which require a high magnetic field to resolve, magnetic hysteresis only occurs below the upper critical field, H_{c2}. Therefore, only a low magnetic field is needed. As can be seen, the whole hysteresis loop appears as the field is swept up and down from -1 T to 1 T.

Even from just a select few curves, a pattern is clear. The magnitude of the hysteresis loop is almost zero at 30° and 90°, and non-zero at 0°, 60°, and 120°. In addition, it is

maximum near ϕ = 120°. A more thorough look at the angular dependence below will confirm this periodicity.

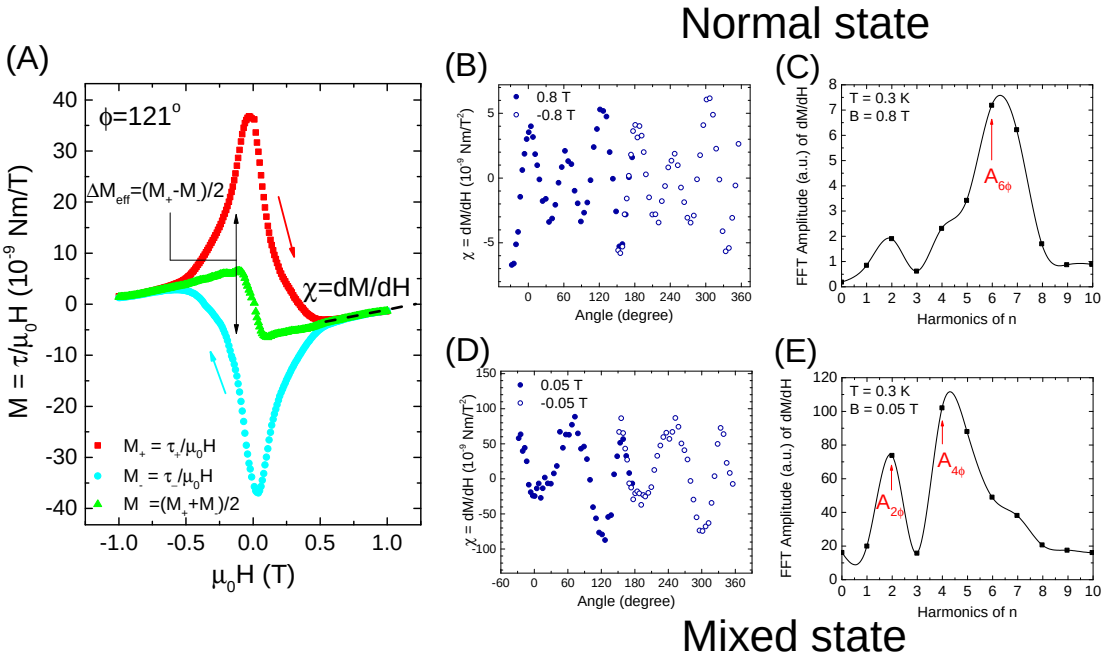

Figure 5.11: (a) An example of the hysteresis in the $M - H$ curve. The definition of M, ΔM, and χ are given. Note that τ_+ (τ_-) is the torque signal from the up-sweep (down sweep) of the magnetic field. (b) Angular dependence of effective susceptibility χ in a normal state at 0.3 K. The azimuthal angle ϕ is defined in Fig. 5.10. The open circles are the negative field data which is equivalent to a 180° cantilever rotation. (c) The FFT plot of the data shown in (b). (d) Angular dependence of effective susceptibility χ in a superconducting state at 0.3 K. (e) FFT plot of the data shown in (d). The contrast between the pattern in the normal state and the superconducting state demonstrates the breaking of the rotational symmetry in the superconducting state.

Figure 5.11(a) shows the definition of the features investigated for rotational symmetry breaking. This is a plot of the sample's magnetization, $M = \tau/\mu_0 H$, as a function of magnetic field. The magnetic torque from the upsweep (downsweep) is defined as τ_+ (τ_-) and the corresponding magnetization is M_+ (M_-). The average magnetization $M = (M_+ + M_-)/2$ gives the intrinsic magnetic susceptibility of the sample, $\chi = dM/dH$.

Rotational symmetry breaking should only occur in the superconducting state; therefore the area in the hysteresis loop, where the sample is in the mixed state, is of interest. By comparison, outside of the mixed state, where the upsweep and downsweep magnetization overlap, there should be no basal plane symmetry breaking. Fig. 5.11(b) and (d) show the magnitude of χ as a function of azimuthal angle ϕ for the normal state ($\mu_0 H = \pm 0.8$ T) and mixed state ($\mu_0 H = \pm 0.05$ T) respectively. The negative field value of the hysteresis

loop corresponds to a rotation of 180° and is represented by open circles.

The FFTs of the angular dependence of χ from Fig. 5.11 panels (b) and (d) are given in panels (c) and (e) respectively. This gives the periodicity of the magnetic susceptibility in the normal and mixed states. The dominate peak in the FFT for the normal state is at 6ϕ - corresponding to the symmetry of the hexagonal crystal. However, in the mixed state, the FFT has peaks at 2ϕ and 4ϕ, which results from an enhancement of χ along one particular crystal axis, breaking the rotational symmetry. For more detail on what harmonics in the FFT are expected, see ref. [42].

The symmetry breaking is even more pronounced in the magnitude of the hysteresis loop itself defined as $\Delta M_{eff} = (M_+ - M_-)/2$ in Fig. 5.11(a). The angular dependence of ΔM_{eff} at different magnetic fields is shown in Fig. 5.12(a).

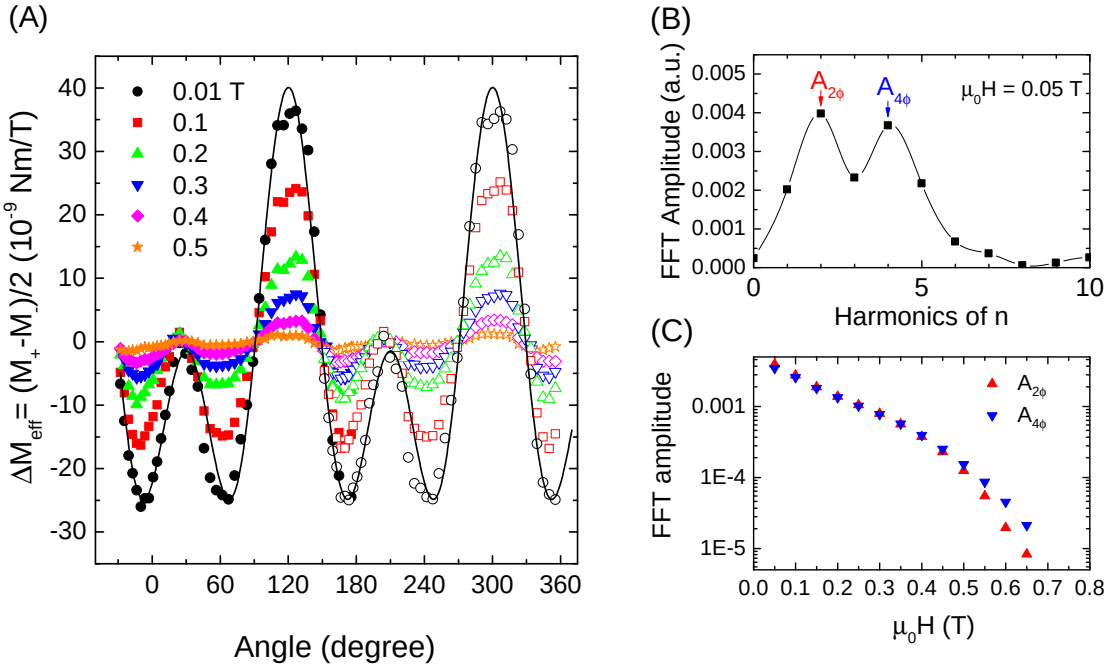

Figure 5.12: (a) The angular dependence of the effective magnetization, ΔM_{eff}. The data were taken at 0.3 K at a few selected H fields. Data taken from the positive field sweep are plotted as filled symbols, and data from the negative field sweep are plotted as open symbols. The solid line is the fitting function $f(\phi) = 2A_{2\phi}\sin(\phi - 30°)\cos 3\phi$. (b) FFT of $\Delta M_{eff} - \phi$ at $\mu_0 H$ = 0.05 T. The first peak, $A_{2\phi}$, is the amplitude of the nematic order term. (c) The magnetic field dependence of the FFT amplitudes $A_{2\phi}$ and $A_{4\phi}$ in the superconducting state of Nb-doped Bi_2Se_3. The FFT amplitude is plotted in logarithmic scale for clarity. Above 0.6 T, the superconducting hysteresis loop quickly vanishes as H approaches the upper critical field.

The FFT of the 0.05 T data in Fig. 5.12(a) shown in panel (b) has the same 2ϕ-4ϕ

feature expected for broken in-plane symmetry. In addition, it is clear from the raw data in panel (a) that the magnitude of ΔM_{eff} is greatly enhanced along 120° and 300°, a 180° difference representing a single nematic axis as predicted by Fu (see chapter 2 section 2.1.3) [12]. Fig. 5.12(c) shows the amplitude of the 2ϕ and 4ϕ components as the sample transitions from the mixed state to the normal state. Though they both dramatically decrease, the 2ϕ component, resulting from the nematic axis, falls of quicker as the sample approaches the normal state.

Since the amplitude of the 2ϕ and 4ϕ components are equal, ΔM_{eff} is fit by the function $f(\phi) = 2A_{2\phi}\sin(\phi - 30°)\cos 3\phi$, which is plotted as a black line in Fig. 5.12(a). The effective superconducting magnetic moment follows the product of $\sin(\phi - 30°)$ and $\cos 3\phi$, rather than the sum of two ordering functions. Therefore, there is a strong coupling between the crystalline symmetry and nematic ordering possibly suggesting that the nematic order is stabilized by the crystalline symmetry, (i.e. the nematic axis is locked to one of the mirror planes of the triangular lattice).

The breaking of rotational symmetry can be seen more easily when the data from Fig. 5.12(a) is plotted in polar coordinates. However, when doing so, the information about the sign is lost. Nonetheless, Fig. 5.13 shows the effective magnetization plotted in polar coordinates. The polar plot has six lobes reflecting the basal plane crystal symmetry of $Nb_xBi_2Se_3$ seen in Fig. 5.10(b). However, one axis is clearly enhanced.

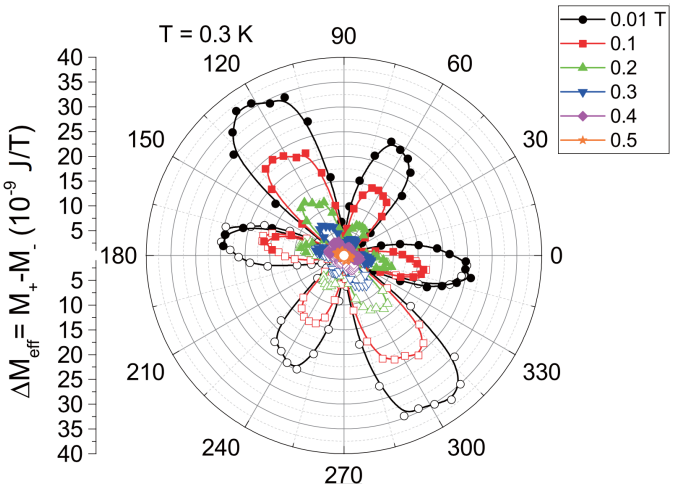

Figure 5.13: Data from Fig. 5.12(a) plotted in polar coordinates. The six lobes correspond to the crystal symmetry, and the nematic axis is evident.

As pointed out in ref. [12], the nematic order verifies the two-component nature of the superconducting order parameter. Thus, an odd-parity, E_u superconducting order is very likely to exist in the ground state, which creates promise for topological superconductivity in Nb-doped Bi_2Se_3.

5.6 Discussion

One question that could arise is whether the second family of Fermi pockets are an intrinsic property of Nb-doped Bi_2Se_3 or if they comes from crystallized domains of other materials such as $NbSe_2$, $NbSe_3$, or elemental Nb present in the samples. $NbSe_3$ is not superconducting unless under pressure, and it shows dominant quantum oscillation frequencies under 100 T [184, 185, 186]. This is much smaller than either Fermi pocket seen in these Nb-doped Bi_2Se_3 samples. Moreover, 2H-$NbSe_2$ shows superconductivity, but the T_c = 7.2 K [187] is much higher than the critical temperature in Nb-doped Bi_2Se_3. Quantum oscillations in 2H-$NbSe_2$ show only one Fermi pocket with F_0 = 150 T that increases up to 400 T at $\sim$80° [187, 188]. This is distinctly different from the Fermi surfaces observed here, suggesting that the dHvA signal in Nb-doped Bi_2Se_3 is not from unintended crystallization of $NbSe_2$ and $NbSe_3$. The smallest orbital observed in elemental Nb is 8.1 nm^{-2} [189, 190] corresponding to a dHvA frequency of 850 T, which is much higher than the quantum oscillation frequencies reported here in Nb-doped Bi_2Se_3.

This leads to an important question: Why does Nb intercalation in Bi_2Se_3 lead to multiple Fermi surfaces when Cu and Sr intercalations do not? It is possible that Nb introduces d-orbital electrons causing the multiple-orbit feature observed in this study. A preliminary calculation of the band structure suggests the Nb d states are very close to the chemical potential in Nb-doped Bi_2Se_3. These results call for a detailed electronic band structure calculation, the results of which can be compared to the observed quantum oscillation patterns reported here. These further steps will map the exact electronic ground state of the newly discovered superconductor Nb-doped Bi_2Se_3.

The observation of the multiple orbits in the superconducting Nb-doped Bi_2Se_3 also points to Fermi surface nesting as a possible superconducting mechanism. In many families of Fe-based superconductors, where unconventional s-wave pairing is believed to exist, the superconducting pairing mechanism has been attributed to the nesting between electron and hole pockets [191, 192, 193]. To check this possibility for Nb-doped Bi_2Se_3, further experiments are needed to look for the charge density wave that would arise from the Fermi surface nesting. Such a charge density wave pattern may be detected by scanning tunneling microscopy or photoemission.

CHAPTER 6

Conclusion

In conclusion, quantum oscillations are observed in the magnetization of $Cu_xBi_2Se_3$ and $Nb_xBi_2Se_3$. Based on the quantum oscillation pattern, only one Fermi pocket exists in $Cu_xBi_2Se_3$; however, for $Nb_xBi_2Se_3$, there are several Fermi pockets showing that Nb dopants change the band structure of the parent compound. In addition, the second family of Fermi pockets in $Nb_xBi_2Se_3$ only occur in the superconducting samples. The observation of this multi-orbital nature reveals the complex electronic ground state of superconducting Nb-doped Bi_2Se_3. It also sheds light on the superconducting pairing mechanism in this unconventional superconductor.

By comparing the quantum oscillations in $Cu_xBi_2Se_3$ with the undoped topological insulator Bi_2Se_3, it is found that the doping of Cu increases the carrier density and the effective mass without changing the mean free path. The Fermi velocity stays the same after the Cu doping, which implies the band structure is Dirac-like and is not affected by the insertion of Cu.

Higher field quantum oscillations in $Cu_xBi_2Se_3$ reveal that the single ellipsoidal Fermi pocket increasingly elongates as carriers are added, going from being a closed ellipsoid at low carrier concentration to being quasicylindrical at high carrier concentration. This disagrees with the theory of topological superconductivity developed by Fu and Berg [5].

Therefore, the analysis of the quantum oscillations has cast doubt that $Cu_xBi_2Se_3$ will be the first topological superconductor. However, given the Dirac-band structure, it is still a prime candidate in the low doped regime when the Fermi surface is elliptical.

$Nb_xBi_2Se_3$ is an exciting new candidate for topological superconductivity. The observation of multiple Fermi surfaces fails to answer whether the Fermi surface contains an odd-number of TRI momenta. However, it does show the unique role of Nb-dopants as compared to the Cu or Sr dopants. Exotic magnetic transitions at 9 T suggest that $Nb_xBi_2Se_3$ holds more interesting physics unseen in other doped Bi_2Se_3 compounds, and thus it is a worthwhile candidate for further study. Finally, as predicted for E_u topological

superconductivity, the observation of basal plane rotational symmetry breaking in the superconducting state makes $Nb_xBi_2Se_3$ a platform for exciting new physics. This work is among the very first studies on $Nb_xBi_2Se_3$.

The properties of $Cu_xBi_2Se_3$ and $Nb_xBi_2Se_3$ are quite different. The later has a much higher superconducting volume, which is more robust over time. As far as their electronic properties, they both have an ellipsoidal Fermi surface similar to the parent compound Bi_2Se_3. The size of the ellipsoidal pocket in $Nb_xBi_2Se_3$ is similar to Bi_2Se_3 though it is much larger in $Cu_xBi_2Se_3$. Despite this, the carrier concentration in $Nb_xBi_2Se_3$ is higher than in $Cu_xBi_2Se_3$ due to its extra Fermi surfaces. These differences show that though both materials are candidates for topological superconductivity, they likely host different physics.

APPENDIX A

Time-reversal Polarization

An article by Fu and Kane derives equation 1.1 from the time reversal polarization for a one dimensional insulator [43]. They further argue that this topological invariant is equivalent to the Z_2 topological order that describes the quantum spin hall effect [27, 28]. These results are novel because the Chern number derived from the change in the charge polarization, which gives rise to the Hall conductivity of a band insulator, is zero for a TRI system [51, 194, 195]. Here I will go through the derivation of equation 1.1 for a TRI insulator by looking at a one dimensional insulator.

For a TRI insulator, the Bloch eigenstates come in degenerate Kramers pairs given by

$$\left|u_n^I(-\mathbf{k})\right\rangle = -\mathrm{e}^{i\chi_{\mathbf{k},n}}\Theta\left|u_n^{II}(\mathbf{k})\right\rangle \tag{A.1}$$

where the indices, I and II, label the Kramer's pair and the index, n, labels the band. This is the same as the notation in section 1.2.1 except with the Kramers pairs labeled explicitly. $\mathrm{e}^{i\chi_{\mathbf{k},n}}$ is the phase factor from the time-reversal operation. Fig. A.1 shows the bands of a one dimensional insulator with with the time-reversed Kramer's pairs. Γ_i are the TRI momenta.

The Berry vector potential is the defined as

$$A^s(\mathbf{k}) = i\sum_n \left\langle u_n^s(\mathbf{k})\right| \nabla_{\mathbf{k}} \left|u_n^s(\mathbf{k})\right\rangle, \tag{A.2}$$

where s is the Kramer's index I or II. The charge polarization from one of the Kramer's pairs is given by

$$P^s = \frac{1}{2\pi}\oint_C d\mathbf{k}A^s(\mathbf{k}) = \frac{1}{2\pi}\int_{-\Gamma_2}^{\Gamma_2} d\mathbf{k}A^s(\mathbf{k}), \tag{A.3}$$

where C is a closed loop in the Brillouin zone containing the TRI momenta. The second equality for a one dimensional insulator holds because of the periodic nature of the Brillouin zone - the integral from $-\Gamma_2$ to Γ_2 is a closed loop.

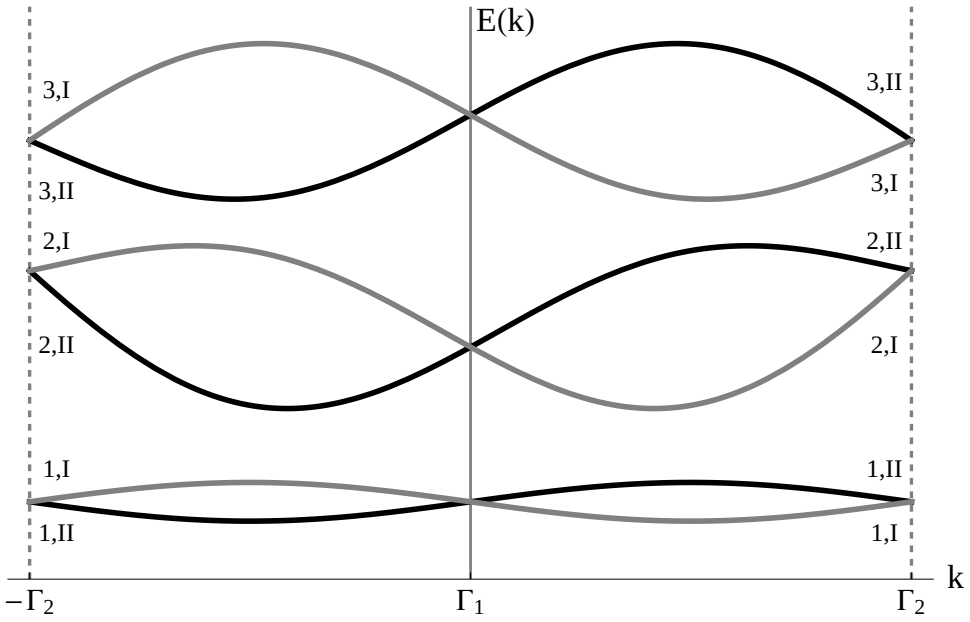

Figure A.1: Bands of a one dimensional insulator. Time-reversed Kramer's pairs are in black and gray and denoted by roman numerals I and II. Γ_i are the TRI momenta.

The total charge polarization, which gives the Chern number in a system that breaks time reversal symmetry, is then given by

$$P_\rho = P^I + P^{II}, \tag{A.4}$$

and the time reversal polarization, which gives rise to topological properties in TRI systems, is

$$P_\Theta = P^I - P^{II}. \tag{A.5}$$

To calculate P^I, equation A.3, which integrates half the bands over the whole Brillouin zone, can be converted to integrate all the bands over half the Brillouin zone as below

$$\begin{aligned} P^I &= \frac{1}{2\pi}\int_{-\Gamma_2}^{\Gamma_2} d\mathbf{k} A^I(\mathbf{k}) \\ &= \frac{1}{2\pi}\int_{\Gamma_1}^{\Gamma_2} d\mathbf{k}(A^I(\mathbf{k}) + A^I(-\mathbf{k})) \\ &= \frac{1}{2\pi}\int_{\Gamma_1}^{\Gamma_2} d\mathbf{k}(A^I(\mathbf{k}) + A^{II}(\mathbf{k}) - \sum_n \nabla_k \chi_{\mathbf{k},n}) \end{aligned}$$

The the last line comes from $A^I(-\mathbf{k}) = A^{II}(\mathbf{k}) - \sum_n \nabla\chi_{\mathbf{k},n}$ as worked out explicitly

in ref. [51] equations (10.39)-(10.41). The gradient of the phase preserves gauge invariance and arises from inserting equation A.1 into A.2 then utilizing the product rule.

Integrating the last term gives P^I to be

$$P^I = \frac{1}{2\pi}[\int_{\Gamma_1}^{\Gamma_2} d\mathbf{k} A(\mathbf{k}) - \sum_n (\chi_{\Gamma_2,n} - \chi_{\Gamma_1,n})] \tag{A.6}$$

Similarly, P^{II} can be derived to be

$$P^{II} = \frac{1}{2\pi}[\int_{\Gamma_2}^{\Gamma_1} d\mathbf{k} A(\mathbf{k}) + \sum_n (\chi_{\Gamma_2,n} - \chi_{\Gamma_1,n})] \tag{A.7}$$

Inserting equations A.6 and A.7 into equation A.5 gives the time-reversal polarization:

$$P_\Theta = \frac{1}{\pi}[\int_{\Gamma_1}^{\Gamma_2} d\mathbf{k} A(\mathbf{k}) - \sum_n (\chi_{\Gamma_2,n} - \chi_{\Gamma_1,n})]. \tag{A.8}$$

This result can be rephrased in terms of the matrix, $w_{mn}(\mathbf{k}) = \langle u_m(-\mathbf{k})| \Theta |u_n(\mathbf{k})\rangle$, given in equation 1.2. To start, utilizing the property that $\Theta^\dagger\Theta = -1$, $A(\mathbf{k})$ can be restated as

$$A(\mathbf{k}) = -i \sum_n \langle u_n(\mathbf{k})| \Theta^\dagger \Theta \nabla_\mathbf{k} |u_n(\mathbf{k})\rangle \tag{A.9}$$

The identity operator $I = \sum_n |u_n(-\mathbf{k})\rangle \langle u_n(-\mathbf{k})|$ can be placed inside equation A.9 yielding

$$A(\mathbf{k}) = -i \sum_{n=m} \langle u_n(\mathbf{k})| \Theta^\dagger |u_m(-\mathbf{k})\rangle \langle u_m(-\mathbf{k})| \Theta \nabla_\mathbf{k} |u_n(\mathbf{k})\rangle . \tag{A.10}$$

Then by noting,

$$\begin{aligned} \nabla_\mathbf{k} \langle u_m(-\mathbf{k})| \Theta |u_n(\mathbf{k})\rangle &= \langle \nabla_\mathbf{k} u_m(-\mathbf{k})| \Theta |u_n(\mathbf{k})\rangle + \langle u_m(-\mathbf{k})| \Theta |\nabla_\mathbf{k} u_n(\mathbf{k})\rangle \\ &= 2 \langle u_m(-\mathbf{k})| \Theta \nabla_\mathbf{k} |u_n(\mathbf{k})\rangle , \end{aligned}$$

$A(\mathbf{k})$ reduces to

$$A(\mathbf{k}) = \frac{1}{2i} \sum_{n=m} \langle u_n(\mathbf{k})| \Theta^\dagger |u_m(-\mathbf{k})\rangle \nabla_\mathbf{k} \langle u_m(-\mathbf{k})| \Theta |u_n(\mathbf{k})\rangle \tag{A.11}$$

$$= \frac{1}{2i} \mathrm{Tr}[w^\dagger \nabla_\mathbf{k} w]. \tag{A.12}$$

Jacobi's formula gives the relation

$$\nabla_{\mathbf{k}} \det[w] = \mathrm{Tr}[\mathrm{adj}[w]\nabla_{\mathbf{k}} w], \tag{A.13}$$

where $\mathrm{adj}[w]$ is the adjunct of w defined as $w\mathrm{adj}[w] = \det[w]I$. Since w is unitary, this can be written as

$$\mathrm{adj}[w] = w^{\dagger} \det[w]. \tag{A.14}$$

Thus

$$\begin{aligned}
A(\mathbf{k}) &= \frac{1}{2i}\mathrm{Tr}[w^{\dagger}\nabla_{\mathbf{k}} w] && \text{(A.15)}\\
&= \frac{1}{2i}\mathrm{Tr}[\frac{\mathrm{adj}[w]}{\det[w]}\nabla_{\mathbf{k}} w] && \text{(A.16)}\\
&= \frac{1}{2i}\frac{\mathrm{Tr}[\mathrm{adj}[w]\nabla_{\mathbf{k}} w]}{\det[w]} && \text{(A.17)}\\
&= \frac{1}{2i}\frac{\nabla_{\mathbf{k}} \det[w]}{\det[w]} && \text{(A.18)}\\
&= \frac{1}{2i}\nabla_{\mathbf{k}} \log[\det[w]] && \text{(A.19)}\\
&= -i\nabla_{\mathbf{k}} \log[\sqrt{\det[w]}] && \text{(A.20)}
\end{aligned}$$

The phase term in equation A.8, can be rephrased in terms of the Pfaffian of w. In terms of the Kramer's indices in equation A.1, w can be written as

$$w = \begin{bmatrix}
\langle u_1^I(-\mathbf{k})|\,\Theta\,|u_1^I(\mathbf{k})\rangle & \langle u_1^I(-\mathbf{k})|\,\Theta\,|u_1^{II}(\mathbf{k})\rangle & \langle u_1^I(-\mathbf{k})|\,\Theta\,|u_2^I(\mathbf{k})\rangle & \dots & \langle u_1^I(-\mathbf{k})|\,\Theta\,|u_N^{II}(\mathbf{k})\rangle \\
\langle u_1^{II}(-\mathbf{k})|\,\Theta\,|u_1^I(\mathbf{k})\rangle & \langle u_1^{II}(-\mathbf{k})|\,\Theta\,|u_1^{II}(\mathbf{k})\rangle & \langle u_1^{II}(-\mathbf{k})|\,\Theta\,|u_2^I(\mathbf{k})\rangle & \dots & \langle u_1^{II}(-\mathbf{k})|\,\Theta\,|u_N^{II}(\mathbf{k})\rangle \\
\vdots & \vdots & \vdots & \ddots & \vdots \\
\langle u_N^{II}(-\mathbf{k})|\,\Theta\,|u_1^I(\mathbf{k})\rangle & \langle u_N^{II}(-\mathbf{k})|\,\Theta\,|u_1^{II}(\mathbf{k})\rangle & \langle u_N^{II}(-\mathbf{k})|\,\Theta\,|u_2^I(\mathbf{k})\rangle & \dots & \langle u_N^{II}(-\mathbf{k})|\,\Theta\,|u_N^{II}(\mathbf{k})\rangle
\end{bmatrix} \tag{A.21}$$

At the TRI momenta, $-\mathbf{k} = \mathbf{k}$. Then utilizing equation A.1, most of the elements go to zero leaving only certain off diagonal elements equal to $\pm e^{i\chi_{\Gamma_i,n}}$. w is thus a $2N \times 2N$, antisymmetric matrix with a Pfaffian given by

$$\mathrm{Pf}[w(\Gamma_i)] = \prod_n e^{i\chi_{\Gamma_i,n}} = e^{i\sum_n \chi_{\Gamma_i,n}}. \tag{A.22}$$

Therefore,

$$\sum_n (\chi_{\Gamma_2,n} - \chi_{\Gamma_1,n}) = -i \log[\frac{\mathrm{Pf}[w(\Gamma_2)]}{\mathrm{Pf}[w(\Gamma_1)]}] \tag{A.23}$$

Thus by inserting equations A.20 and A.23 into equation A.8, the time-reversal polarization in terms of the matrix w is given by

$$P_\Theta = \frac{1}{\pi i}[\int_{\Gamma_1}^{\Gamma_2} d\mathbf{k}(\nabla_\mathbf{k} \log[\sqrt{\det[w]}]) - \log[\frac{\mathrm{Pf}[w(\Gamma_2)]}{\mathrm{Pf}[w(\Gamma_1)]}] \tag{A.24}$$

After integrating the first term, the time-reversal polarization can be written in a single logarithm,

$$P_\Theta = \frac{1}{\pi i} \log[\frac{\sqrt{\det[w(\Gamma_2)]}\mathrm{Pf}[w(\Gamma_1)]}{\sqrt{\det[w(\Gamma_1)]}\mathrm{Pf}[w(\Gamma_2)]}] \tag{A.25}$$

or

$$\mathrm{e}^{i\pi P_\Theta} = \frac{\sqrt{\det[w(\Gamma_2)]}}{\mathrm{Pf}[w(\Gamma_2)]} \frac{\mathrm{Pf}[w(\Gamma_1)]}{\sqrt{\det[w(\Gamma_1)]}}. \tag{A.26}$$

Since the determinate is equal to the Pfaffian squared, $\frac{\sqrt{\det[w(\Gamma_i)]}}{\mathrm{Pf}[w(\Gamma_i)]} = \pm 1$. Therefore, P_Θ is an integer. The second quotient can be inverted (since it is equal to ± 1) to reframe the result as it is in Fu and Kane [43],

$$\mathrm{e}^{i\pi P_\Theta} = (-1)^{P_\Theta} = \frac{\sqrt{\det[w(\Gamma_2)]}}{\mathrm{Pf}[w(\Gamma_2)]} \frac{\sqrt{\det[w(\Gamma_1)]}}{\mathrm{Pf}[w(\Gamma_1)]}. \tag{A.27}$$

Equation A.27 is not gauge invariant; however, the change in the time-reversal polarization due to Kramer's pairs switching partners (leading to topologically protected surface states) is gauge invariant and defines a Z_2 topological invariant [44].

The change in the time-reversal polarization is clearest to see in 2D. There are four TRI momenta: (k_x,k_y): Γ_1 = (0,0), Γ_2 = (π,0), Γ_3 = (0,π), and Γ_4 = (π,π).

The one dimensional the time-reversal polarization at k_y=0 is

$$P_\Theta(k_y = 0) = \frac{1}{\pi i} \log[\frac{\sqrt{\det[w(\Gamma_2)]}}{\mathrm{Pf}[w(\Gamma_2)]} \frac{\sqrt{\det[w(\Gamma_1)]}}{\mathrm{Pf}[w(\Gamma_1)]}] \tag{A.28}$$

and the one dimensional the time-reversal polarization at k_y=π is

$$P_\Theta(k_y = \pi) = \frac{1}{\pi i} \log[\frac{\sqrt{\det[w(\Gamma_4)]}}{\mathrm{Pf}[w(\Gamma_4)]} \frac{\sqrt{\det[w(\Gamma_3)]}}{\mathrm{Pf}[w(\Gamma_3)]}]. \tag{A.29}$$

The difference of the one dimensional the time-reversal polarizations at k_y=0 and k_y = π is then given by

$$e^{P_\Theta(k_y=\pi)-P_\Theta(k_y=0)} = \prod_{i=1}^{4} \delta_i, \tag{A.30}$$

where $\delta_i = \frac{\sqrt{\det[w(\Gamma_i)]}}{\mathrm{Pf}[w(\Gamma_i)]}$ is given in equation 1.1. This change in time-reversal polarization is related to how the Kramer's pairs at the TRI momenta are connected [44]. A non-zero change in the time-reversal polarization occurs when the Kramer's pairs switch partners leading to an energy band spanning the gap as depicted in fig. A.2. This band will cross the Fermi level an odd number of times leading to a topologically protected edge state. This is discussed more thoroughly in ref. [51].

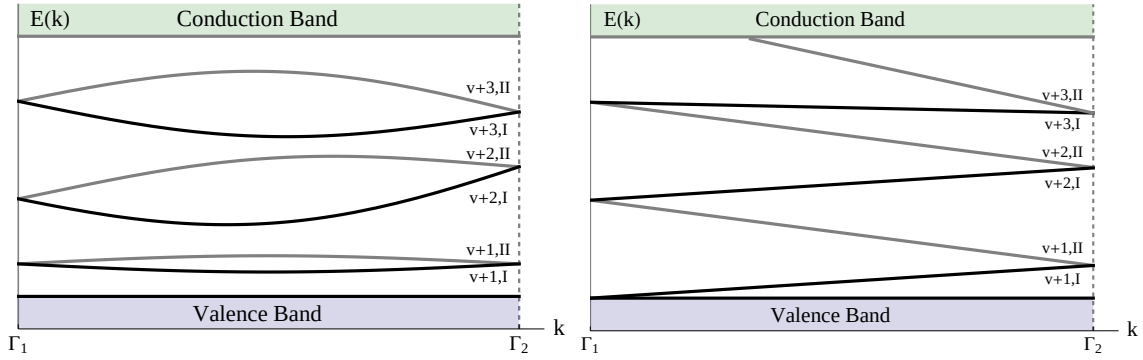

Figure A.2: Modification of fig. A.1. v is the band number of the top of the valence band, thus the bands shown are in the gap. The left panel shows the topologically trivial insulator. In the right panel, Kramer's pairs switch partners causing an energy band to span the gap.

Equation A.30 is the same as equation 1.8 from chapter 1 section 1.2.1. Thus, $P_\Theta(k_y = \pi) - P_\Theta(k_y = 0)$ defines the 2D topological invariant, ν. A similar argument by Fu, Kane, and Mele in ref. [44] derives equation 1.9 for a 3D topological insulator. This is the topological invariant used for a 3D topological superconductor.

APPENDIX B

Bean Model

An external magnetic field kills the superconducting state in a type I superconductor at the critical field, H_c. However, in a type II superconductor, there is a mixed state between the lower critical field, H_{c1}, and the upper critical field, H_{c2}. For $H_{c1} < H < H_{c2}$, magnetic flux penetrates the superconductor creating a lattice of vortices. Due to defects in the sample, these vortices are pinned in place. In order for the vortices to move, the Lorentz force from a current near the vortices would need to overcome this pinning force. Thus, the pinned magnetic flux has an irreversible response to a changing external magnetic field. This gives rise to hysteresis in the magnetic response of the superconductor.

The Bean model [196, 197] successfully explained the hysteresis feature in type II superconductors. In this model, we assume that the current density in the superconductor can only take the values of 0 and J_c, where J_c is the critical current density. Due to the Ampere's law, the spacial profile of J_c determines $\mathbf{b}(\mathbf{x})$, the magnetic flux density per unit volume at each location $\mathbf{x}$ in the superconductor. Integrating $\mathbf{b}(\mathbf{x})$ gives the total magnetic field density B inside the superconductor.

Figure B.1 shows the magnetic flux density inside the superconductor (represented by the grey shaded region) for (A) field increasing from $H = 0$ to H_0 and (B) field decreasing to H_0 after an applied external field greater than H_{c2}. Due to the flux-pinning, the internal magnetic flux density $b(x)/\mu_0$ cannot respond to the change in the sweep direction of the external magnetic field. Fig. B.1(A) represents the magnetic flux density $b(x)/\mu_0$ as the applied magnetic field is swept up from zero to H_0. In this one dimensional analysis, $J_c = \frac{1}{\mu_0}\nabla\mathbf{b}(\mathbf{r}) = \frac{\mathbf{1}}{\mu_\mathbf{0}}\frac{\mathbf{db(x)}}{\mathbf{dx}}$ would be simply the slope of $\frac{b(x)}{\mu_0}$ vs. x. The spacial profile of J_c is constant, as shown in the right panel of Fig B.1(A).

The situation of field-sweeping-down is different. As the applied field is swept from a large field to the same H_0, the $b(x)/\mu_0$ profile response lags, as show in Fig. B.1(B).

The magnetization of the sample is given by the difference between the average magnetic flux density within the sample, B, and the applied field, H, outside:

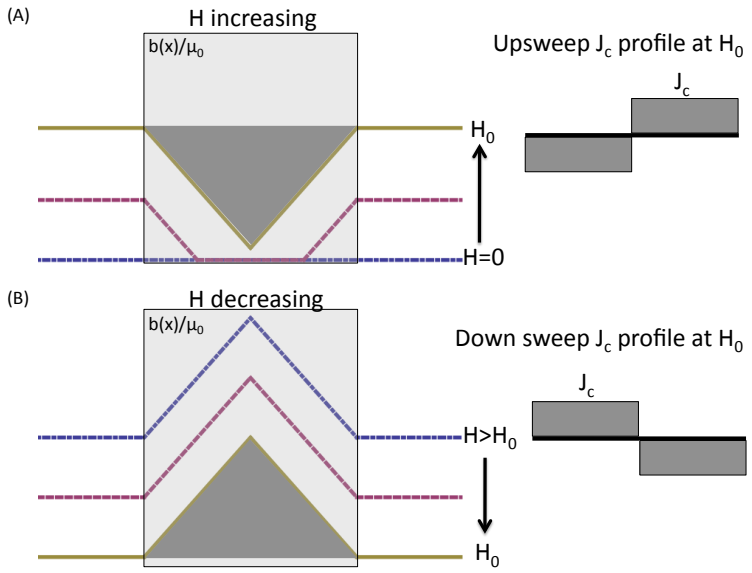

Figure B.1: Schematic of magnetic flux density in type II superconductors. (A) Magnetic flux density in a type II superconductor as external magnetic field is swept up from $H = 0$ to $H_0 > 0$ according to the Bean model. The right inset shows a sketch of the critical current density profile at H_0 during the upsweep. Magnetization M corresponds to the dark shaded area. (B) Magnetic flux density in a type II superconductor as external magnetic field is swept down from $H > H_{c2}$ to H_0. The lagging of the internal magnetic flux density due to flux pinning gives rise to hysteresis in magnetization. The sample's critical current density profile for the down sweep is shown in the right panel.

$$M = \frac{B}{\mu_0} - H = \frac{1}{w}\int dx \frac{b(x)}{\mu_0} - H \tag{B.1}$$

where w is the typical width of the domain size in the superconductor, or the sample size of the whole sample if it has only a single domain. In the case of Panel A, equation B.1 would be simply the shaded area $-wJ_c$ which gives M_+, the magnetization at field sweeping up.

Furthermore, the difference between panels A and B demonstrates the hysteresis in the magnetization of type II superconductors. Going through the same analysis as above, we find the magnetization of field sweeping down $M_- = wJ_c$ As a result, the hysteresis loop size $\Delta M(H) \equiv M_+ - M_- = 2wJ_c$. Therefore, the measurement of the hysteresis loop is a direct probe of the critical current density in a type II superconductor.

BIBLIOGRAPHY

[1] Hashimoto, T., Yada, K., Yamakage, A., Sato, M., and Tanaka, Y., "Bulk electronic state of superconducting topological insulator," *Journal of the Physical Society of Japan*, Vol. 82, No. 4, 2013, pp. 044704.

[2] Sasaki, S. and Mizushima, T., "Superconducting doped topological materials," *Physica C: Superconductivity and its Applications*, Vol. 514, 2015, pp. 206–217.

[3] Hor, Y. S., Williams, A. J., Checkelsky, J. G., Roushan, P., Seo, J., Xu, Q., Zandbergen, H. W., Yazdani, A., Ong, N. P., and Cava, R. J., "Superconductivity in $\mathrm{Cu}_x\mathrm{Bi}_2\mathrm{Se}_3$ and its Implications for Pairing in the Undoped Topological Insulator," *Phys. Rev. Lett.*, Vol. 104, Feb 2010, pp. 057001.

[4] Wray, L. A., Xu, S.-Y., Xia, Y., Hor, Y. S., Qian, D., Fedorov, A. V., Lin, H., Bansil, A., Cava, R. J., and Hasan, M. Z., "Observation of topological order in a superconducting doped topological insulator," *Nat Phys*, Vol. 6, No. 11, 11 2010, pp. 855–859.

[5] Fu, L. and Berg, E., "Odd-Parity Topological Superconductors: Theory and Application to $\mathrm{Cu}_x\mathrm{Bi}_2\mathrm{Se}_3$," *Phys. Rev. Lett.*, Vol. 105, Aug 2010, pp. 097001.

[6] Kriener, M., Segawa, K., Ren, Z., Sasaki, S., and Ando, Y., "Bulk Superconducting Phase with a Full Energy Gap in the Doped Topological Insulator $\mathrm{Cu}_x\mathrm{Bi}_2\mathrm{Se}_3$," *Phys. Rev. Lett.*, Vol. 106, Mar 2011, pp. 127004.

[7] Bay, T. V., Naka, T., Huang, Y. K., Luigjes, H., Golden, M. S., and de Visser, A., "Superconductivity in the Doped Topological Insulator $\mathrm{Cu}_x\mathrm{Bi}_2\mathrm{Se}_3$ under High Pressure," *Phys. Rev. Lett.*, Vol. 108, Jan 2012, pp. 057001.

[8] Sasaki, S., Kriener, M., Segawa, K., Yada, K., Tanaka, Y., Sato, M., and Ando, Y., "Topological Superconductivity in $\mathrm{Cu}_x\mathrm{Bi}_2\mathrm{Se}_3$," *Phys. Rev. Lett.*, Vol. 107, Nov 2011, pp. 217001.

[9] Levy, N., Zhang, T., Ha, J., Sharifi, F., Talin, A. A., Kuk, Y., and Stroscio, J. A., "Experimental Evidence for s-Wave Pairing Symmetry in Superconducting $\mathrm{Cu}_x\mathrm{Bi}_2\mathrm{Se}_3$ Single Crystals Using a Scanning Tunneling Microscope," *Phys. Rev. Lett.*, Vol. 110, Mar 2013, pp. 117001.

[10] Peng, H., De, D., Lv, B., Wei, F., and Chu, C.-W., "Absence of zero-energy surface bound states in $Cu_xBi_2Se_3$ studied via Andreev reflection spectroscopy," *Phys. Rev. B*, Vol. 88, Jul 2013, pp. 024515.

[11] Lahoud, E., Maniv, E., Petrushevsky, M. S., Naamneh, M., Ribak, A., Wiedmann, S., Petaccia, L., Salman, Z., Chashka, K. B., Dagan, Y., and Kanigel, A., "Evolution of the Fermi surface of a doped topological insulator with carrier concentration," *Phys. Rev. B*, Vol. 88, Nov 2013, pp. 195107.

[12] Fu, L., "Odd-parity topological superconductor with nematic order: Application to $Cu_xBi_2Se_3$," *Phys. Rev. B*, Vol. 90, Sep 2014, pp. 100509.

[13] Yonezawa, S., Tajiri, K., Nakata, S., Nagai, Y., Wang, Z., Segawa, K., Ando, Y., and Maeno, Y., "Thermodynamic evidence for nematic superconductivity in $Cu_xBi_2Se_3$," *Nat Phys*, Vol. advance online publication, 10 2016, pp. –.

[14] Matano, K., Kriener, M., Segawa, K., Ando, Y., and Zheng, G.-q., "Spin-rotation symmetry breaking in the superconducting state of $Cu_xBi_2Se_3$," *Nat Phys*, Vol. 12, No. 9, 09 2016, pp. 852–854.

[15] Liu, Z., Yao, X., Shao, J., Zuo, M., Pi, L., Tan, S., Zhang, C., and Zhang, Y., "Superconductivity with Topological Surface State in $Sr_xBi_2Se_3$," *Journal of the American Chemical Society*, Vol. 137, No. 33, 2015, pp. 10512–10515.

[16] Han, C., Li, H., Chen, W., Zhu, F., Yao, M.-Y., Li, Z., Wang, M., Gao, B. F., Guan, D., Liu, C., et al., "Electronic structure of a superconducting topological insulator Sr-doped Bi_2Se_3," *Applied Physics Letters*, Vol. 107, No. 17, 2015, pp. 171602.

[17] Du, G., Shao, J., Yang, X., Du, Z., Fang, D., Zhang, C., Wang, J., Ran, K., Wen, J., Yang, H., et al., "Drive the Dirac Electrons into Cooper Pairs in $Sr_xBi_2Se_3$," *arXiv preprint arXiv:1604.08198*, 2016.

[18] Zhou, Y., Chen, X., Zhang, R., Shao, J., Wang, X., An, C., Zhou, Y., Park, C., Tong, W., Pi, L., et al., "Pressure-induced reemergence of superconductivity in topological insulator $Sr_{0.065}Bi_2Se_3$," *Physical Review B*, Vol. 93, No. 14, 2016, pp. 144514.

[19] Pan, Y., Nikitin, A., Araizi, G., Huang, Y., Matsushita, Y., Naka, T., and De Visser, A., "Rotational symmetry breaking in the topological superconductor $Sr_xBi_2Se_3$ probed by upper-critical field experiments," *Scientific Reports*, Vol. 6, 2016.

[20] Qiu, Y., Sanders, K. N., Dai, J., Medvedeva, J. E., Wu, W., Ghaemi, P., Vojta, T., and Hor, Y. S., "Time reversal symmetry breaking superconductivity in topological materials," *arXiv preprint arXiv:1512.03519*, 2015.

[21] Smylie, M., Claus, H., Welp, U., Kwok, W.-K., Qiu, Y., Hor, Y., and Snezhko, A., "Evidence of nodes in the order parameter of the superconducting doped topological insulator $Nb_xBi_2Se_3$ via penetration depth measurements," *Physical Review B*, Vol. 94, No. 18, 2016, pp. 180510.

[22] Singleton, J., *Band theory and electronic properties of solids*, Vol. 2, Oxford University Press, 2001.

[23] Shoenberg, D., *Magnetic oscillations in metals*, Cambridge University Press, 2009.

[24] Pobell, F., *Matter and methods at low temperatures*, Springer Science & Business Media, 2007.

[25] Steglich, F., Aarts, J., Bredl, C. D., Lieke, W., Meschede, D., Franz, W., and Schäfer, H., "Superconductivity in the Presence of Strong Pauli Paramagnetism: $CeCu_2Si_2$," *Phys. Rev. Lett.*, Vol. 43, Dec 1979, pp. 1892–1896.

[26] Thouless, D. J., Kohmoto, M., Nightingale, M. P., and den Nijs, M., "Quantized Hall Conductance in a Two-Dimensional Periodic Potential," *Phys. Rev. Lett.*, Vol. 49, Aug 1982, pp. 405–408.

[27] Kane, C. L. and Mele, E. J., "Quantum Spin Hall Effect in Graphene," *Phys. Rev. Lett.*, Vol. 95, Nov 2005, pp. 226801.

[28] Kane, C. L. and Mele, E. J., "Z 2 topological order and the quantum spin Hall effect," *Physical review letters*, Vol. 95, No. 14, 2005, pp. 146802.

[29] Hsieh, D., Qian, D., Wray, L., Xia, Y., Hor, Y. S., Cava, R. J., and Hasan, M. Z., "A topological Dirac insulator in a quantum spin Hall phase," *Nature*, Vol. 452, No. 7190, 04 2008, pp. 970–974.

[30] Wilczek, F., "Majorana returns," *Nat Phys*, Vol. 5, No. 9, 09 2009, pp. 614–618.

[31] Beenakker, C., "Search for Majorana fermions in superconductors," *Annu. Rev. Condens. Matter Phys.*, Vol. 4, No. 1, 2013, pp. 113–136.

[32] Nayak, C., Simon, S. H., Stern, A., Freedman, M., and Das Sarma, S., "Non-Abelian anyons and topological quantum computation," *Rev. Mod. Phys.*, Vol. 80, Sep 2008, pp. 1083–1159.

[33] Checkelsky, J. G., Hor, Y. S., Liu, M.-H., Qu, D.-X., Cava, R. J., and Ong, N. P., "Quantum Interference in Macroscopic Crystals of Nonmetallic Bi_2Se_3," *Phys. Rev. Lett.*, Vol. 103, Dec 2009, pp. 246601.

[34] Zhang, Y., Tan, Y.-W., Stormer, H. L., and Kim, P., "Experimental observation of the quantum Hall effect and Berry's phase in graphene," *Nature*, Vol. 438, No. 7065, 2005, pp. 201–204.

[35] Qu, D.-X., Hor, Y., Xiong, J., Cava, R., and Ong, N., "Quantum oscillations and Hall anomaly of surface states in the topological insulator Bi_2Te_3," *Science*, Vol. 329, No. 5993, 2010, pp. 821–824.

[36] Kriener, M., Segawa, K., Ren, Z., Sasaki, S., Wada, S., Kuwabata, S., and Ando, Y., "Electrochemical synthesis and superconducting phase diagram of $Cu_xBi_2Se_3$," *Phys. Rev. B*, Vol. 84, Aug 2011, pp. 054513.

[37] Wray, L. A., Xu, S., Xia, Y., Qian, D., Fedorov, A. V., Lin, H., Bansil, A., Fu, L., Hor, Y. S., Cava, R. J., and Hasan, M. Z., "Spin-orbital ground states of superconducting doped topological insulators: A Majorana platform," *Phys. Rev. B*, Vol. 83, Jun 2011, pp. 224516.

[38] Sato, M., "Topological odd-parity superconductors," *Phys. Rev. B*, Vol. 81, Jun 2010, pp. 220504.

[39] Lawson, B. J., Hor, Y. S., and Li, L., "Quantum Oscillations in the Topological Superconductor Candidate $\mathrm{Cu_{0.25}Bi_2Se_3}$," *Phys. Rev. Lett.*, Vol. 109, Nov 2012, pp. 226406.

[40] Lawson, B. J., Li, G., Yu, F., Asaba, T., Tinsman, C., Gao, T., Wang, W., Hor, Y. S., and Li, L., "Quantum oscillations in $\mathrm{Cu}_x\mathrm{Bi_2Se_3}$ in high magnetic fields," *Phys. Rev. B*, Vol. 90, Nov 2014, pp. 195141.

[41] Lawson, B., Corbae, P., Li, G., Yu, F., Asaba, T., Tinsman, C., Qiu, Y., Medvedeva, J., Hor, Y., and Li, L., "Multiple Fermi surfaces in superconducting Nb-doped $\mathrm{Bi_2Se_3}$," *Physical Review B*, Vol. 94, No. 4, 2016, pp. 041114.

[42] Asaba, T., Lawson, B. J., Tinsman, C., Chen, L., Corbae, P., Li, G., Qiu, Y., Hor, Y. S., Fu, L., and Li, L., "Rotational Symmetry Breaking in a Trigonal Superconductor Nb-doped $\mathrm{Bi_2Se_3}$," *Phys. Rev. X*, Vol. 7, Jan 2017, pp. 011009.

[43] Fu, L. and Kane, C. L., "Time reversal polarization and a Z 2 adiabatic spin pump," *Physical Review B*, Vol. 74, No. 19, 2006, pp. 195312.

[44] Fu, L., Kane, C. L., and Mele, E. J., "Topological insulators in three dimensions," *Physical Review Letters*, Vol. 98, No. 10, 2007, pp. 106803.

[45] Fu, L. and Kane, C. L., "Topological insulators with inversion symmetry," *Phys. Rev. B*, Vol. 76, Jul 2007, pp. 045302.

[46] Anderson, P. W., "Random-phase approximation in the theory of superconductivity," *Physical Review*, Vol. 112, No. 6, 1958, pp. 1900.

[47] Konschelle, F., "Transport equations for superconductors in the presence of spin interaction," *arXiv preprint arXiv:1403.1797*, 2014.

[48] Nambu, Y., "Quasi-particles and gauge invariance in the theory of superconductivity," *Physical Review*, Vol. 117, No. 3, 1960, pp. 648.

[49] Flokstra, M. G. et al., *Proximity effects in superconducting spin-valve structures*, Faculty of Science, Leiden University, 2010.

[50] Xia, J., Maeno, Y., Beyersdorf, P. T., Fejer, M. M., and Kapitulnik, A., "High Resolution Polar Kerr Effect Measurements of $\mathrm{Sr_2RuO_4}$: Evidence for Broken Time-Reversal Symmetry in the Superconducting State," *Phys. Rev. Lett.*, Vol. 97, Oct 2006, pp. 167002.

[51] Bernevig, B. A. and Hughes, T. L., *Topological insulators and topological superconductors*, Princeton University Press, 2013.

[52] Das Sarma, S., Nayak, C., and Tewari, S., "Proposal to stabilize and detect half-quantum vortices in strontium ruthenate thin films: Non-Abelian braiding statistics of vortices in a p_x+ip_y superconductor," *Phys. Rev. B*, Vol. 73, Jun 2006, pp. 220502.

[53] Schnyder, A. P., Ryu, S., Furusaki, A., and Ludwig, A. W. W., "Classification of topological insulators and superconductors in three spatial dimensions," *Phys. Rev. B*, Vol. 78, Nov 2008, pp. 195125.

[54] Qi, X.-L. and Zhang, S.-C., "Topological insulators and superconductors," *Rev. Mod. Phys.*, Vol. 83, Oct 2011, pp. 1057–1110.

[55] Hsieh, T. H. and Fu, L., "Majorana Fermions and Exotic Surface Andreev Bound States in Topological Superconductors: Application to $\mathrm{Cu}_x\mathrm{Bi}_2\mathrm{Se}_3$," *Phys. Rev. Lett.*, Vol. 108, Mar 2012, pp. 107005.

[56] Kitaev, A. Y., "Unpaired Majorana fermions in quantum wires," *Physics-Uspekhi*, Vol. 44, No. 10S, 2001, pp. 131.

[57] Fu, L. and Kane, C. L., "Superconducting Proximity Effect and Majorana Fermions at the Surface of a Topological Insulator," *Phys. Rev. Lett.*, Vol. 100, Mar 2008, pp. 096407.

[58] Wang, M.-X., Liu, C., Xu, J.-P., Yang, F., Miao, L., Yao, M.-Y., Gao, C., Shen, C., Ma, X., Chen, X., et al., "The coexistence of superconductivity and topological order in the $\mathrm{Bi}_2\mathrm{Se}_3$ thin films," *Science*, Vol. 336, No. 6077, 2012, pp. 52–55.

[59] Veldhorst, M., Snelder, M., Hoek, M., Gang, T., Guduru, V., Wang, X., Zeitler, U., Van der Wiel, W., Golubov, A., Hilgenkamp, H., et al., "Josephson supercurrent through a topological insulator surface state," *Nature materials*, Vol. 11, No. 5, 2012, pp. 417–421.

[60] Sau, J. D., Lutchyn, R. M., Tewari, S., and Das Sarma, S., "Generic New Platform for Topological Quantum Computation Using Semiconductor Heterostructures," *Phys. Rev. Lett.*, Vol. 104, Jan 2010, pp. 040502.

[61] Sato, M. and Fujimoto, S., "Existence of Majorana Fermions and Topological Order in Nodal Superconductors with Spin-Orbit Interactions in External Magnetic Fields," *Phys. Rev. Lett.*, Vol. 105, Nov 2010, pp. 217001.

[62] Lu, Y.-M. and Wang, Z., "Majorana Fermions in Spin-Singlet Nodal Superconductors with Coexisting Noncollinear Magnetic Order," *Phys. Rev. Lett.*, Vol. 110, Feb 2013, pp. 096403.

[63] Read, N. and Green, D., "Paired states of fermions in two dimensions with breaking of parity and time-reversal symmetries and the fractional quantum Hall effect," *Phys. Rev. B*, Vol. 61, Apr 2000, pp. 10267–10297.

[64] Ivanov, D. A., "Non-Abelian Statistics of Half-Quantum Vortices in p-Wave Superconductors," *Phys. Rev. Lett.*, Vol. 86, Jan 2001, pp. 268–271.

[65] Maeno, Y., Kittaka, S., Nomura, T., Yonezawa, S., and Ishida, K., "Evaluation of spin-triplet superconductivity in $\mathrm{Sr_2RuO_4}$," *Journal of the Physical Society of Japan*, Vol. 81, No. 1, 2011, pp. 011009.

[66] Yan, B. and de Visser, A., "Half-Heusler topological insulators," *MRS Bulletin*, Vol. 39, No. 10, 2014, pp. 859–866.

[67] Nakajima, Y., Hu, R., Kirshenbaum, K., Hughes, A., Syers, P., Wang, X., Wang, K., Wang, R., Saha, S. R., Pratt, D., et al., "Topological RPdBi half-Heusler semimetals: A new family of noncentrosymmetric magnetic superconductors," *Science advances*, Vol. 1, No. 5, 2015, pp. e1500242.

[68] Butch, N. P., Syers, P., Kirshenbaum, K., Hope, A. P., and Paglione, J., "Superconductivity in the topological semimetal YPtBi," *Phys. Rev. B*, Vol. 84, Dec 2011, pp. 220504.

[69] Sasaki, S., Ren, Z., Taskin, A. A., Segawa, K., Fu, L., and Ando, Y., "Odd-Parity Pairing and Topological Superconductivity in a Strongly Spin-Orbit Coupled Semiconductor," *Phys. Rev. Lett.*, Vol. 109, Nov 2012, pp. 217004.

[70] Kirshenbaum, K., Syers, P., Hope, A., Butch, N., Jeffries, J., Weir, S., Hamlin, J., Maple, M., Vohra, Y., and Paglione, J., "Pressure-induced unconventional superconducting phase in the topological insulator $\mathrm{Bi_2Se_3}$," *Physical review letters*, Vol. 111, No. 8, 2013, pp. 087001.

[71] Zhang, J., Zhang, S., Weng, H., Zhang, W., Yang, L., Liu, Q., Feng, S., Wang, X., Yu, R., Cao, L., et al., "Pressure-induced superconductivity in topological parent compound $\mathrm{Bi_2Te_3}$," *Proceedings of the National Academy of Sciences*, Vol. 108, No. 1, 2011, pp. 24–28.

[72] Hasan, M. Z. and Kane, C. L., "*Colloquium* : Topological insulators," *Rev. Mod. Phys.*, Vol. 82, Nov 2010, pp. 3045–3067.

[73] Xia, Y., Qian, D., Hsieh, D., Wray, L., Pal, A., Lin, H., Bansil, A., Grauer, D., Hor, Y. S., Cava, R. J., and Hasan, M. Z., "Observation of a large-gap topological-insulator class with a single Dirac cone on the surface," *Nat Phys*, Vol. 5, No. 6, 06 2009, pp. 398–402.

[74] Chen, Y. L., Chu, J.-H., Analytis, J. G., Liu, Z. K., Igarashi, K., Kuo, H.-H., Qi, X. L., Mo, S. K., Moore, R. G., Lu, D. H., Hashimoto, M., Sasagawa, T., Zhang, S. C., Fisher, I. R., Hussain, Z., and Shen, Z. X., "Massive Dirac Fermion on the Surface of a Magnetically Doped Topological Insulator," *Science*, Vol. 329, No. 5992, 2010, pp. 659–662.

[75] Qi, X.-L., Hughes, T. L., Raghu, S., and Zhang, S.-C., "Time-Reversal-Invariant Topological Superconductors and Superfluids in Two and Three Dimensions," *Phys. Rev. Lett.*, Vol. 102, May 2009, pp. 187001.

[76] Hor, Y., Checkelsky, J., Qu, D., Ong, N., and Cava, R., "Superconductivity and non-metallicity induced by doping the topological insulators Bi_2Se_3 and Bi_2Te_3," *Journal of Physics and Chemistry of Solids*, Vol. 72, No. 5, 2011, pp. 572–576.

[77] Das, P., Suzuki, Y., Tachiki, M., and Kadowaki, K., "Spin-triplet vortex state in the topological superconductor $Cu_xBi_2Se_3$," *Phys. Rev. B*, Vol. 83, Jun 2011, pp. 220513.

[78] Vaško, A., Tichý, L., Horák, J., and Weissenstein, J., "Amphoteric nature of copper impurities in Bi_2Se_3 crystals," *Applied physics*, Vol. 5, No. 3, 1974, pp. 217–221.

[79] Kondo, R., Yoshinaka, T., Imai, Y., and Maeda, A., "Reproducible Synthetic Method for the Topological Superconductor $Cu_xBi_2Se_3$," *Journal of the Physical Society of Japan*, Vol. 82, No. 6, 2013, pp. 063702.

[80] Schneeloch, J. A., Zhong, R. D., Xu, Z. J., Gu, G. D., and Tranquada, J. M., "Dependence of superconductivity in $Cu_xBi_2Se_3$ on quenching conditions," *Phys. Rev. B*, Vol. 91, Apr 2015, pp. 144506.

[81] Wang, M., Song, Y., You, L., Li, Z., Gao, B., Xie, X., and Jiang, M., "A combined method for synthesis of superconducting Cu doped Bi_2Se_3," *Scientific reports*, Vol. 6, 2016.

[82] Koski, K. J., Cha, J. J., Reed, B. W., Wessells, C. D., Kong, D., and Cui, Y., "High-density chemical intercalation of zero-valent copper into Bi_2Se_3 nanoribbons," *Journal of the American Chemical Society*, Vol. 134, No. 18, 2012, pp. 7584–7587.

[83] Zhang, H., Liu, C.-X., Qi, X.-L., Dai, X., Fang, Z., and Zhang, S.-C., "Topological insulators in Bi_2Se_3, Bi_2Te_3 and Sb_2Te_3 with a single Dirac cone on the surface," *Nat Phys*, Vol. 5, No. 6, 06 2009, pp. 438–442.

[84] Padamsee, H., Neighbor, J. E., and Shiffman, C. A., "Quasiparticle phenomenology for thermodynamics of strong-coupling superconductors," *Journal of Low Temperature Physics*, Vol. 12, No. 3, 1973, pp. 387–411.

[85] Tachiki, M., Matsumoto, H., and Umezawa, H., "Mixed state in magnetic superconductors," *Phys. Rev. B*, Vol. 20, Sep 1979, pp. 1915–1927.

[86] Tachiki, M. and Koizumi, H., "Vortex state of topological superconductor $Cu_xBi_2Se_3$," *Phys. Rev. B*, Vol. 91, Mar 2015, pp. 104505.

[87] Clogston, A. M., "Upper Limit for the Critical Field in Hard Superconductors," *Phys. Rev. Lett.*, Vol. 9, Sep 1962, pp. 266–267.

[88] Chandrasekhar, B., "A note on the maximum critical field of high-field superconductors," *Applied Physics Letters*, Vol. 1, No. 1, 1962, pp. 7–8.

[89] Werthamer, N. R., Helfand, E., and Hohenberg, P. C., "Temperature and Purity Dependence of the Superconducting Critical Field, H_{c2}. III. Electron Spin and Spin-Orbit Effects," *Phys. Rev.*, Vol. 147, Jul 1966, pp. 295–302.

[90] Maki, K., "Effect of Pauli Paramagnetism on Magnetic Properties of High-Field Superconductors," *Phys. Rev.*, Vol. 148, Aug 1966, pp. 362–369.

[91] Tinkham, M., *Introduction to superconductivity*, Courier Corporation, 1996.

[92] Hardy, F. and Huxley, A. D., "p-Wave Superconductivity in the Ferromagnetic Superconductor URhGe," *Phys. Rev. Lett.*, Vol. 94, Jun 2005, pp. 247006.

[93] Huy, N. T., de Nijs, D. E., Huang, Y. K., and de Visser, A., "Unusual Upper Critical Field of the Ferromagnetic Superconductor UCoGe," *Phys. Rev. Lett.*, Vol. 100, Feb 2008, pp. 077002.

[94] Mackenzie, A. P., Haselwimmer, R. K. W., Tyler, A. W., Lonzarich, G. G., Mori, Y., Nishizaki, S., and Maeno, Y., "Extremely Strong Dependence of Superconductivity on Disorder in $\mathrm{Sr_2RuO_4}$," *Phys. Rev. Lett.*, Vol. 80, Jan 1998, pp. 161–164.

[95] Maki, K., Puchkaryov, E., Wang, G.-F., and Won, H., "Aspects of p-Wave Superconductivity," *Chinese Journal of Physics*, Vol. 38, No. 2S, 2000, pp. 386–394.

[96] Scharnberg, K. and Klemm, R. A., "p-wave superconductors in magnetic fields," *Phys. Rev. B*, Vol. 22, Dec 1980, pp. 5233–5244.

[97] Balian, R. and Werthamer, N. R., "Superconductivity with Pairs in a Relative p Wave," *Phys. Rev.*, Vol. 131, Aug 1963, pp. 1553–1564.

[98] Orlando, T. P., McNiff, E. J., Foner, S., and Beasley, M. R., "Critical fields, Pauli paramagnetic limiting, and material parameters of $\mathrm{Nb_3Sn}$ and $\mathrm{V_3Si}$," *Phys. Rev. B*, Vol. 19, May 1979, pp. 4545–4561.

[99] Martin, C., Craciun, V., Miller, K. H., Uzakbaiuly, B., Buvaev, S., Berger, H., Hebard, A. F., and Tanner, D. B., "Bulk Fermi surface and electronic properties of $\mathrm{Cu_{0.07}Bi_2Se_3}$," *Phys. Rev. B*, Vol. 87, May 2013, pp. 201201.

[100] Michaeli, K. and Fu, L., "Spin-Orbit Locking as a Protection Mechanism of the Odd-Parity Superconducting State against Disorder," *Phys. Rev. Lett.*, Vol. 109, Oct 2012, pp. 187003.

[101] Kriener, M., Segawa, K., Sasaki, S., and Ando, Y., "Anomalous suppression of the superfluid density in the $\mathrm{Cu}_x\mathrm{Bi_2Se_3}$ superconductor upon progressive Cu intercalation," *Phys. Rev. B*, Vol. 86, Nov 2012, pp. 180505.

[102] Foster, M. S., Xie, H.-Y., and Chou, Y.-Z., "Topological protection, disorder, and interactions: Survival at the surface of three-dimensional topological superconductors," *Phys. Rev. B*, Vol. 89, Apr 2014, pp. 155140.

[103] Nagai, Y., Ota, Y., and Machida, M., "Nonmagnetic impurity effects in a three-dimensional topological superconductor: From p- to s-wave behaviors," *Phys. Rev. B*, Vol. 89, Jun 2014, pp. 214506.

[104] Nagai, Y., "Robust superconductivity with nodes in the superconducting topological insulator $\mathrm{Cu}_x\mathrm{Bi}_2\mathrm{Se}_3$: Zeeman orbital field and nonmagnetic impurities," *Phys. Rev. B*, Vol. 91, Feb 2015, pp. 060502.

[105] Kirzhner, T., Lahoud, E., Chaska, K., Salman, Z., and Kanigel, A., "Point-contact spectroscopy of $\mathrm{Cu}_{0.2}\mathrm{Bi}_2\mathrm{Se}_3$ single crystals," *Physical Review B*, Vol. 86, No. 6, 2012, pp. 064517.

[106] Chen, X., Huan, C., Hor, Y., de Melo, C., and Jiang, Z., "Point-contact Andreev reflection spectroscopy of candidate topological superconductor $\mathrm{Cu}_{0.25}\mathrm{Bi}_2\mathrm{Se}_3$," *arXiv preprint arXiv:1210.6054*, 2012.

[107] Ando, Y., Segawa, K., Sasaki, S., and Kriener, M., "Experimental studies of the topological superconductor $\mathrm{Cu}_x\mathrm{Bi}_2\mathrm{Se}_3$," *Journal of Physics: Conference Series*, Vol. 449, IOP Publishing, 2013, p. 012033.

[108] Yamakage, A., Yada, K., Sato, M., and Tanaka, Y., "Theory of tunneling conductance and surface-state transition in superconducting topological insulators," *Phys. Rev. B*, Vol. 85, May 2012, pp. 180509.

[109] Peng, H., De, D., Wu, Z., and Diaz-Pinto, C., "Observation of multiple superconducting gaps in $\mathrm{Fe}_{1+y}\mathrm{Te}_{1-x}\mathrm{Se}_x$ via a nanoscale approach to point-contact spectroscopy," *Journal of Physics: Condensed Matter*, Vol. 24, No. 45, 2012, pp. 455703.

[110] Daghero, D. and Gonnelli, R., "Probing multiband superconductivity by point-contact spectroscopy," *Superconductor Science and Technology*, Vol. 23, No. 4, 2010, pp. 043001.

[111] Mizushima, T., Yamakage, A., Sato, M., and Tanaka, Y., "Dirac-fermion-induced parity mixing in superconducting topological insulators," *Phys. Rev. B*, Vol. 90, Nov 2014, pp. 184516.

[112] Takami, S., Yada, K., Yamakage, A., Sato, M., and Tanaka, Y., "Quasi-classical theory of tunneling spectroscopy in superconducting topological insulator," *Journal of the Physical Society of Japan*, Vol. 83, No. 6, 2014, pp. 064705.

[113] Hashimoto, T., Yada, K., Yamakage, A., Sato, M., and Tanaka, Y., "Effect of Fermi surface evolution on superconducting gap in superconducting topological insulator," *Superconductor Science and Technology*, Vol. 27, No. 10, 2014, pp. 104002.

[114] Ando, Y. and Fu, L., "Topological crystalline insulators and topological superconductors: from concepts to materials," *Annu. Rev. Condens. Matter Phys.*, Vol. 6, No. 1, 2015, pp. 361–381.

[115] Shiozaki, K. and Sato, M., "Topology of crystalline insulators and superconductors," *Phys. Rev. B*, Vol. 90, Oct 2014, pp. 165114.

[116] Hosur, P., Ghaemi, P., Mong, R. S. K., and Vishwanath, A., "Majorana Modes at the Ends of Superconductor Vortices in Doped Topological Insulators," *Phys. Rev. Lett.*, Vol. 107, Aug 2011, pp. 097001.

[117] Yang, S. A., Pan, H., and Zhang, F., "Dirac and Weyl Superconductors in Three Dimensions," *Phys. Rev. Lett.*, Vol. 113, Jul 2014, pp. 046401.

[118] Hao, L. and Lee, T. K., "Surface spectral function in the superconducting state of a topological insulator," *Phys. Rev. B*, Vol. 83, Apr 2011, pp. 134516.

[119] Yip, S.-K., "Models of superconducting Cu:Bi_2Se_3: Single- versus two-band description," *Phys. Rev. B*, Vol. 87, Mar 2013, pp. 104505.

[120] Brydon, P. M. R., Das Sarma, S., Hui, H.-Y., and Sau, J. D., "Odd-parity superconductivity from phonon-mediated pairing: Application to $Cu_xBi_2Se_3$," *Phys. Rev. B*, Vol. 90, Nov 2014, pp. 184512.

[121] Hao, L., Wang, G.-L., Lee, T.-K., Wang, J., Tsai, W.-F., and Yang, Y.-H., "Anisotropic spin-singlet pairings in $Cu_xBi_2Se_3$ and Bi_2Te_3," *Phys. Rev. B*, Vol. 89, Jun 2014, pp. 214505.

[122] Chen, L. and Wan, S., "Surface spectral function of momentum-dependent pairing potentials in a topological insulator: application to CuxBi2Se3," *Journal of Physics: Condensed Matter*, Vol. 25, No. 21, 2013, pp. 215702.

[123] Wan, X. and Savrasov, S. Y., "Turning a band insulator into an exotic superconductor," *arXiv preprint arXiv:1308.5615*, 2013.

[124] Yip, S., "Pseudospin bases for a model of Cu: Bi_2Se_3," *arXiv preprint arXiv:1609.04152*, 2016.

[125] Roy, B., Alavirad, Y., and Sau, J. D., "Global phase diagram of a three dimensional dirty topological superconductor," *arXiv preprint arXiv:1604.01390*, 2016.

[126] Nagai, Y., Nakamura, H., and Machida, M., "Rotational isotropy breaking as proof for spin-polarized Cooper pairs in the topological superconductor $Cu_xBi_2Se_3$," *Phys. Rev. B*, Vol. 86, Sep 2012, pp. 094507.

[127] Tanaka, Y., Nakayama, K., Souma, S., Sato, T., Xu, N., Zhang, P., Richard, P., Ding, H., Suzuki, Y., Das, P., Kadowaki, K., and Takahashi, T., "Evolution of electronic structure upon Cu doping in the topological insulator Bi_2Se_3," *Phys. Rev. B*, Vol. 85, Mar 2012, pp. 125111.

[128] Kondo, T., Nakashima, Y., Ota, Y., Ishida, Y., Malaeb, W., Okazaki, K., Shin, S., Kriener, M., Sasaki, S., Segawa, K., and Ando, Y., "Anomalous Dressing of Dirac Fermions in the Topological Surface State of Bi_2Se_3, Bi_2Te_3, and Cu-Doped Bi_2Se_3," *Phys. Rev. Lett.*, Vol. 110, May 2013, pp. 217601.

[129] Ribak, A., Chashka, K. B., Lahoud, E., Naamneh, M., Rinott, S., Ein-Eli, Y., Plumb, N. C., Shi, M., Rienks, E., and Kanigel, A., "Internal pressure in superconducting Cu-intercalated Bi_2Se_3," *Phys. Rev. B*, Vol. 93, Feb 2016, pp. 064505.

[130] He-Mian, Y., Chao-Yu, C., Xuan, S., Zhuo-Jin, X., Ya, F., Ai-Ji, L., Ying-Ying, P., Shao-Long, H., Lin, Z., Guo-Dong, L., et al., "Electronic structure, irreversibility line and magnetoresistance of $Cu_{0.3}Bi_2Se_3$ superconductor," *Chinese Physics Letters*, Vol. 32, No. 6, 2015, pp. 067401.

[131] Wang, Y.-L., Xu, Y., Jiang, Y.-P., Liu, J.-W., Chang, C.-Z., Chen, M., Li, Z., Song, C.-L., Wang, L.-L., He, K., Chen, X., Duan, W.-H., Xue, Q.-K., and Ma, X.-C., "Structural defects and electronic properties of the Cu-doped topological insulator Bi_2Se_3," *Phys. Rev. B*, Vol. 84, Aug 2011, pp. 075335.

[132] Mann, C., West, D., Miotkowski, I., Chen, Y. P., Zhang, S., and Shih, C.-K., "Observation of Coulomb repulsion between Cu intercalants in $Cu_xBi_2Se_3$," *Phys. Rev. B*, Vol. 89, Apr 2014, pp. 155312.

[133] Sandilands, L. J., Reijnders, A. A., Kriener, M., Segawa, K., Sasaki, S., Ando, Y., and Burch, K. S., "Doping-dependent charge dynamics in $Cu_xBi_2Se_3$," *Phys. Rev. B*, Vol. 90, Sep 2014, pp. 094503.

[134] Tao, D., Rui-Hua, Y., You-Guo, S., and Nan-Lin, W., "Temperature-Induced Plasma Frequency Shift in Bi_2Te_3 and $Cu_xBi_2Se_3$," *Chinese Physics Letters*, Vol. 30, No. 12, 2013, pp. 127801.

[135] Das, T., Bhattacharyya, S., Joshi, B. P., Thamizhavel, A., and Ramakrishnan, S., "Direct evidence of intercalation in a topological insulator turned superconductor," *Materials Letters*, Vol. 93, 2013, pp. 370–373.

[136] Shimizu, Y., Yamakage, A., and Nomura, K., "Quantum thermal Hall effect of Majorana fermions on the surface of superconducting topological insulators," *Phys. Rev. B*, Vol. 91, May 2015, pp. 195139.

[137] Shirasawa, T., Sugiki, M., Hirahara, T., Aitani, M., Shirai, T., Hasegawa, S., and Takahashi, T., "Structure and transport properties of Cu-doped Bi_2Se_3 films," *Phys. Rev. B*, Vol. 89, May 2014, pp. 195311.

[138] Fu, L., "Hexagonal Warping Effects in the Surface States of the Topological Insulator Bi_2Te_3," *Phys. Rev. Lett.*, Vol. 103, Dec 2009, pp. 266801.

[139] Chen, Y., Analytis, J., Chu, J.-H., Liu, Z., Mo, S.-K., Qi, X.-L., Zhang, H., Lu, D., Dai, X., Fang, Z., et al., "Experimental realization of a three-dimensional topological insulator, Bi_2Te_3," *Science*, Vol. 325, No. 5937, 2009, pp. 178–181.

[140] Nagai, Y., "Field-Angle-Dependent Low-Energy Excitations around a Vortex in the Superconducting Topological Insulator $\mathrm{Cu}_x\mathrm{Bi}_2\mathrm{Se}_3$," *Journal of the Physical Society of Japan*, Vol. 83, No. 6, 2014, pp. 063705.

[141] Venderbos, J. W. F., Kozii, V., and Fu, L., "Identification of nematic superconductivity from the upper critical field," *Phys. Rev. B*, Vol. 94, Sep 2016, pp. 094522.

[142] Sakakibara, T., Yamada, A., Custers, J., Yano, K., Tayama, T., Aoki, H., and Machida, K., "Nodal structures of heavy fermion superconductors probed by the specific-heat measurements in magnetic fields," *Journal of the Physical Society of Japan*, Vol. 76, No. 5, 2007, pp. 051004.

[143] Vekhter, I., Hirschfeld, P. J., Carbotte, J. P., and Nicol, E. J., "Anisotropic thermodynamics of d-wave superconductors in the vortex state," *Phys. Rev. B*, Vol. 59, Apr 1999, pp. R9023–R9026.

[144] Matsuda, Y., Izawa, K., and Vekhter, I., "Nodal structure of unconventional superconductors probed by angle resolved thermal transport measurements," *Journal of Physics: Condensed Matter*, Vol. 18, No. 44, 2006, pp. R705.

[145] Shruti, V., Neha, P., Srivastava, P., Patnaik, S., et al., "Superconductivity by Sr intercalation in the layered topological insulator $\mathrm{Bi}_2\mathrm{Se}_3$," *Phys Rev B*, Vol. 92, No. 020506, 2015, pp. 020506.

[146] Neupane, M., Ishida, Y., Sankar, R., Zhu, J.-X., Sanchez, D. S., Belopolski, I., Xu, S.-Y., Alidoust, N., Hosen, M. M., Shin, S., et al., "Electronic structure and relaxation dynamics in a superconducting topological material," *Scientific reports*, Vol. 6, 2016.

[147] Nikitin, A., Pan, Y., Huang, Y., Naka, T., and de Visser, A., "High-pressure study of the basal-plane anisotropy of the upper critical field of the topological superconductor $\mathrm{Sr}_x\mathrm{Bi}_2\mathrm{Se}_3$," *Physical Review B*, Vol. 94, No. 14, 2016, pp. 144516.

[148] Du, G., Li, Y., Schneeloch, J., Zhong, R., Gu, G., Yang, H., and Wen, H.-H., "Superconductivity with two-fold symmetry in topological superconductor $\mathrm{Sr}_x\mathrm{Bi}_2\mathrm{Se}_3$," *arXiv preprint arXiv:1607.06357*, 2016.

[149] Novoselov, K. S., Geim, A. K., Morozov, S., Jiang, D., Katsnelson, M., Grigorieva, I., Dubonos, S., and Firsov, A., "Two-dimensional gas of massless Dirac fermions in graphene," *nature*, Vol. 438, No. 7065, 2005, pp. 197–200.

[150] Li, G., Xiang, Z., Yu, F., Asaba, T., Lawson, B., Cai, P., Tinsman, C., Berkley, A., Wolgast, S., Eo, Y. S., et al., "Two-dimensional Fermi surfaces in Kondo insulator SmB_6," *Science*, Vol. 346, No. 6214, 2014, pp. 1208–1212.

[151] Shruti, Maurya, V., Srivastava, P., Patnaik, S., Chitra, R., Bhattacharya, S., and Sahoo, N., "Emergence of superconductivity in topological insulator $\mathrm{Bi}_2\mathrm{Se}_3$ by Sr intercalation," *AIP Conference Proceedings*, Vol. 1731, AIP Publishing, 2016, p. 130046.

[152] Sun, L., Chen, X.-J., Guo, J., Gao, P., Huang, Q.-Z., Wang, H., Fang, M., Chen, X., Chen, G., Wu, Q., et al., "Re-emerging superconductivity at 48 kelvin in iron chalcogenides," *Nature*, Vol. 483, No. 7387, 2012, pp. 67–69.

[153] Vilaplana, R., Santamaría-Pérez, D., Gomis, O., Manjón, F., González, J., Segura, A., Muñoz, A., Rodríguez-Hernández, P., Pérez-González, E., Marín-Borrás, V., et al., "Structural and vibrational study of Bi_2Se_3 under high pressure," *Physical Review B*, Vol. 84, No. 18, 2011, pp. 184110.

[154] Manikandan, K., Shruti, Neha, P., Maurya, V., Kalai Selvan, G., Wang, B., Uwatoko, Y., Ishigaki, K., Jha, R., Awana, V. P. S., Arumugam, S., and Patnaik, S., "Evidence for conventional superconductivity in $Sr_{0.1}Bi_2Se_3$ from high pressure studies," *ArXiv e-prints:1702.08829*, Feb. 2017.

[155] Wolgast, S., Eo, Y. S., Öztürk, T., Li, G., Xiang, Z., Tinsman, C., Asaba, T., Lawson, B., Yu, F., Allen, J., et al., "Magnetotransport measurements of the surface states of samarium hexaboride using Corbino structures," *Physical Review B*, Vol. 92, No. 11, 2015, pp. 115110.

[156] Yuan, N. F., He, W.-Y., and Law, K., "Superconductivity-Induced Ferromagnetism and Weyl Superconductivity in Nb-doped Bi_2Se_3," *arXiv preprint arXiv:1608.05825*, 2016.

[157] Chirolli, L., de Juan, F., and Guinea, F., "Time-Reversal symmetry breaking superconductivity in Dirac materials: application to $Nb_xBi_2Se_3$," *arXiv preprint arXiv:1611.02173*, 2016.

[158] Saxena, S., Agarwal, P., Ahilan, K., Grosche, F., Haselwimmer, R., Steiner, M., Pugh, E., Walker, I., Julian, S., Monthoux, P., et al., "Superconductivity on the border of itinerant-electron ferromagnetism in UGe_2," *Nature*, Vol. 406, No. 6796, 2000, pp. 587–592.

[159] Aoki, D., Huxley, A., Ressouche, E., Braithwaite, D., Flouquet, J., Brison, J.-P., Lhotel, E., and Paulsen, C., "Coexistence of superconductivity and ferromagnetism in $URhGe$," *Nature*, Vol. 413, No. 6856, 2001, pp. 613–616.

[160] Huy, N., Gasparini, A., De Nijs, D., Huang, Y., Klaasse, J., Gortenmulder, T., de Visser, A., Hamann, A., Görlach, T., and Löhneysen, H. v., "Superconductivity on the border of weak itinerant ferromagnetism in $UCoGe$," *Physical review letters*, Vol. 99, No. 6, 2007, pp. 067006.

[161] Kobayashi, S., Oike, H., Takeda, M., and Itoh, F., "Central peak position in magnetization hysteresis loops of ferromagnet/superconductor/ferromagnet trilayered films," *Physical Review B*, Vol. 66, No. 21, 2002, pp. 214520.

[162] Schnyder, A. P. and Brydon, P. M., "Topological surface states in nodal superconductors," *Journal of Physics: Condensed Matter*, Vol. 27, No. 24, 2015, pp. 243201.

[163] Li, L., *Torque magnetometry in unconventional superconductors*, Princeton University, 2008.

[164] Ashcroft, N. W., Mermin, N. D., and Rodriguez, S., *Solid state physics*, AAPT, 1978.

[165] Roth, L. M. and Argyres, P. N., "Magnetic quantum effects," *Semiconductors and Semimetals*, Vol. 1, 1966, pp. 159–202.

[166] de Waele, A. T., "Basic operation of cryocoolers and related thermal machines," *Journal of Low Temperature Physics*, Vol. 164, No. 5, 2011, pp. 179–236.

[167] Moore, J. E., "The birth of topological insulators," *Nature*, Vol. 464, No. 7286, 2010, pp. 194–198.

[168] Scanlon, D. O., King, P., Singh, R., De La Torre, A., Walker, S. M., Balakrishnan, G., Baumberger, F., and Catlow, C., "Controlling Bulk Conductivity in Topological Insulators: Key Role of Anti-Site Defects," *Advanced Materials*, Vol. 24, No. 16, 2012, pp. 2154–2158.

[169] Tichỳ, L. and Horak, J., "Nonparabolicity of the conduction band and anisotropy of the electron effective mass in n-Bi_2Se_3 single crystals," *Physical Review B*, Vol. 19, No. 2, 1979, pp. 1126.

[170] Eto, K., Ren, Z., Taskin, A., Segawa, K., and Ando, Y., "Angular-dependent oscillations of the magnetoresistance in Bi_2Se_3 due to the three-dimensional bulk Fermi surface," *Physical Review B*, Vol. 81, No. 19, 2010, pp. 195309.

[171] Köhler, H. and Fischer, H., "Investigation of the conduction band fermi surface in Bi_2Se_3 at high electron concentrations," *physica status solidi (b)*, Vol. 69, No. 2, 1975, pp. 349–357.

[172] Analytis, J. G., Chu, J.-H., Chen, Y., Corredor, F., McDonald, R. D., Shen, Z., and Fisher, I. R., "Bulk Fermi surface coexistence with Dirac surface state in Bi_2Se_3: A comparison of photoemission and Shubnikov–de Haas measurements," *Physical Review B*, Vol. 81, No. 20, 2010, pp. 205407.

[173] Lifshitz, I. et al., "Anomalies of electron characteristics of a metal in the high pressure region," *Sov. Phys. JETP*, Vol. 11, No. 5, 1960, pp. 1130–1135.

[174] Volovik, G., "Topological Lifshitz transitions," *Low Temperature Physics*, Vol. 43, No. 1, 2017, pp. 47–55.

[175] Peierls, R., "Zur kinetischen theorie der wärmeleitung in kristallen," *Annalen der Physik*, Vol. 395, No. 8, 1929, pp. 1055–1101.

[176] Berber, S., Kwon, Y.-K., and Tománek, D., "Unusually High Thermal Conductivity of Carbon Nanotubes," *Phys. Rev. Lett.*, Vol. 84, May 2000, pp. 4613–4616.

[177] Abrikosov, A. A. and Beknazarov, A., *Fundamentals of the Theory of Metals*, Vol. 1, North-Holland Amsterdam, 1988.

[178] Egorov, V. and Fedorov, A., "Thermopower of lithium-magnesium alloys at the 24-order transition," *Zh. Eksp. Teor. Fiz*, Vol. 85, 1983, pp. 1647–1657.

[179] Reitz, J. R., "Magnetic breakdown in metals," *Journal of Physics and Chemistry of Solids*, Vol. 25, No. 1, 1964, pp. 53–58.

[180] Sigrist, M. and Ueda, K., "Phenomenological theory of unconventional superconductivity," *Rev. Mod. Phys.*, Vol. 63, Apr 1991, pp. 239–311.

[181] Movshovich, R., Jaime, M., Thompson, J. D., Petrovic, C., Fisk, Z., Pagliuso, P. G., and Sarrao, J. L., "Unconventional Superconductivity in $\mathrm{CeIrI}n_5$ and CeCoIn_5: Specific Heat and Thermal Conductivity Studies," *Phys. Rev. Lett.*, Vol. 86, May 2001, pp. 5152–5155.

[182] Hasselbach, K., Kirtley, J. R., and Flouquet, J., "Symmetry of the gap in superconducting $\mathrm{URu_2Si_2}$," *Phys. Rev. B*, Vol. 47, Jan 1993, pp. 509–512.

[183] Mao, Z. Q., Maeno, Y., NishiZaki, S., Akima, T., and Ishiguro, T., "In-Plane Anisotropy of Upper Critical Field in $\mathrm{Sr_2RuO_4}$," *Phys. Rev. Lett.*, Vol. 84, Jan 2000, pp. 991–994.

[184] Monceau, P. and Briggs, A., "Quantum oscillations in $\mathrm{NbSe_3}$," *Journal of Physics C: Solid State Physics*, Vol. 11, No. 11, 1978, pp. L465.

[185] Fleming, R., Polo Jr, J., and Coleman, R., "Oscillatory magnetotransport in $\mathrm{NbSe_3}$ and $\mathrm{TaSe_3}$," *Physical Review B*, Vol. 17, No. 4, 1978, pp. 1634.

[186] Audouard, A., Richard, J., Dubois, S., Ulmet, J., and Askenazy, S., "High field magnetoresistance oscillations in $\mathrm{NbSe_3}$," *Synthetic metals*, Vol. 56, No. 2-3, 1993, pp. 2629–2634.

[187] Corcoran, R., Meeson, P., Onuki, Y., Probst, P.-A., Springford, M., Takita, K., Harima, H., Guo, G., and Gyorffy, B., "Quantum oscillations in the mixed state of the type II superconductor 2H-$\mathrm{NbSe_2}$," *Journal of Physics: Condensed Matter*, Vol. 6, No. 24, 1994, pp. 4479.

[188] Graebner, J. E. and Robbins, M., "Fermi-Surface Measurements in Normal and Superconducting 2H-$\mathrm{NbSe_2}$," *Physical Review Letters*, Vol. 36, No. 8, 1976, pp. 422.

[189] Scott, G. and Springford, M., "The Fermi surface in niobium," *Proceedings of the Royal Society of London A: Mathematical, Physical and Engineering Sciences*, Vol. 320, The Royal Society, 1970, pp. 115–130.

[190] Halloran, M., Condon, J., Graebner, J., Kunzier, J., and Hsu, F., "Experimental study of the fermi surfaces of niobium and tantalum," *Physical Review B*, Vol. 1, No. 2, 1970, pp. 366.

[191] Analytis, J. G., Chu, J.-H., McDonald, R. D., Riggs, S. C., and Fisher, I. R., "Enhanced Fermi-Surface Nesting in Superconducting $\mathrm{BaFe_2(As_{1-x}P_x)_2}$ Revealed by the de Haas-van Alphen Effect," *Phys. Rev. Lett.*, Vol. 105, Nov 2010, pp. 207004.

[192] Paglione, J. and Greene, R. L., "High-temperature superconductivity in iron-based materials," *Nature physics*, Vol. 6, No. 9, 2010, pp. 645–658.

[193] Hirschfeld, P., Korshunov, M., and Mazin, I., "Gap symmetry and structure of Fe-based superconductors," *Reports on Progress in Physics*, Vol. 74, No. 12, 2011, pp. 124508.

[194] Zak, J., "Berry's phase for energy bands in solids," *Phys. Rev. Lett.*, Vol. 62, Jun 1989, pp. 2747–2750.

[195] King-Smith, R. D. and Vanderbilt, D., "Theory of polarization of crystalline solids," *Phys. Rev. B*, Vol. 47, Jan 1993, pp. 1651–1654.

[196] Bean, C. P., "Magnetization of hard superconductors," *Physical Review Letters*, Vol. 8, No. 6, 1962, pp. 250.

[197] Bean, C. P., "Magnetization of high-field superconductors," *Reviews of modern physics*, Vol. 36, No. 1, 1964, pp. 31.